PFC/RR-95-8 DOE/ET-51013-314

Neutral Particle Dynamics in the Alcator C-Mod Tokamak

Artur Niemczewski

August 1995

This work was supported by the U. S. Department of Energy Contract No. DE-AC02-78ET51013. Reproduction, translation, publication, use and disposal, in whole or in part by or for the United States government is permitted.

NEUTRAL PARTICLE DYNAMICS IN THE ALCATOR C-MOD TOKAMAK

by

Artur P. Niemczewski

Master of Science in Engineering, Warsaw Technical University, 1989
Master of Science in Technology and Policy, Massachusetts Institute of Technology, 1995

Submitted to the Department of Nuclear Engineering
in partial fulfillment of the requirements for the degree of

Doctor of Philosophy

at the

Massachusetts Institute of Technology

September 1995

Signature of Author _____
Department of Nuclear Engineering
July 26, 1995

Certified by _____
Dr. Bruce Lipschultz
Principal Research Scientist
Thesis Supervisor

Certified by _____
Dr. Garry M. McCracken
Research Scientist
Thesis Supervisor

Certified by _____
Professor Ian H. Hutchinson
Department of Nuclear Engineering
Thesis Reader

Accepted by _____
Professor Jeffrey P. Freidberg
Department of Nuclear Engineering
Chairman, Departmental Committee on Graduate Studies

NEUTRAL PARTICLE DYNAMICS IN THE ALCATOR C-MOD TOKAMAK

by

Artur P. Niemczewski

Submitted to the MIT Department of Nuclear Engineering
on July 26, 1995 in partial fulfillment of the requirements for the degree of

Doctor of Philosophy

Abstract

This thesis presents an experimental study of neutral particle dynamics in Alcator C-Mod – a high power- and particle-density tokamak with an advanced poloidal divertor. The primary diagnostic used in the study is a set of six neutral pressure gauges, including special-purpose gauges built for *in situ* tokamak operation.

While a low main chamber neutral pressure coincides with high plasma confinement regimes, a high divertor pressure is required for heat and particle flux dispersion in future devices such as ITER. Thus we examine conditions that optimize divertor compression, defined here as a divertor-to-midplane pressure ratio. We find that both pressures depend primarily on the edge plasma regimes defined by the scrape-off-layer heat transport. While the maximum divertor pressure ($p_{div} \approx$30-60 mTorr) is achieved at high core plasma densities ($\overline{n}_e \approx 2\text{-}4 \cdot 10^{20}$ m^{-3}), corresponding to the detached divertor state, the maximum compression (~70) is achieved in the high-recycling regime. Variations in the divertor geometry have a weaker effect on the neutral pressures. For otherwise similar plasmas the divertor pressure and compression are maximized when the strike point is located at the bottom of the vertical target plate.

We introduce a simple flux balance model, which allows us to explain the divertor neutral pressure across a range of plasma densities. In particular, a high pressure sustained in the detached divertor (despite a considerable drop in the recycling

source) can be explained by scattering of neutrals off the cold plasma plugging the divertor throat. Because neutrals are confined in the divertor through scattering and ionization processes (provided the mean-free-paths are much shorter than a typical escape distance) tight mechanical baffling is unnecessary. The analysis suggests that two simple structural modifications may increase the divertor compression in Alcator C-Mod by a factor of ~5. Widening the divertor throat would increase the divertor recycling source, while closing leaks in the divertor structure would eliminate a significant neutral loss mechanism.

Thesis Supervisor:	Dr. Bruce Lipschultz Principal Research Scientist, Plasma Fusion Center
Thesis Supervisor:	Dr. Garry M. McCracken Research Scientist, Plasma Fusion Center
Thesis Reader:	Prof. Ian H. Hutchinson Professor, Department of Nuclear Engineering

Acknowledgments

It has been my great privilege over the years to be a member of the Alcator-group – a team of people with common motivation, goals, achievements, and, sometimes, problems. I would like to acknowledge the effort of every single member of the Alcator-team – students, scientists, engineers, and technicians – without whose dedication and hard work we would have never pushed the frontiers of science. It is within the Alcator-team where I have learned in practice the meaning of the word "team-work".

I wish to thank Bruce Lipschultz, Garry McCracken, and Brian LaBombard for their help and guidance over the years and for their infinite patience in reading numerous lengthy revisions. I am very thankful to Ian Hutchinson for valuable comments significantly improving the quality of the text. I am also grateful to Sergei Krascheninnikov for many fruitful discussions. I would like to thank my fellow graduate students in the Alcator-group, who have made the years at MIT feel shorter. My friendship will always stay with Mike.

Most importantly, my loving thanks go to my wife, Paulina and my father, Lucjan, the two dearest people in my life, who have given me their love and support in moments of frustration.

Table of Contents

List of Figures

List of Tables

Chapter 1

Motivation and Goals of the Thesis

1.1 Plasma-wall interactions

Mankind, in its quest for controlled nuclear fusion power, unfortunately cannot exactly imitate the sun. Any laboratory fusion plasma, even when confined by magnetic fields, always interacts with some material boundaries, for example, the walls of a vessel in which it is contained. The leakage of energetic particles across the confining magnetic field usually causes damage to plasma facing components of the container and contaminates the plasma itself with released wall material. Therefore the scientific community devotes considerable effort to understanding and controlling these "plasma-wall" interactions to the best benefit (or the least harm) of fusion plasma performance and the integrity of the container. Stangeby and McCracken [1] provide a comprehensive review of the field, including the current state of knowledge and problems yet to be resolved.

Neutral particles (atoms and molecules) surrounding the electrically-charged plasma play an important role in the plasma-wall interactions. Heifetz [2] provides an extensive overview of neutral-plasma interactions. When properly controlled, the neutral gas can protect material surfaces from the impact of energetic particles leaving the plasma core. Thus understanding the neutral particle dynamics is of

paramount importance to the future development of magnetic fusion power. This motivated a research effort described in this thesis aimed at an experimental study of neutral particle behavior in the vicinity of a thermonuclear plasma.

Among currently investigated fusion reactor designs, a reactor based on a tokamak principle appears to be the most promising in achieving the fusion ignition [3]. An important development of the tokamak (and stellarator) concept was the introduction of the magnetic divertor configuration as a means to localize and control plasma-surface interactions [4]. It is now considered that any future magnetic fusion reactor device (either tokamak or stellarator) will most likely take advantage of the divertor concept [5]. Thus the study of neutral particle dynamics in a tokamak divertor is an important issue of fusion research.

1.2 International Tokamak Experimental Reactor

Magnetic confinement fusion research, over its 40 year history, has nearly approached the break-even conditions. The next step machine, International Tokamak Experimental Reactor (ITER), will most likely reach fusion ignition conditions and will produce a steady-state thermonuclear burning plasma. Since the ITER project is an international cooperation of US, Japan, Russia, and Euratom the national fusion programs are directed in the most part towards the support of ITER research goals. The Conceptual Design Activities (CDA) phase of ITER design left unresolved the problem of power exhaust in the machine divertor. During the current Engineering Design Activities (EDA) phase, the problem of the power exhaust attracts many research efforts. The conventional

CDA tokamak design would result in a 40-60 MW/m^2 peak surface power density, while the current engineering limit is 5 MW/m^2 [6].

Tilted target plates and swept strike zones provide only a partial solution to the heat-flux problem. A currently proposed "dynamic gas target" concept would rely on the power dispersion through radiation processes and momentum removal by a neutral gas cushion in front of the divertor target [7, 8]. This scheme requires a high neutral gas density to be sustained in the ITER divertor chamber. One of the main goals of this thesis is a study of the conditions that lead to a high neutral density in a tokamak divertor.

Results from a number of tokamaks [9, 10] indicate that high plasma confinement regimes require low neutral pressure near the vicinity of the plasma core. Similarly, experience from the Alcator C-Mod tokamak shows that the ohmic H-modes coincide with much lower main chamber neutral pressure (~0.01 mTorr D_2) than the corresponding L-mode discharges [11]. Therefore a high divertor pressure has to be accompanied by a low main chamber pressure. Divertor neutral compression ratio, defined as a ratio of the divertor to the midplane pressures, is proposed as a convenient measure of the divertor ability to confine neutral particles, and is also investigated throughout the thesis.

1.3 Alcator C-Mod and its role in the fusion program

MIT's Alcator C-Mod tokamak [12] (described in detail in the following chapter), with its near-reactor projected operating parameters and advanced shaped divertor configuration presents great opportunities to examine edge plasma physics issues relevant to the design of an ignition device such as ITER.

Among other areas, the research at Alcator C-Mod is actively pursuing a possible solution to the ITER heat-flux problem. For example the shaped Alcator C-Mod divertor allows investigation of tilted-vertical-plate, horizontal-plate, and slot divertor configurations (Fig. 2-6). In fact, the planned ITER divertor geometry is similar to that of the Alcator C-Mod shaped divertor. In addition, the parameter space accessible for Alcator C-Mod allows investigation of modes of operation that are of interest to ITER design. These include radiative- , gas-target-, recycling-, and detached-divertor operation.

1.4 Thesis goals

Fig. 1-1 shows an example of Alcator C-Mod plasma discharge during which a pressure of 60 mTorr is sustained in the divertor chamber in steady state for over 0.5 sec. This pressure corresponds to a neutral gas density exceeding the average core plasma density by an order of magnitude. Such high gas pressure is desired in a tokamak divertor to help disperse focused high heat and particle fluxes.

This thesis is devoted to experimental study, analysis, and understanding of the phenomena governing neutral particle dynamics and confinement in a tokamak divertor. These include plasma characteristics, geometry effects, and neutral particle transport, both in vacuum and across a background plasma. These questions, key to the ITER divertor design, attract a lot of modeling and theoretical effort. It seems, however that there are disproportionally few experimental studies

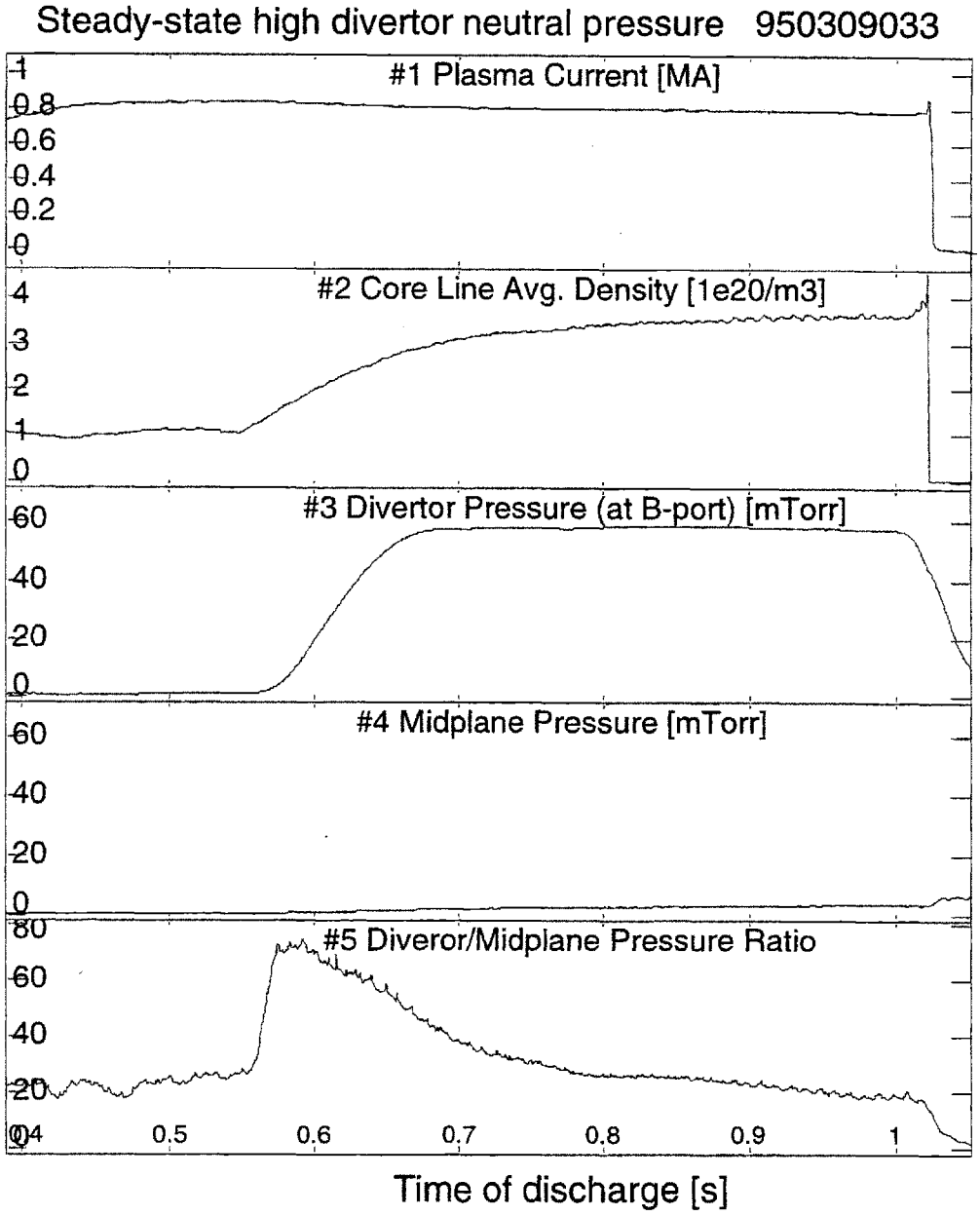

Fig. 1-1: Time history of a high plasma-density Alcator C-Mod discharge. A strong deuterium gas injection between t =0.55-0.7 sec causes the core plasma density (trace #2) to increase by about a factor of three but the divertor pressure (trace #3), to increase by about a factor of one hundred. While the 60 mTorr divertor pressure remains constant until the end of the discharge (disruption at t=1.02 sec), the midplane pressure (trace #4) gradually increases, leading to a decreasing divertor-to-midplane pressure ratio (trace #5). This thesis is devoted to experimental study of the phenomena governing the neutral particle dynamics, manifested, e.g., by pressure dependencies shown above.

of neutral particle behavior in the vicinity of a thermonuclear plasma. More specifically, no extensive experimental study exists (to the author's knowledge) examining the dependence of neutral particle confinement in the divertor on plasma characteristics and tokamak geometry. It is the author's hope that the work reported here will help validate numerical and theoretical efforts in the next generation tokamak design, and that it will contribute to our understanding of the neutral particle dynamics.

1.5 Thesis outline

The thesis combines experimental observations with interpretation and analysis. Its organization is such that the later parts draw on and expand concepts introduced in the earlier ones.

- Chapter 2 describes the Alcator C-Mod tokamak and some of its diagnostic systems that are relevant to the thesis. The emphasis is placed on the neutral pressure gauges installed in the tokamak.
- Chapter 3 describes a special-purpose ionization gauge developed for *in situ* Alcator C-Mod operation.
- Chapter 4 reports neutral pressure experimental observations, specifically the dependence on edge plasma regimes. Special emphasis is placed on divertor detachment.
- Chapter 5 introduces a divertor neutral particle flux balance model - a simple physics-based model aimed at interpreting the divertor neutral pressure dependence across the edge plasma regimes identified in Chapter 4.

- Chapter 6 summarizes experimental observations of neutral pressure dependence on plasma geometry, including ion B×∇B-drift direction, strike-point position, and flat- vs. vertical-plate divertor configurations.
- Chapter 7 uses the divertor neutral particle flux balance model to predict changes in neutral pressures upon planned modifications of the Alcator C-Mod divertor structure.
- Finally, Chapter 8 summarizes the major findings of the thesis. Most importantly, it proposes measures that lead to the optimal neutral particle confinement in the divertor chamber.
- In addition, Appendix A reports wall pumping studies.
- Appendices B, C, and D support the analysis in Chapter 5 with atomic physics data, a summary of the background plasma model, and a description of the diffusive neutral transport respectively.
- Appendix E investigates the impact of atom-ion momentum-transfer rate uncertainty on the divertor particle flux balance results.

Chapter 2

Alcator C-Mod and Particle Diagnostics

This chapter describes the Alcator C-Mod tokamak and selected diagnostic systems. Section 2.2 reviews the diagnostics (and tokamak fueling systems) relevant to the topics discussed in the thesis. Section 2.3 describes neutral pressure diagnostics, installed in the tokamak by the author. A separate chapter (Chapter 3) is devoted to a description of a special-purpose pressure gauge, developed for operation in the Alcator C-Mod magnetic field.

2.1 Alcator C-Mod - the tokamak and its divertor

Alcator C-Mod is a compact, high-field, diverted tokamak. It continues the tradition of high magnetic field tokamak research at MIT and is the third in the series of MIT tokamaks, following Alcator A, and Alcator C; the latter being the first tokamak in the world to reach the Lawson criterion [13, 14]. Alcator C-Mod is the first high-field tokamak with an advanced poloidal magnetic divertor [15].

Table 2-1 lists the major parameters of Alcator C-Mod tokamak [16, 17] while Fig. 2-1 presents the cross-section of the machine. All the magnets are made of copper, cooled by liquid nitrogen. The six-fold increase in copper conductivity at

Major parameters of Alcator C-Mod

Parameter	symbol	unit	achieved June 1995	designed/ predicted
Major radius	R	[m]		**0.67**
Minor radius	a	[m]		**0.21**
Toroidal field	B_t	[T]	**8**	**9**
Plasma current	I_p	[MA]	**1.2**	**3**
RF ion-cyclotron heating	P_{rf}	[MW]	**3.5**	**3.5-8**
Elongation	κ	[1]	**0.85-1.85**	**1-1.8**
Pulse length at B_t=5T	t	[sec]	**1**	**7**
Core electron density	n_e	[m-3]	**10^{21}**	**10^{21}**
Core electron temperature	T_e	[keV]	**6**	**3-6**
Divertor electron density	n_{div}	[m-3]	**10^{21}**	**10^{21}**
Divertor electron temperature	T_{div}	[eV]	**0.5 - 40**	**~20**

Table 2-1: Key parameters of the Alcator C-Mod tokamak. The achieved parameters (by Summer 1995) are compared with the design or expected values.

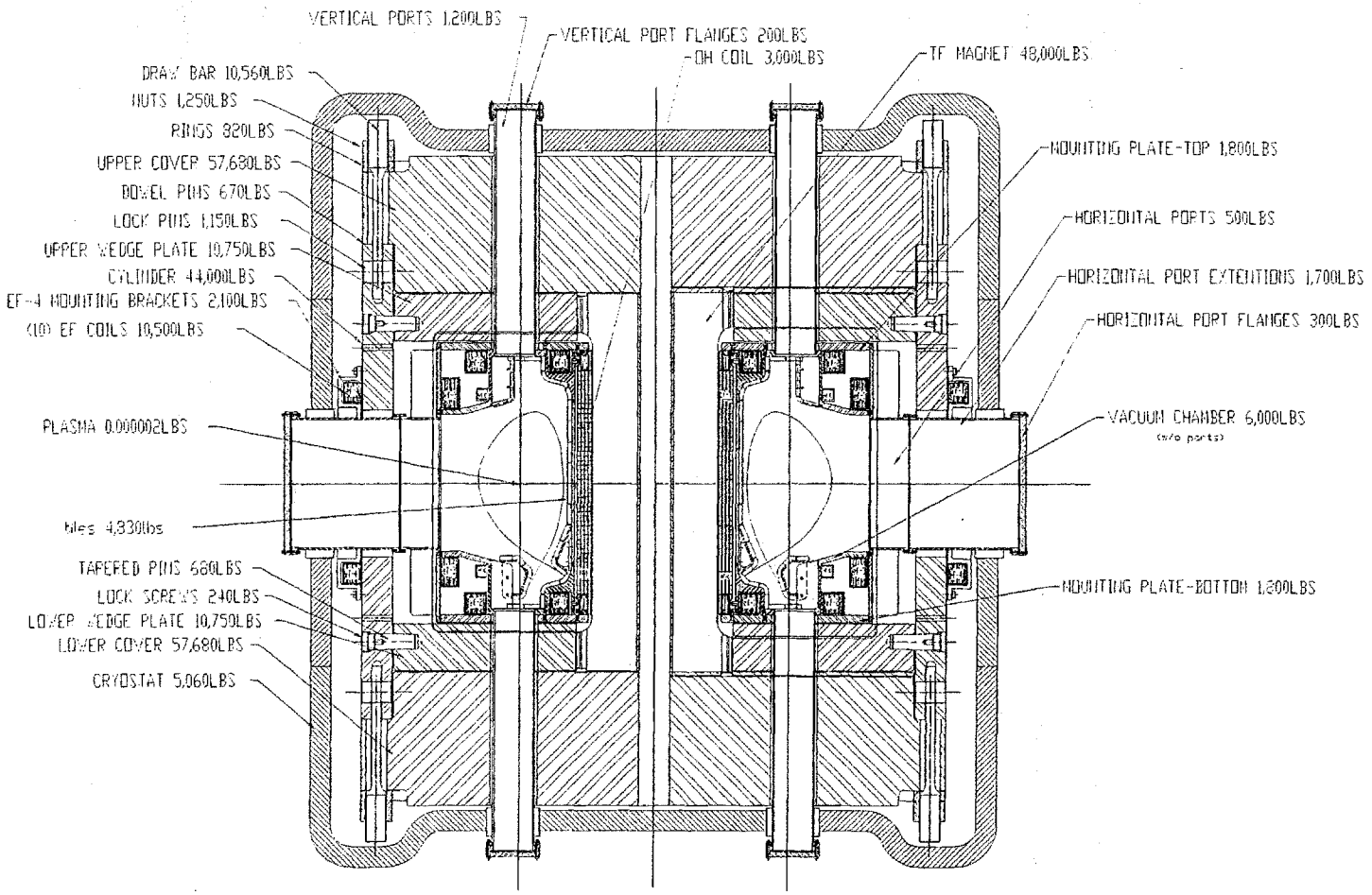

Fig. 2-1: Cross-section of the Alcator C-Mod tokamak. The vacuum crosses, carrying diagnostic feedthroughs are omitted for picture clarity. There are 20 crosses attached to top and bottom vertical ports, similar to the one shown on Fig. 2-12.

this temperature reduces ohmic losses and permits higher current density than in room-temperature coils. The toroidal field coils incorporate a unique engineering design of sliding finger joints between the different section of the coils [18]. This allows the vacuum vessel to be constructed as a single unit and the poloidal field coils to be positioned inside the TF coils. A massive stainless steel external superstructure is also shown on Fig 2-1: cylinder, bottom, and top covers. The TF coils bear directly against this superstructure, which is designed to resist the Lorentz force resulting from the production of the 9T toroidal magnetic field. Fig. 2-2 shows the ohmic transformer (OH) and the poloidal field (EF) coils. The ohmic transformer coil, wound over the central section of the TF coils, induces the plasma current. The poloidal field coils, mounted in the vacuum vessel pockets, maintain plasma magnetic equilibrium. Since the coils are cooled by liquid nitrogen the entire structure is surrounded by a thermally isolating cryostat.

One of the unique features of the Alcator C-Mod is its single-piece, thick-wall vacuum vessel. The vessel has sufficient mechanical integrity to support most of the poloidal field coils. The problems associated with the thick conducting vessel are large eddy current forces [19] and more complex control of plasma [20]. Future reactor designs will face similar problems. A 3D schematic of the vacuum vessel is shown on Fig. 2-3. There are 20 vertical (top and bottom) and 10 horizontal access ports used for plasma diagnostic and RF heating. The length of the access ports is dictated by the magnetic coils and tokamak superstructure design. The horizontal ports are just large enough (8" wide) to allow personnel access for work inside the vessel.

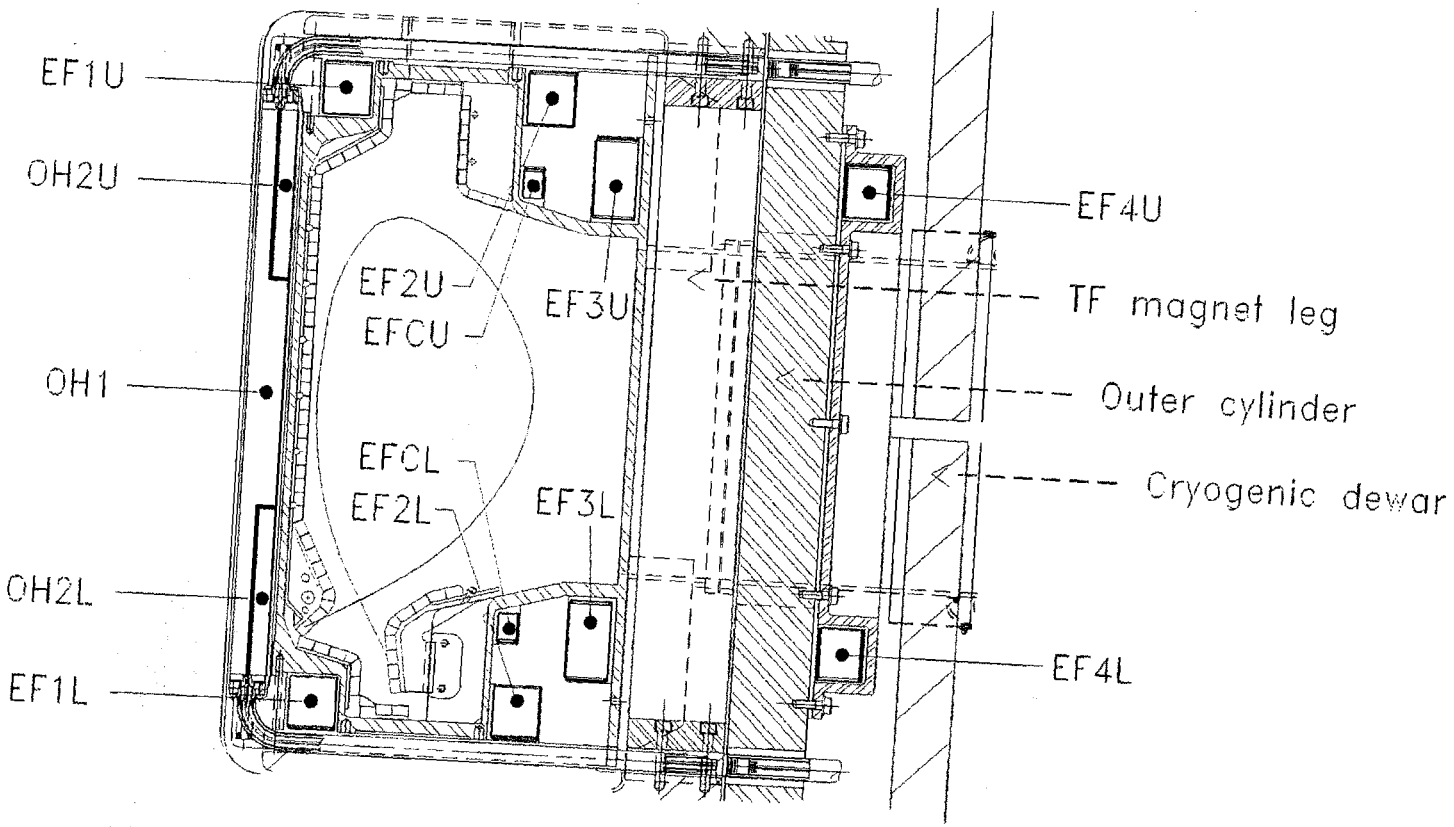

Fig. 2-2: The cut-away section of the Alcator C-Mod tokamak, showing the ohmic tranformer (OH) and poloidal field (EF) coils, which produce plasma current and magnetic equillibria.

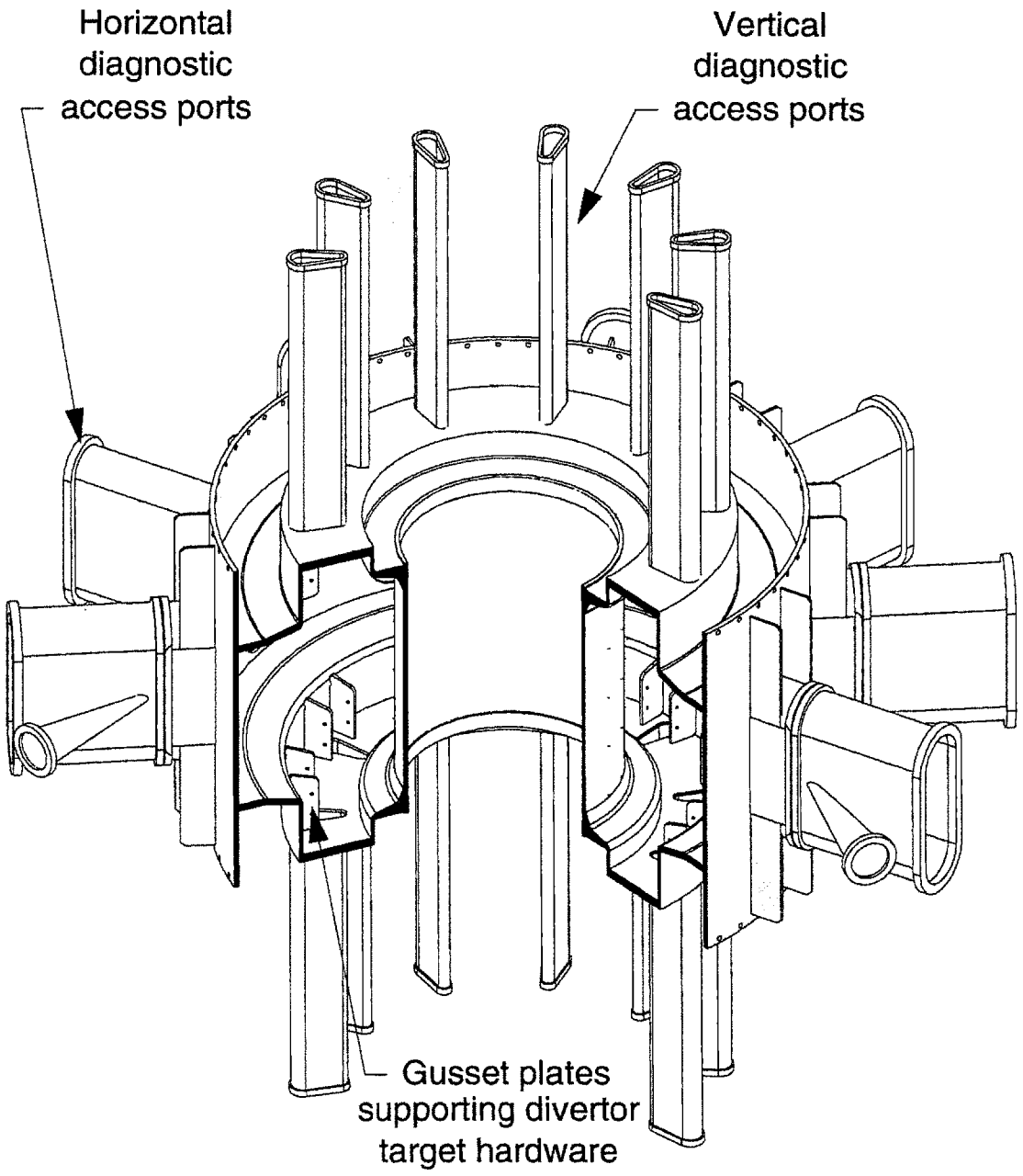

Fig. 2-3: Three-dimensional cross-section view of the Alcator C-Mod vacuum vessel. A considerable length of the horizontal and vertical diagnostic access ports is dictated by the tokamak coils and mechanical super structure (removed for clarity from this picture). The gusset plates, visible inside the vessel, support the divertor target hardware. The plates also divide the volume behind the divertor target into a set of non-toroidally continous "gas-boxes".

The "gusset" plates visible in the bottom corner of the vessel provide the mounting support for the divertor hardware. During operation the plates are hidden behind the divertor target plates (Fig. 2-4). The gusset plates also divide the volume behind the divertor target into 20 "gas boxes" such that this volume is no longer toroidally continuous. This feature is important for the results reported in this thesis because the divertor pressure measurements are performed in the volume behind the divertor target.

Fig 2-4 shows the poloidal cross-section of the vacuum vessel. The plasma facing areas are lined with 6834 molybdenum tiles [21], covering the stainless steel vessel walls. Approximately 50% of the main chamber, and ~100% of plasma interacting walls are lined with molybdenum. The magnetic and mechanical geometry allows a very flexible plasma configuration. Plasmas can be limited on the inner wall, diverted with the x-point at the top open divertor, or diverted with the x-point at the bottom closed divertor. The most frequently produced configurations are the inner wall limited and lower-divertor plasmas (the latter is shown on Fig. 2-4).

Fig. 2-5 shows a photograph of the Alcator C-Mod shaped divertor. The portion of the divertor where the outer target plate changes its orientation from approximately horizontal to vertical is referred to as the outer divertor "nose". The inner divertor "nose" is defined by analogy. A narrowing between the inner and outer divertor "noses" separates the divertor chamber from the main tokamak chamber. This narrowing also provides mechanical baffling of the divertor volume, thus helping to confine neutral particles there.

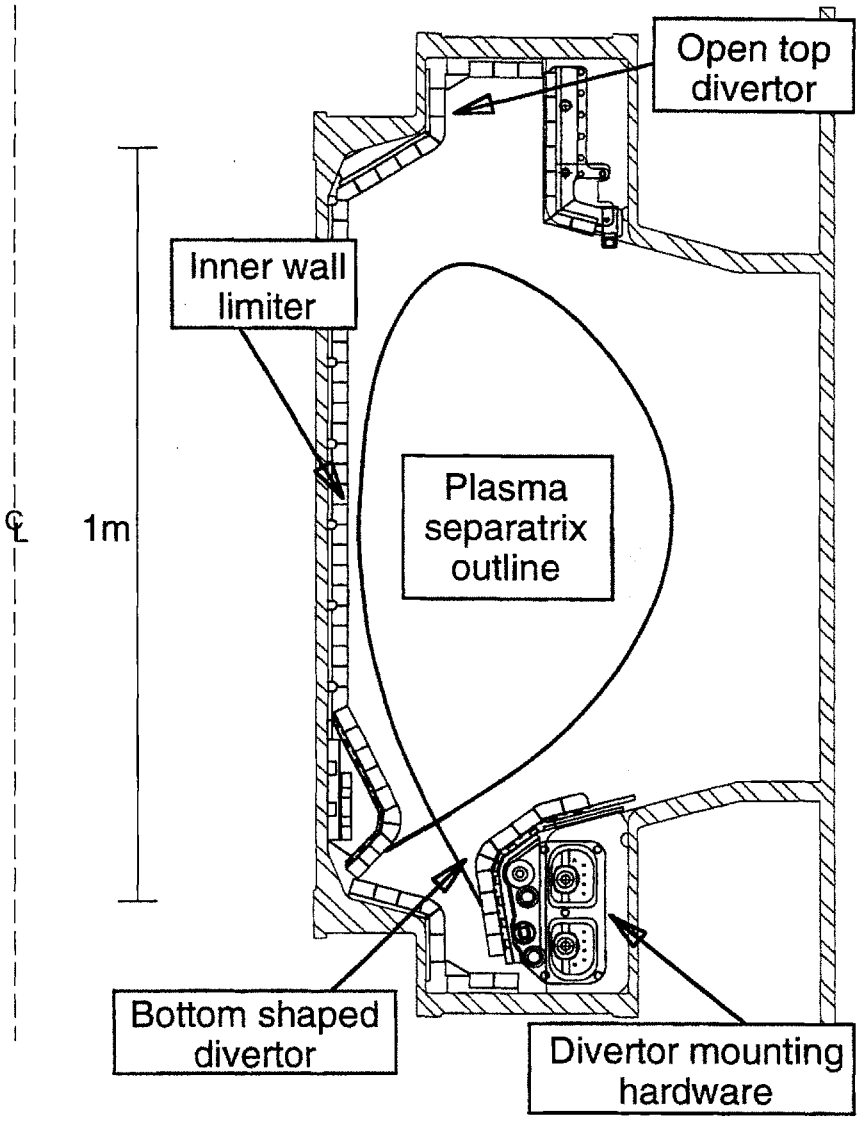

Fig. 2-4: Poloidal view of the plasma facing components (PFC) inside the Alcator C-Mod vacuum vessel. Plasma can be diverted towards the top open divertor, towards the bottom shaped divertor, or limited on the inner wall. The divertor mounting hardware, shown behind the target plates is not toroidally continous, it attaches to the 'gusset' plates shown on Fig. 2-3.

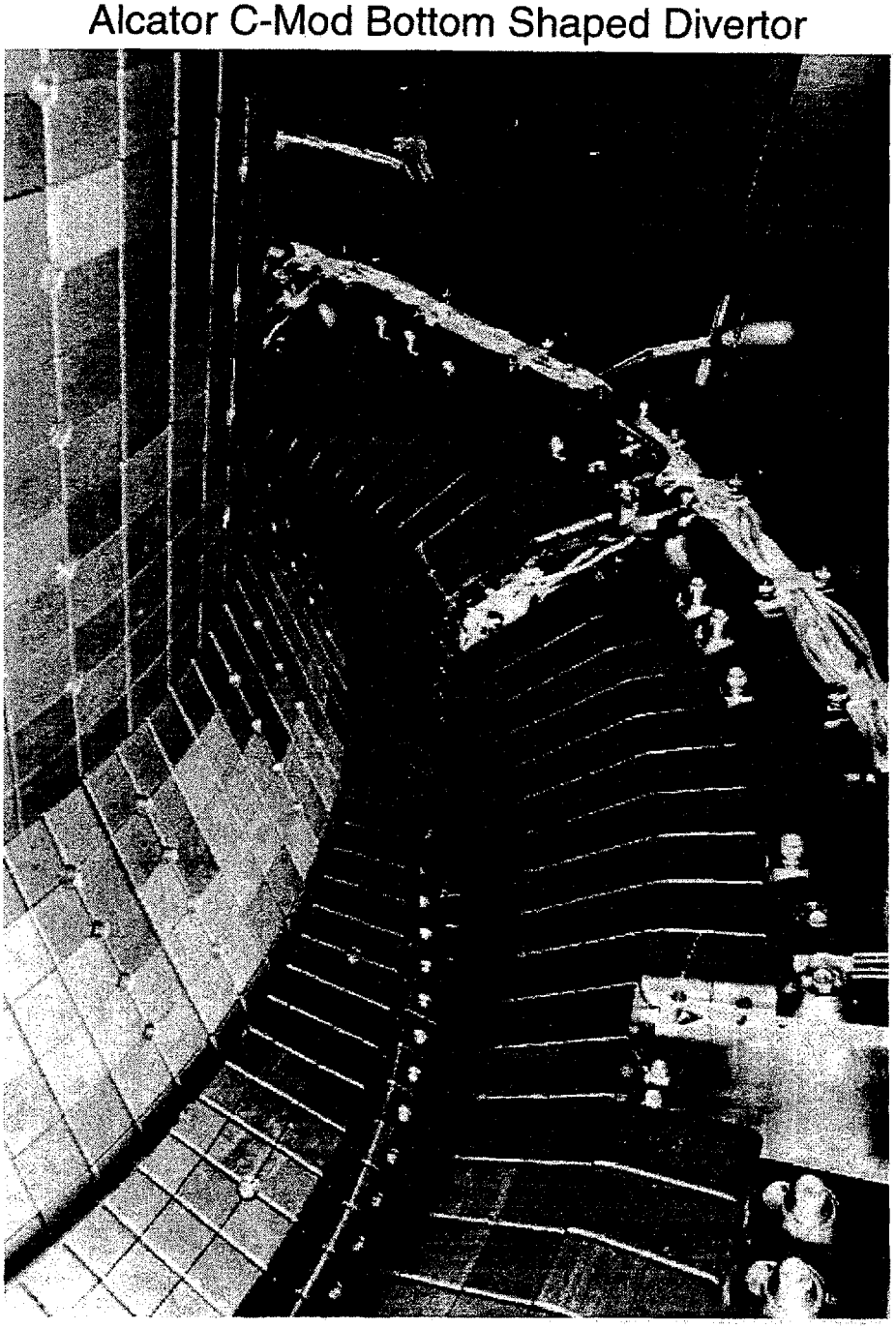

Fig. 2-5: Photograph of the Alcator C-Mod bottom shaped divertor. The narrowing between the target plate "noses" defines the divertor "throat". The noses divide the target plates into "vertical" and "horizontal" portions. A toroidal discontinuity in the outer divertor plate marks one of the five diagnostic slots.

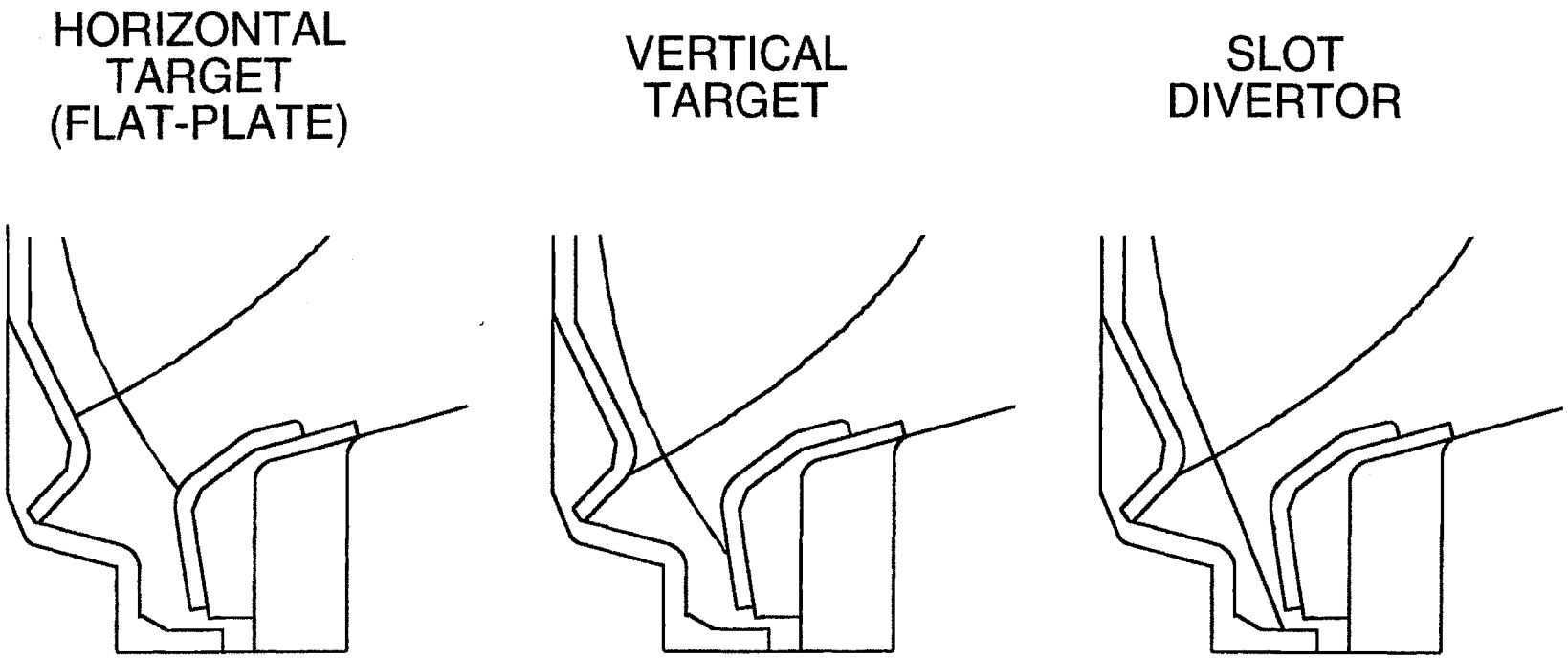

Fig. 2-6: Divertor configurations that can be realized using the Alcator C-Mod bottom shaped divertor geometry.

The Alcator C-Mod shaped divertor allows high flexibility in divertor configurations. The vertical-target, horizontal-target ("flat-plate"), and slot divertor geometries, shown on Fig. 2-6 can all be realized. This highly flexible divertor geometry enables ITER-relevant divertor research to be carried out. The impact of the divertor geometry on neutral dynamics is discussed in detail in Chapter 6.

2.2 Particle diagnostics in Alcator C-Mod

2.2.1 Core plasma density

A two-color heterodyne interferometer (TCI) measures the core plasma density [22, 23]. The TCI system consists of a CO_2 (10.6 μm) laser diagnostic beam and a HeNe (0.64 μm) laser vibration-compensation beam (hence the name "two-color"). There are seven parallel diagnostic chords running vertically through the plasma. Each chord delivers a line integrated electron density. Using the assumption of constant plasma density on a flux surface, a reconstruction of plasma density profile is possible. Details of the reconstruction technique are given by Luke [24]. One of the most important reconstruction results, which is used extensively in this analysis, is the total plasma electron count and the core plasma electron density. Where possible the volume-averaged core plasma density, derived from the complete poloidal reconstruction is used. In many cases, however, the reconstruction led to a significant error. For these cases the line-averaged core plasma density is estimated from a single interferometer chord

measurement by dividing it by an approximate path length through the core plasma [25].

A Thomson scattering system [26] has been recently brought on-line as an independent measure of the core plasma electron density and temperature. Unfortunately, the system has not been operational during the collection of most of the data used in this thesis.

2.2.2 Langmuir probes

The most complete picture of the divertor and the scrape-off-layer (SOL) plasma parameters is provided by an array of tile-mounted Langmuir probes [27], complemented by a fast-scanning (reciprocating) Langmuir probe [28]. The array, shown on Fig. 2-7, has an extensive poloidal coverage on the divertor target plates and records the time history of the target density and electron temperature profiles throughout a discharge. Fig. 2-7 also shows the position of the scanning probe, which measures the SOL plasma parameters upstream (away from the target).

There are three probes located at each poloidal location of Fig. 2-7; two probe heads are flush with the tile surface and one head has a 'domed' end protruding from the surface. In principle, each probe triplet, shown in detail on Fig. 2-8, can be operated in single, double or triple-probe mode. For the data reported here, all probes were operated as single, independent units.

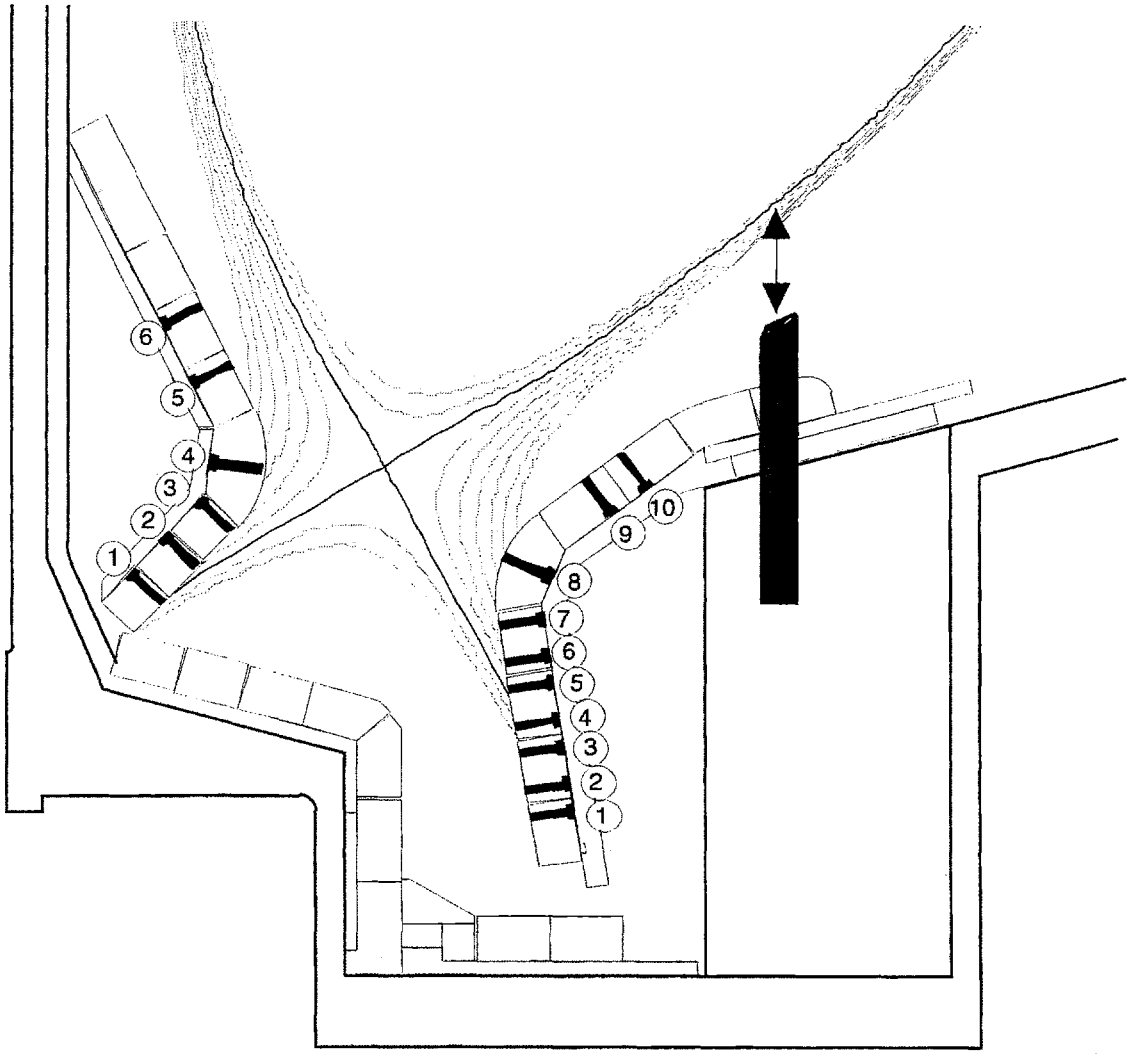

Fig. 2-7: Location of the tile-mounted Langmuir probe arrays, measuring divertor target plasma parameters. The fast-scanning (reciprocating) Langmuir probe measures the upstream SOL-plasma parameters during a ~30 ms vertical scan.

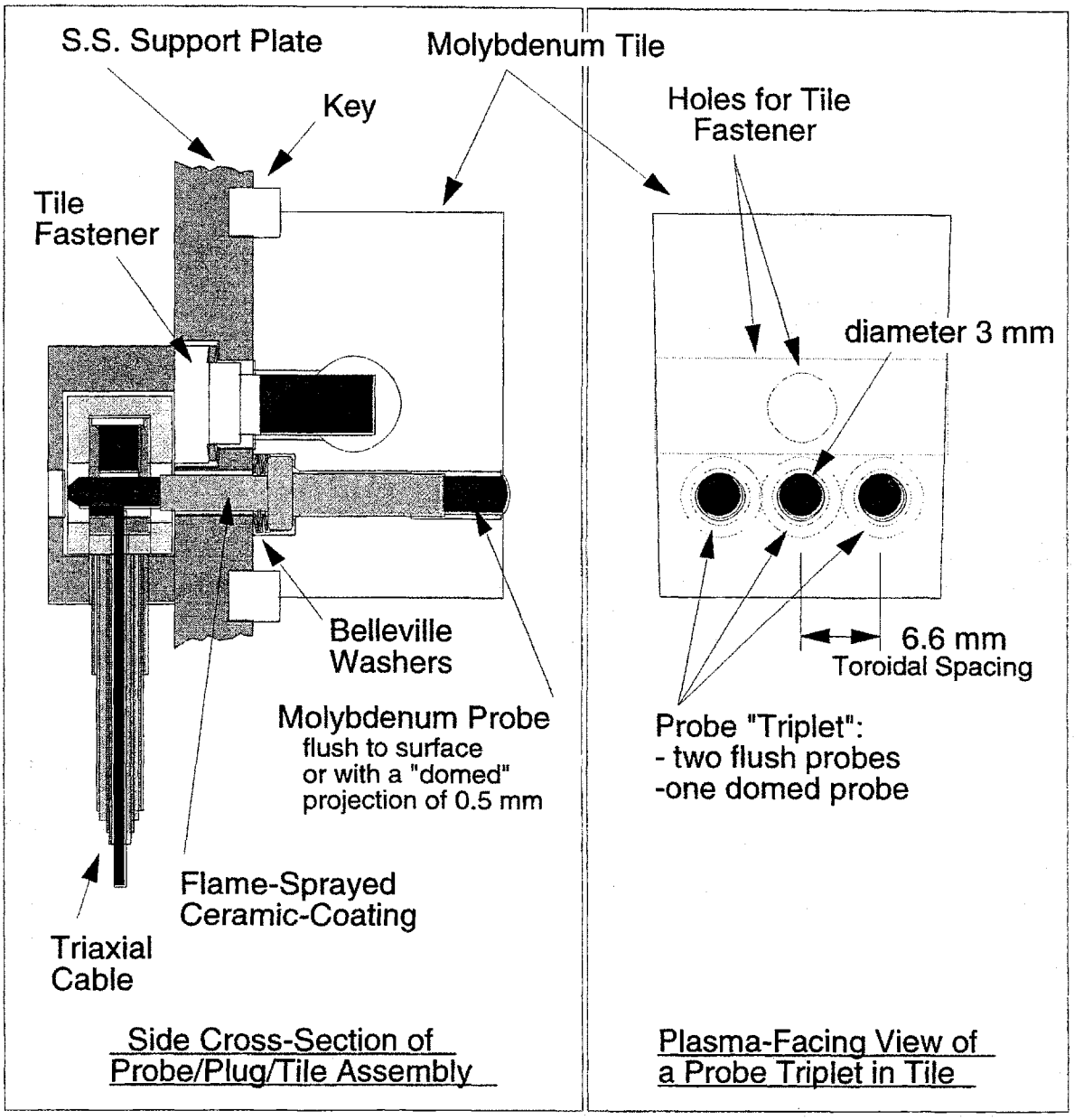

Fig. 2-8: Flush-mount triplet assembly in a divertor tile. Last (downstream along magnetic field) probe is the domed one. The remaining two probes are flush with the tile surface.

The domed probes have a well-defined area projected parallel to magnetic field lines and, when operated with swept bias voltage, allow determination of plasma potential, density, and electron temperature, [27]. One of the two flush probes is also operated with swept bias voltage. Its characteristic, however, is extremely difficult to interpret due to the very shallow angle of incidence of magnetic field lines in the divertor (0.5-1°) and the resulting uncertainty in the perpendicular particle and heat transport [29].

A second flush probe is operated with a fixed negative bias (-125V, relative to the surrounding tile surface), and is used for measuring the fast time history of the ion saturation current. The measurements from this probe are used to estimate particle flux onto the divertor target plate. However due to sheath expansion [30] this measurement delivers an overestimate of the particle flux. For a more detailed discussion of the particle flux estimate see Section 5.7.

The target-plate measurements of plasma parameters are complemented by the measurements using the fast-scanning probe upstream (away from the divertor target). The scanning probe cannot be inserted permanently into the upstream plasma, because the parallel heat flux in the Alcator C-Mod scrape-off-layer ($q_{//}$ >200 MW/m^2) would melt the probe within ~100 ms. The probe residence time within the SOL plasma is 30 ms. There are four probe heads, facing different directions relative to the magnetic field. These are used to investigate SOL plasma flows [31]. For the purpose of the analysis presented here the upstream plasma parameters (n_e, T_e) are determined as an average value between the four probe-head measurements. The measurements from the inbound and outbound scanning probe travel are compared to verify signal quality [31]. The disadvantage of the

fast scanning probe is that it produces at most to three profiles per plasma discharge at predetermined time-points, compared to the continuous measurements at the target.

In the near future Alcator C-Mod divertor will be equipped with an edge Thomson scattering diagnostic [32] which will deliver spatially resolved plasma temperature and density measurements across a chord through the x-point. Additionally an Omegatron-type probe [33] will allow a simultaneous measurement of the ion temperature in the SOL.

The extensive poloidal coverage of the tile-mounted probes, combined with spatially resolved scanning-probe measurements, can be used to reconstruct the entire profile of the plasma parameters (n_e, T_e, V_f, I_{sat}) across the scrape-off-layer, both upstream and downstream. Proper assumptions about the SOL heat and particle transport, and knowledge of boundary conditions (both, up- and down-stream) should, in principle, allow the plasma parameters to be determined everywhere in between. Such a reconstruction technique is extensively used in Chapter 5 to study neutral particle transport. The divertor and SOL plasma profiles (e.g., particle fluxes), measured directly by the Langmuir probes, are also correlated with neutral pressure measurements in the later chapters of this thesis.

2.2.3 H_α arrays and reconstruction

Alcator C-Mod is equipped with an extensive H_α diagnostic set. There are 382 H_α measurement channels, [34] each being a photo-diode viewing the plasma through an H_α interference filter. Additionally there is an equal number of viewing chords with another interference filter, allowing specific impurity lines to

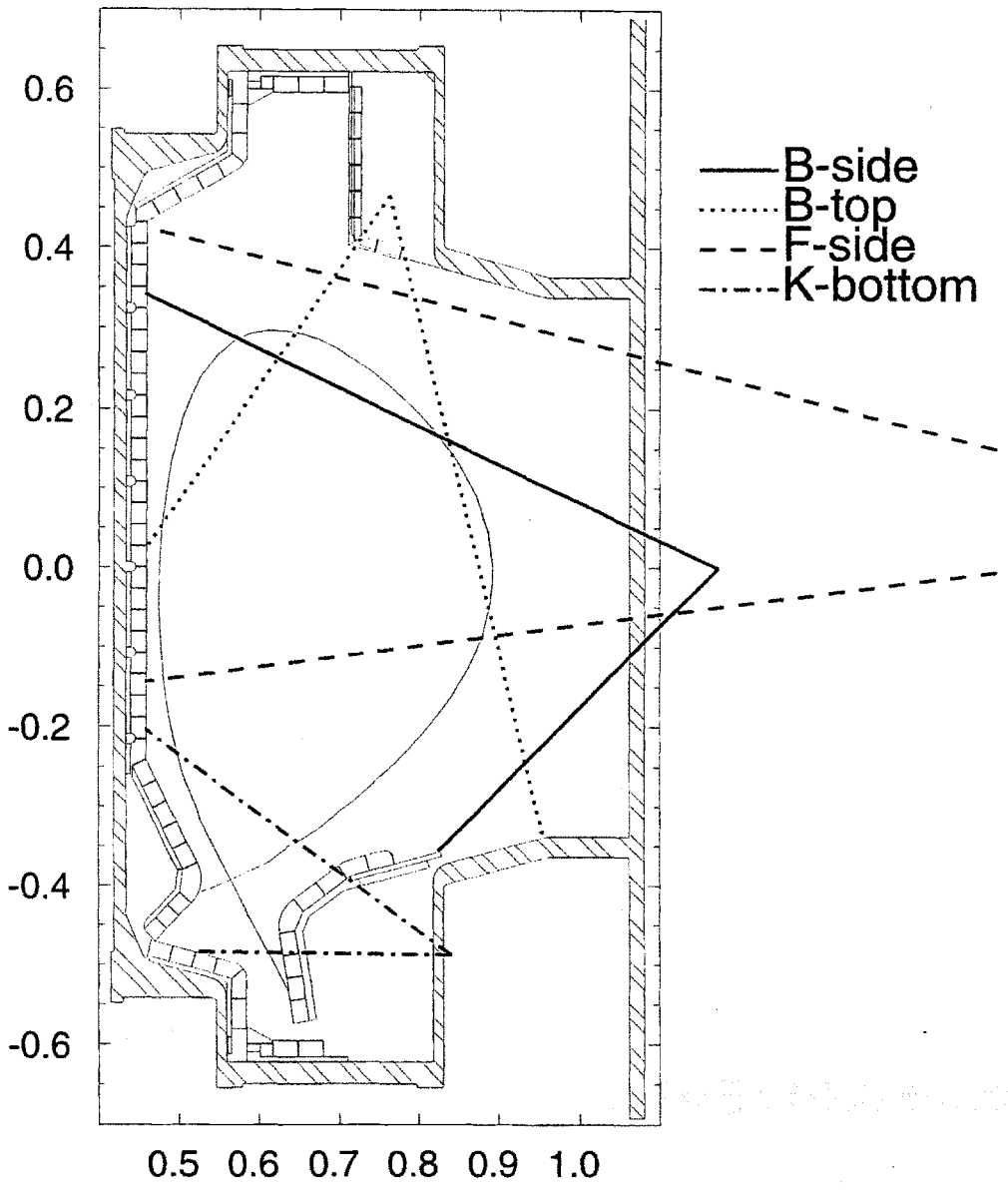

Fig. 2-9: Field of view of the photo-diode imaging arrays. The photo-diode signal, when inverted with a tomographic reconstruction algorithm yields a measurement of a local H_α (or Carbon II/IV) emissivity everywhere in the plasma.

be measured, and TV cameras recording views of the plasma discharge in H_α, carbon II, and total visible light [35]. The orientation of the H_α photo-diode array views is shown on Fig. 2-9. For data analysis the assumption of toroidal symmetry has been used because of different toroidal location of various arrays. A least-squares fit tomographic technique is used to reconstruct 2D spatial emissivity profiles [36], an example of which is shown in Fig. 5-10.

Neutral hydrogen (deuterium) emits H_α light when it is excited by plasma electrons. Thus a knowledge of the 2D electron density profile is required to obtain the neutral hydrogen (deuterium) spatial distribution [37]. The atomic deuterium density obtained in this way is compared with direct measurement of molecular deuterium density in Chapter 5.

2.2.4 Gas fueling system

The main fueling source of the Alcator C-Mod plasmas is neutral gas injection. For routine tokamak operation a piezo-electric gas valve is used [38]. The main fueling valve is mounted on the A horizontal port. Despite a single injection point the H_α observations (1/10 versus 1/2 torus circumference away) do not indicate significant toroidal asymmetry [39]. The piezo-electric valve is operated in a continuous voltage mode, i.e., the valve throughput is adjusted by the applied DC voltage, in contrast to other tokamaks [40] where the piezo valve voltage is modulated at a high frequency. This approach is simpler to implement in practice. It complicates, however, an absolute calibration of the fueling source due to the inherent non-linearity of the piezo valves.

The measurement of the particle fueling source is important for the neutral particle dynamics analyzed here, and especially for the particle balance and wall pumping

calculations, described in Appendix A. Therefore an attempt to calibrate the piezo valve was made. During a series of experiments the valve was pulsed into an empty vacuum chamber. The driving voltage program was compared with the chamber pressure change, recorded by a midplane ionization gauge (described in Section 2.3). This procedure gives a simple expression for the valve throughput as a function of its driving voltage. The expression has to be used with caution, because the throughput depends also on the fueling plenum pressure and the valve operating history. In practice it means that the calibration has to be repeated every time there is a significant change in the driving voltage program.

The Alcator C-Mod discharges are either feed-forward or feed-back fueled. In the feed-forward fueling mode the tokamak operator pre-programs the piezo valve driving voltage before the discharge. The calibration procedure described above applies to this mode of operation only. The operator uses feed-forward fueling when a constant or predictable gas source is desired for the discharge. When a constant plasma density is desired, the tokamak is feedback fueled. In this mode of operation the plasma density diagnostic (two-color interferometer) controls the piezo valve driving voltage through a PID controller. This results in a constant plasma density, but makes the gas fuel source more difficult to estimate.

Some of the discharges are additionally fueled by frozen deuterium pellet injections. For this purpose a multi-pellet pneumatic cryogenic injector was developed at MIT [41]. The pellet injection experiments are, however, outside of the scope of this thesis.

Additionally, Alcator C-Mod is equipped with a special-purpose capillary gas injection system [42]. A large number of capillary tubes, mounted behind the

plasma-facing hardware, deliver gas to the immediate vicinity of the plasma boundary, thus allowing a high flexibility in the fueling location. It is possible, for example, to fuel the plasma into the private-flux zone, common flux zone, and inside mid-plane region independently. Most of the tubes are located at the B-port of the tokamak. A few of the tube outlets are installed at other toroidal locations allowing investigation of toroidal asymmetry effects.

The capillary system is used for both impurity injections and fueling experiments [42]. The advantage of a capillary system is its very localized injection point and an absolute calibration of the amount of the gas injected. The inlet solenoid valve can be fully opened or fully closed. During the discharge the gas flows out of a sealed plenum of a known volume. The volume pressure is recorded, thus providing a measure of gas depletion from the plenum. The disadvantage of the system is its long time delay before the injection reaches the plasma and a long "dripping-out" time following the injection. This is associated with the nature of capillary tubes several meters long and of a few millimeters diameter. Modeling of the gas flow through the system is underway [43].

2.3 Neutral pressure measurements

2.3.1 Location and type of neutral pressure gauges

Neutral pressure is measured by a total of six gauges in four different locations of the Alcator C-Mod vessel. The poloidal location of the gauges is shown on Fig. 2-10 and the toroidal location, on Fig. 2-11.

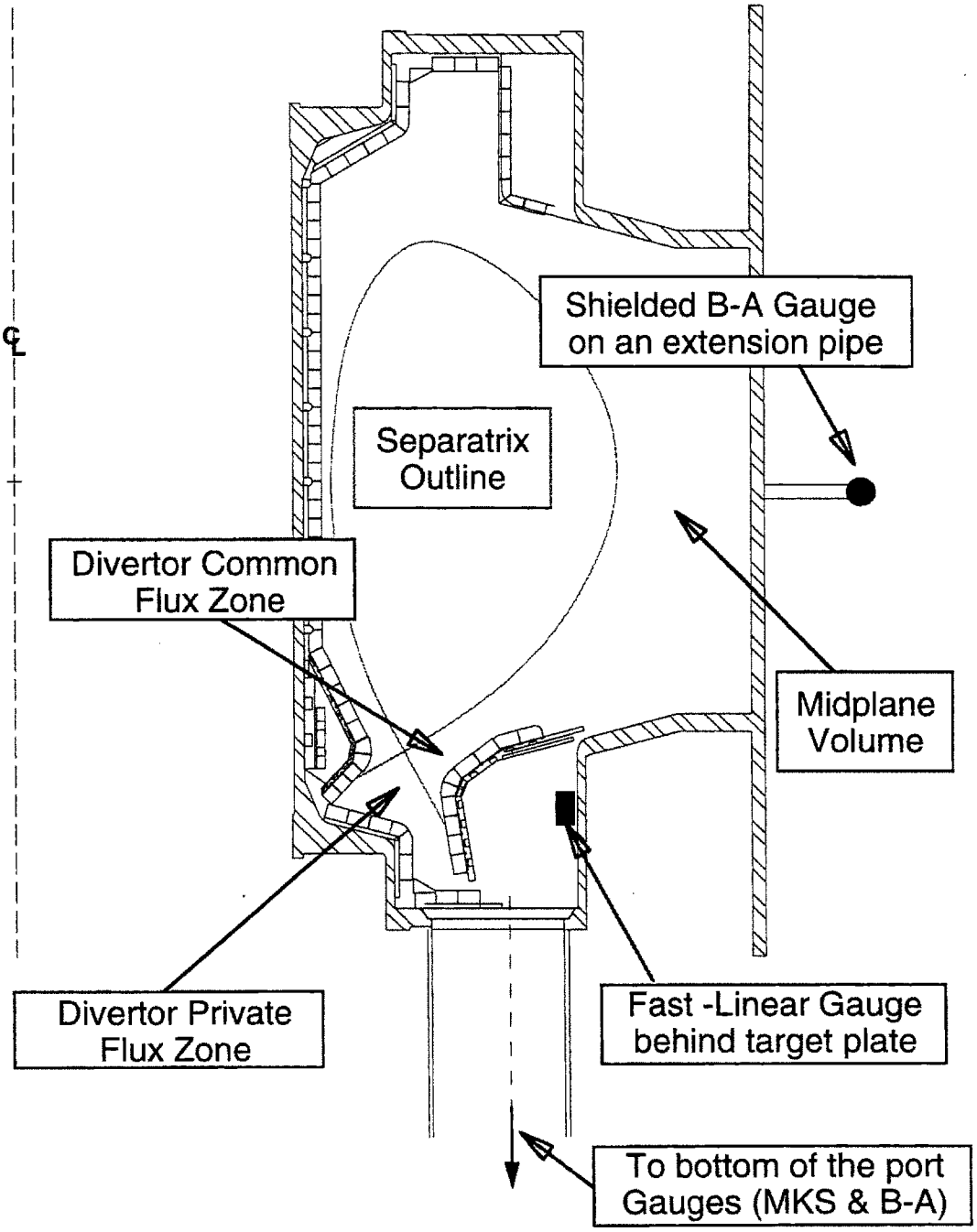

Fig. 2-10: Poloidal schematic view of the neutral pressure measurement locations in the Alcator C-Mod vessel. Divertor mounting hardware is removed from the picture clarity.

The neutral pressure in the shaped divertor is measured by a pair of fast linear gauges, described in detail in Chapter 3. Both gauges have the same poloidal location in the "gas-box" behind the divertor outer target plate (shown on Fig. 2-10). The first gauge is installed in a divertor module with low gas conductance to the main chamber (J-port module). The second one is mounted in a divertor module with a diagnostic-laser-beam opening (E-port module), and thus with a high gas conductance to the main chamber. Because of the gusset plates dividing the volume behind the divertor target (Fig. 2-3), the different module plena are not in contact, other than through the plasma private flux zone. Thus the two measurements are independent. The closed divertor module gauge delivers an estimate of the neutral pressure in the Alcator C-Mod shaped divertor. The open divertor module gauge measures a "mid-stream" pressure resulting from the flow of neutrals escaping from the divertor towards the midplane volume through the diagnostic opening.

The diagnostic-beam openings, located at ports D, E, G, H, and K, shown on Fig. 2-11, occupy no more than 10% of the toroidal divertor extent. Thus for most purposes, the toroidal symmetry of the divertor geometry is a good approximation. However, the neutral flux leaking through the non-symmetric diagnostic-openings is discussed during the subsequent flux-balance calculations (Chapters 5 and 7).

The *in situ* divertor measurement is complemented by a slower but more accurate pressure measurement at the bottom of the vertical port (B-module), shown on Fig. 2-12. The vertical port connects directly to the gas-box volume behind the outer gas target, where the divertor gauges are located, but at a different toroidal location. The difficulty with the port measurement is its slow time response,

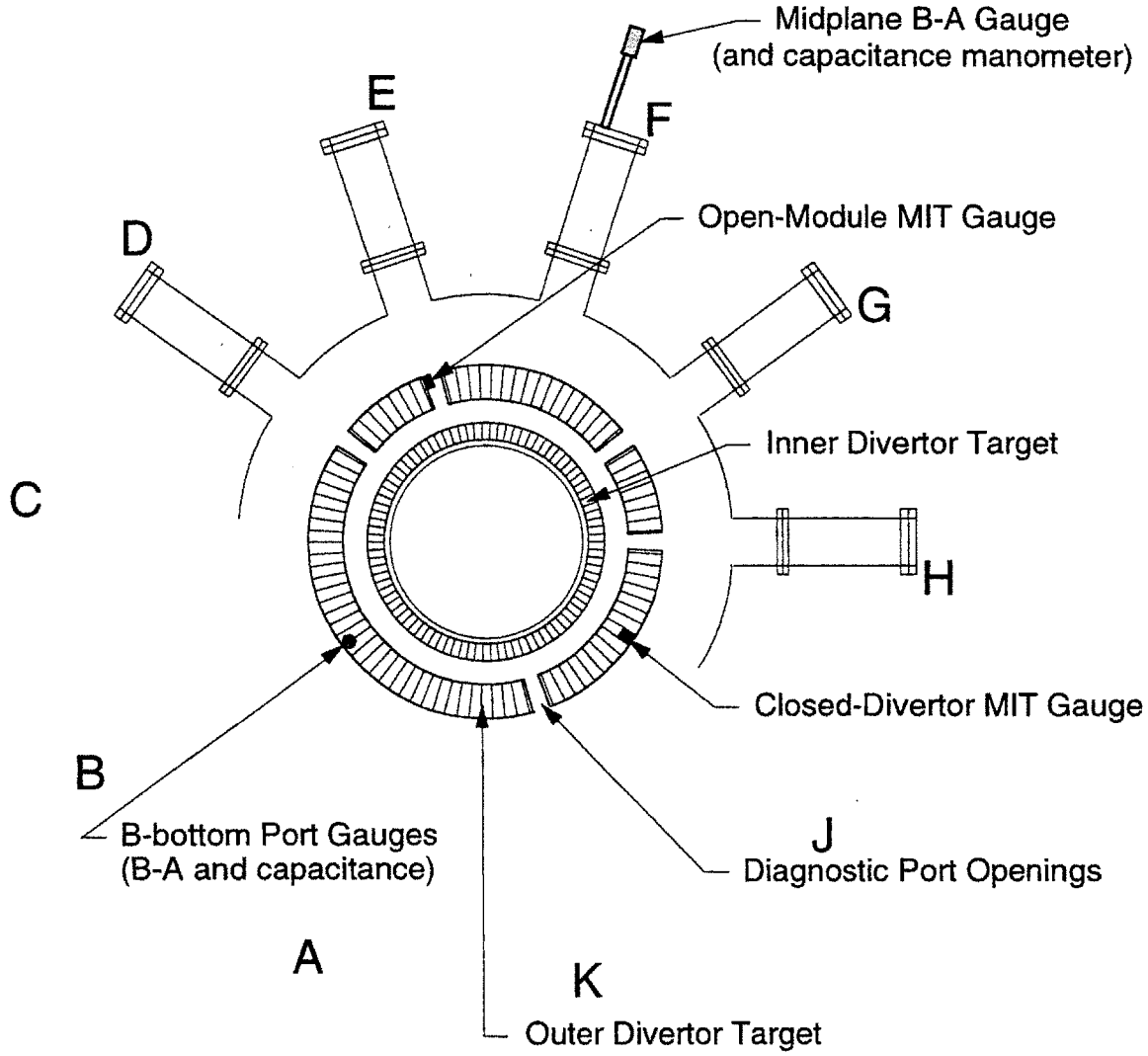

Fig. 2-11: Toroidal location of the neutral pressure measurements shown on the partial top view of the Alcator C-Mod vacuum chamber. Midplane pressure is measured at the F-horizontal port, closed divertor module pressure - at J, open divertor module pressure - at E, and bottom vertical port pressure - at B. The discontinuities (diagnostic openings) in the outer divertor target are located at ports: D, E, G, H, and K. Capillary gas feed outlets are located in between ports: A/B,C/ D, E/F, G/H, and J/K.

resulting from the considerable length of the vertical ports (Fig. 2-4). The vacuum crosses attached to the vertical ports, necessary for instrumentation feed-throughs, add an additional "dead" volume, further extending the time constant of a potential pressure measurement located there. The problem was alleviated by a fairly tight vacuum baffle. The baffle cuts-off the "dead" cross volume. The pressure gauges are located directly above the baffle as shown on Fig. 2-12. This design allowed the time response of a measurement to be improved from 200 ms (calculated) to 30-50 ms (measured) in deuterium.

There are two gauges located at the bottom of the vertical B-port (Fig. 2-12). The first one is an industry-standard Bayard-Alpert (B-A) ionization gauge. It is shielded from a local vertical magnetic field of 0.2 T by an iron/mu-metal magnetic shield. The second gauge is an MKS-626 capacitance manometer [44], protected by an iron shield and mechanically isolated from the tokamak vibrations. The B-A gauge is used for pressure range 0.01~3 mTorr, and the capacitance manometer for pressure range 1~100 mTorr (and possibly higher in the future).

The neutral pressure is also measured in the tokamak main chamber. The same type of Bayard-Alpert gauge as the one in the bottom cross is used. The gauge is mounted on a horizontal extension port (shown on Figs. 2-3, 2-10, and 2-11). To protect the gauge from energetic photons and fast CX-neutrals it is mounted behind two elbows and the baffle. This results in a noise-free pressure signal but with a fairly long time response, ~17 ms in deuterium. The gauge is screened from the tokamak stray magnetic field (0.02 T) by an iron/mu-metal shield. An MKS-131 [45] capacitance manometer is mounted at the same location. Unfortunately, the manometer failed to function during the tokamak discharges, most likely due

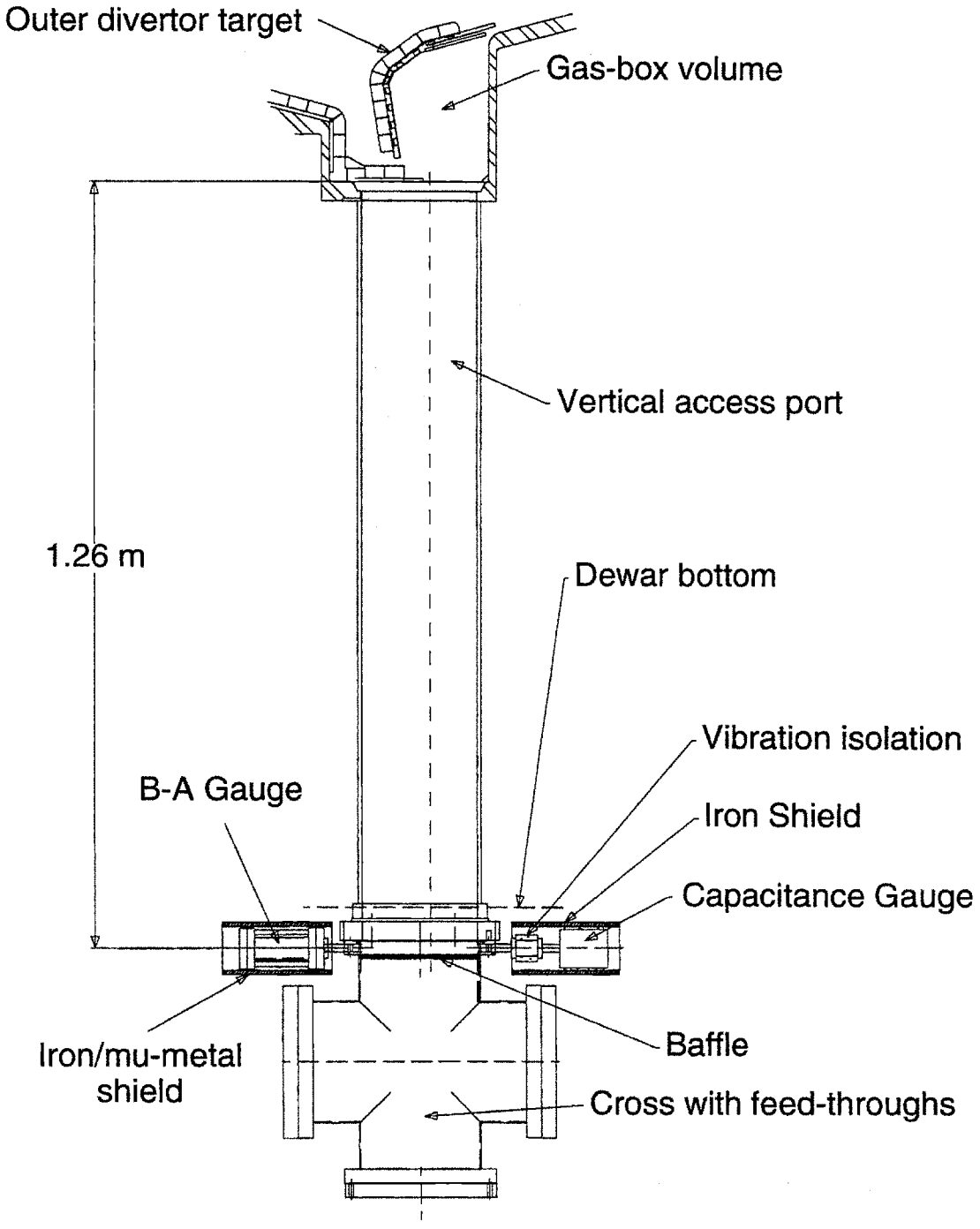

Fig. 2-12: Lower "B" vertical access port. with B-A and MKS gauges, located at the bottom of the port. The baffle installed immediatelly below the gauges "disconnects" the dead volume of the cross, improving the time response of the gauges from ~200 ms (in deuterium) to 30-50 ms. To show details the gauge axes are projected onto the drawing plane.

to vibration, despite efforts of mechanical isolation. The manometer still plays an important role as a pressure standard (one of three) during off-line calibrations of other gauges.

2.3.2 Capacitance manometers

Capacitance gauges deliver well calibrated absolute pressure measurements. A known problem with these gauges is, however, a time- and temperature-related zero drift. The vacuum vessel is filled with the working gas to a constant pre-fill pressure of ~0.01 mTorr before every plasma discharge. The pre-fill pressure provides a zero reference for the capacitance gauges before every shot, thus the drift problem becomes unimportant.

The second problem that has to be addressed is temperature stability of the capacitance manometer. In most applications, capacitance manometers are operated under controlled temperature of its mechanical components. There is no space under Alcator C-Mod to accommodate an external heater for the gauge. However, the vibration- (silicon rubber foam) and magnetic field- (iron pipe) shields minimize convection heat exchange with the surrounding air mass. Most likely the dominant heat exchange channel is conduction between the gauge measuring head and the vacuum feed-throughs because of a tight metal contact. During normal operation mode (no bake-out) the bottom of the vertical port is maintained at about ~70°C. This corresponds to about ~50°C at the capacitance manometer location. It is however difficult to estimate deviations from this temperature, which may be as large as +/- 20°C. According to preliminary data from the National Institute of Standards and Technology [46], the calibration of the capacitance gauge changes only by 0.5-2% between 23°C and 45°C (note that

the zero drift is affected more strongly). Moreover, the cross-calibration of the F-horizontal-port and B-vertical-port capacitance manometers did not reveal any calibration differences bigger than 5% (again, neglecting zero-drift) despite both gauges operating at different temperatures.

The two in-vessel MKS manometers were compared with a high-pressure capacitance manometer (also MKS brand) measuring the gas depletion from the capillary injection plenum (described in Section 2.2.4). During gas puffs into an empty tokamak chamber, the pressure ratio, in steady-state, is determined only by the volume ratio of the two reservoirs involved. The 10% disagreement between the capillary-plenum and the in-vessel manometers is well within the Alcator C-Mod vacuum vessel volume uncertainty (end part of traces on Fig. 2-13).

All of the facts, presented above, allow us to believe that the accuracy of the B-bottom capacitance manometer, under Alcator C-Mod operating conditions is better than 10%, potentially even 5%. Thus this manometer serves as an absolute reference for other pressure gauges in the Alcator C-mod vessel.

2.3.3 Bayard-Alpert gauges

The performance of ionization gauges in magnetic fields was first investigated by Martin [47] and, more recently, carefully examined by Filippelli [48]. Filippelli concluded that a magnetic field above 50 Gauss severely affects a Bayard-Alpert gauge response. The iron/mu-metal magnetic shield, protecting B-A gauges installed on Alcator C-Mod, limits the magnetic field at the gauge axis to ≤ 10 Gauss (calculated). No negative effects of the magnetic field on protected B-A gauge measurements have been observed on Alcator C-Mod.

Ionization gauges are also known to exhibit a time- and pressure-varying calibration characteristic. The researchers of the Granville-Phillips Company have recently investigated this problem thoroughly and proposed counter-measures [49,50,51]. The Bayard-Alpert gauges, installed in Alcator C-Mod are carefully monitored against the capacitance manometers. Contrary to the Granville-Phillips reports, ionization gauges installed in Alcator C-Mod do not exhibit a significant pressure non-linearity during a transient, ~1 sec., high-pressure (up to few mTorr) operation. However considerable variation of the gauge sensitivity with the electron emission level has been observed (though the pressure-linearity was still preserved). Additionally, the calibration changes with time. For example, between January and February 1995, after about 1000 hr. of operation, the sensitivity of both gauges (F-horizontal and B-bottom) increased by a similar 10% amount. To maintain a low experimental error (<10%), both ionization gauges are checked against the capacitance manometers at regular intervals.

An example of a B-A gauge calibration experiment is presented on Fig. 2-13. The capillary system puffs deuterium into an empty tokamak vessel and the pressure time-evolution is followed by all five gauges (including the capillary plenum gauge). The sensitivity of each B-A gauge is adjusted for the readings to match the corresponding capacitance manometer. The sensitivity being adjusted is a single, pressure-independent scalar value only. Thus, the good agreement between the corresponding traces on Fig. 2-13 indicates that the two B-A gauges installed in Alcator C-Mod exhibit a very good high-pressure linearity. This result has also been confirmed for other gases (Ne, N_2). The pressure differential between the two pairs of traces on Fig. 2-13 results from the finite time response of the bottom-of-the-port measurement. The pressure equilibrates between the two measurement

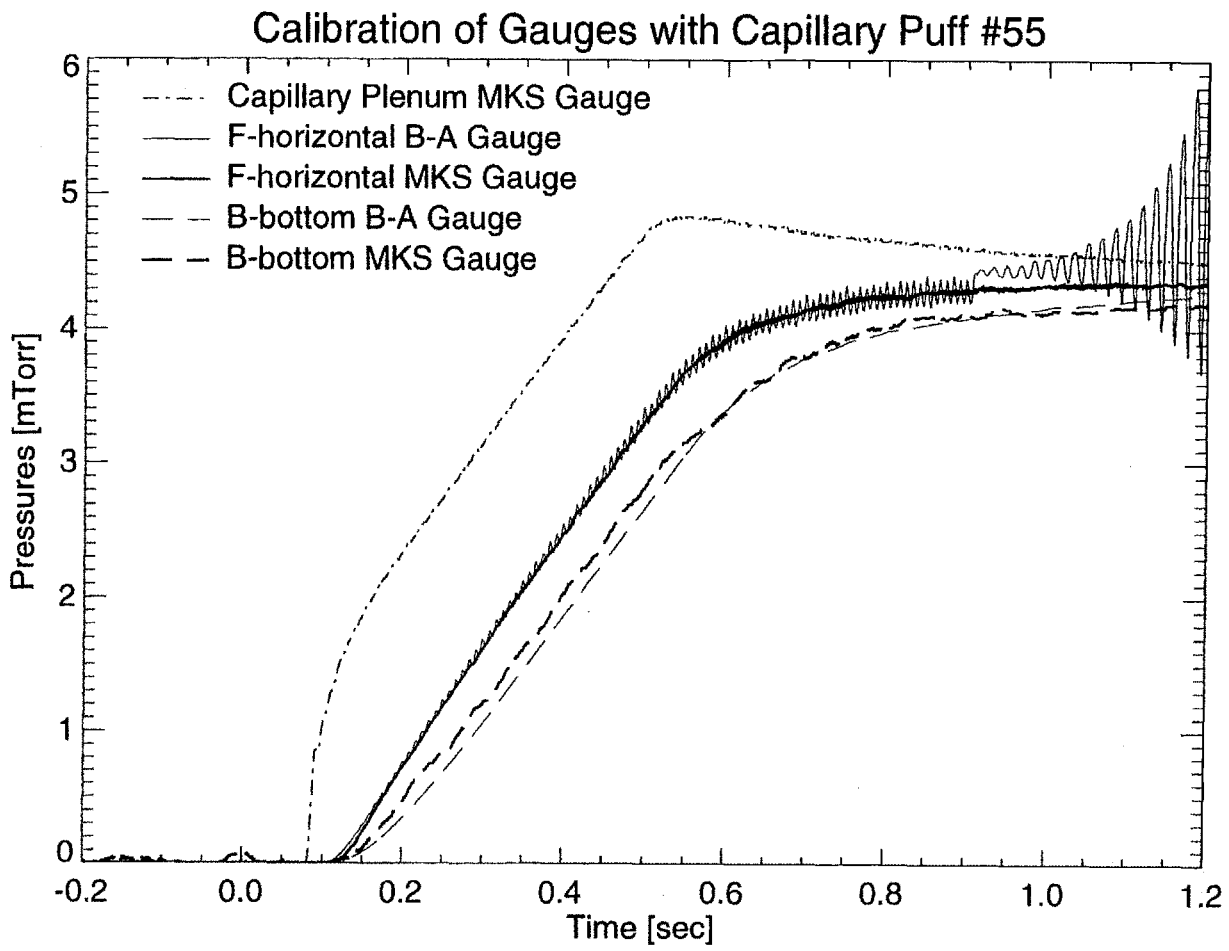

Fig. 2-13: Example of a Bayard-Alpert (B-A) gauge calibration experiment against MKS capacitance manometers using a capillary deuterium injection. Both B-A gauges follow the respective manometers up to 4 mTorr pressure. The F-port B-A gauge is turned off by its protective circuit at t=0.9 sec.

points about 1 sec. after the end of the gas pulse (this long equilibration time is due to the baffled volume of the B-port cross, directly below the measurement). At that time, however, a filament protection circuit has turned both B-A gauges off, F-port gauge starts to turn off at $t \approx 0.9$ sec. A slight delay in pressure rise measured by B-bottom B-A gauge compared to the B-MKS pressure trace is due to lower conductance (by ~20 ms) of the B-A gauge measuring volume. Note that during the steady-state portion of the pulse the two measurements match well.

The B-A ionization gauges are controlled by a VARIAN 843 ratiomatic controller [52]. The instrument has been modified in-house. The AC filament heating was substituted by a DC heating circuit, to reduce the 60Hz noise. Additionally, some of the RC internal components have been replaced, to improve the controller time-response to below 5 ms. Recently, some of the internal relays have also been replaced to allow interfacing of the ratiomatic with an Allen-Bradley PLC controller (see section 3.2.3 for PLC control description). The ratiomatic has a safety protection circuit, turning the filament heating off at a pressure above 1 mTorr. A 0.5-1 sec. time delay of the protection circuit allows a transient high pressure measurement, yet still protects the gauge filament from an extended exposure to high pressure gas .

2.3.4 Toroidal pressure symmetry

One of the most important questions is whether the above set of diagnostic delivers a complete picture of neutrals in the tokamak. As seen on Fig. 2-11, the pressure measurements are performed at different toroidal locations.

If the neutral pressure results from plasma recycling on the material surfaces, then the toroidal equilibration time is dictated primarily by the plasma toroidal equilibration time. A toroidally localized plasma perturbation (e.g., density, temperature, but not electromagnetic) propagates along field lines (toroidally) with the ion sound speed. Thus, even for cold (T =5 eV) divertor plasma such a perturbation, would circle around the torus within a time:

$$\tau_{D+}^{tor} = 2\pi R / v_{D+}^{0}(5eV) \approx 0.15 \text{ ms} \qquad (2.1)$$

If the neutral pressure involves slow-neutral free flight, (e.g. capillary gas injections) then a toroidal perturbation travels at a molecular sound speed, which is much less than the ion speed, primarily, because of molecules being injected at room temperature. The resulting equilibration time is then:

$$\tau_{D2}^{tor} = 2\pi R / v_{D2}^{0}(0.03eV) \approx 3 \text{ ms} \qquad (2.2)$$

In practice, the above time is a rather large underestimate because neutrals fly ballistically, along straight trajectories; in contrast with ions, which are guided along the field lines conforming to the torus curvature. An additional complication, in the case of molecular transport, is the finite conductance of the toroidal duct and the strong pumping action of the plasma. An experimental investigation, during toroidally localized capillary injection experiments [53], resulted in an estimate of the molecular toroidal equilibration time: $\tau_{D2}^{tor} \leq 100$ ms, thus much longer than given by Eq. 2.2. An estimate of the ion toroidal equilibration time $\tau_{D+}^{tor} < 0.5$ ms, obtained during the same experiments, is in agreement with Eq. 2.1.

The assumption of toroidal symmetry can only be used if the investigated phenomena last longer than the toroidal equilibration time. Additionally, the response time of various gauges must be taken into account when interpreting the experimental results. That is why the mid-plane and the vertical port gauges are used to investigate the steady state phenomena, and the divertor gauges are used for transient events. Because the neutral pressure data reported in the following chapters were recorded during piezo-valve fueling operation, the divertor plasma and recycled neutral particle population are assumed toroidally symmetric.

2.4 Chapter conclusions

Alcator C-Mod has a very extensive set of diagnostics. Here we have described only particle diagnostics. Among others the plasma interferometer, Langmuir probes, photo-diode arrays, and neutral pressure gauges provide invaluable tools to investigate edge plasma phenomena. More specifically the pressure gauges deliver a comprehensive picture of neutral pressures at various locations inside the vessel.

Chapter 3

The MIT Gauge

The remote location of the standard Bayard-Alpert (B-A) and capacitance gauges, described in Section 2.3, severely limits the time response of the measurements. A solution to this problem is an *in situ* neutral pressure measurement. However, because of high magnetic fields, vibrations, limited access, and high-energy photon and particle fluxes, the standard off-the-shelf gauges cannot be used for *in situ* tokamak operation.

This motivated the development of a dedicated neutral pressure measuring instrument, to be located close to the Alcator C-Mod divertor plasma. The new instrument has been developed by the author in cooperation with B. Lipschultz and S. Kochan.

3.1 New linear-geometry ionization gauge

3.1.1 *In situ* neutral pressure measurements in magnetic fusion devices

Techniques for neutral pressure measurements in magnetic fusion devices (reviewed by Dylla [54]) have been investigated since the early days of the fusion program. Among others, a hot-filament ionization gauge is of value for *in situ*, fast

time response operation. However, as initially pointed out by Martin [47], the response of such a gauge depends on its geometry and orientation relative to the magnetic field. Various gauge geometries, including cylindrical [55] and spherical [56], have been proposed for use in magnetic fields.

For Alcator C-Mod a linear-geometry hot-filament ionization gauge was chosen as the most suitable for very high magnetic fields (ultimately 9T). A linear-geometry ionization gauge of the Schulz-Phelps type was first used in fusion experiments by Lewin and Martin [57] in Princeton stellarators. More recently, a similar-principle gauge, but with a different electrode arrangement, was developed by Haas and first used in the ASDEX tokamak [58]. The ASDEX-type gauge [59], as it will be referred to herein, is commercially available and is being used at a number of other tokamaks (e.g., JET, DIII-D, Tore-Supra, ASDEX-UG) and is planned for the next-generation TPX experiment [60]. This gauge, however, did not satisfy Alcator C-Mod requirements of compact design and mechanical robustness.

The *in situ* ionization gauge developed at MIT, which will be referred here to as the "MIT gauge", employs the same operational principle as the Lewin-Martin and ASDEX gauges, i.e. electron emission modulation to discriminate against background noise. It has the same geometry as the ASDEX gauge but with different support structure and a ceramic-coated body (Fig. 3-2). Additionally, the electronic circuitry employs a synchronous demodulation technique rather than a sample-and-hold method used in the ASDEX gauge.

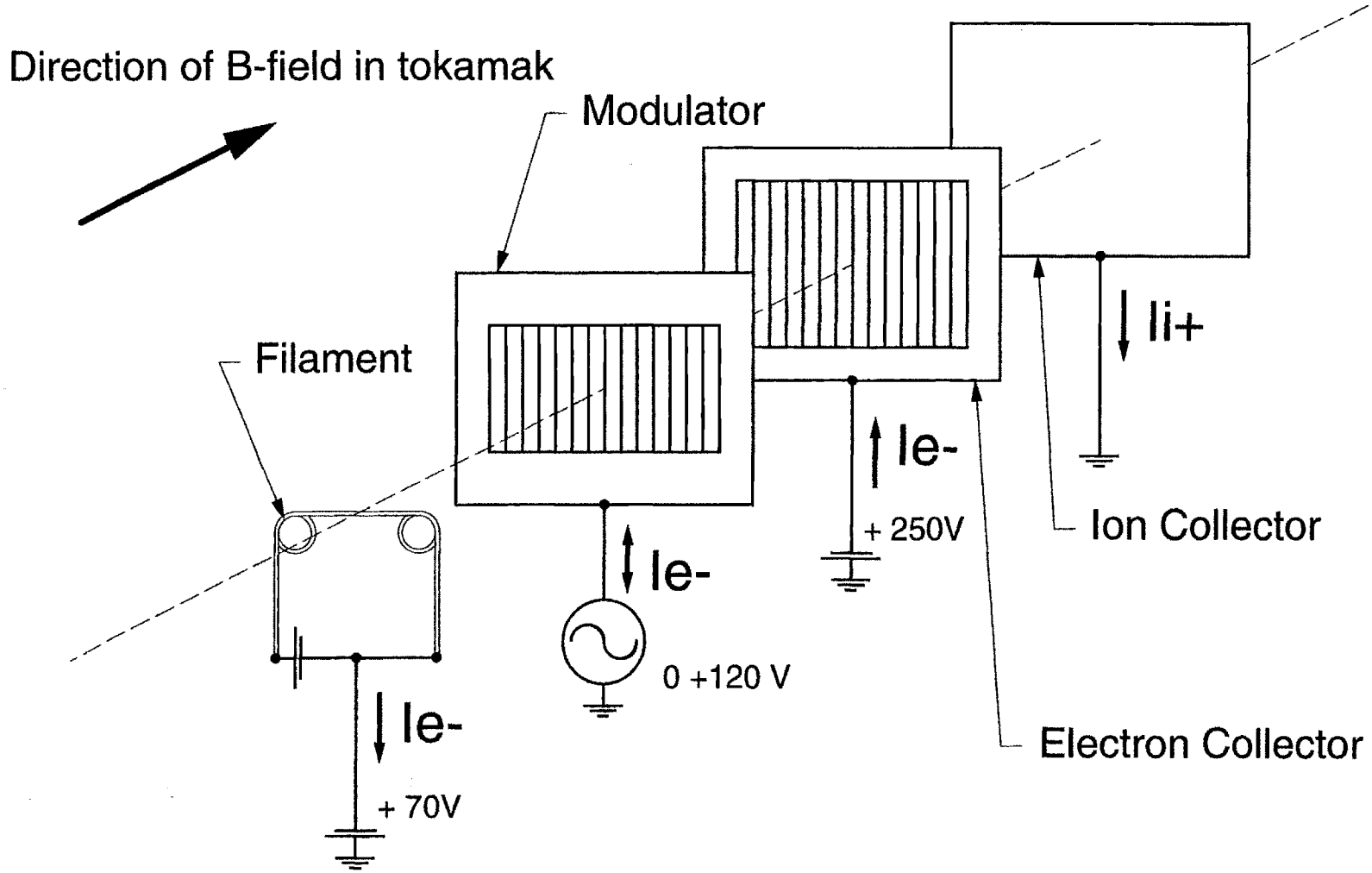

Fig. 3-1: The operational principle of an ASDEX-type, linear-geometry, modulated ionization gauge – the "MIT-gauge" – installed in the Alcator C-Mod tokamak.

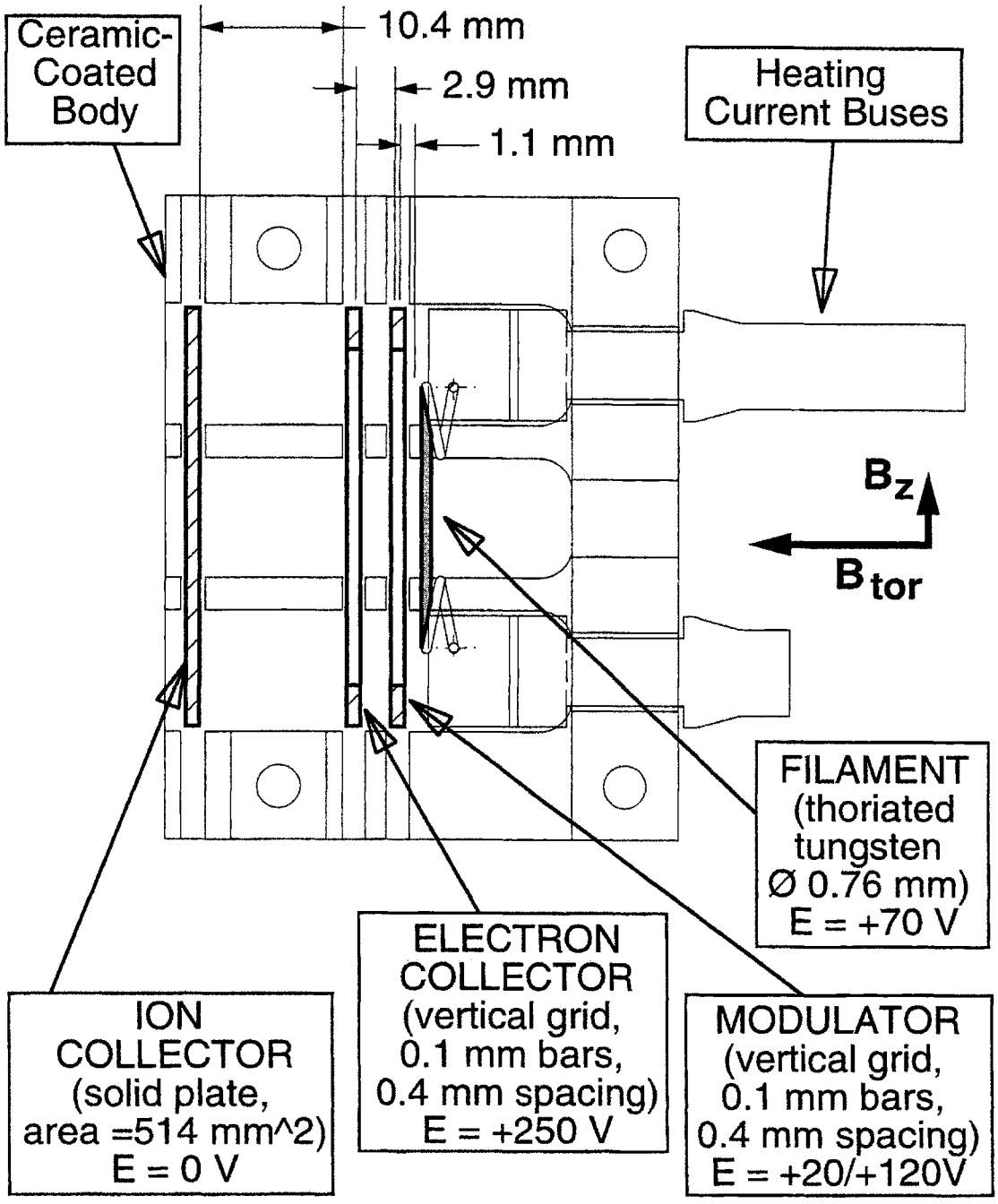

Fig. 3-2: Top view of the partially assembled MIT-gauge – a linear-geometry, modulated, ionization gauge. Additionally the direction (with respect to gauge axis) of the magnetic field components in Alcator C-Mod is indicated.

3.1.2 MIT gauge principle and mechanical design

Fig. 3-1 depicts the operational principle of a linear-geometry, modulated, ionization gauge , while Fig. 3-2 presents the schematic of a partially assembled gauge.

The electrons are emitted from a filament, biased at +70V, heated by a DC current (15-30 A). The filament is made from a low-work-function material, thoriated tungsten, 0.7 mm diameter wire. Emitted electrons are accelerated by a positive potential (+250V vs. +70V) of an electron collector. The electron collector is made of an 80%-transparent molybdenum grid: 0.1 mm vertical bars with 0.4 mm spacing. After several oscillations in the potential well the electrons are collected on the grid and the resulting electron current is measured by an electronic circuit. An additional electrode, the modulator, positioned between the filament and the electron collector is used to modulate on/off the electron current by applying an AC voltage modulation (0-120V at 10 kHz). The modulator is made from the same grid as an electron collector. Ions resulting from volumetric ionizations are collected by the ion collector, maintained at a ground potential. The resulting ion current is measured by an electronic circuit. The ion collector is made of a solid molybdenum plate.

The MIT gauge can be used in two primary modes of operation:

(1) The active feedback mode, which maintains the total electron current constant by adjusting the filament heating current. The feedback loop time constant is dominated by the heating time (50-300 ms) of the filament and its support.

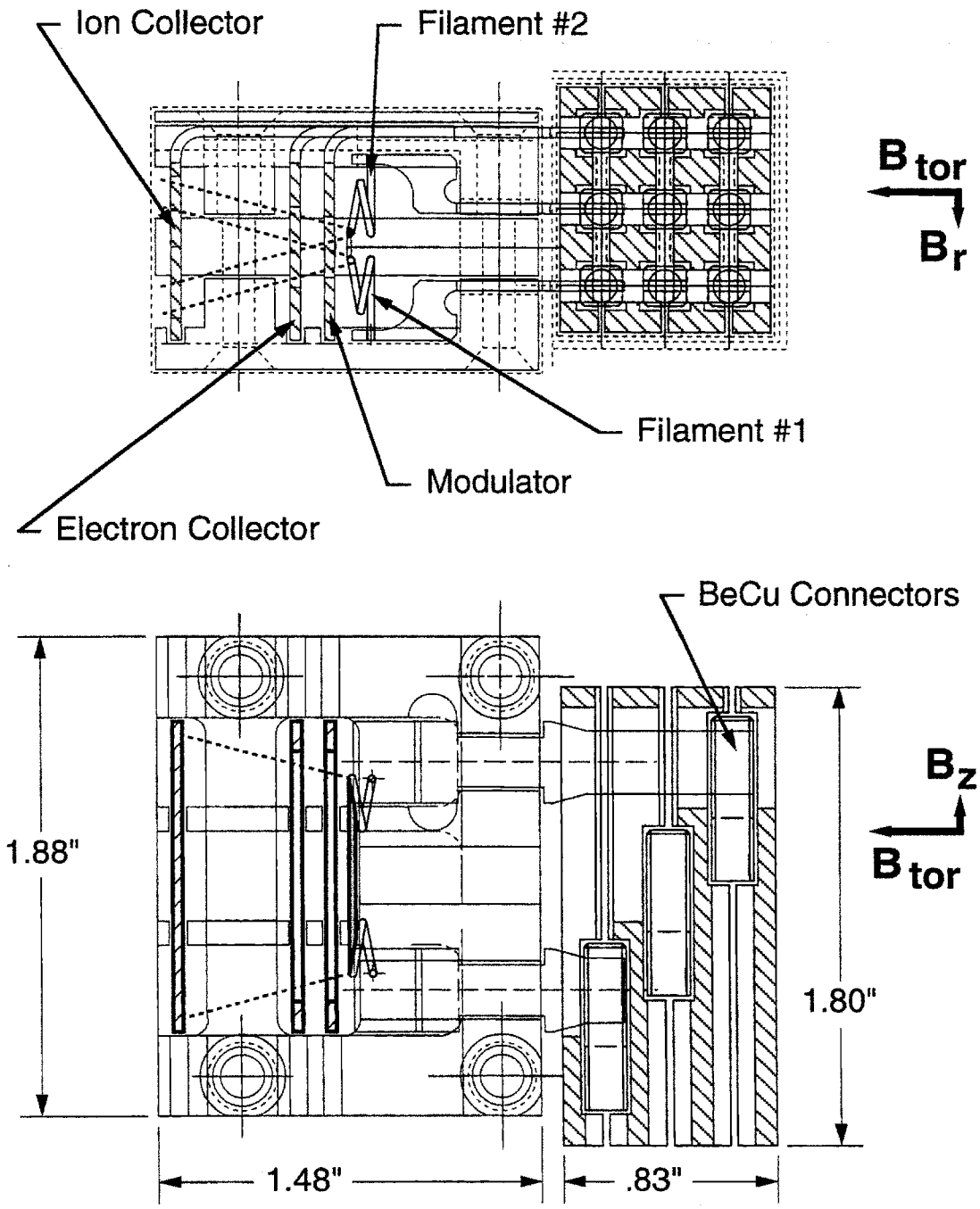

Fig. 3-3: Two views of the gauge and plug assemblies. The drawing also shows the 15° acceptance angles (with respect to the Alcator C-Mod magnetic field components) of electrons emitted from the filament. The nominal dimensions of the assembly elements are also indicated.

(2) The constant filament heating voltage mode, which maintains the primary electron emission approximately constant, drifting slowly (typically a few percent per second).

During plasma discharges the gauge is operated in the electron current feedback mode. The constant filament heating voltage mode serves mainly for test purposes.

The choice of bias voltages (Fig. 3-1) was based on earlier designs mentioned above and on *ex situ* tests performed at MIT in weak magnetic fields ($\leq$ 0.1 T). The bias voltages chosen for the MIT gauge are near the maximum ionization efficiency and have not been altered after the final installation of the gauges in Alcator C-Mod.

All the electrodes are aligned with each other (hence the name linear-geometry) and with the tokamak toroidal magnetic field. The gauge has a 15° acceptance angle, i.e., a deflection of magnetic field axis from the gauge axis by 15 degrees in any direction should still allow a 100% electron transmission and ion collection. The electrodes are mounted in the gauge "body" made of ceramic-coated molybdenum. All the electrodes have extension bars which engage into BeCu connectors mounted in a plug. Fig. 3-3 shows a completely assembled gauge with the mating plug. The design of the gauge as a plug-in unit allows for its replacement without removing the mounting and electrical hardware.

There are two identical gauges, with identical mounting hardware, installed in Alcator C-Mod vessel at two different toroidal locations: in J and E divertor modules (see Section 2.3.1). Each gauge is positioned behind the lower divertor target plates, held by a mounting bracket shown on Fig. 3-4. The bracket holding

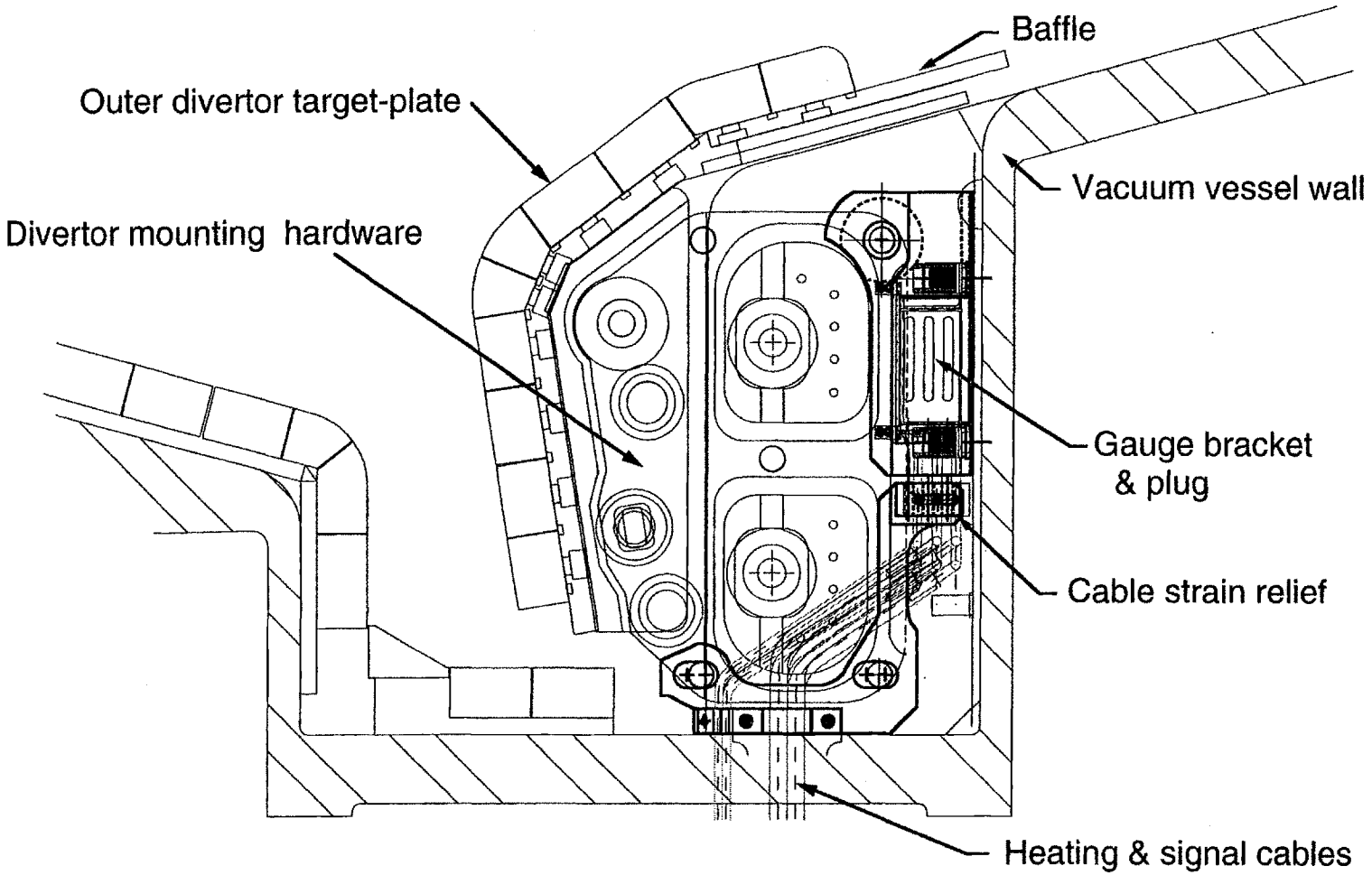

Fig. 3-4: MIT-gauge mounting brackets located behind the Alcator C-Mod outer divertor target. The gauge, which is not shown for picture clarity, engages into the plug, located behind the gauge holding bracket. For simplicity only the top section of current and signal cables is shown. The cables run a ~1.5m-long path in vacuum, before reaching electrical feedthroughs.

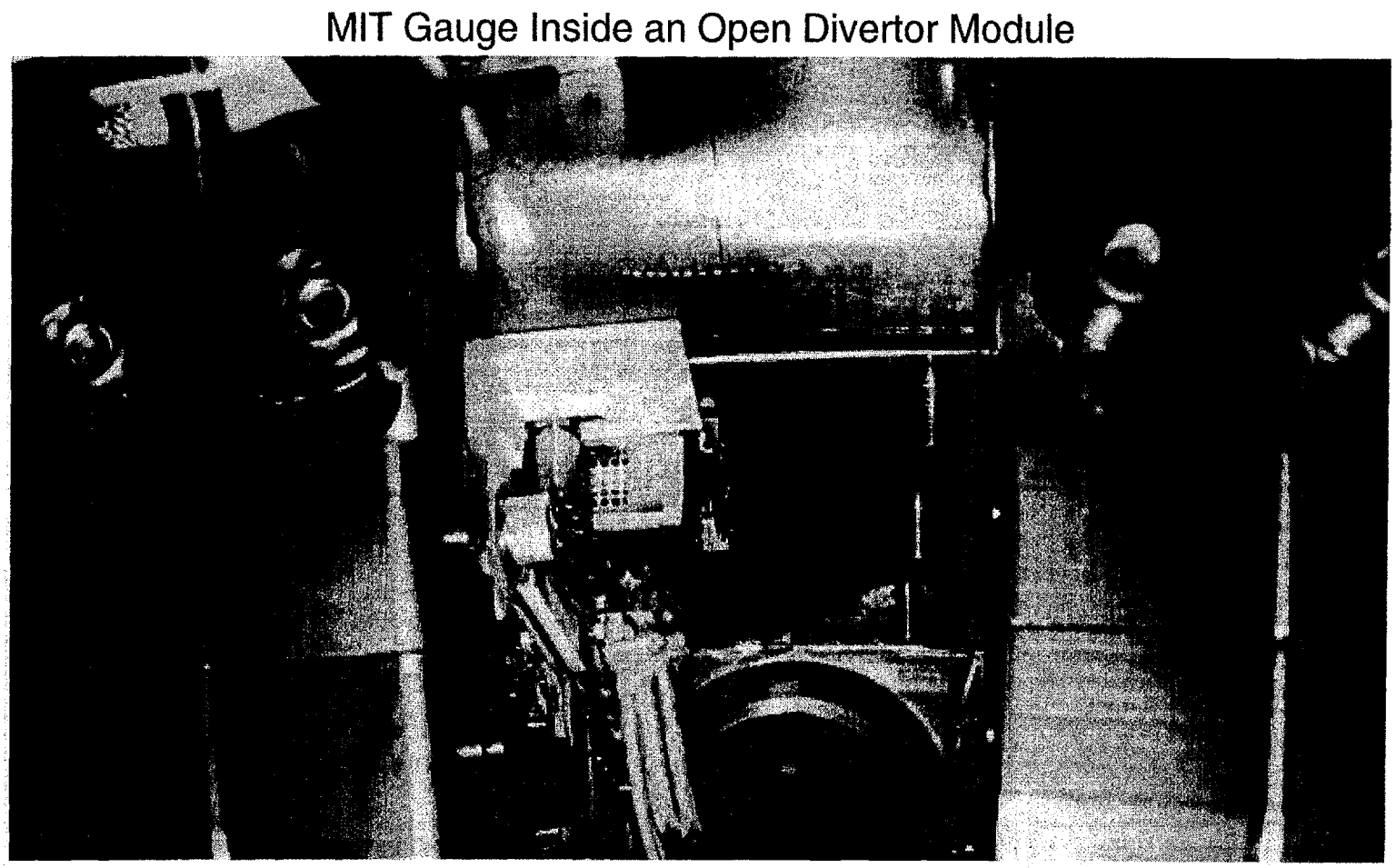

Fig. 3-5: Photograph of the MIT gauge installed in an open port of the Alcator C-Mod shaped divertor. The gauge is protected by a Faraday shield with gas admission holes visible on the photograph. During plasma operation there is an additional "sun-screen" mounted above the holes to eliminate line-of-sight photon-flux-induced noise. The white mounting bracket is made from ceramic-coated molybdenum to isolate the gauge electrically from the vessel.

the gauge also plays the role of a Faraday-shield (with gas admission holes). Fig. 3-5 shows a photograph of one of the gauges installed in the open divertor module-E. The mounting hardware is electrically isolated (flame-sprayed-ceramic) from the tokamak vessel, so that the gauge can be grounded externally. This facilitates signal shielding and compliance with Alcator C-Mod electrical safety requirements. Each gauge has two completely independent, electrically isolated, redundant filaments (unlike the B-A gauge, where the filaments have a common return wire). This design requires additional leads, but it has already proven to considerably increase the life-span of the gauge, which is not accessible for 6-12 months at a time.

Each of the gauge electrical connections runs a complicated 1.5m path in vacuum before reaching a feed-through. The filament heating leads are made of 0.25" diameter copper bars, the signal leads are made of stainless steel, ceramic insulated, in-house made coaxial cable. A 50 Ohm impedance match was not necessary due to the low frequency of the transmitted signal. The stainless steel coax design was dictated by a requirement of mechanical robustness. The 1.5 meter cable length combined with the difficult access required the above mentioned hardware to be mounted permanently in the vessel, thus reinforcing the need for the plug-in gauge design.

3.1.3 Control and data-acquisition electronics

The ionization gauge control and data acquisition was entirely designed and developed in-house by the author for the purpose of the Alcator C-Mod experiment. The analog electronics is mounted in a Eurocard-standard crate and is

interfaced with a CAMAC-standard data acquisition system and an Allen-Bradley programmable logic controller (PLC), allowing for its remote operation.

Fig. 3-6 shows a simplified schematic of the gauge electronics. The three most important functions performed by the analog circuit are:

(1) supplying the necessary voltage bias for the electrodes, including the AC modulator voltage;

(2) measuring the collected ion current;

(3) measuring and maintaining a constant electron current through the feedback on the filament heating.

These functions of the analog circuit are describe in detail below.

(1) The DC bias (filament +70V, electron collector +250V) is supplied by Apex PA41 high voltage operational amplifiers (op-amps). The same op-amp type is used to amplify the 10 kHz sine wave produced by a Burr-Brown 4423 oscillator. The actual bias voltages are monitored through a voltage divider by the PLC control system.

(2) The ion current is measured by a low-noise Burr-Brown OPA627 operational amplifier used in a transimpedance mode. The signal, however, besides collected ion current contains also a displacement current induced by a capacitive coupling between the modulator and the ion collector. Because of the sine wave modulation the pick-up current contains only a single harmonic and is easy to correct for. This is performed by adjusting the amplitude and the phase-shift of the portion of the oscillator output and subtracting it from the ion signal, using a Burr-Brown INA101 instrumentation amplifier. The ion signal is still modulated at a base 10 kHz

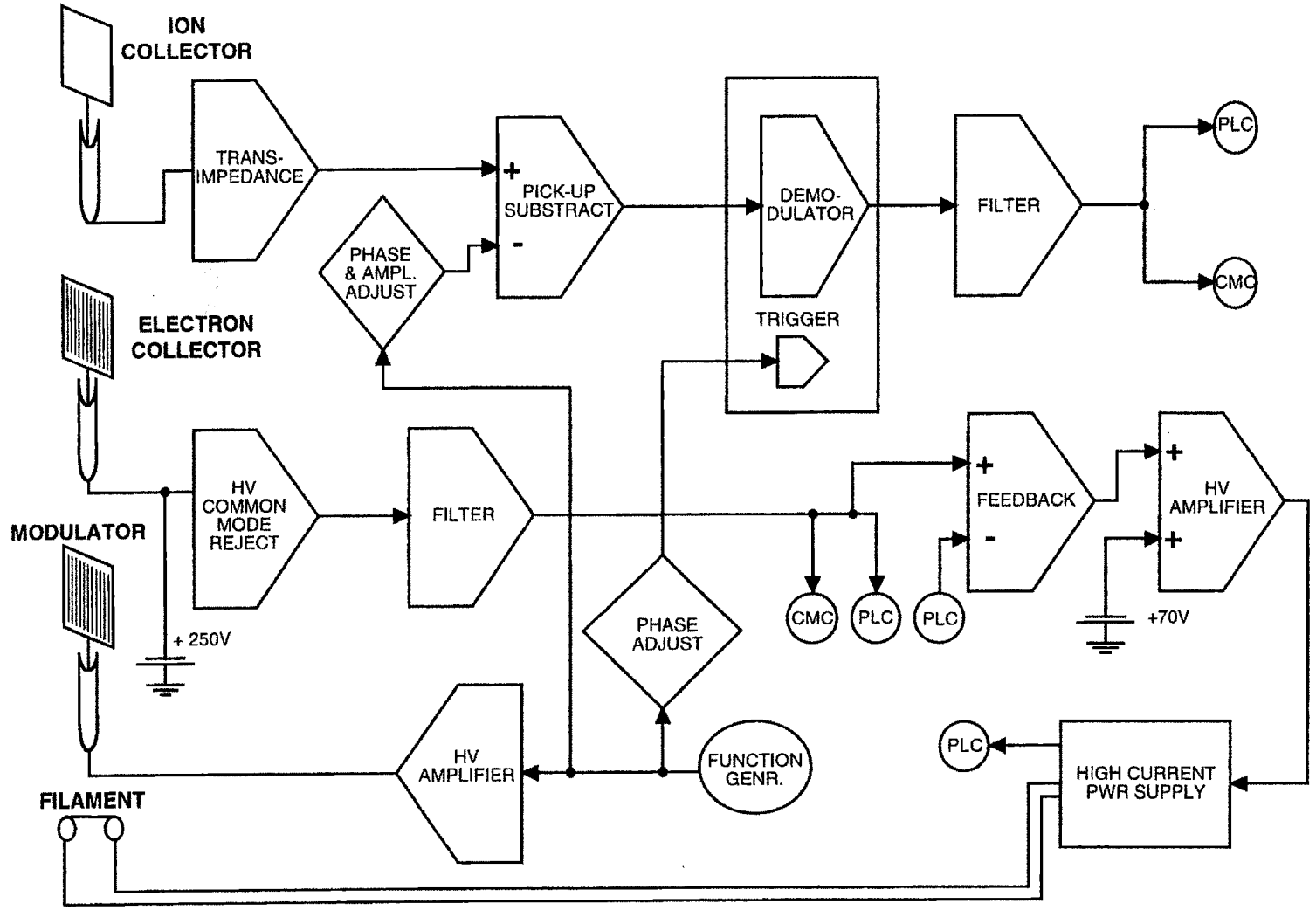

Fig. 3-6: Simplified schematic of the MIT-gauge control and data-acquisition electronics.

frequency and needs to be demodulated This is performed by a specialized synchronous demodulator, Analog Devices AD630. The demodulator output is integrated with a 2 ms time constant. Finally, to improve the dynamic range, the ion signal is split into two channels with different analog amplification. The two channels are read by a CAMAC digitizer and monitored by the PLC.

(3) The electron current signal (from the electron collector electrode) is initially superimposed on top of a +250V DC bias. Therefore, the 250 V bias level needs to be rejected before the much weaker electron signal voltage can be measured. Out of many tested common-mode rejection schemes most proved unsatisfactory (e.g., opto-isolators, capacitance-isolators, inductance isolators). Finally, we adopted the simplest solution. The Burr-Brown INA117 is a laser-trimmed resistor network with an op-amp on a single chip. However, its rated common-mode voltage rejection is only 200V. In order to use it for a 250V rejection, a metal-package chip with an oversized heat-sink was accepted after extensive testing.

The electron current signal is subsequently integrated with a 2 ms time constant. It is then read by a CAMAC digitizer and monitored by the PLC. The gauge operator sets the desired electron current level through the PLC controller. This reference level is compared to the actual measured electron current with a Burr-Brown OPA627 operational amplifier. The error is used as a control signal in the feedback loop. Initially proportional and integral controls were tested. In the final design it turned out that there was enough stray capacitance on the circuit board to provide the integral part, so that only the proportional part of the controller was connected. The control

signal, however, is at this point referenced to ground. Thus the signal is summed with a +70V bias by an Apex PA41 op-amp before being supplied to the control input of a KEPCO ATE 6-50M power supply [61].

It is also possible to operate the gauge in a constant-heating-voltage mode rather than in a constant electron current mode. This option requires a simple change of a jumper position in the feedback circuit. The constant voltage mode was used for the test purposes only (described in Section 3.2.2).

The description given here is, out of necessity, a very simplified one. Besides the main functions listed above there are numerous over-voltage protection, safety, and noise-reduction measures incorporated in the gauge circuit design. For all non-critical functions a National Semiconductor LF356 operational amplifier is used across all parts of the analog circuit.

The gauge output signals are digitized by a CAMAC digitizer and the resulting data are stored for subsequent analysis. The analog circuit is complemented by a PLC. The controller is interfaced through a fiber-optic link, with a PC station in the tokamak control room. The PC display informs the gauge operator about the current diagnostic status. The PC/PLC allows remote manual or automatic operation of the gauge [62]. In the automatic operation mode the gauge is entirely controlled by the PLC, following the Alcator C-Mod state cycle [63]. The bias voltage is applied ~2 min. before a machine pulse (at transition to the "init" state) and the filament heating, only ~30 sec. before the pulse (at transition to the "check" state). Both the heating and the bias are turned off ~5 sec. after the pulse

(at transition to the "recool" state). This operational procedure extends gauge life by limiting its exposure to high voltage and metal-vapors from the hot filament.

3.2 MIT gauge calibration

Absolute pressure measurements are essential for the Alcator C-Mod divertor physics program. Thus a considerable effort was devoted to understand MIT gauge operation and its response to pressure and other external and internal variables. During each operational campaign of Alcator C-Mod (typically divided by vacuum-breaks and rearrangements in gauge connections) both MIT divertor gauges were subjected to extensive calibration experiments.

During the 1993 tokamak operation the J-divertor-module gauge failed due to an electrical short-circuit connection to another diagnostic sharing a vacuum feed-through. Also the B-port gauges were not yet installed. Thus the only calibration experiments performed, involved an off-line comparison of the E-divertor-module gauge with the midplane B-A and capacitance gauges.

During the Spring 1994 tokamak operation the B-port gauges were installed. However, the capacitance manometer there did not have any vibration isolation and did not deliver pressure data during tokamak discharges. Thus a cross-calibration technique was used: First, the three capacitance gauges were cross-checked off-line with respect to each other. Next, the B-A ionization gauges were calibrated against the MKS manometers at the corresponding locations (see example in Section 2.3.3). The J-divertor-module MIT gauge was calibrated against the B-port B-A gauge, during actual plasma discharges.

Finally, during the Winter-1994/Spring-1995 tokamak operation all Alcator C-Mod neutral pressure gauges, were installed and functional. Dedicated tokamak run-time was allocated specifically for the gauge calibration. This allowed a direct calibration of the MIT gauge against a capacitance manometer, and confirmation of results from the previous calibrations.

3.2.1 Magnetic field effect

By definition, an ionization gauge relies on neutral particle ionization and subsequent charged particle motion in defined electrostatic fields to measure the background neutral particle density. Any magnetic field, superimposed on the electric field, considerably alters the charged particle dynamics inside the ionization gauge [48]. The MIT gauge is no exception. It is very sensitive to external magnetic field magnitude and direction.

During a series of experiments only one component of the tokamak magnetic field was varied at a time while the vacuum-chamber pressure was held at a constant value of a few mTorr.

As expected, the tokamak toroidal magnetic field (B_{tor}) significantly affects gauge response. The gauge sensitivity increases monotonically with the applied toroidal magnetic field (parallel to gauge axis and direction of the gauge electric field). Fig. 3-7 shows enhancement of the gauge sensitivity (expressed in the form discussed in the next section), normalized to unity at B_{tor} =0. The sensitivity rises quickly (factor of 5) up to 0.5 T, and then exhibits a much slower rise (adding a factor of 1.5 per 1 T). There is no sign of saturation in the range examined (0-4.3T).

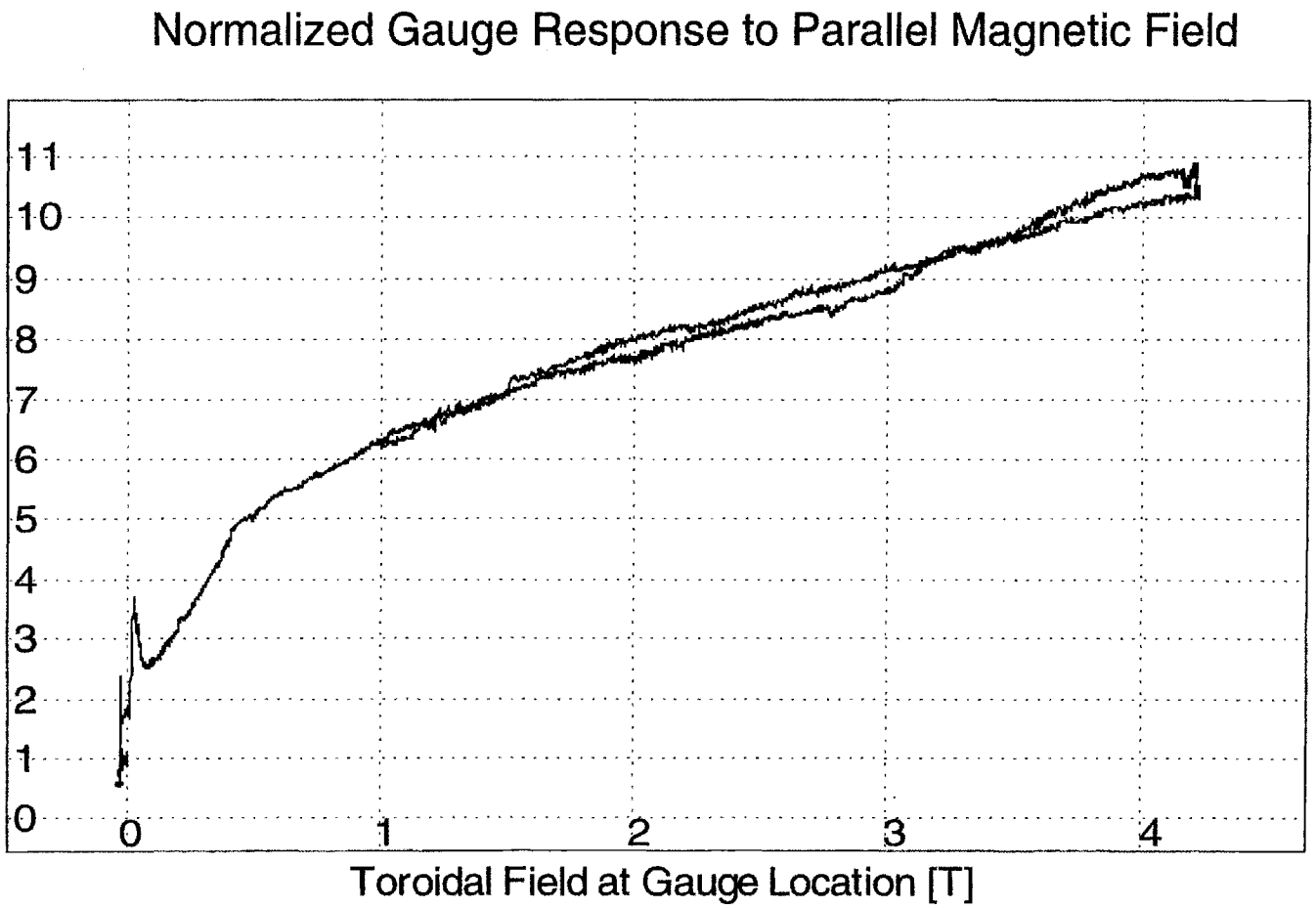

Fig. 3-7: Gauge response to the tokamak toroidal magnetic field (parallel to the gauge axis). The signal is normalized to unity at B_{tor} =0. The traces recorded during the field ramp-up and ramp-down are overlaid. At B_{tor} =0.5T the slope of the curve changes.

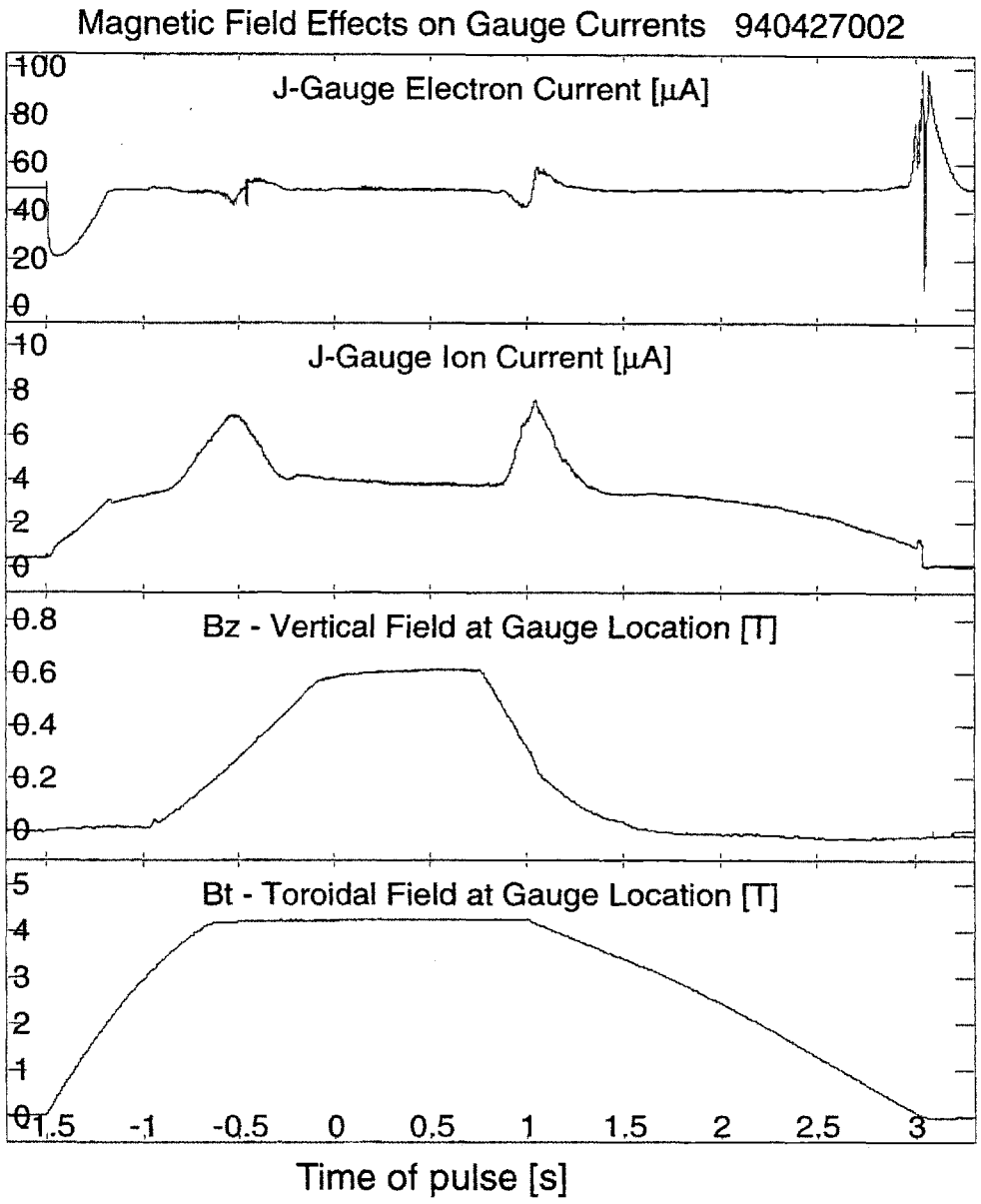

Fig. 3-8: Effects of the tokamak magnetic fields on the MIT gauge signals. The electron current is perturbed during toroidal field start-up and termination. The ion current is perturbed by fast changes in the tokamak vertical field. Such changes occur during plasma current ramp-up and termination. During the steady-state portion of a plasma discharge the gauge responds to pressure changes only.

A possible explanation of the sensitivity enhancement is increasing confinement of electrons along magnetic field lines with increasing parallel field. This in turn would extend electron life-time in the resulting magneto-electrostatic trap and lead to a larger number of ionizations per collected electron. An observation in support of this hypothesis is that at a field above 0.01 T (which corresponds to the electron Larmor radius < grid spacing) the collected electron current drops dramatically, e.g., from 300 μA to 30 μA (with constant filament heating voltage), most likely due to emission limitation by the space charge of trapped electrons. A similar change in the electron current occurs when the gauge is operated in the feedback mode. The feedback circuit corrects the deviations in electron current as illustrated on Fig. 3-8 (top trace).

The MIT gauge is designed in such a way that a 15° angle between the magnetic field direction and gauge axis in any direction should still allow 100% collection of both ions and electrons (Fig. 3-2). None of the users of the ASDEX gauge have reported any change in sensitivity due to perpendicular fields (with respect to the gauge axis) within a similar 15° angle limit [64, 65]. The MIT gauge, in contrast, is sensitive to the perpendicular magnetic field component and its changes. The gauge sensitivity (bottom part of Fig. 3-9) is reduced by the presence of a steady state perpendicular field (B_Z in Alcator) superimposed onto the parallel field, even though the 15° angle limit is not exceeded.

During some experiments transient changes in gauge behavior were observed. Fig. 3-8 illustrates effects of changes in magnetic fields on gauge currents. During a test pulse the vacuum vessel was maintained at a constant pressure ~1 mTorr D_2 while the tokamak magnetic-field coils were energized. The top trace shows the time history of the electron current measured in the J-module MIT gauge

(feedback reference was set to 50 μA); the second trace, the ion current. The third trace shows the vertical component of the tokamak field, evaluated at the gauge location using a magnetic reconstruction program [66]; and the last trace, the toroidal component of the tokamak magnetic field.

The toroidal field starts to ramp-up at t= -1.5 sec. The electron current drops suddenly to ~20 μA right after the field initiation. As mentioned before this occurs at a magnetic field strength which corresponds to electron Larmor-radius decreasing below the gauge grid spacing. The building space-charge of trapped electrons may be responsible for inhibiting the emission from the gauge filament. The feedback-controller responds to this signal change by increasing filament heating power. As a result the electron current recovers to its reference value within about ~300 ms. This slow response time is determined primarily by the long thermal time-constant of the filament. Also note that the collected ion current increases with the toroidal field - this is a direct evidence of the gauge sensitivity rise, seen already on Fig. 3-7. At t =-0.7 sec. the toroidal field reaches its steady-state value.

At t =-1sec. the vertical field ramp-up starts and it lasts until t =-0.3 sec., when the field reaches its steady-state level. During the flat-top portion of the vertical field the ion current remains relatively constant (except for a small drift). It exhibits, however, a sharp transient increase during both the vertical-field ramp-up and ramp-down. Note that this, always positive, transient perturbation occurs at a large dB_Z/dt value independent of its sign. If it was caused by an EMF pick-up (e.g., closed conducting loop in the instrument setup) it would have different sign for different dBz/dt direction.

It is difficult to explain this phenomenon without actually modeling the charged particle trajectories due to the internal electrostatic fields (including space charge of trapped particles) with superimposed external magnetic fields. We speculate that the observed phenomenon results from transient changes in particle trajectories inside the gauge. The electron current is also affected by the vertical-field changes, but to a much lesser extent. The perturbations observed in the electron current results from changes in secondary electron production ($I_{es}= \alpha I_i$ - see below), due to changing ion current, and the feedback-controller corrective action.

After t=1sec. the toroidal field is ramped down. The associated decrease in the ion current (gauge sensitivity) is clearly visible during that time. When the toroidal field approaches its zero value (t =3 sec.) a sudden rise in the electron current occurs. This is a mirror image of the effect observed at t =-1.5 sec. Electrons which have been trapped in the magneto-electric trap are now being suddenly released, when their Larmor-radius exceeds the grid spacing, leading to the electron-current burst. The feedback controller again responds to this sudden change by adjusting the filament heating power. The equilibrium is reached within ~200 ms due to the long thermal time-constant of the filament.

Since the transient phenomena, caused by changes in magnetic fields, are not critical to the results reported in this thesis they have not been investigated further. The plasma discharge occurs only during the flat-top phase of the toroidal field. Moreover, during the steady-state portion of the discharge dB_Z/dt does not exceed 0.5 T/s. In this phase of the pulse the gauge is insensitive to the small changes in the perpendicular fields and provides a reliable pressure measurement. During the plasma current ramp or termination the gauge output has to be used with caution.

3.2.2 Low pressure calibration

Standard ionization gauge theory [67] proposes the following expression for pressure measured by such a gauge:

$$p = 1/S \cdot I_i / I_e \tag{3.1}$$

where:

p - is measured pressure, expressed in pressure units, e.g. Torr;

I_i - is collected ion current;

I_e - is collected electron current;

S - is gauge sensitivity, expressed in 1/Torr.

We should remember, however, that an ionization gauge actually measures number density (particles/volume) of a background gas, which only for convenience is expressed in pressure units, assuming standard gas conditions.

The most important assumption in Eq. 3.1, is that I_i/I_e «1. This condition was also listed by Schulz and Phelps [68] as a necessary requirement for a linear response of their high pressure ionization gauge. In a later work, Martin and Lewin [69] reported a decrease of their gauge sensitivity with increasing pressure. From the graph published there, a ratio $I_i/I_e \approx 0.1$ can be deduced, violating the Schulz-Phelps prescription. Similarly the ASDEX gauge was also found to change sensitivity in the high pressure range, with $I_i/I_e \approx 0.5$, as reported by Klepper [70]. A similar problem is encountered on Alcator C-Mod, when the ratio I_i/I_e reaches 0.5, due to the high magnetic fields and high pressure operation (up to tens of mTorr).

In order to extend the ionization gauge theory beyond the $I_i/I_e \ll 1$ limit we have proposed in an earlier work [71] to include the effect of secondary electrons (other than emitted from a filament). The electron collector current (I_e) can be expressed as:

$$I_e = I_{ep} + I_{es} \tag{3.2}$$

where:

I_{ep} - is the primary electron current consisting of the filament emission (I_e^{fil}), less the modulator collection (I_e^{mod}):

$$I_{ep} = I_e^{fil} - I_e^{mod} \tag{3.3}$$

I_{es} - is the electron current resulting from the volumetric ionization (second and higher generations) and secondary electrons emitted from the ion collector. For convenience it will be referred here to as a "secondary electron" current.

The number of electrons produced by ionization should be proportional to the ion current. We can therefore express the primary electron current in the following form:

$$I_{ep} = I_e - \alpha I_i \tag{3.4}$$

where:

α - is the "secondary electron" coefficient.

We postulate that Eq. 3.1 remains valid beyond the $I_i/I_e \ll 1$ limit if the current ratio excludes secondary electrons. We can therefore calculate the pressure from the gauge measurement using a modified version of Eq. 3.1:

$$p = 1/S \cdot I_i/I_{ep} \tag{3.5}$$

It is extremely difficult to derive value of the secondary electron coefficient from first principles. For practical purposes it is more accurate and convenient to measure it experimentally. During a series of experiments, in a constant parallel field, I_i and I_e were measured as a function of pressure, p. The sensitivity defined in Eq. 3.5 was found to be a linear (within 20%) function of pressure over the range of 0.03 - 7 mTorr deuterium and the secondary electron coefficient - α was found empirically to be α =2.1 (±0.2). For simplicity $\alpha \approx 2$ was assumed for calculations described in this section.

Similar to the Lewin-Martin gauge, the MIT gauge sensitivity was found to depend on electron current. The sensitivity defined above was found to be a strongly decreasing function of the primary electron current (but not the collected electron current I_e), when I_{ep} is expressed by Eq. 3.4.

This dependence (shown in Fig. 3-9), is different for different modes of operation of the gauge (e.g. feedback vs. constant voltage control and presence of a perpendicular magnetic field). For a constant magnetic field and a constant (or determined) primary electron current Eq. 3.5 provides a satisfactory expression for the neutral pressure measured by the gauge up to ~7 mTorr deuterium.

The conclusion drawn from above experiments is that it is desirable to operate the gauge at higher electron current (30-60 μA), i.e. at points where the sensitivity does not vary significantly. Such operation lowers the danger of developing a self-sustained discharge inside the gauge and improves signal-to-noise ratio for I_e measurement. Another conclusion is that the most desirable mode of operation would be an active feedback control of the primary electron current I_{ep}, maintaining constant gauge sensitivity. This is, however, very difficult in practice.

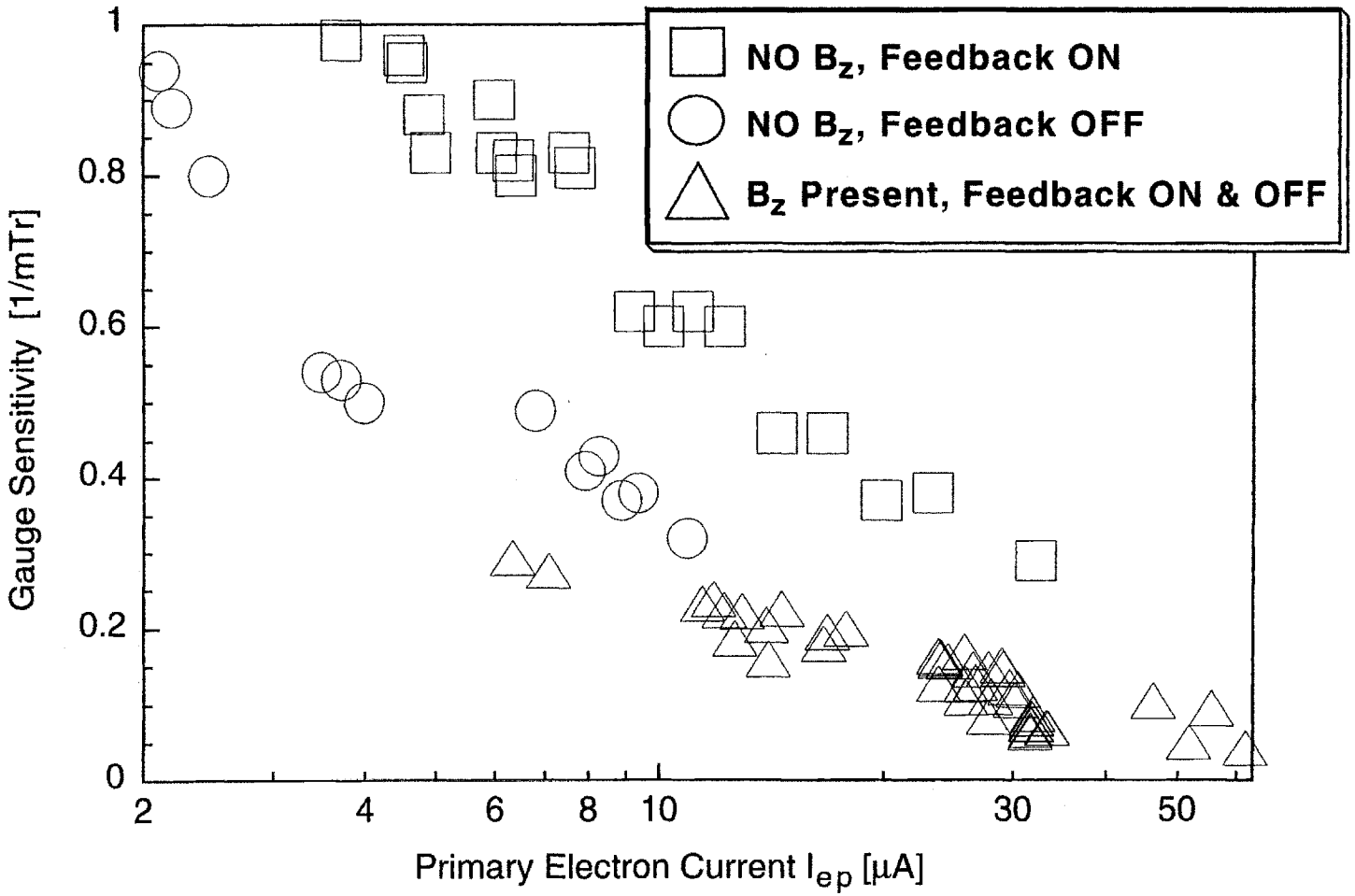

Fig. 3-9: MIT gauge sensitivity as a function of the primary electron current for pressure range 0.03-7 mTorr.

An active feedback control of the collected electron current I_e, does not provide constant sensitivity with pressure (due to changing I_i). It is, however, preferred to the constant heating voltage operation because of better predictability of one of the measured quantities (I_e).

The above low-pressure calibration allowed reliable, accurate data to be obtained for pressures up to 7 mTorr. This pressure limit, however, turned out to be unsatisfactory for a high-density tokamak operation.

3.2.3 High pressure calibration

During the 1994 and 1995 tokamak operation very high neutral pressures have been produced in the Alcator C-Mod divertor, approaching ~70 mTorr. Therefore it was necessary to extend the previously described calibrations into this high pressure regime.

A practical calibration procedure was to use gauge readings during a steady-state portion of actual plasma discharges. In the steady state neutral gas should reach pressure equilibrium between the "gas-box" volume (behind divertor target plate) and the bottom of a vertical port. Thus a comparison of pressure readings from the two gauges located at the B-port bottom with the J-module MIT gauge readings delivers direct calibration data for the latter.

During the Spring 1994 operation of the B-A gauge served as a reference (calibrated earlier against a capacitance manometer) for pressures up to 30 mTorr. During the Winter 1994/Spring 1995 operation the MKS capacitance manometer served as a reference for pressures up to 70 mTorr, and possibly higher in the future.

During high pressure operation (7-70 mTorr) the expression in Eq. 3.5, using $\alpha = 2$, led to divergence in calculated pressure, when I_i/I_e exceeded 0.5. This corresponds to a physical limit, when the number of higher population electrons collected by the electron collector equals that of the primary electrons (emitted minus collected by the modulator).

Clearly $I_i/I_e=1$ constitutes the ultimate gauge operating limit. $I_i=I_e$ corresponds to a self sustained discharge (break-down) inside the gauge and would most likely lead to its failure. Fortunately these conditions have not yet been observed in the gauge, but because Alcator C-Mod produces higher neutral pressures in each campaign, they may become reality. A solution to the problem would be to alter the bias voltages in the gauge to move the operating point away from the maximum ionization efficiency.

Again, since the gauge theory is not the subject of this thesis (its complexity, however, easily warrants a dissertation-caliber research) we postulate a modified expression for the gauge response and derive all necessary coefficients from appropriate experiments. Specifically, we postulate that the measured pressure can still be expressed as a monotonic function of the current ratio, when the primary electron current is properly calculated:

$$p = \text{function}(I_i/I_{ep}) \tag{3.6}$$

Because the value $\alpha = 2$ led to divergence in the pressure equation, we introduce a modified expression for the secondary electron coefficient:

$$\alpha' = 2 - f(\text{pressure}) \tag{3.7}$$

where:

f(pressure) - is a monotonic, positive function of a background gas pressure (density).

The difficulty in using Eq. 3.7 in combination with Eq. 3.5 is that a value of α' is required to calculate measured pressure which in turn would be necessary to calculate α' itself. Since pressure is a monotonic (but not linear) function of I_i/I_e, we substitute the current ratio for pressure in Eq. 3.7 and seek the simplest form of the function-f that agrees with the experimental observations. We find a satisfactory agreement using a very simple expression for the secondary electron coefficient:

$$\alpha' = 2 - 0.75 \cdot (I_i/I_e) \tag{3.8}$$

Note that Eq. 3.8 leads to $\alpha' \rightarrow 2$, at low pressure, thus agreeing with results described in the previous section

There are two possible ways of calculating the resulting neutral pressure:

(1) Insist on linearity in pressure response but allow non-linearity in gauge sensitivity due to variations in the primary electron current. This leads to an equation, identical with the Eq. 3.5, except for a variable α':

$$p = \frac{1}{S} \cdot \frac{I_i}{(I_e - \alpha' I_i)} \tag{3.9}$$

where:

S - the gauge sensitivity is a monotonic function of the primary electron current, fitted experimentally. The best fit was obtained using a logarithmic function of I_{ep}.

(2) Allow non-linearity in the gauge pressure response but simplify the final expression, avoiding a complicated sensitivity function. We find the best agreement with the experimental data, using a power law of the form:

$$p = const. \cdot \left(\frac{I_i}{I_e - \alpha' \, I_i} \right)^{0.8} \tag{3.10}$$

Fig. 3-10 shows a comparison between the two pressure expressions for a two-decades pressure range: 0.3 - 30 mTorr. The pressure from the MIT gauge, calculated with Eqs. 3.9 and 3.10, is plotted versus the pressure measured by the B-bottom B-A gauge (calibrated earlier against a capacitance manometer at the same location to within 15%). Additionally a result of ChiSq goodness-of-fit test is printed next to the plots. The minimal difference between the tests of the two expressions is well below experimental noise. Thus based solely on these experiments it is not possible to decide in favor of any of the pressure calculation methods and draw conclusions with respect to underlying physics.

Eq. 3.10 was selected for automated pressure calculations as easier to use and modify. Moreover, subsequent higher pressure (7-70 mTorr D_2) calibrations against the MKS capacitance manometer confirmed Eq. 3.10, as the more precise one.

A dedicated calibration experiment delivered less data than collected during the plasma discharges. It confirmed earlier calibrations, however, and allowed a comparison between E- and J-module MIT gauges. Whereas the J-module gauge has been calibrated during plasma discharges, the E-module gauge could not be calibrated in this way due to lack of a direct reference (comparable to the

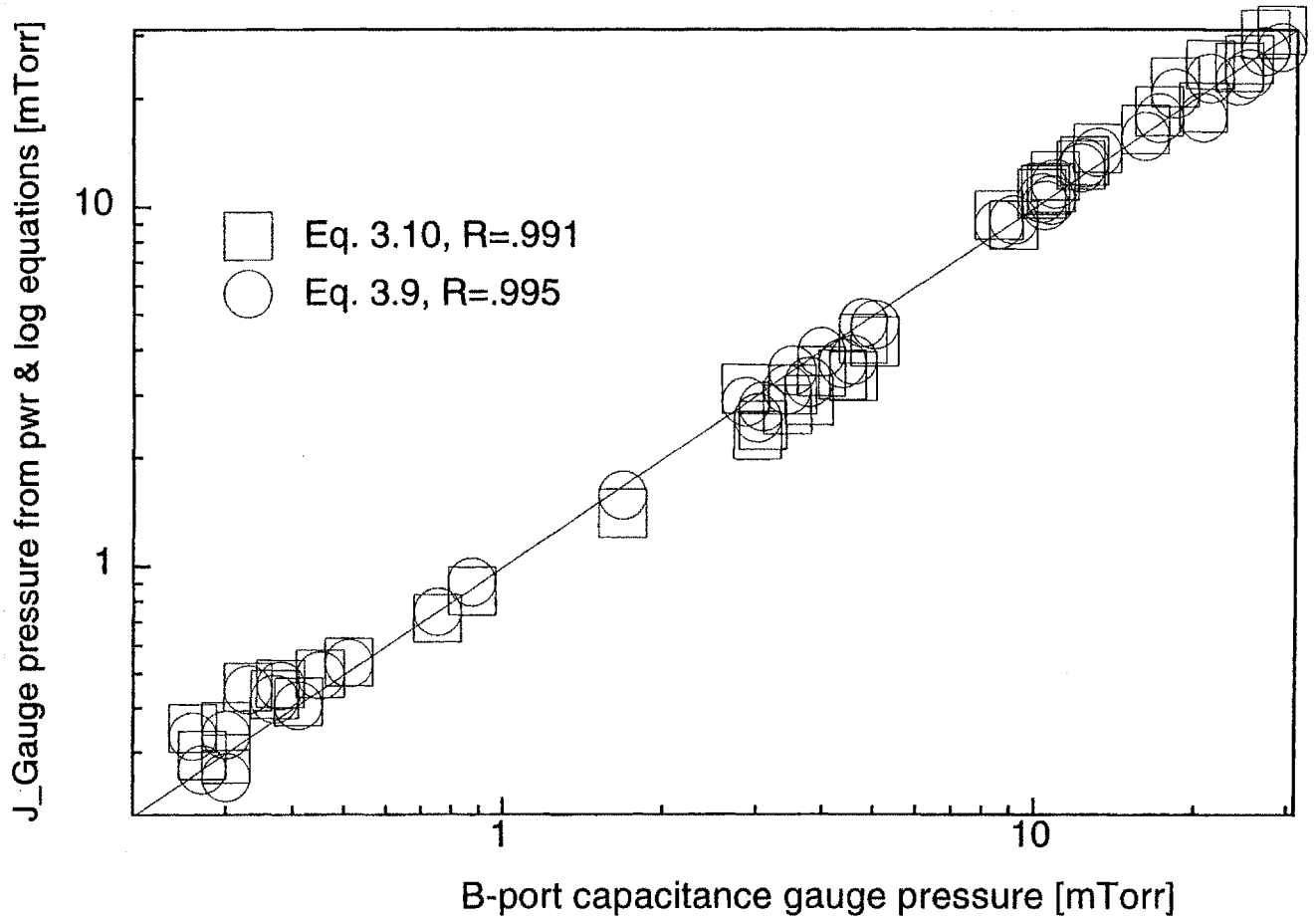

Fig. 3-10: Goodness-of-fit test for linear-with-logarithmic-sensitivity (Eq. 3.9) and power-law (Eq. 3.10) pressure dependencies. Both formulae result in a very good fit across two decades of pressure.

B-bottom gauges providing the reference for the J-module gauge). The dedicated calibration experiment showed that the two gauges follow each other only to within 20-30%, most likely due to slight geometric differences between them. For simplicity the same expression has been adopted for interpretation of the E-module gauge data as the J-module gauge. This procedure leads to a higher error in pressure measurement in the E-divertor-module (~40%), but the E-port measurement is of secondary importance and is primarily used for the leakage-flux estimates (Section 5.7). The J-module gauge, in contrast, is calibrated to within 15%, thus delivering an accurate pressure measurement there.

3.3 Chapter summary

The linear geometry hot-filament ionization gauge design of the ASDEX-type is probably the most suitable one for fast-response *in situ* tokamak operation. The gauge, however, has its drawbacks. The most significant one is difficulty in interpreting its measurements. Because of high magnetic field, high-pressure operation and the geometry effects, the phenomena occurring inside the gauge are very complex.

Through extensive calibration experiments, supported by the standard ionization gauge theory and theory of particle motion in electromagnetic fields, we were able to derive practical expressions, allowing us to use the MIT gauge (even under certain limitation) as a relatively accurate and reliable pressure instrument. We succeeded in this for a very broad pressure range: 0.03-70 mTorr.

At this writing the pair of the MIT gauges has been working reliably for over 5000 Alcator C-Mod cycles.

Chapter 4

Neutral Pressure Scaling with Edge Plasma Regimes

This chapter reviews edge plasma regimes identified in Alcator C-Mod and correlates them with neutral pressure observations. A detailed description and analysis of the divertor detachment is provided, since this operating regime is in the center of attention today because of its potential for reducing target-plate heat-loads thus alleviating the divertor target problem in ITER (recall Section 1.2).

For clarity the initial analysis concentrates on a series of experiments, during which only one major plasma parameter was varied. First, the dependence of edge plasma and neutral parameters on the volume averaged core plasma density over the range $\langle n_e \rangle \approx 0.4\text{-}2.5 \cdot 10^{20}$ m^{-3} is analyzed. These discharges were ohmically heated with plasma current $I_p \approx 800$ kA. Next, the dependence of the neutral pressure on the plasma ohmic heating currents is examined.

All the discharges described in this chapter were single-null diverted, with geometry similar to the one shown on Fig. 2-10. The geometry varied slightly between shots, but the outer strike point was always located near the middle of the vertical portion of the outer target plate, below the divertor "nose". The ion B×∇B-drift was directed towards the closed divertor at the bottom on the machine. About 10% of the pulses shown were fueled in the divertor private-flux zone

(through the capillary-injection system), while the rest were fueled at the tokamak outer midplane (through the piezo-valve). Within the parameter range investigated in this chapter, the fueling location did not influence the steady-state neutral pressure results.

Analysis of additional parameter scaling experiments, including ion B×∇B-drift direction and divertor geometry, follows in Chapter 6. All the experiments reported throughout the thesis were conducted with a constant toroidal field B_t =5.3 T.

4.1 Edge plasma regimes

4.1.1 Edge plasma parameters

Based on the Langmuir-probe data analysis and parallel heat-transport modeling, LaBombard [72] has identified three distinctive edge plasma regimes in Alcator C-Mod:

(1) "sheath-limited";

(2) "high-recycling";

(3) "detached divertor".

Fig. 4-1 illustrates the three edge plasma regimes by comparing plasma parameters upstream in the SOL (measured by the fast-scanning probe - see Section 2.2.2) with target plasma parameters (measured by the flush-mounted probes - Section 2.2.2).

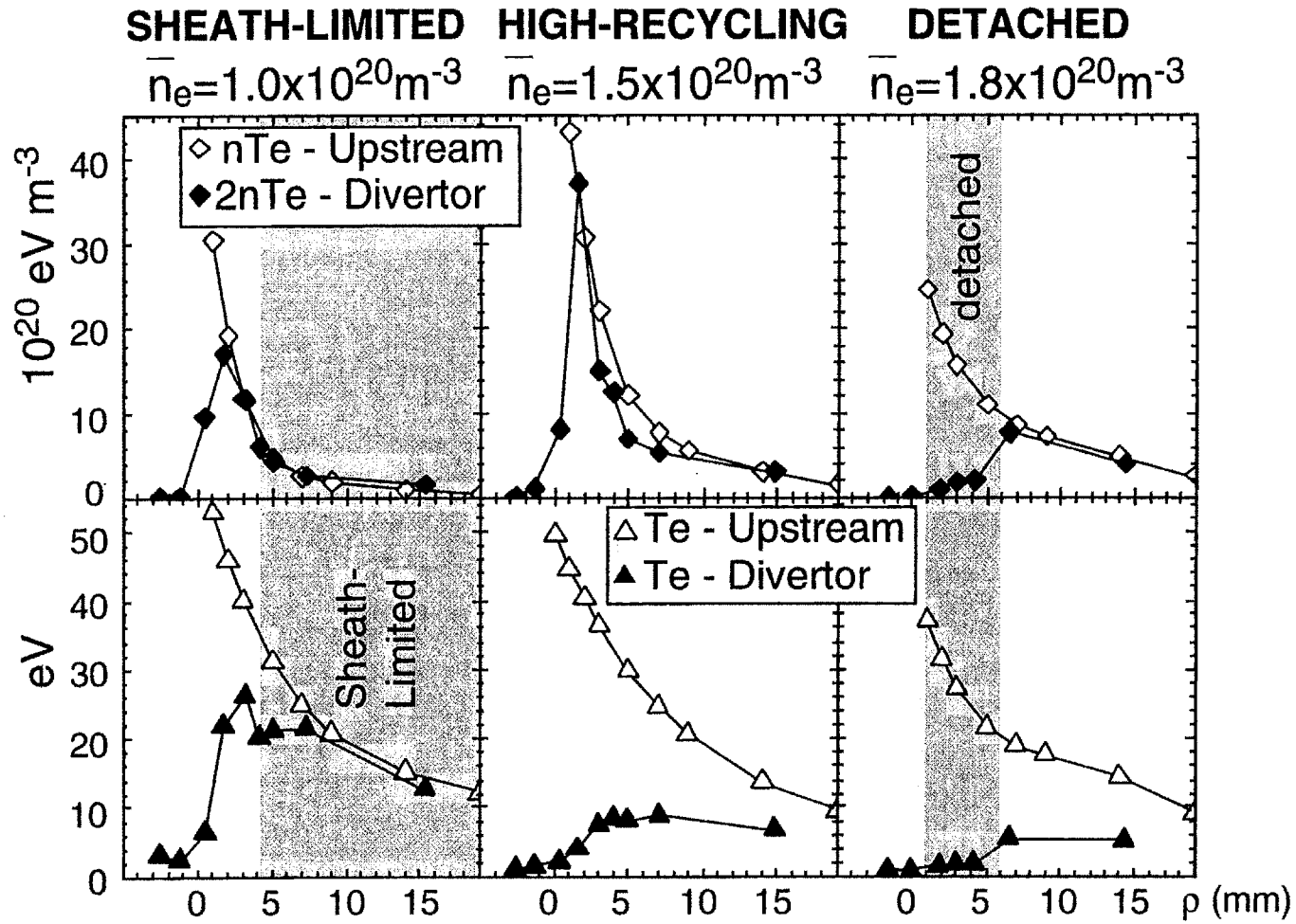

Fig. 4-1: Edge plasma regimes determined from the parallel heat transport. Target and SOL (upstream) plasma parameters are mapped onto the same coordinate system; ρ – midplane flux surface distance from the separatrix. Used with pemission from ref. [72].

The coordinate used on the plots (and universally for the Alcator C-Mod edge plasma description) is ρ - the distance from the plasma separatrix to a given magnetic flux surface measured at the midplane. Both sets of probe measurements are mapped to the same coordinate system (ρ), following the plasma magnetic geometry - rather than true space geometry. Note that in this coordinate system $\rho=0$ corresponds to the separatrix position; $\rho>0$ to the common-flux-zone (CFZ) edge plasma; and $\rho<0$ to the private-flux-zone (PFZ) plasma for divertor measurements or core plasma for upstream measurements above the X-point. The ρ-coordinate system simplifies comparison between plasma measurements performed at different SOL locations. It has to be used with caution, however, when interpreting results with respect to the real-space tokamak geometry (e.g., for neutral dynamics).

The three vertical panel pairs on Fig. 4-1 show plasma pressure and temperature profiles, each corresponding to one of the three edge plasma regimes:

1) At low core plasma densities (by Alcator standards), below $\overline{n}_e \approx 1 \cdot 10^{20}$ m^{-3} for ~800 kA ohmic plasmas, the parallel scrape-off-layer (SOL) transport is limited by the power flux through the plasma sheath in front of the target surface. Hence the name "sheath-limited" regime. There is little or no resistive impedance to the heat flow in the SOL. As a result the same edge plasma temperature is measured both down- and upstream (Fig. 4-1). The plasma pressure is constant along the field lines. The high target plasma temperature associated with the "sheath-limited" regime may lead to excessive sputtering of the target material and thus is unfavorable for tokamak operation.

2) At moderate core plasma densities ($\bar{n}_e \approx 1.5 \cdot 10^{20}$ m^{-3}) the dominant SOL heat transport impedance is electron conduction. In order to sustain the heat flow a large temperature gradient forms along the open field lines, i.e., the temperature in front of the target drops significantly (Fig. 4-1). Because the plasma pressure is conserved (as in case 1) the density in front of the target increases considerably (Fig. 4-2) through particle recycling. Hence the name "high-recycling" regime. While the temperature decrease limits the danger of target sputtering, the heat load onto the target plate can still be very high (unless reduced by radiation); the energy being just redistributed among many particles.

3) Above a certain "threshold" core plasma density ($\bar{n}_e \geq 1.7 \cdot 10^{20}$ m^{-3} for ~800 kA ohmic discharges) the edge plasma "detaches" from the divertor target, i.e. the particle and heat fluxes are significantly reduced from the upstream values. This "detached divertor" regime is described in detail in Section 4.2. Here we only point-out its most important feature - a gradient in the plasma pressure along magnetic field lines. As shown in Fig. 4-1, both plasma pressure and temperature are significantly reduced from their upstream values. This leads to a decrease in particle and heat fluxes impacting the target plate. For this reason divertor detachment is of profound interest to designers of future experiments (e.g., ITER), where target heat-load is a significant problem.

LaBombard has also pointed out that a given SOL-plasma regime may not extend through the entire SOL width but may be limited to a portion, as the shaded regions on Fig. 4-1 indicate.

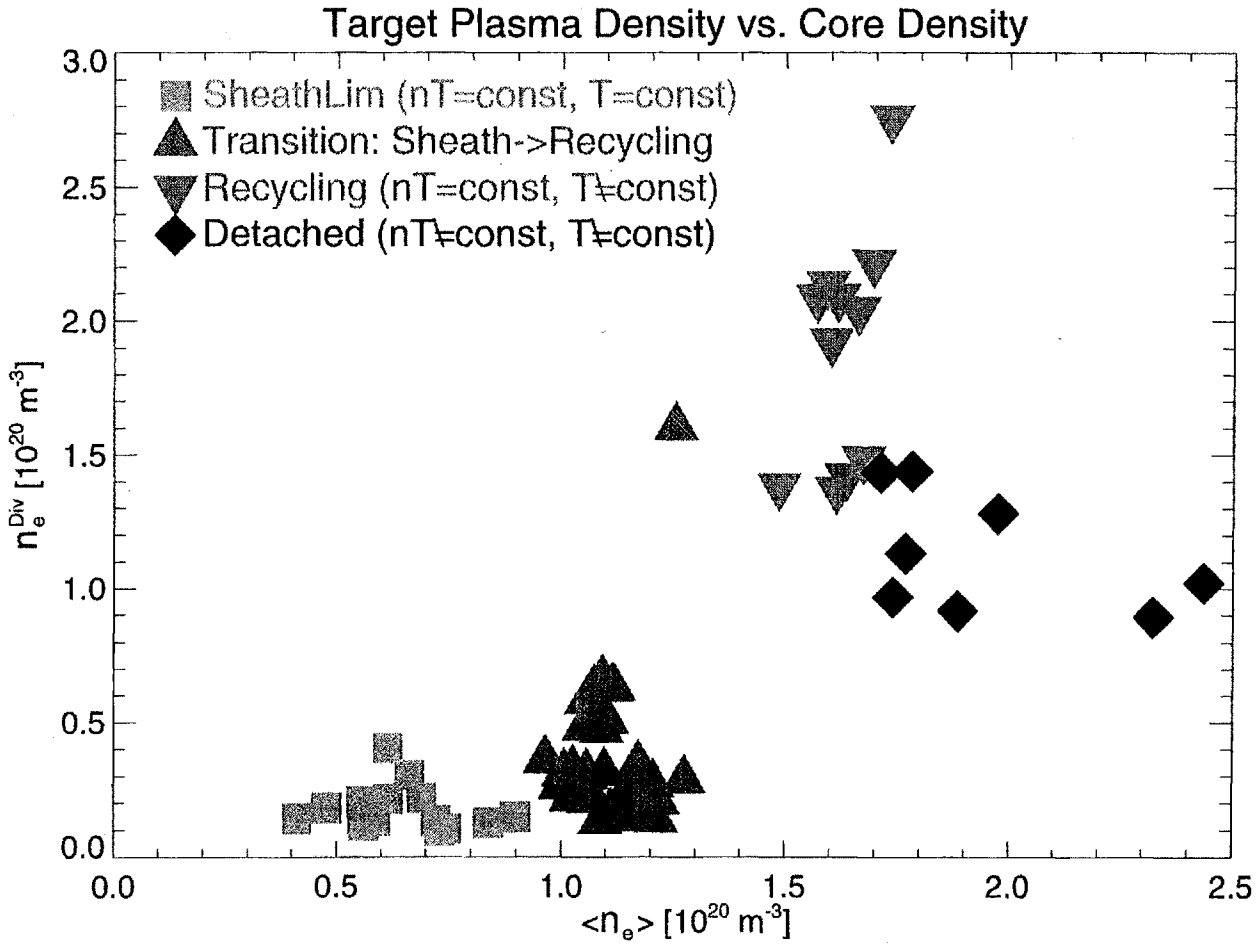

Fig. 4-2: Target plasma density at ρ =4 mm versus volume averaged core plasma density. Symbols distinguish edge plasma regimes illustrated on Fig. 4-1.

4.1.2 Neutral pressure scaling

As a reference for the following neutral pressure analysis it is useful to first examine the target plasma density scaling resulting from the edge plasma regimes described above.

Fig. 4-2 shows a plot, where data from a large number of discharges have been summarized, using the Alcator Edge Database [25]. The plot shows the target plasma density at the flux surface of ρ = 4mm versus line averaged core plasma density. Different symbols are used to distinguish between the edge plasma regimes. In addition to the three regimes described before, an additional "transition" regime between the sheath-limited and the high-recycling ones has also been distinguished, to help categorize neutral pressure data.

In the sheath-limited regime the target plasma density is low and independent of the core density (within experimental error). It rises rapidly through the transition and high-recycling regimes. In the detached divertor regime the target plasma density is considerably lower than its maximum value in the high-recycling case and it does not vary strongly with the core density.

Fig. 4-3 shows a similar database plot of the divertor neutral pressure, measured in the closed module by the MIT gauge, versus the core plasma density. The divertor neutral pressure scales similarly to the divertor plasma density. It is at a low value (~0.5 mTorr) and almost constant in the sheath-limited regime. In the transition and high-recycling regimes it increases rapidly with the core density. The pressure scaling does not follow the density scaling during the divertor detachment, where

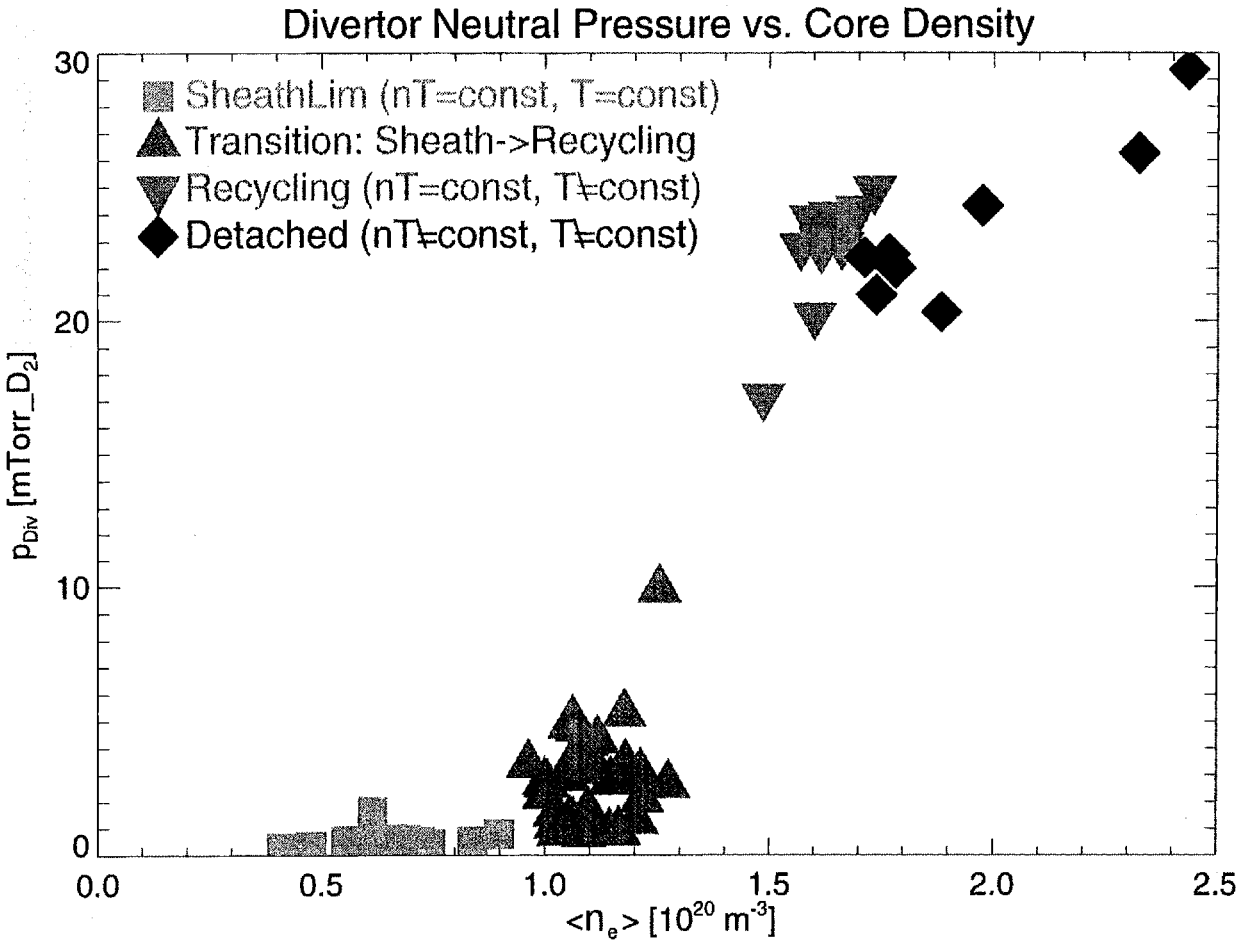

Fig 4-3: Divertor neutral pressure (measured by the MIT gauge) versus volume-averaged core plasma density. The symbols identify the edge plasma regimes.

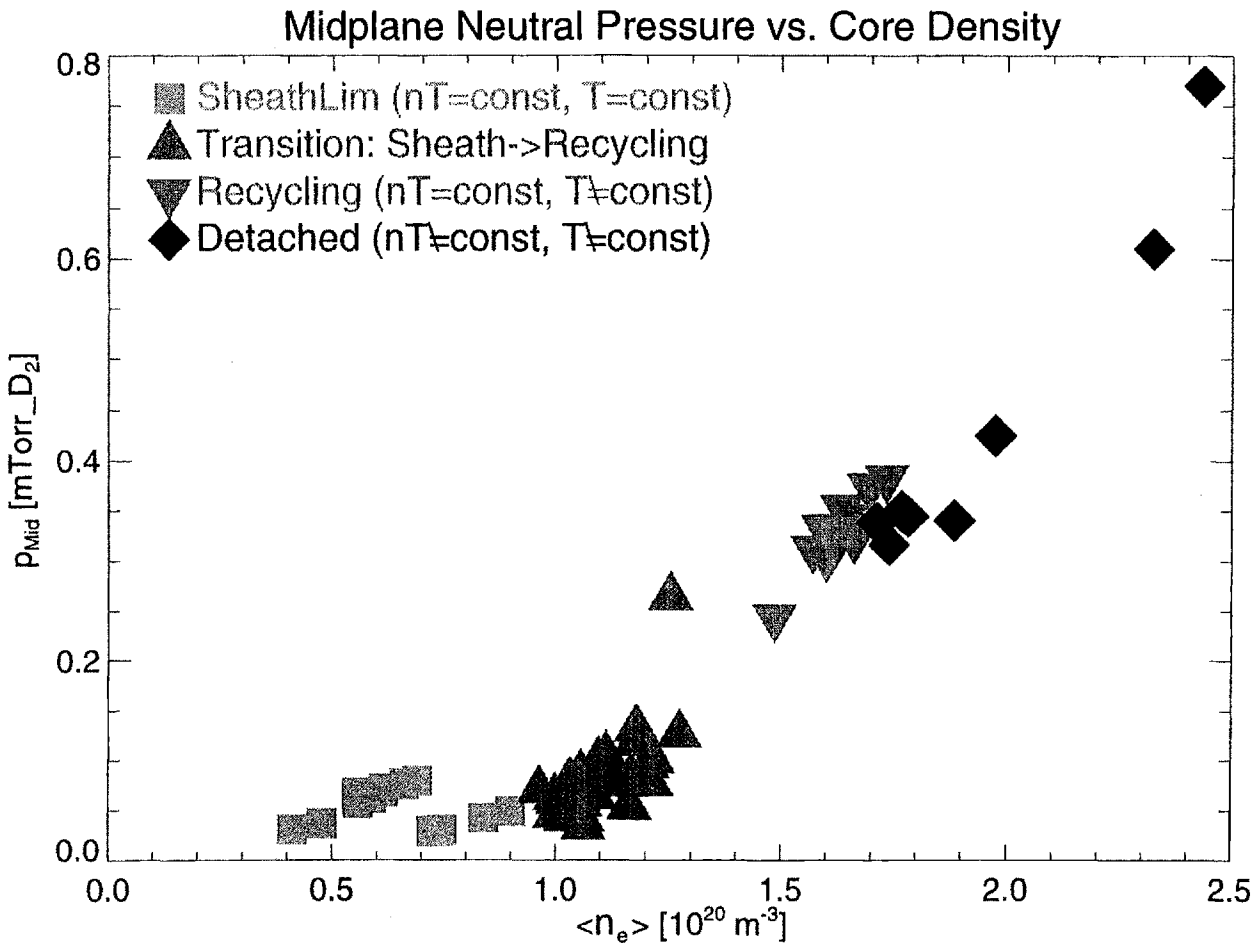

Fig. 4-4: Midplane neutral pressure (measured by the Bayard-Alpert gauge) versus core plasma density. Same symbols are used as on the previous figures.

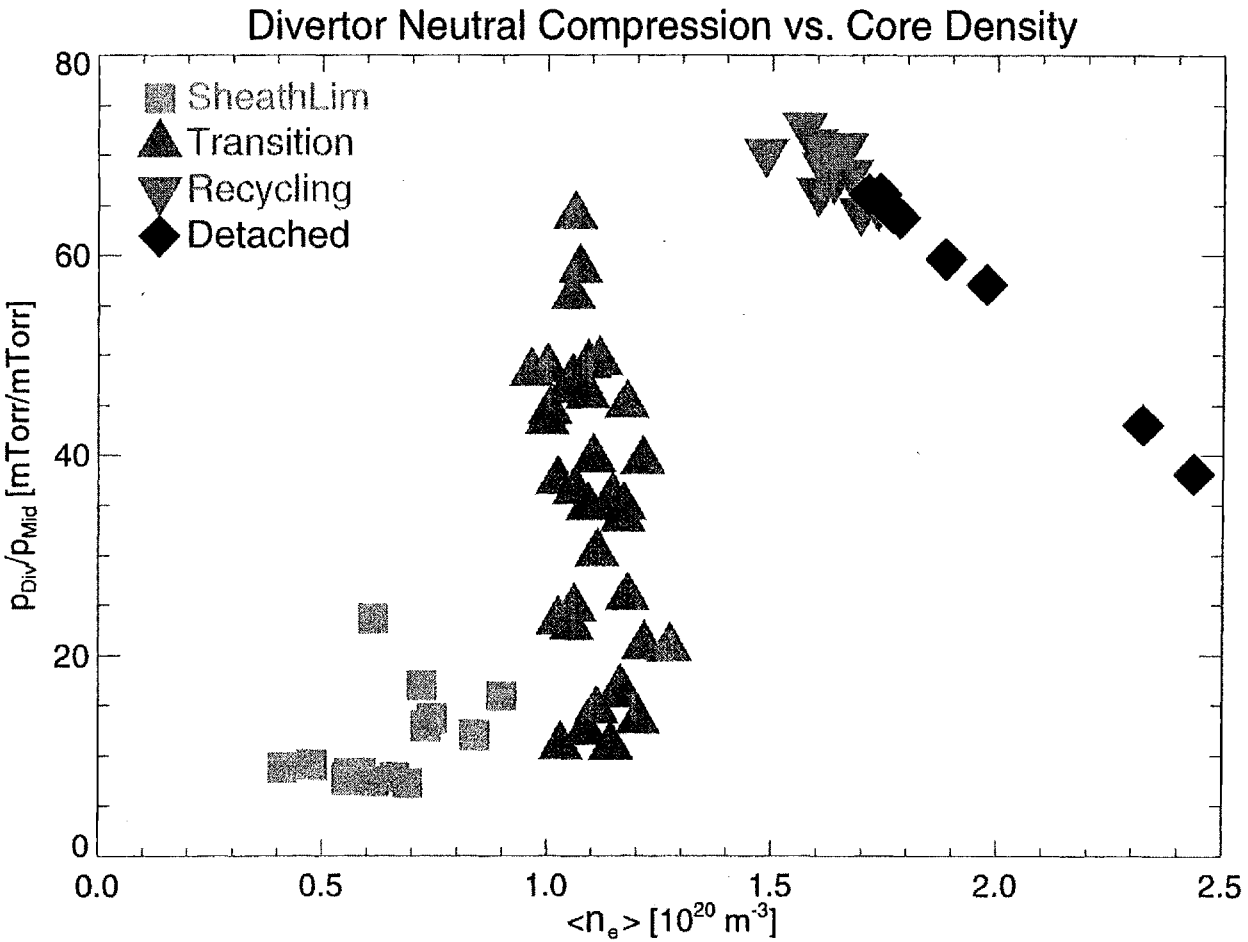

Fig. 4-5: Divertor neutral compression, defined as the ratio of divertor to midplane pressures, is a convenient measure of neutral confinement in the divertor. It is plotted here versus core density with the edge-regime symbols.

neutral pressure is approximately unchanged from the maximum value (25-30 mTorr) in the high-recycling case and continues to rise slowly with the core density.

Fig 4-4 shows a database plot of the midplane neutral pressure, measured by the B-A gauge, versus the core plasma density. In the sheath-limited regime the midplane pressure is relatively low (~0.05 mTorr), than increases rapidly through the other regimes. Note that in the detached regime the midplane pressure increases faster then the divertor pressure.

Divertor compression, defined as a ratio between the two pressures (divertor over midplane), is a convenient measure of neutral confinement in the divertor chamber. Plotting the divertor compression ratio (p_{div}/p_{mid}), again versus the core density, in Fig. 4-5, it is interesting to note that it also follows the divertor regimes, defined by the edge parallel heat transport. The compression is low (~10-20) and steady in the sheath-limited regime, rises rapidly through the transition regime to a maximum steady value of ~70 in the high-recycling regime, and drops subsequently (with increasing core density) throughout the detached divertor state.

4.2 Divertor detachment

Divertor detachment was first observed on DIIID and JET tokamaks [73, 74] and was recently thoroughly reviewed by Matthews [75]. The detached divertor has been proposed as a mode of operation of ITER [7].

The currently accepted explanation of the divertor detachment mechanism is a combination of the upstream SOL power loss through radiation and the

downstream momentum loss through charge-exchange and elastic collisions with neutrals [76]. Observations from other tokamaks often quote a necessary radiative power [77] and a high neutral pressure in the divertor [78].

4.2.1 Divertor detachment in Alcator C-Mod

On Alcator C-Mod the divertor detachment was already observed during the first 1993 operational campaign. The phenomenon is characterized by a considerable drop in the energy and particle fluxes to the divertor target surfaces. The most visible signature of detachment is a dramatic drop of the ion saturation currents measured on the vertical portion (below the "nose") of the divertor target, as shown on Fig. 4-6 (based on ref. [27]). In contrast, the ion saturation currents on the horizontal portion (above the "nose") increase as a result of the transition. Divertor detachment is also accompanied by an increase in the central plasma density, as seen on the top trace of Fig. 4-6. Luke [24], however, has shown that there is no change in underlying particle transport processes in the plasma core. The increase in the central plasma density, observed after detachment, results from a change in the edge particle source and/or screening.

Two types of the divertor detachment have been observed on Alcator C-Mod [79]: (1) a fast detachment with transition time 10-30 ms, and (2) a slow, gradual detachment occurring within 100-400 ms. Fig. 4-7 compares the two types of detachment transition. In the case of fast detachment the plasma pressure drop is sudden (10-30 ms) and occurs across the entire plate, at t ≈0.65 sec. (left panel on Fig. 4-7). During the slow detachment, in contrast, the pressure drop gradually

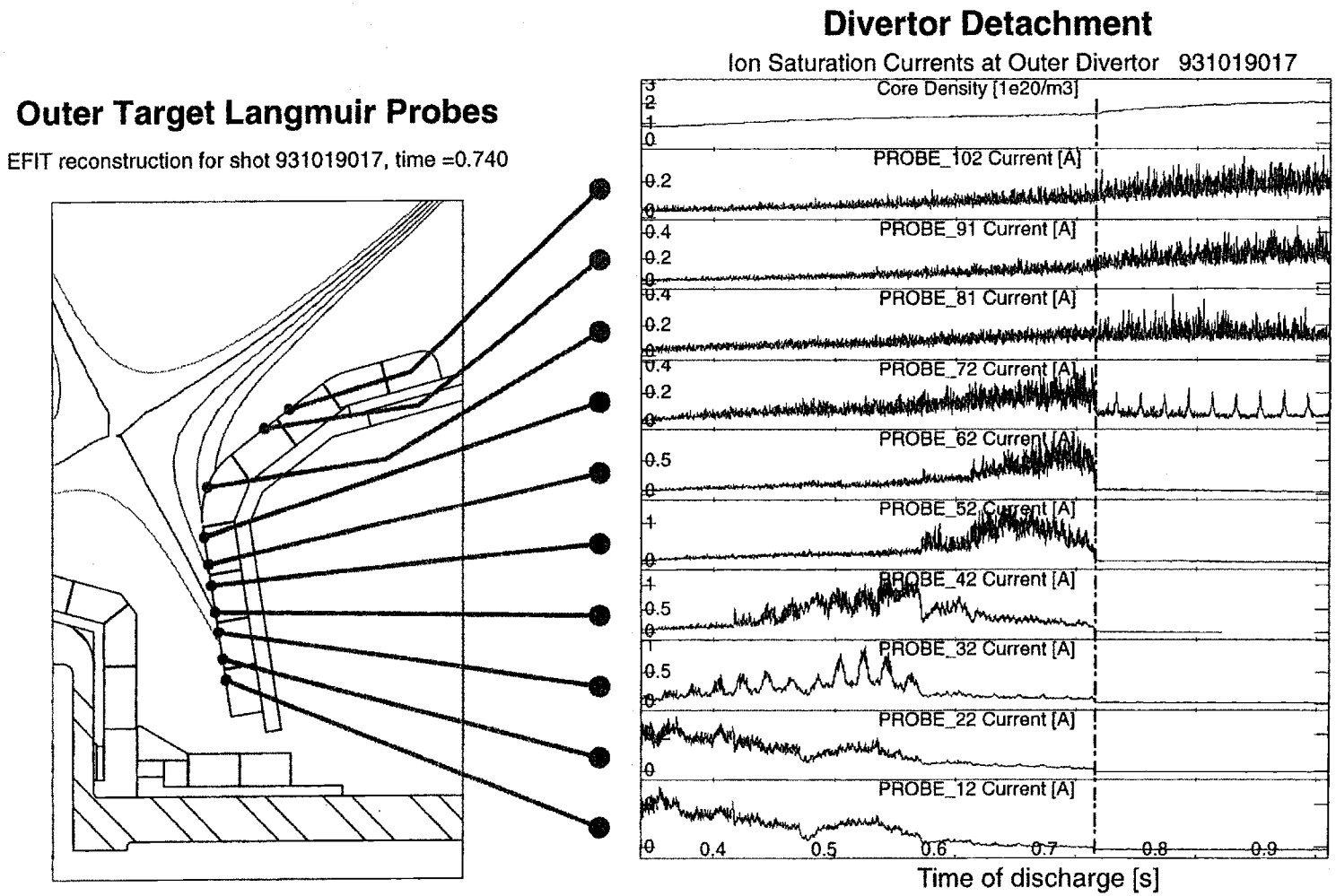

Fig. 4-6: Divertor detachment is characterized in Alcator C-Mod by a significant drop of the ion flux towards the vertical divertor target plate (bellow the nose), as illustrated here by the ion-saturation current traces measured by the divertor Langmuir probes. The core plasma density increases after the detachment. The plot adopted after ref. [27].

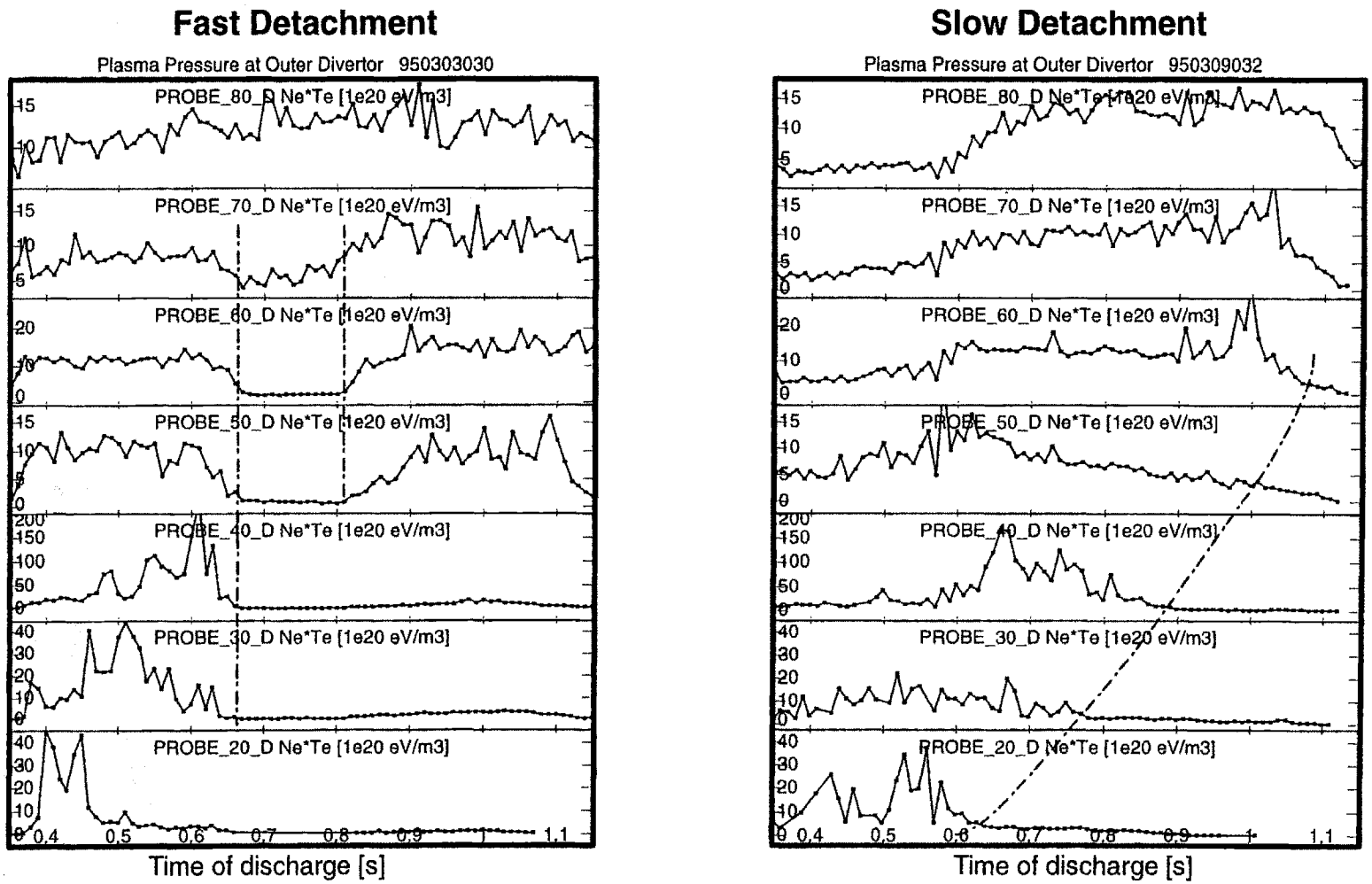

Fig. 4-7: Time history of target plasma pressure illustrating fast (left panel) and slow (right panel) divertor detachment. Fast detachment, triggered by a methane puff occurs ~0.65 sec., plasma partially reattaches after 0.8 sec. Slow detachment is caused by a core density rise and progresses up the divertor plate starting at ~0.6 sec.

progresses up along the divertor plate over ~400 ms (right panel on Fig. 4-7). The slow transition is the naturally occurring one, caused by a central plasma density rise. The fast transition, shown on Fig. 4-7 (left panel), was induced by impurity injection (methane) which triggered a significant increase in radiation near the x-point. Spontaneous fast detachments were observed during 1993 tokamak operation. They might have been triggered by release of intrinsic impurities covering the tiles.

The edge plasma and neutral gas parameters scale in a very similar fashion for the two detachment transition types. Therefore, for scalings reported here, no distinction is made between the fast and slow detachments. An example of a fast (spontaneous) detachment is used, however, to illustrate its prompt effect on neutral dynamics in Section 4.2.4.

4.2.2 Role of neutrals in divertor detachment

Using the simplified theory of Stangeby [76] the plasma pressure drop, observed in the detached state, must be balanced by a momentum loss through ion-neutral charge-exchange and elastic collisions:

$$0 = -\nabla p_{nT} - m_i n_i v_i^{\parallel} n_0^{FC} K_{cx+el} \qquad (4.1)$$

where the symbols used are as follows:

∇p_{nT} - is the parallel plasma pressure gradient within the detachment zone;

m_i - is the ion mass;

n_i - is the ion density;

$v_i^{\parallel}$ - is the ion parallel velocity;

n_0^{FC} - is the neutral atom density, assumed to be dominated by the Franck-Condon atoms (see discussion in Section 5.2);

K_{cx+el} - is the reaction rate for charge-exchange and elastic collisions.

It is assumed in Eq. 4.1 that the entire ion parallel momentum is lost to neutrals through collisions. Upon the assumption that both ions and atoms are at T ≈3 eV, i.e. near the Franck-Condon energy due to molecular dissociation, the reaction rates can be replaced with respective cross-sections. Eq. 4.1 then simplifies to:

$$\frac{\Delta p_{nT}}{L} \approx m_i \Gamma_i^{\parallel} n_0^{FC} (\sigma_{cx} + \sigma_{el}) \mathrm{v}_0^{FC} \tag{4.2}$$

where the symbols used are as follows:

Δp_{nT} - is plasma pressure drop within the detachment zone;

L - is the length of the ion-neutral interaction region, measured along a field line;

$\Gamma_i^{\parallel}$ - is the ion parallel flux;

σ_{cx} is the charge exchange cross-section evaluated at the Franck-Condon energy;

σ_{el} is the ion-atom elastic collision cross-section assuming a hard-sphere collision model;

v_0^{FC} - is the neutral atom velocity at the Franck-Condon energy.

Additional assumptions about the plasma pressure gradient are also needed. The interaction length - L is assumed to be equal to the connection length between the X-point and the target plate; in Alcator C-Mod L >2m. In order to calculate the plasma pressure drop, the upstream value (for which no probe data were available for this data-set) is approximated by the pressure measured at the plate just before

the detachment transition and the downstream value is assumed to drop to zero after detachment.

The assumptions included in Eq. 4.2 are very crude ones, but allow us to make simple estimates of the minimum atomic density to support a detached plasma. Assuming the Frank-Condon atom energy and a neutral molecular flow regime the above density can be translated (using Eqs. 5.6 and 5.3 from Section 5.2) into the room-temperature molecular density and pressure, and compared directly with pressure measurement performed behind the divertor target.

Fig. 4-8 shows the results of such a comparison. The neutral pressure measured in the divertor is plotted versus the pressure necessary to support plasma momentum loss (calculated with Eq. 4.2) at a particular flux surface of ρ=2mm. The data set from Section 4.1 is used for calculations with the symbols indicating the edge plasma regimes. It is clearly seen that, except for sheath-limited regime, there is always more than sufficient neutrals in the divertor to remove plasma momentum. It appears therefore that the neutral pressure does not control the detachment transition

According to LaBombard [72], the key controlling parameter of the detachment transition is the local electron temperature, which has to drop below 5 eV for charge-exchange and elastic collisions to dominate over ionization events. This occurs only when radiation upstream from the momentum-loss region cools the plasma edge sufficiently.

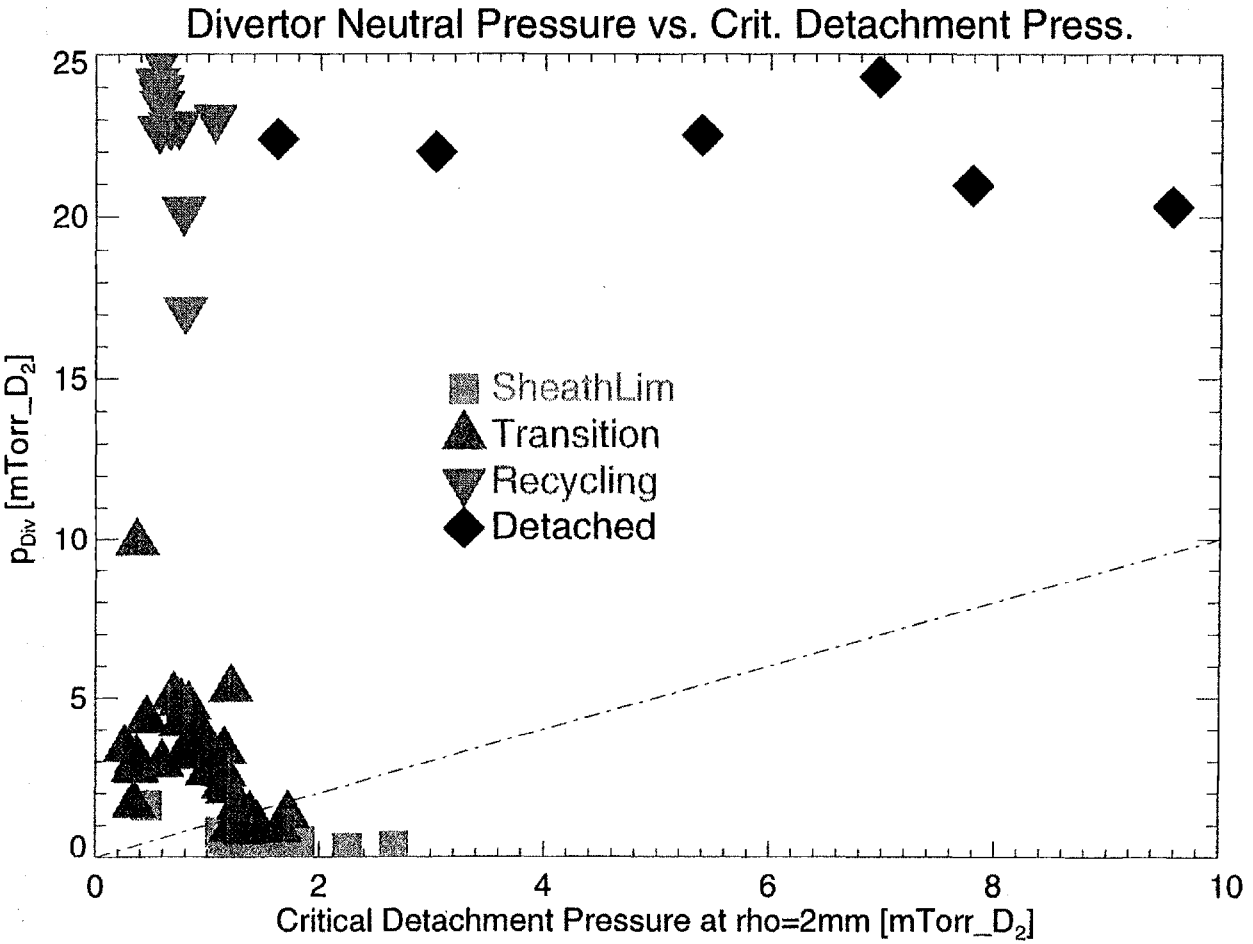

Fig. 4-8: Measured neutral pressure compared to a critical detachment pressure – equivalent to a neutral density required to remove plasma momentum at ρ =2 mm flux surface.

4.2.3 Neutral fluid flow hypothesis

The discrepancy between the measured neutral pressure and that required for detachment (Fig. 4-8) suggests that neutrals are very inefficient in removing plasma-fluid momentum. In Eq. 4.2 we have assumed that a neutral is initially at rest then undergoes a momentum-transfer collision (elastic or charge-exchange) and escapes from the edge plasma without any subsequent interaction, depositing the entire gained momentum directly onto the walls. If the neutral continued to interact with the plasma or other neutrals after the first collision its effectiveness in removing plasma momentum would be significantly reduced. While collision mean-free-paths calculated in Chapter 5 seem to exclude a possibility of frequent neutral-neutral collisions, multiple ion-neutral collisions are highly probable. The ion-neutral momentum-transfer mean-free-path is typically $\lambda_{mt} \approx$ 3-8 mm over a range of divertor plasma conditions (T ≈5-25 eV, n ≈0.5-3·10^{20} m^{-3}), which is smaller then the average distance to the wall L >1 cm. As a result of such collisions the neutral-fluid would acquire a macroscopic flow velocity.

Even though direct experimental evidence is yet to be obtained (e.g. through a Doppler-shift measurement of neutral line emission) a number of observations point indirectly to the possibility of a significant neutral-fluid flow in the Alcator C-Mod divertor region:

1) The surplus of neutrals reported above, as measured by the neutral pressure gauges.

2) Kurz [37] has estimated from H_α measurements neutral density within the plasma channel itself. This neutral density, shown on Fig. 5-3, is much higher than that required for a simple momentum-loss mechanism.

3) Indirect supporting evidence of a neutral fluid flow comes from observation of a "death-ray" phenomenon on the target plate [80]. In many instances, just before divertor detachment, the plasma pressure in a narrow radial layer at the target exceeds its upstream value. A possible explanation suggested by LaBombard [79] is that the neutral fluid transfers plasma momentum between the adjacent magnetic flux surfaces. This transfer mechanism requires the neutral-fluid to acquire a significant flow velocity.

4) Preliminary modeling results of Alcator C-Mod -like plasmas, reported by Knoll [81, 82] indicate a significant neutral flow, which reaches Mach = 0.6 (referenced to ion thermal speed) in the detached state, in contrast to Mach = 0.2 in the attached state.

4.2.4 Effect of divertor detachment on neutrals

The divertor detachment, being a rearrangement of the target plasma, affects the divertor neutral density itself. Fig. 4-9 shows a time history of a representative tokamak discharge. The divertor detachment (fast) occurs at t=0.86 sec. as indicated by the ion saturation current signature (traces #1 and #2). For illustration purposes the selected discharge also shows a divertor re-attachment - a reverse phenomenon occurring at t=0.94 sec.

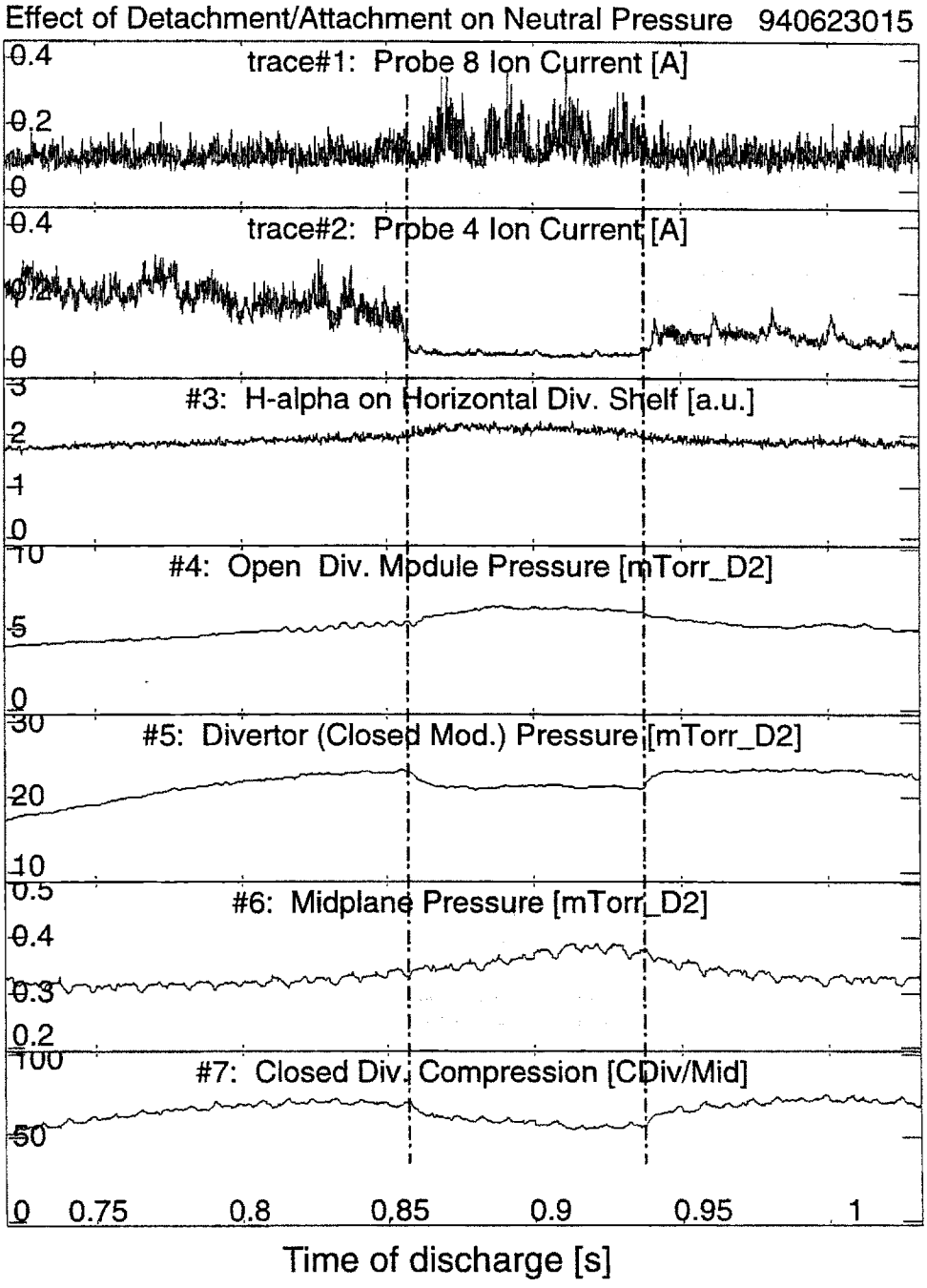

Fig. 4-9: Effect of a fast divertor detachment (at t=0.86 sec.) and attachment (at t=0.94 sec.) on neutral pressures. A detailed description is provided in the main text.

Fig. 4-9 also shows time history of the pressure measurements. Trace #4 depicts the open-module and trace #5 (suppressed zero), the closed module divertor pressure. The closed divertor module pressure drops at detachment typically by about 20% of its pre-detachment value. At the attachment an opposite transition occurs, the pressure returns to its initial value. The changes are relatively fast with a ~10 ms exponential decay/rise time. In contrast the opened divertor module pressure (trace #4) increases as a result of detachment and drops as a result of attachment. The changes are also about 20% of the initial value, the characteristic exponential time is somewhat slower, about 30 ms.

The closed divertor module pressure is measured in a "gas box", connected to the plasma private flux zone (Fig. 2-10). Therefore it is not sensitive to the horizontal target plate recycling but only to the vertical plate one. At detachment the ion current to the vertical plate drops typically by a factor of four. In contrast, the pressure drops only by about 20%. An exactly opposite transition occurs at detachment. This dependence is analyzed quantitatively in Chapter 5.

A quantitative analysis of the open divertor module pressure is extremely difficult because of an intrinsic three-dimensionality of the problem (lack of toroidal symmetry) and is not attempted here. The experimental observations, however, yield to a qualitative interpretation. The source function for the neutral particle reservoir in the divertor "opening" (Fig. 3-5) is the recycling occurring at the leading edge of the opening. In the attached state the dominant source is on the vertical portion of the target plate. The dynamic equilibrium is established where the neutral particles flow from the vertical plate towards the main chamber through the opening in the divertor. The neutral pressure is hence measured in the middle

of this particle flow. After the divertor detachment occurs the ion current striking the plate rearranges such that the dominant source moves onto the horizontal portion of the target plate (Fig. 4-6), i.e., above the pressure measurement. The measurement volume becomes connected to the "other" side of the particle source - a stagnation region of the particle flow, where a higher pressure exists. An additional observation supporting this interpretation is the H_α radiation measured at the horizontal divertor shelf, shown on trace #3 of Fig. 4-9. The time history of the H_α radiation, a particle recycling measure, correlates with the open divertor module pressure observations.

Fig. 4-9 shows also the main chamber pressure (trace #6). There is no sudden change in the main chamber pressure at detachment, but rather a change of slope i.e., a faster rise. This behavior can be explained by increased losses from the closed divertor or increased recycling on the horizontal shelf and is examined more closely in Chapter 7. As a result of the main chamber pressure rise the divertor compression (p_{div}/p_{mid}) continues to drop throughout the detached state; it recovers, however, to its pre-detachment value after the divertor attachment (trace #7 on Fig. 4-9).

4.3 Pressure scaling with input power

The second major scaling parameter is plasma input power. Unfortunately neutral pressure data collected during RF-heating experiments are difficult to interpret due to RF-induced noise, especially on the B-A gauge signal. Thus only results from ohmically heated discharges are reported here.

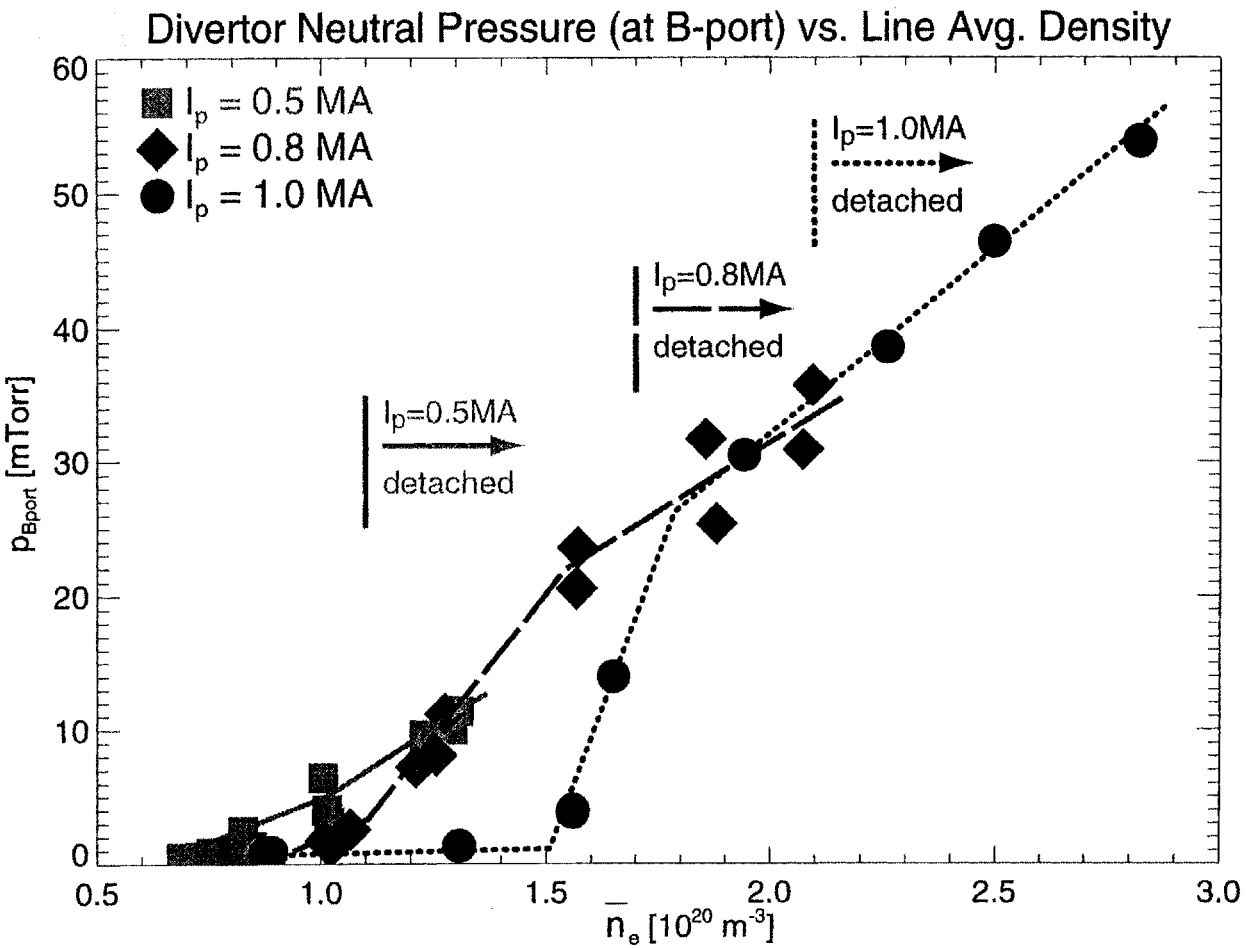

Fig. 4-10: Dependence of the divertor neutral pressure (measured by the B-port capacitance manometer) on the ohmic heating current. Symbols indicate constant-current data sets plotted versus line averaged core plasma density. Lines are intended to guide the eye.

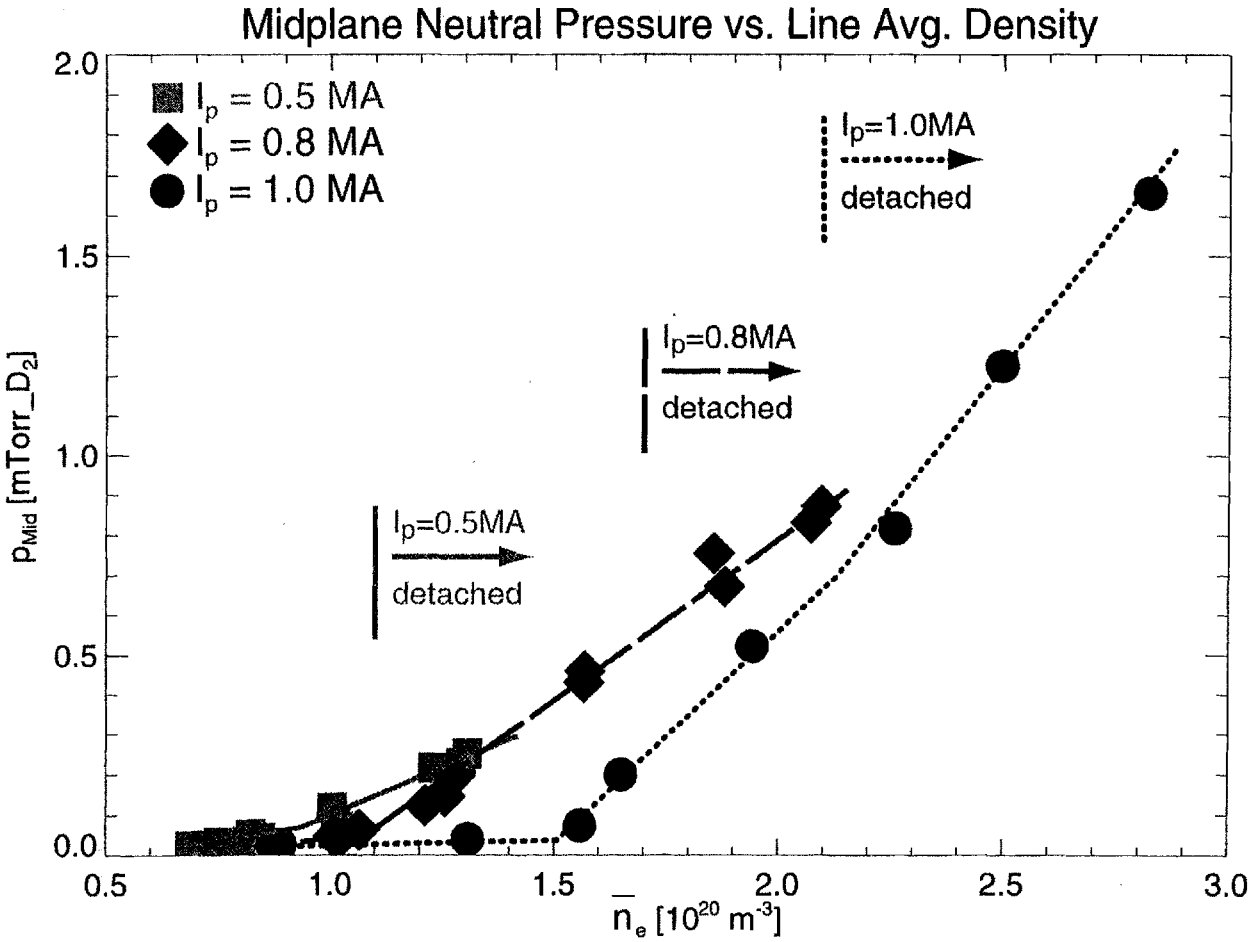

Fig. 4-11: Dependence of the midplane pressure on the ohmic heating current. Constant current data sets are plotted versus core density. Lines are intended to guide the eye.

Fig. 4-10 shows the divertor, and Fig. 4-11 the midplane pressure for three different values of the ohmic heating current I_p =0.5; 0.8, and 1.0 MA. The data points are plotted as a function of the line average core density (for which only one interferometer channel was used due to reconstruction uncertainties). A comparison of Figs. 4-10 & 4-11 with the earlier Figs. 4-3 & 4-4 reveals that the monotonic dependence of pressures on the core density is universal across all the input power levels examined here. At a fixed core density, however, a higher plasma current leads to lower neutral pressures.

Fig. 4-12 shows the divertor-to-midplane neutral compression ratio. The shape of the compression ratio dependence on the plasma density described in Section 4.1 is reproduced for all levels of input power except the curves are shifted with respect to each other. Fig. 4-13 shows the ion flux striking the vertical target plates (measured by the flush Langmuir probes) to help us identify transitions between different edge plasma regimes. The ion flux is low in the sheath-limited regime, rises throughout the high-recycling regime and drops suddenly upon divertor detachment. A comparison of Figs. 4-12 with 4-13 leads us to conclude that the compression ratio depends primarily on the edge plasma regimes determined by the SOL parallel heat transport (Section 4.1) and the dependence on the core density is secondary. For low input power and greater connection length (I_p = 0.5 MA) the respective edge plasma regimes occur at lower core plasma density than for high input power and smaller connection length (e.g., I_p = 1.0 MA) The neutral compression ratio curve shifts accordingly towards lower core density at low input power and towards higher core density at high input power. At any fixed heating current level compression ratio goes through its low

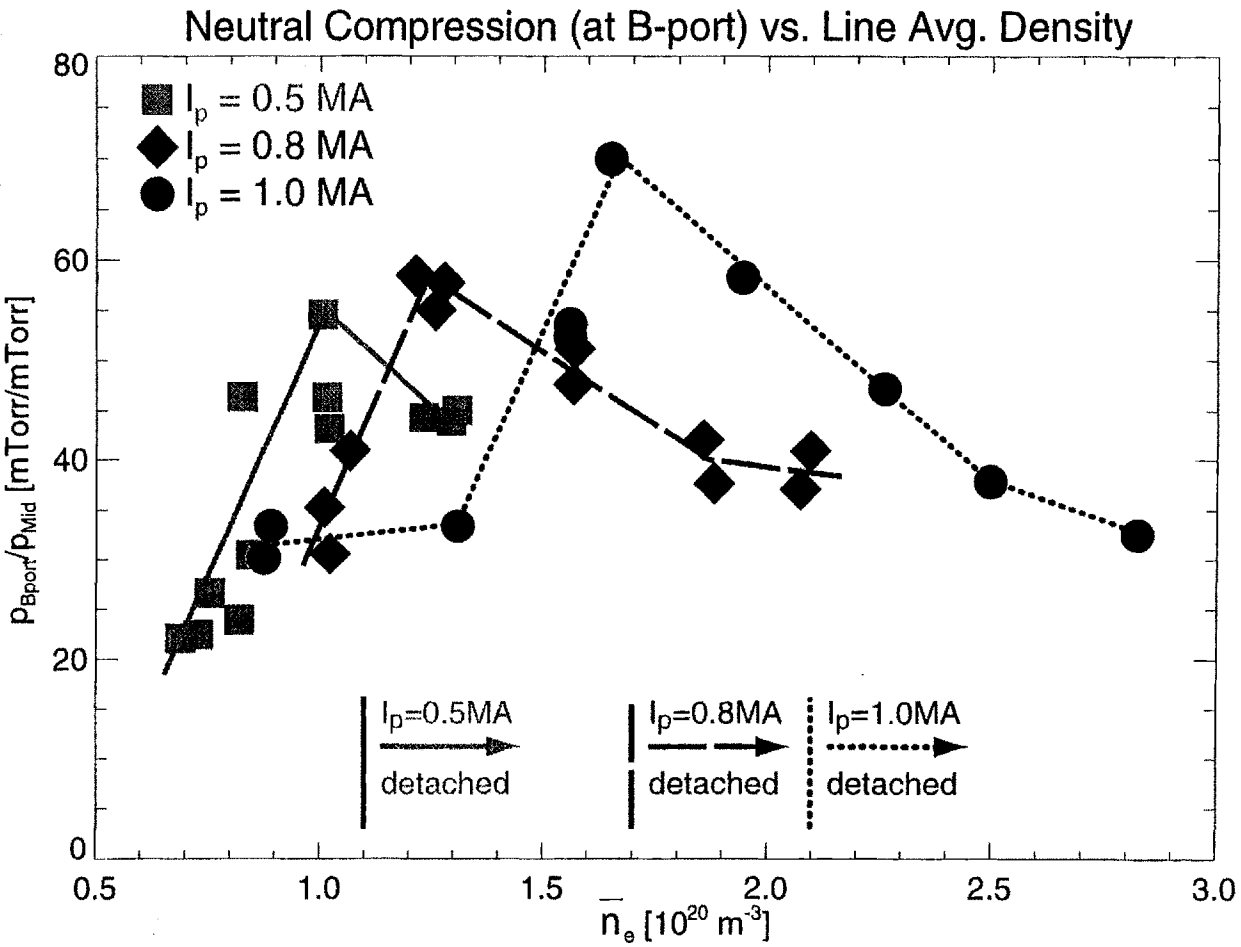

Fig. 4-12: Dependence of the divertor-to-midplane pressure ratio on the ohmic heating current. Lines are intended to guide the eye.

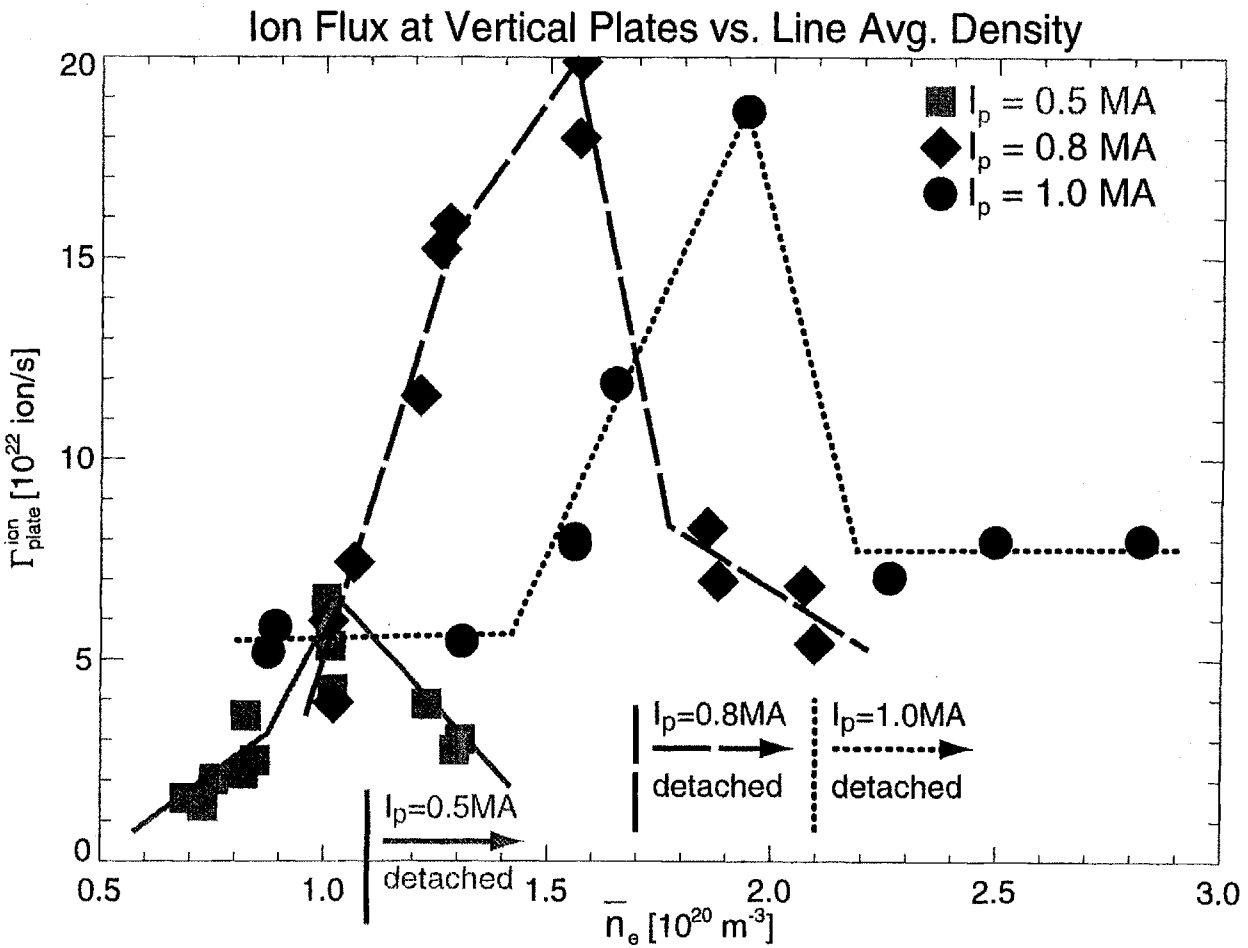

Fig. 4-13: Total ion flux (measured by the flush Langmuir probes) striking vertical target plates at different plasma current levels. Strong drop of the ion flux marks divertor detachment. Lines are intended to guide the eye.

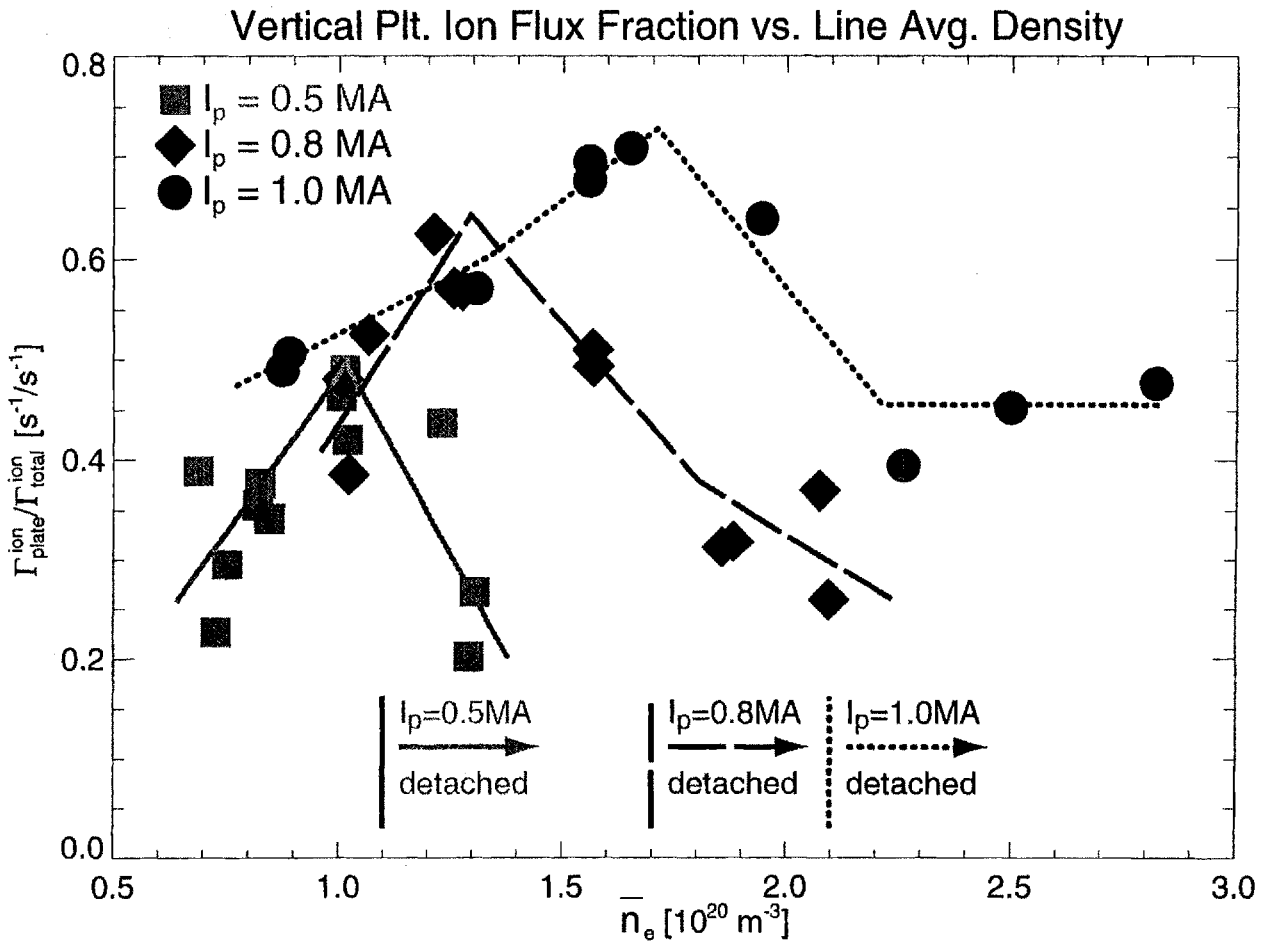

Fig. 4-14: Fraction of the ion flux striking the vertical plates (with respect to the total divertor ion flux) at different current levels. The fraction starts to decrease at core densities ~20% lower than those marked by the maximum of the vertical-plate flux. Lines are intended to guide the eye.

value in the sheath-limited regime (visible for I_p = 1.0 MA data only), increases through the high-recycling divertor regime, and decreases through the detached divertor regime.

Upon closer examination of Fig. 4-12 it appears, however, that the compression ratio starts to decrease at a core density, which is about 20% lower than that corresponding to the divertor detachment threshold (as marked by a sudden drop in ion flux in Fig. 4-13). Fig. 4-14 introduces an important figure of merit which help us to qualitatively explain the above discrepancy. A vertical plate ion flux fraction is defined as a ratio of ion flux striking the vertical target plates (inner and outer) to the total divertor ion flux (all target plates). Because the divertor neutral particle reservoir is fueled by ions recycling on the vertical target plate and the midplane-reservoir is fueled (to some extent) by ions recycling on the horizontal target plate there should exist a relationship between the vertical plate ion flux fraction and the neutral divertor-to-midplane compression ratio. Figs. 4-13 and 4-14 confirm this hypothesis. The maxima of the ion flux fraction correspond exactly to the maxima of the neutral compression ratio and both quantities start to decrease before the actual detachment occurs.

Unfortunately the above relationship is of a qualitative nature only. The following section presents the first attempt to understand mechanisms responsible for the observed neutral pressure scaling.

4.4 Pressure – ion flux correlation

The scaling shown in the previous section suggests some correlation between the ion flux striking target plates and the pressures measured in the vessel. In the

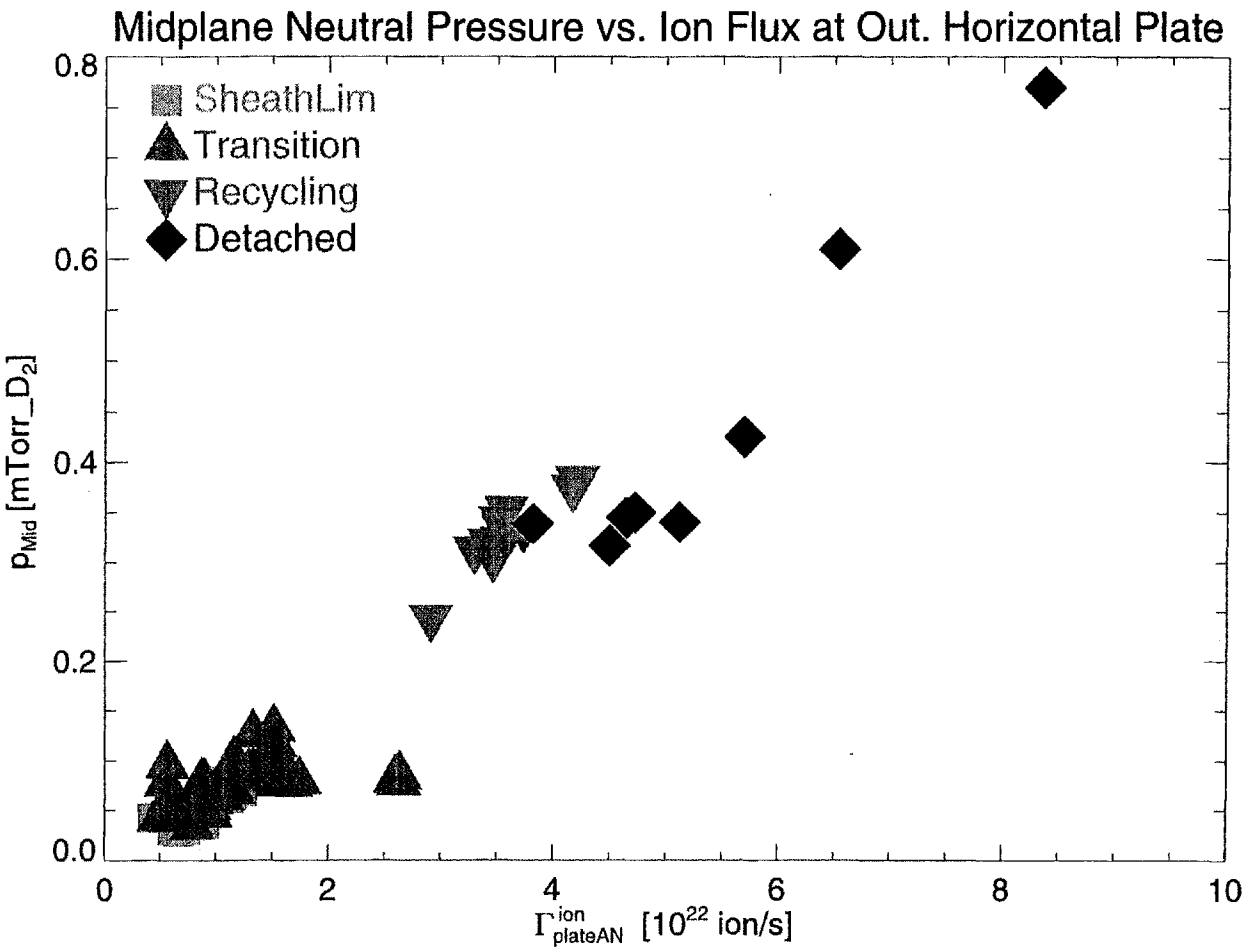

Fig. 4-15: Midplane pressure appears to be proportional to the ion flux striking the outer horizontal divertor target plate.

most simplistic intuitive view one can treat a measuring volume as a lump vacuum component with a constant plasma pumping speed determined by geometry only, and with a particle source determined by ion flux recycling on material surfaces. In such a simple model measured pressure should be directly proportional to the ion flux fueling the volume of interest. It is surprising how well this simple approach describes the midplane pressure measurement. Fig. 4-15 plots the neutral pressure measured by the midplane B-A gauge as a function of the ion flux striking the outer horizontal target plate (above the nose) as measured by the flush Langmuir probes. The dependence between the two quantities is very close to linear. As it is shown in Section 7.1 (where a more detailed flux balance analysis of the midplane volume is carried out), however, the midplane pressure is only partially determined by the recycling source on the outer horizontal divertor target.

Fig. 4-16 illustrates an attempt of a similar simple-minded interpretation of the divertor neutral pressure. The figure plots the divertor neutral pressure as a function of the ion flux striking the inner and outer vertical target plates (below the nose), measured by the flush Langmuir probes. The simple descriptions breaks-down in this case. An order of magnitude higher divertor pressure may be sustained in the detached divertor regime than in the sheath limited regime by the same low ion flux. Close to an order of magnitude drop in the ion flux during the transition from high-recycling to the detached divertor regime, has almost negligible effect on the divertor pressure.

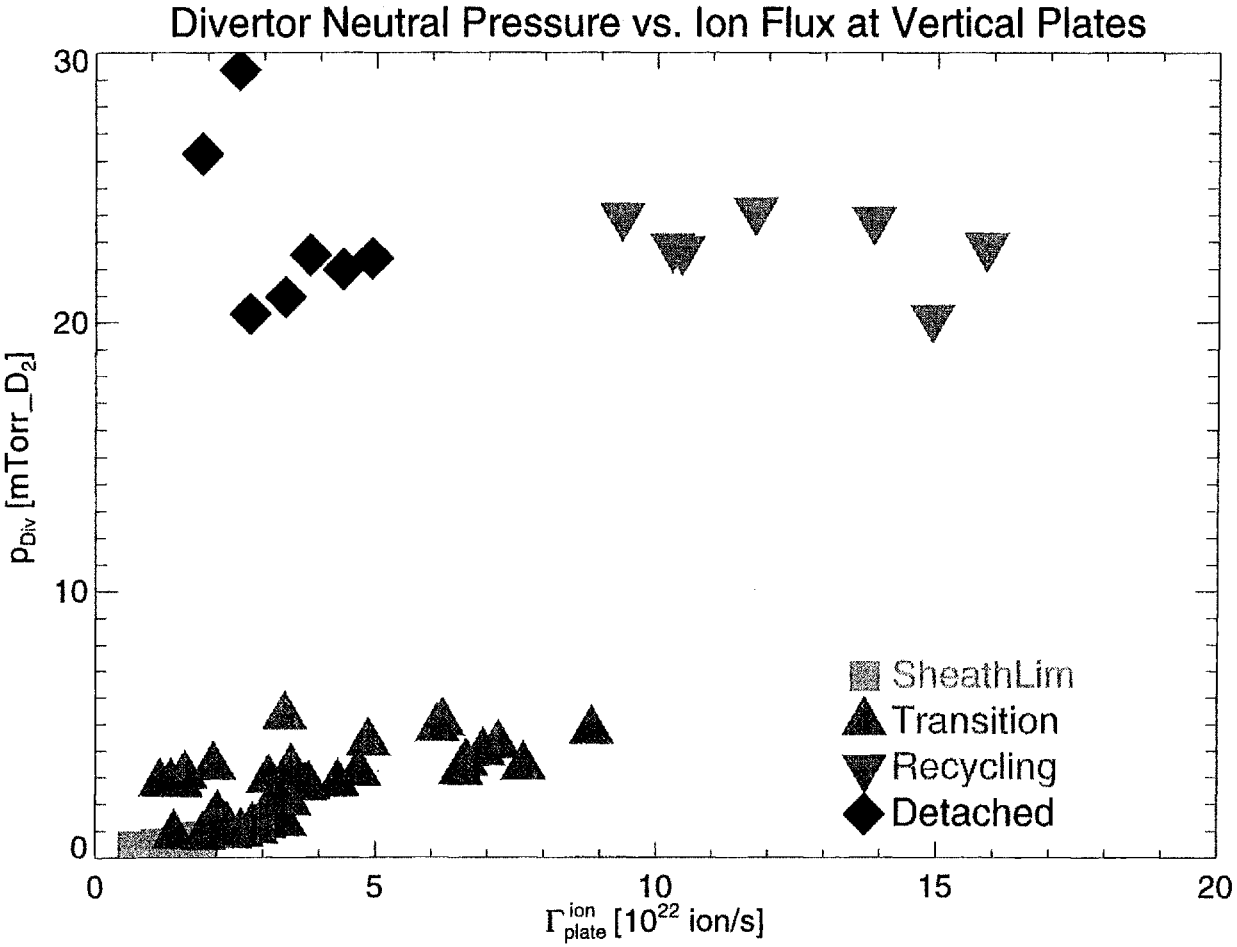

Fig. 4-16: Divertor neutral pressure plotted versus ion flux towards the vertical target plates indicates lack of a simple relationship between the two quantities.

Fig. 4-17 presents an attempt to reconcile the divertor volume fueling flux with the neutral escape flux. The ion flux measured by the flush Langmuir probes is integrated over both vertical target plates:

$$\Gamma^{ion}_{plateBN} = \int_{S^{out}_{divBN}} \left(J^{i}_{\perp sat} / \sigma \right) ds + \int_{S^{in}_{divBN}} \left(J^{i}_{\perp sat} / \sigma \right) ds \qquad (4.3)$$

where:

$\Gamma^{ion}_{plateBN}$ - is the total ion flux striking the vertical target plates;

$J^{i}_{\perp sat}$ - is the ion saturation current density perpendicular to the plate measured by a Langmuir probe "i";

σ - is the electron charge;

and the integration is carried over:

S^{in}_{divBN} - inner vertical target plate (below the nose) and

S^{out}_{divBN} - outer vertical target plate (below the nose).

The kinetic flux of neutrals determined by the pressure measurements (see discussion in Section 5.2) is multiplied by the private-flux-zone separatrix area and reduced by the return flux (1/2) resulting from isotropic dissociation and scattering processes [83]:

$$\Gamma^{atom}_{div} = (1 - \tfrac{1}{2}) \cdot 2 \cdot \tfrac{1}{4} \mathrm{v}_0 \cdot n_{div} \cdot S^{pfz}_{sep} \qquad (4.4)$$

where:

v_0 - is the kinetic speed of a room-temperature deuterium molecule;

n_{div} - is the neutral molecular density inferred from the divertor pressure measurement;

S^{pfz}_{sep} - is the private-flux-zone plasma separatrix area;

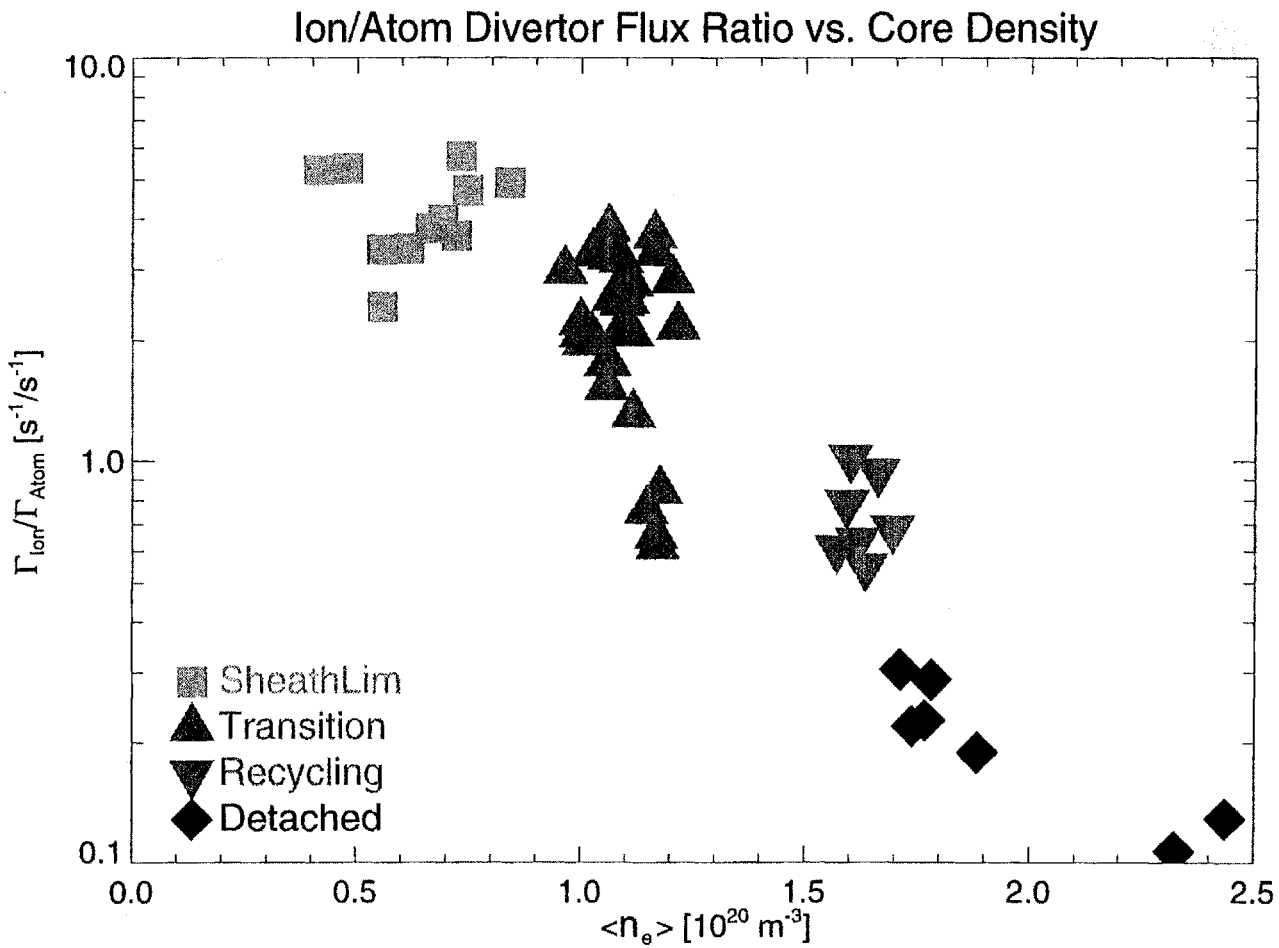

Fig. 4-17: Ratio of the vertical-plate ion flux (Eq. 4.3) to the kinetic atom escape flux (Eq. 4.4) versus core plasma density. A large discrepancy between the ratio at low and high core densities indicates a need to examine the impact of plasma characteristics on the divertor pressure balance.

the factor of one half accounts for isotropic dissociation and scattering processes;

and the factor of two accounts for the dissociation process.

Fig. 4-17 plots the ratio of the two fluxes, i.e., a potential fueling-to-escape flux ratio as a function of the core plasma density. Due to oversimplification of the calculated fluxes the numerical result is highly uncertain. Two important conclusions, however, can be drawn from Fig. 4-17:

1) There is extremely large difference (by almost two orders of magnitude) between the flux ratio at low and at high plasma densities.
2) It seems as if there were many times more particles leaving the divertor volume than can possibly be produced by recycling in the detached divertor state.

The discrepancies described above (of pressures and fluxes) prompted the author to develop a detailed divertor particle flux balance model in Chapter 5. The analysis results are presented in Fig. 5-16 in the same form of the source-to-loss flux ratio as in Fig. 4-17, allowing for a direct comparison with the simple approach attempted here.

4.5 Scaling summary and need for a more detailed modeling

This chapter summarizes experimental observations of neutral pressure (in the divertor and the midplane volumes) scaling with core plasma density and input power. The neutral pressures measured in the Alcator C-Mod vessel depend

primarily on the edge plasma regimes, determined by the SOL parallel heat transport. This can be understood upon recalling that neutral particle reservoirs both in the midplane- and in the divertor volume do not communicate directly with the core- but only with the edge-plasma: SOL- and divertor-plasmas respectively.

A divertor-to-midplane pressure ratio - a "neutral compression ratio" is defined as a convenient measure of divertor ability to confine neutral particles. The compression ratio is maximized in the high-recycling regime. Whereas divertor detachment sustains high neutral pressure in the divertor, it leads to a considerable decrease in the compression ratio.

A simple-minded comparison of ion and neutral fluxes reveals a large discrepancy (a factor of twenty across the density range of interest) between potential divertor source and sink fluxes. A more detailed analysis aimed at explaining neutral pressures across the entire range of edge plasma parameters is required. More specifically a model describing dependence of the fueling and escaping fluxes on the edge plasma characteristics is necessary. Such a model is proposed in the following chapter.

Chapter 5

Divertor Neutral Particle Flux Balance Model

One of the key findings of Chapter 4 was the dependence of the divertor neutral pressure on the edge plasma regimes. As illustrated in Fig. 4-18, however, the incident ion flux does not balance the neutral-kinetic-escape flux.

The goal in this chapter is to develop a simple physics-based model that can explain the divertor neutral pressure measurements and identify the dominant neutral particle physics mechanisms. Upon reassessing the fueling and the escape fluxes, while including mechanisms of neutral transmission and reflection in the divertor plasma, we evaluate the neutral particle flux balance for the divertor volume. As illustrated in Fig. 5-16, the model proposed in this chapter allows us to obtain a factor of two agreement in the particle flux balance across a range of plasma parameters spanning the sheath-limited, high-recycling, and detached divertor regimes.

5.1 Goals and means of the analysis

As concluded in Chapter 4, there is no simple dependence between the observed divertor neutral pressure and the ion flux striking divertor target plates. More specifically, it is difficult to reconcile the high pressure sustained in the divertor

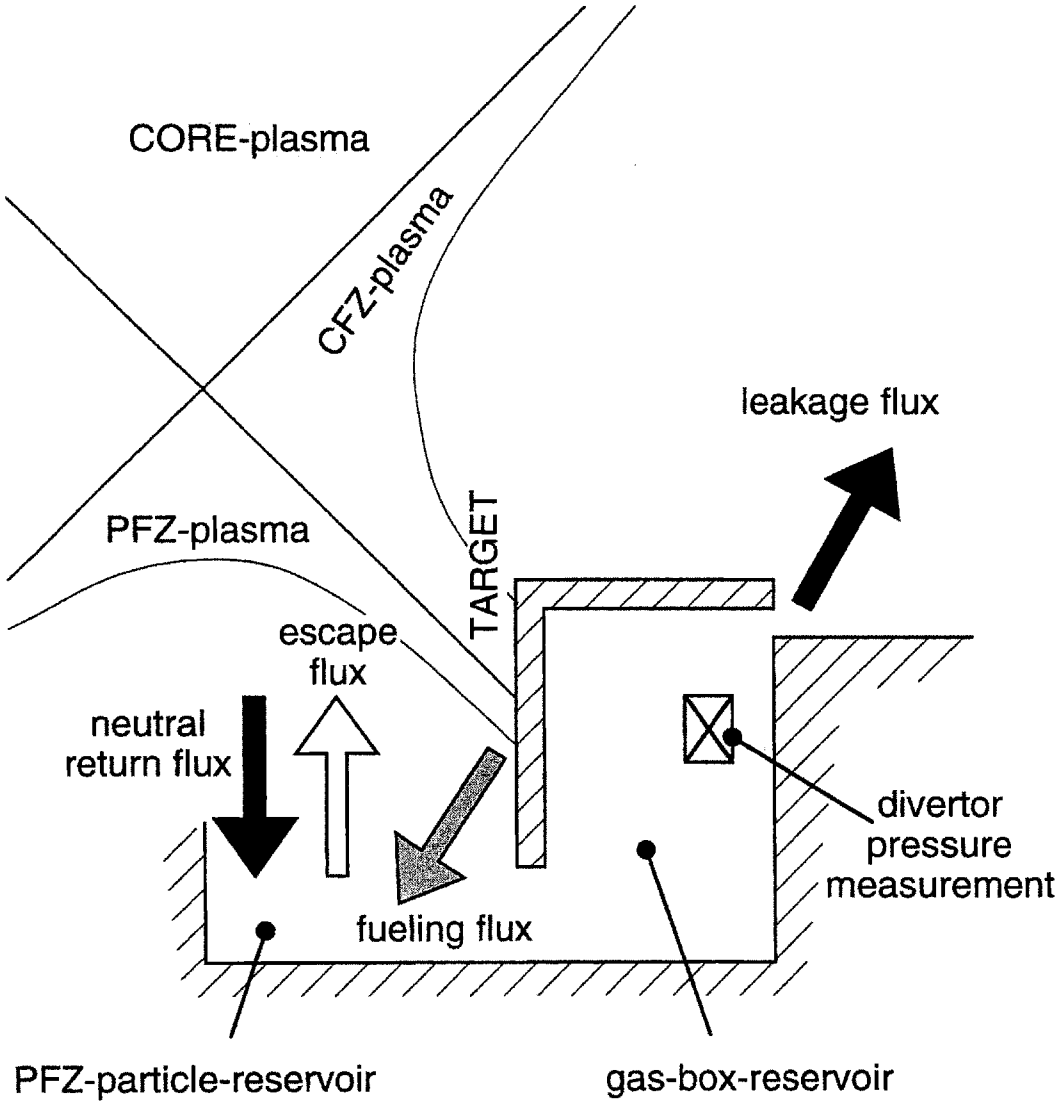

Fig. 5-1: Simplified picture of particle fluxes that determine the divertor neutral pressure.

after detachment with a considerable drop in the ion flux striking vertical target plates. Early experiments in the DITE tokamak [84] reported a similarly high neutral pressure in the DITE bundle divertor (~30 mTorr), that could not be correlated with the ionization source measurement using the H_α emission. The proposed explanation of this observation by momentum transfer from hot to cold neutrals that could inhibit neutral flow towards the plasma leaves some doubt because of a long mean-free-path for neutral-neutral collisions. More recently similar "unexplainable" high neutral pressures have been observed in DIIID [85, 86] and JET [87] tokamaks. Haas proposes [88] an ion-molecule elastic scattering process as a mechanism that could reduce the molecular flux towards hot plasma regions. This mechanism is discussed in more detail in Section 5.5.

A highly simplified model is proposed here for interpretation of the Alcator C-Mod data because of the insight it provides into the relevant mechanisms. The model evaluates the most important particle fluxes, shown in Fig. 5-1, that determine the divertor neutral pressure. The major deficiency of the initial calculation carried out in Section 4.4 was that it considered only the ballistic loss (white arrow on Fig. 5-1) and the ion recycling source (gray arrow) fluxes. The analysis here includes an additional return flux (black arrow) of neutrals scattered from the plasma or reflected from the target plate, as well as an additional loss flux that leaks through openings in the divertor structure (black arrow). Also the neutral fueling flux is corrected to include transmission across the plasma fan.

A more complete picture of the neutral transport in a tokamak requires a two-dimensional treatment, including a full range of atomic physics phenomena. Reiter [89] provides an extensive review of existing neutral transport codes suitable for such a task. A comprehensive modeling study of Alcator C-Mod experiments,

using DEGAS Monte-Carlo neutral transport code [90, 91], is being carried out by Stotler et al. [92]. So far the modeling has had only moderate success in interpreting Alcator C-Mod experimental data. For example, the divertor neutral pressure predicted by the code is ten times lower then the measured one; the $H\alpha$ emission is reproduced with somewhat better accuracy (factor of two) [93]. Similarly DEGAS modeling failed to reproduce neutral pressures measured in the DIIID tokamak [94]. The discrepancy between the code predictions and experimental observations in Alcator C-Mod is the subject of an ongoing investigation [95].

5.2 Model equations and assumptions

5.2.1 Neutral flux balance

Because the neutral particle build-up in the divertor volume is measured only at one spatial location, it is convenient to model it as a lump component and examine the balance between its source and sink terms. If there is no net particle pumping at the target plate (the recycling coefficient R=1; see Appendix A), then the neutral particle contents in the divertor volume should be determined by the balance between incoming and escaping particle fluxes only. In its simplest form, a steady-state divertor neutral flux balance equation can be written as:

$$0 = \frac{dN_{pfz}}{dt} = f_{trans} \cdot \Gamma_{plate} - (1\text{-}A)\, \Gamma_{pfz}^{kin} - \Gamma_{leak} \qquad (5.1)$$

where:

N_{pfz} - is the neutral particle contents in the divertor reservoir;

Γ_{plate} - is the total ion flux striking the vertical target plates (Section 5.7);

f_{trans} - is the average transmission coefficient plate→PFZ-reservoir (Section 5.3);

Γ_{pfz}^{kin} - is the kinetic flux of neutrals crossing the plasma/neutral-reservoir boundary (Section 5.6);

A - is the average plasma albedo to neutrals attempting to escape from the PFZ-reservoir (Section 5.6);

Γ_{leak} - is the flux of neutrals escaping through leaks in the divertor structure (Section 5.4).

A major difficulty of the analysis lies in calculating the components of the neutral flux balance. A separate section is devoted to evaluation of each of the quantities in Eq. 5.1. All the calculations focus on particle fluxes with no attempt to reproduce spatial neutral density profiles. The neutral profiles shown on some of the following figures depict neutrals only with a specific characteristics (e.g., reflected at a given energy) and are used only to calculate the necessary transmission/reflection coefficients.

The source-to-sink flux ratio provides a useful figure of merit, which will be used in Sections 5.6 and 5.7 to evaluate the accuracy of the balance calculation:

$$\frac{\text{Source}}{\text{Sink}} = \frac{f_{trans} \cdot \Gamma_{plate}}{(1\text{-A})\,\Gamma_{pfz}^{kin} + \Gamma_{leak}} \tag{5.2}$$

where a result close to unity would indicate a success of the model.

5.2.2 Modeled discharges

Five discharges selected from the run 950202, summarized in Table 5-1, cover the range of core plasma densities of interest yet do not differ (to within allowable

Key Plasma Parameters of the 950202 discharges selected for modeling.

parameter	symbol	units	hot/attached divertor ...				... cold/detached divertor
Discharge Number:			6	7	10	11	13
Core Plasma Parameters							
plasma current	Ip	[MA]	0.82	0.82	0.82	0.81	0.81
ohmic heating power	Poh	[MW]	0.94	1.10	1.20	1.26	1.30
core electron density	Ne_bar	[1e20/m3]	1.01	1.26	1.57	1.86	2.09
Divertor Plasma Parameters:							
divertor elec. temperature (~sep.)	Te_div	[eV]	22.7	14.7	3.5	1.8	1.5
divertor elec. density (~separatrix)	Ne_div	[1e20/m3]	1.46	6.65	2.20	0.89	0.53
domed probe total div. ion flux	Gion_domed	[1e22 D+/s]	1.53	2.84	5.08	3.07	2.81
flush probe total div. ion flux	Gion_flush	[1e22 D+/s]	12.4	26.6	40.3	26.5	20.8
horizontal shelf fraction (above nose)	f_ANose	[1]	0.52	0.43	0.51	0.69	0.74
Neutral Pressures:							
midplane pressure	p_Mid	[mTorr]	0.048	0.147	0.460	0.755	0.874
divertor pressure (capacitance)	p_Bport	[mTorr]	1.7	8.1	23.6	31.7	35.7
divertor pressure (MIT-gauge)	p_Div	[mTorr]	1.8	8.4	25.9	32.7	38.2
divertor compression	p_Div / p_Mid	[1]	38	57	56	43	44
open/closed div. module ratio	p_Open/p_Div	[1]	0.36	0.25	0.32	0.45	0.42

Table 5-1: Key plasma parameters of the discharges selected for modeling from the 950202 run. The top panel lists the core plasma parameters: plasma current, ohmic heating power, and line averaged core electron density. The second panel lists the divertor plasma parameters: electron temperature and density near the separatrix, measured by the domed divertor Langmuir-probes; perpendicular ion flux integrated over the entire divertor surface area (inner and outer), measured by the domed and flush divertor probes; and a fraction (similar for both probe systems) of the ion flux striking the horizontal shelves (above the nose) to the total divertor ion flux. The last panel lists the neutral pressures measured: by the midplane B-A gauge, by the B-port divertor capacitance manometer, and by the divertor MIT-gauge. The panel also includes divertor-to-midplane compression ratio and a ratio between the divertor open-port (E) and the closed-port (J) pressures.

limits) in other aspects. In addition, the discharges are almost consecutive assuring repeatability of such uncontrolled parameters as wall conditioning or intrinsic impurity levels. In these 800 kA ohmic discharges the only undesired variation was a change in heating power due to increasing plasma resistivity with collisionality. The line averaged core density listed in Table 5-1 (and throughout Chapters 6 and 7) is derived from a single interferometer channel (channel no. 5) because of uncertainties involved in the reconstruction of volume averaged density [96].

Table 5-1 lists key divertor plasma parameters and measured neutral pressures. The selected set of discharges represents a transition from a hot divertor plasma (shot #6 being in a transition regime between sheath-limited and high-recycling) through a high recycling cold-plasma (shot #7), partially detached (shot #10) to fully detached divertor plasma (shots #11 and #13). The magnetic divertor geometry, constant throughout all the discharges, was such that the outer strike point was located on or near probe #2 and the inner strike-point just below the inner divertor nose.

5.2.3 Background plasma model

Neutral transport analysis requires a detailed knowledge of plasma parameters in the divertor space (away from the target plates) where currently no direct measurement is available. Because the results depend critically on the background plasma conditions, we carry the neutral transport calculations for two alternative plasma descriptions in parallel and compare their effect *a posteriori* in Section 5.6.

(1) The "electron-conduction" model, as it is referred to throughout the thesis, assumes that the only parallel heat transport mechanism is the electron-conduction. This SOL-plasma description, proposed initially by Keilhacker, Lackner, and Behringer [97], is widely used for simple 1D or two-point calculations [98]. Here we adopt a specific realization of the 1D description, suggested by Kesner [99], in which SOL-radiation is modeled by a delta-function. Appendix C gives details of this realization.

The "electron-conduction" model predicts the radiation zone, defined there as a T =10 eV isotherm, to be located in the vicinity of the target plate, in both attached and detached plasma states, which is inconsistent with experimental observations. Bolometric measurements show that the radiation peak moves from near the target to the vicinity of X-point upon the detachment transition [100]. Therefore it is possible that the electron-conduction model overestimates the parallel electron temperature gradient by neglecting other heat transport mechanisms (e.g., convection) or by simplifying the radiation profile. In a subsequent analysis the electron-conduction model is used to provide an upper estimate of the temperature gradient. Rather than attempting to reproduce plasma conditions exactly (a formidable task by itself), we bracket the solution by placing a lower bound on the parallel electron temperature gradient in the second, alternative description.

(2) The "constant-Te" model, as it is referred to throughout the thesis, assumes a constant plasma temperature and pressure along the field lines between the target plate and any point in space below the divertor throat. The radial plasma profile measured by the divertor Langmuir probes is simply mapped (using ρ-coordinate system) onto a modeling chord of interest (#1 - #7). The constant-temperature assumption is not extended beyond the divertor

throat because there are no experimental observations to justify the spatial position of the detachment front above the divertor throat [101]. Plasma parameters along the modeling chords #9-11 are always described by the electron-conduction model. To simplify the notation this combined description is referred to as a "constant-Te" model in the reminder of the thesis.

5.2.4 Neutral populations and geometry of the problem

Fig. 5-2 shows the geometry of the divertor neutral transport problem. A number of simplifying assumptions are necessary in order to make the problem tractable. We divide the divertor volume into three main regions and associated neutral particle populations:

(1) The "gas-box particle reservoir" encompasses neutral particles residing in the volume behind the divertor target plate, where the pressure measurement is performed. Because neutrals have to collide many times with the walls or with each other before reaching the gauge, they are in molecular state with the energy close to the room temperature (T_{box} =0.03 eV). Even if the temperature of the gas-box neutrals exceeds 0.03 eV, the gauge there is calibrated against the B-bottom manometer measuring room temperature molecules. Thus the MIT divertor gauge (or B-bottom capacitance gauge) pressure measurement (p_{div}) can be directly translated into gas-box particle density (n_{box}) using the Loschmidt number divided by the atmospheric pressure (L_0/p_0):

$$n_{box} = (L_0/p_0)\, p_{div} \tag{5.3}$$

Geometry of the divertor neutral particle flux balance problem.

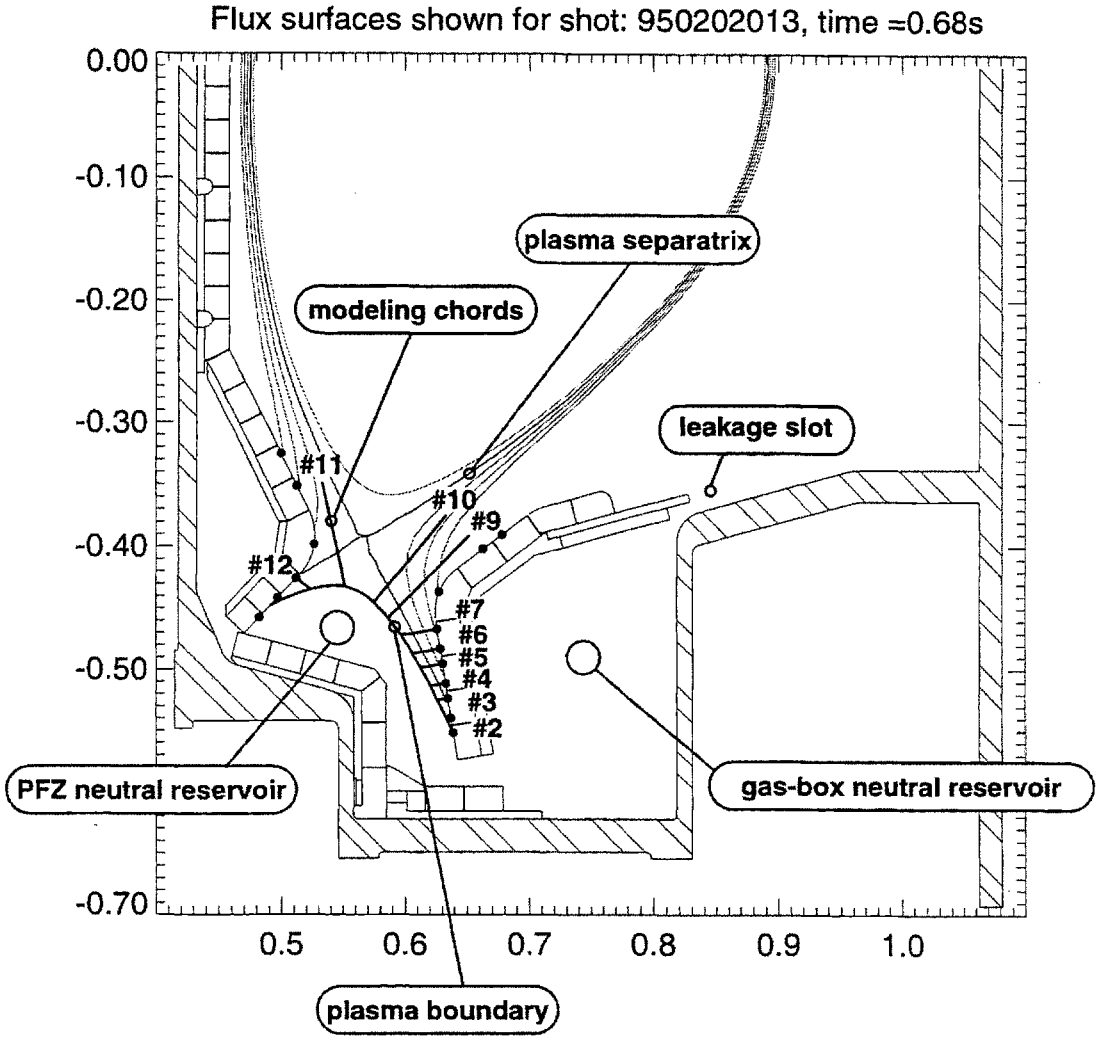

Fig. 5-2: Geometry of the divertor neutral particle flux balance problem. Numbers mark 1D spatial chords used for neutral transport calculations across the plasma-fan. The black circles indicate position of the Langmuir probes. The boundary between the PFZ-particle-reservoir and the plasma-fan is marked by the ρ = -2mm flux surface.

(2) The "private-flux-zone particle reservoir (PFZ-reservoir)" encompasses neutral particles residing in the divertor volume (in-between the vertical target plates) below an imaginary plasma boundary. For the purpose of the following analysis we arbitrarily set the plasma boundary at a private-flux-zone flux coordinate $\rho = -2$ mm. It is assumed that no plasma exists in the private-flux-zone at $\rho < -2$ mm and that the neutrals can only interact with the plasma across the boundary. In the discharges analyzed here this boundary intersects outer probe #1 and inner probe #2.

(3) The divertor plasma fan encompasses all $\rho > -2$ mm. Either a direct measurement (Langmuir probe) or a heat-conduction model determines plasma conditions within the fan. Upon crossing the plasma boundary neutrals interact with plasma ions and electrons.

Fig. 5 -2 shows modeling chords (#1 - #12) used to investigate neutral particle transport across the background plasma. Each of the chords serves as a path for a separate 1D neutral transport calculation. The calculation assumes local symmetry of plasma and neutral gas parameters in the two perpendicular dimensions. Some of the modeling chords connect with the probe locations (below the divertor nose) and are perpendicular to the vertical (lower) part of the divertor target plates. These are used for neutral penetration calculation between the PFZ-reservoir and the target plate. Other chords fan away from the PFZ-reservoir in the direction of the main chamber. These are used for calculations of neutral particle escape probability through the divertor throat.

Final results are obtained by integrating the results from individual chords either over the target plate area (vertical portions only) or over the PFZ-reservoir

bounding surface, depending on the origin of the neutral particles of interest. Trial calculations have shown that variations in exact position of the modeling chords did not influence the final result significantly.

5.2.5 PFZ-reservoir vs. gas-box neutral populations

One of the most difficult problems is how to relate the characteristics of the neutral population in the PFZ-reservoir with the neutral population inside the gas-box behind the outer divertor.

The assumption of gas pressure (density) uniformity inside the gas-box is well justified because of its relatively closed geometry. In contrast, the neutral population in the PFZ-reservoir has almost certainly a non-uniform density and temperature. For the purpose of the flux balance calculation only a knowledge of neutral gas condition along the plasma boundary is required. In order to make the problem tractable we assume a uniform temperature and density of neutrals in contact with the plasma fan (along the boundary).

Because of the low electron temperature, the neutral gas in the immediate vicinity of the plasma is dominated by Franck-Condon atoms (resulting from a molecular dissociation) and thus it is reasonable to approximate the neutral temperature by $E_{FC} = 3$ eV. Preliminary experimental observations of the Doppler broadening of neutral line radiation from the vicinity of the divertor inner nose confirm that the mean energy of neutrals there is near 3 eV [102].

Under steady-state conditions (Eq. 5.1) the density of this gas, assumed to consist of atoms only, is determined by its flow regime and a pressure measured in the

gas-box. A gas can be either in a viscous or a molecular flow regime depending on the Knudsen number (Kn):

$$\mathrm{Kn} = \lambda_{nn} / \mathrm{L} \tag{5.4}$$

where:

λ_{nn} - is the mean-free-path for the momentum-transfer neutral-neutral collisions;

L - is a characteristic size of a gas-duct, here:

L = 20 cm is the width of the gas-box,

L = 5 cm is the width of the channel leading from the PFZ to the bottom of the divertor (leading to the gas-box).

For Kn>1 gas particles collide mostly with the chamber walls, i.e., they are in a molecular flow regime [103]. In the molecular flow regime particle flux across any imaginary surface is conserved. This leads to a simple conservation of flux relationship between the two populations of particles under consideration.

$$n_{pfz} \cdot v_{pfz} = 2\, n_{box} \cdot v_{box} \tag{5.5}$$

where:

n_{box} - is the neutral gas density (molecules) inside the gas-box;

v_{box} - is the kinetic speed of a room-temperature deuterium molecule;

n_{pfz} - is the neutral gas density (atoms) in the PFZ-reservoir along the plasma-fan boundary;

v_{pfz} - is the kinetic speed of a 3 eV deuterium atom;

and the factor of two accounts for the dissociation process.

Eq. 5.5 leads to an expression for the atom density in the vicinity of the plasma-fan, involving the appropriate mass and temperature ratio:

$$n_{pfz} = n_{box} \cdot 2 \sqrt{\frac{m_{D_0} T_{box}}{m_{D_2} T_{pfz}}} \tag{5.6}$$

For Kn<0.01 neutral particles collide mostly with each other, i.e., are in a viscous flow (or fluid) regime [103]. In the viscous flow regime particles are free to exchange momentum, thus in equilibrium the pressure must be constant across a fluid. The expression for atom density simplifies in this case to:

$$n_{pfz} = n_{box} \frac{T_{box}}{T_{pfz}} \tag{5.7}$$

In order to select the appropriate neutral flow regime we carry out the calculations using both Eqs. 5.6 and 5.7 in parallel and examine the resulting Knudsen number *a posteriori.*

Table 5-2 summarizes neutral-neutral collision mean-free-paths and Knudsen numbers calculated for the two populations of neutrals. The most recent neutral collision cross-section data, reported by Schultz et al. [104], have been used in compiling Table 5-2. The left panel of the table shows the molecular density, mean free-path , and Knudsen number (with respect to the gas box width: L =20 cm) for molecules inside the gas box at room temperature as a function of pressure measured by the gauge there. For pressures above 10 mTorr (possibly even above 1 mTorr) the neutral gas in the box is in the viscous flow regime.

The middle panel of Table 5-2 shows atomic density, mean-free-path, Kn (with respect to the divertor slot with L=5 cm.) for atoms at 3 eV assuming flux conservation condition (Eq. 5.6). For measured pressures below 30 mTorr the atoms are clearly in the molecular flow regime. Only at highest pressure are the atoms entering the transition regime. The right panel of Table 51-1 shows the same

Neutral density, mean-free-path, and Knudsen number at 0.03eV and 3eV

	Measured at Room T			**Flux Conservation**			**Constant Pressure**		
	species	molecules	D2	species	atoms	D0	species	atoms	D0
Gauge	temperature	T [eV]	0.03	temperature	T [eV]	3	temperature	T [eV]	3
Pressure	box-size	L [cm]	20	box-size	L [cm]	5	box-size	L [cm]	5
p_Div [mTorr]	D2 density [1e20/m3]	Lmfp_D2 [cm]	*Knudsen [1]*	D0 density [1e20/m3]	Lmfp_D0 [cm]	*Knudsen [1]*	D0 density [1e20/m3]	Lmfp_D0 [cm]	*Knudsen [1]*
0.1	0.04	70.0	*3.50*	0.005	1273	*254.6*	0.0004	18000	*3600*
0.3	0.11	23.3	*1.17*	0.015	424	*84.9*	0.0011	6000	*1200*
1	0.35	7.0	*0.35*	0.050	127	*25.5*	0.0035	1800	*360*
3	1.06	2.3	*0.12*	0.149	42	*8.5*	0.0106	600	*120*
10	3.52	0.7	*0.04*	0.498	13	*2.5*	0.0352	180	*36*
30	10.56	0.2	*0.01*	1.493	4	*0.8*	0.1056	60	*12*
60	21.12	0.1	*0.01*	2.987	2	*0.4*	0.2112	30	*6*

Table 5-2: Neutral density, mean-free-path and Knudsen number – calculated for room-temperature molecules (left panel); Franck-Condon atoms, using flux conservation condition (middle panel); and Franck-Condon atoms, using constant pressure condition (right panel) – as a function of the neutral pressure measured in the gas-box.

quantities calculated using a constant pressure condition (Eq. 5.7). Clearly the Knudsen number does not justify viscous treatment of hot atoms for any of the measured pressures. We conclude therefore that Franck-Condon atoms in the PFZ-reservoir are always in or very near to the molecular flow regime.

Fig. 5-3 (used with permission from ref. [37]) shows a comparison of the PFZ-reservoir neutral density, obtained from pressure measurement using Eq. 5.6, with the neutral density deduced from H_α measurements. The reasonably good agreement of the densities obtained with the two methods provides additional evidence that neutrals are in the molecular flow regime.

The long mean-free-path for Franck-Condon atom-atom collisions (calculated in Table 5-2) allows us to treat various neutral populations of interest separately (e.g. neutrals reflected from the plate vs. neutrals escaping from the PFZ-reservoir). The neutral-neutral mean-free-path is much longer than the momentum transfer mean-free-path in ion-neutral collisions (compare with Figs. 5-13 and 5-14). This allows us to neglect neutral-neutral collisions in the diffusive treatment of neutral transport, described in Section 5.5.

A complication of the analysis is the flow of neutrals out of the gas-box. Because the gas-box is not completely closed, some of the neutrals escape through a slot between the outer edge of the horizontal divertor plate and the vacuum vessel (Fig. 5-2). This leakage flux, analyzed in more detail in Section 5.4, induces a neutral particle flow from the divertor volume into the gas-box through a slot opening below the outer vertical target plate. In order to sustain this flow a pressure (density) gradient must exists between the bottom of the divertor and the gas-box.

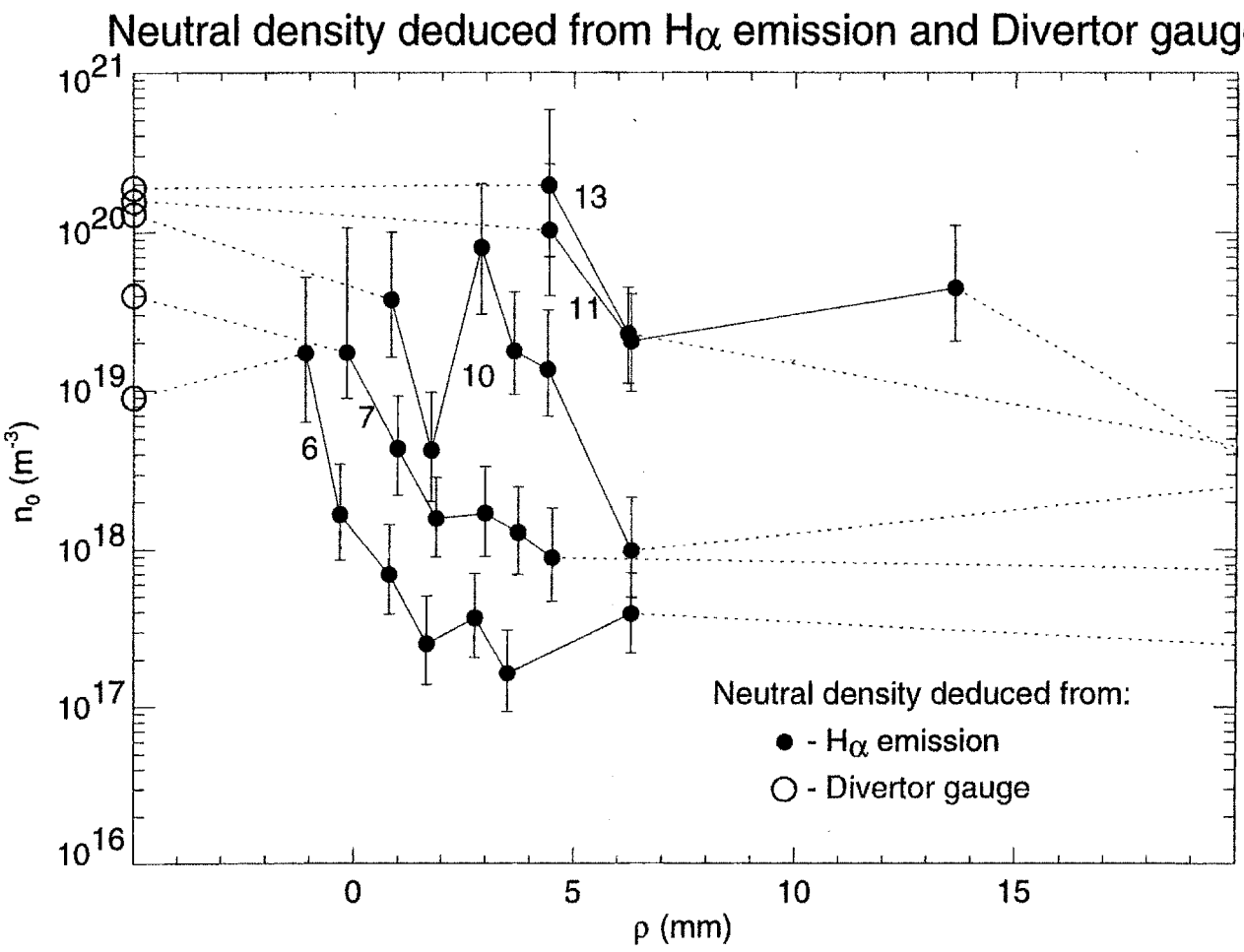

Fig. 5-3: Neutral atomic density deduced from Hα emission in the vicinity of the outer divertor Langmuir probes (denoted by their ρ-coordinate) for the five discharges listed in Table 5-1. The leftmost symbols indicate density calculated from the neutral pressure measurements with Eq. 5.6. Used with permission from ref. [37].

Estimates of the gas-box entrance and exit conductances indicate that it is possible for the actual pressure at the entrance to the gas-box to be about 20% higher than the measured one. This potential correction to the measured pressure is well below other uncertainties involved in the calculation here. Therefore it is not included in any model described in this chapter. Similarly, elsewhere in the thesis the data are always reported in terms of the measured gas-box pressure without an additional uncertainty of connecting the two plena. The correction is reported here for the completeness of the argument.

5.2.6 Atomic physics assumptions

The atomic physics underlying neutral transport in a tokamak is extremely complex and possibly not yet fully understood. For a detailed overview see for example a recent review edited by Janev and Drawin [105]. It has been argued that many complex phenomena (e.g., multi-step processes) may have to be considered in order to reach agreement between neutral transport codes and experiments in a cold dense divertor plasma [106].

A different approach is adopted here. The atomic physics is simplified to its minimum such that only the key phenomena are retained. The phenomena included in the following analysis are:

1) Reflection and recycling of ions on the divertor target. These are described by the particle (R_n) and energy (R_e) reflection coefficients.

2) Ion-atom momentum transfer, including both charge-exchange and elastic collisions. A convenient quantity describing the process is the momentum-transfer mean-free-path:

$$\lambda_{mt} = \frac{v_0}{nK_{mt}} \tag{5.8}$$

where:

n - is the plasma density (ions or electrons);

v_0 - is the atom thermal speed (assumed constant for a given atom);

and the momentum transfer reaction rate (K_{mt}) is the sum of the charge-exchange and elastic collision rates:

$$K_{mt} = K_{cx} + K_{el} \tag{5.9}$$

As discussed in Appendix B, there is currently some disagreement in the literature about the relative importance of the two terms in Eq. 5.9. Calculations in Chapters 5 and 7 are carried out, assuming that elastic collisions have a negligible contribution to the momentum transfer rate compared with charge-exchange events. Appendix E assumes that the elastic collisions have a contribution equal to that of the charge-exchange events and compares the results under the two assumptions

3) Electron-impact ionization of atoms, described by the ionization mean-free-path:

$$\lambda_{ion} = \frac{v_0}{nK_{ion}} \tag{5.10}$$

where:

K_{ion} - is the electron-impact ionization reaction rate.

4) Molecular dissociation is included only in a very simplified form. It is assumed to be the first reaction occurring immediately upon a molecule coming into contact with a plasma (i.e., an infinite reaction rate).

Appendix B summarizes formulae adopted here, from a vast and sometimes conflicting body of literature, to describe the atomic processes listed above.

It is a common practice, especially in plasma-description codes, to neglect molecular processes altogether due to their considerable complexity. A number of researchers strongly argue against this practice. For example, Howe [107] has shown how inclusion of molecular phenomena may change the results of fueling calculations in a limiter tokamak. The molecular processes are omitted in the analysis presented here. This omission does not influence the results strongly as discussed below and in Section 5.5. The most important omitted phenomena are:

1) Molecular ionization -

   For low plasma temperatures (T <10 eV) molecular dissociation significantly dominates over ionization. In fact Howe reproduces a plot after Heifetz [108] of a fractional yield of H^0 and H^+ from the dissociation and the ionization followed by dissociation of a deuterium molecule. At T <10 eV the ratio of H^0/H^+ is 85%/15%; it approaches ~50% at T >50 eV. The temperature of the private-flux-zone plasma in Alcator C-Mod rarely exceeds T ≈6 eV. Only in the lowest core-density cases ($\bar{n}_e \approx 0.5$ -$1 \cdot 10^{20}$ m^{-3}) do the molecules escaping from the divertor encounter hotter plasma. Therefore the omission of molecular ionization may introduce a significant error only in the lowest density case considered here (shot #6). Had the molecular ionization been included it would have moved the

ionization source deeper into the divertor volume, thus reducing the plasma albedo calculated in Section 5.6. The omission does not introduce any significant error in the medium density cases (#7 and #10) or the two detached cases (#11 and #13) analyzed in this chapter.

2) Molecular dissociation and

3) Ion-molecule elastic collisions -

Each of the two processes has an opposite effect on the plasma albedo to neutrals. As is discussed in Section 5.5, their omission does not introduce significant error.

Two additional assumptions about neutral atom characteristics are included in the neutral transport analysis:

1) A constant neutral temperature assumption allows us to follow monoenergetic atoms thus considerably simplifying the analysis. The omission of the neutral temperature gradient leads to an overestimate of the diffusive flux and an underestimate of the plasma albedo, calculated in Section 5.5. The error is small, however, because the albedo is determined in the cold plasma region ($T < 6$ eV), where the ion temperature and atom energy are similar. A more detailed discussion is carried out in Appendix D.

2) Neutral-neutral collisions are omitted because their mean-free-path is much longer than the ion-neutral collision mean-free-path for the conditions modeled here.

Clearly the analysis presented in this chapter could be extended to include a more complete set of atomic processes. At this stage, however, the included phenomena allow us to achieve satisfactory agreement with the experiment.

5.3 Neutral transport between the target and the PFZ-reservoir

5.3.1 Neutralization and recycling on the divertor target

The PFZ-neutral-reservoir is fueled by ions neutralizing on the target plates. Thus a knowledge of the incident ion flux onto the divertor target surfaces is required to calculate the neutral particle source. The Langmuir probe ion saturation current perpendicular to the plate would provide a measure of this flux. A major difficulty lies, however, in interpreting conflicting data from the domed and flush Langmuir probes. Experience from other tokamaks [109, 110] indicates that the domed Langmuir probes significantly underestimate perpendicular ion flux at shallow field line angles (e.g., 0.5° in the Alcator C-Mod divertor). On the other hand, the flush probes overestimate this quantity because of their negative bias (applied to repel electrons) and a resulting potential sheath expansion [30]. The analysis here is initially carried out using the ion flux estimate obtained from the biased flush Langmuir probes. This assumption, leading to an overestimate of particle source, is subsequently reexamined in Section 5.7, where the different ion flux estimates are discussed from the perspective of the neutral particle balance.

Any solid surface has some pumping capability, i.e., it can retain some of the particles striking it for a period of time exceeding the length of a plasma discharge.

As shown in Appendix A, however, the divertor target plates in Alcator C-Mod become saturated with the gas in less than first ~10 ms of the diverted phase of the discharge [111]. Thus during a steady-state portion of the discharge all impacting ions leave the divertor target surface (as neutrals).

The ions strike the material surface with the energy which is a sum of the ion thermal energy (calculated assuming $T_i = T_e$) and the kinetic energy gained through the acceleration within the surface sheath. Following the standard sheath theory [112], we approximate the surface-sheath potential drop as $\Delta V = 3 \times T_e$ (which is an upper limit at grazing angles of incidence). Upon impact some of the ions are reflected off of the surface as atoms with a significant fraction of their initial energy. The fraction of the promptly reflected neutrals - R_n - can be expressed as a function of the target plate material atomic mass and the mass and reduced energy of the projectile. The plot of the particle reflection coefficient (R_n) of deuterium on molybdenum as a function of energy [113] is given in Appendix B. Some of the impact energy is retained as expressed by the energy reflection coefficient - R_e , which is also plotted in Appendix B. The fast reflected neutrals carry the R_e/R_n fraction of the initial impact energy ($E = 5 \times T_e$). Fig. 5-4 shows the particle (R_n) and energy (R_e) reflection coefficients calculated at each of the outer vertical-target probe locations for representative hot-attached divertor plasma and cold-detached divertor plasma discharges. In the attached case both R_n and R_e are somewhat lower because of the hotter plasma being in contact with the material surface.

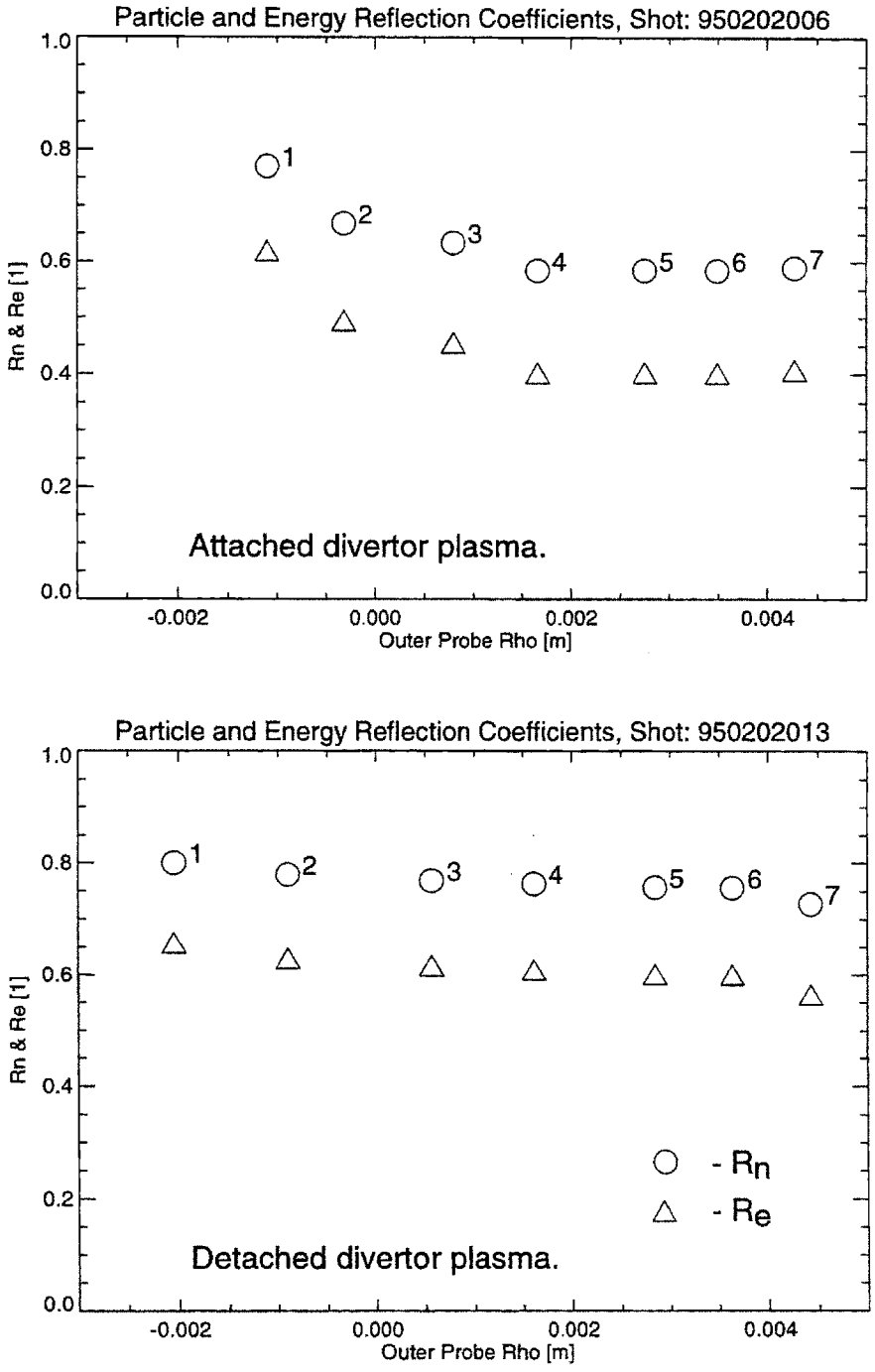

Fig. 5-4: Particle (R_n) and energy (R_e) reflection coefficients, calculated at each of the outer vertical-target probes, plotted as a function of the probe ρ-coordinate. The top graph shows an example of a hot-attached divertor plasma, the bottom, an example of a cold-detached divertor plasma.

The remaining ions ($1\text{-}R_n$) recycle, i.e., are absorbed onto the surface and reside there sufficiently long to fully thermalize and to associate into deuterium molecules, which are subsequently emitted. Upon emission a molecule can be ionized or dissociated. For simplicity we assume (see Section 5.2.6) that the first process the molecule undergoes is a dissociation and that the dissociation occurs in an immediate vicinity of the target. As a result the recycled neutrals (absorbed/emitted) propagate across the plasma channel as slow atoms with the Franck-Condon energy (FC-population). Substituting a single energy value E_{FC} =3 eV for the F-C energy distribution [114] introduces an insignificant error, compared to other atomic physics assumptions made earlier.

Both neutral populations (Fast-reflected and FC-recycled) leave the surface with an approximately cosine-law angular distribution of velocities. For simplicity the cosine distribution is approximated as a normal-angle reflection, which results in an overestimate of the neutral transmission calculated here. The potential error is significant, however, only when transmission is low, i.e., for detached discharges described by the electron-conduction model. The error is small for high (near unity) transmission cases, e.g., for all calculations using the constant-Te plasma model.

The Alcator C-Mod divertor geometry is such that the neutrals created (either by reflection or recycling) on the vertical portion of the target plate can penetrate into the private flux zone (PFZ). The neutrals that are created on the horizontal portion of the target plates (i.e., above the nose) do not have a direct view of the private flux zone and have insignificantly small probability of penetrating there. Thus only

the contribution from the vertical plate recycling (inner and outer) is included the PFZ-reservoir particle balance.

5.3.2 Penetration towards the PFZ-reservoir

Upon reflection or emission the neutrals have to penetrate the divertor plasma fan, before entering the PFZ-reservoir. The neutral transport across the plasma can be either ballistic or diffusive (the latter described in Section 5.5) depending on its step size, which is the ion-neutral momentum-transfer mean-free-path - λ_{mt} (recall that the neutral-neutral collisions have much longer mean-free-path, and thus are neglected here). The transport is diffusive if:

$$\lambda_{mt} \ll L_{path} \tag{5.11}$$

where:

L_{path} - is the scale length of the problem; here, it is the distance between the target and the boundary of the PFZ-reservoir , i.e., the path-length of a modeling chord.

The transport is ballistic if:

$$\lambda_{mt} \geq L_{path} \tag{5.12}$$

Reiter [89] actually suggests automatic switching between the two descriptions in a code upon examination of the condition λ_{mt}/L_{path}. Here the calculations are carried out for the two descriptions in parallel. The condition λ_{mt}/L_{path} is then examined *a posteriori* and the appropriate result is selected for further analysis.

It turns out that most of the cases modeled satisfy Eq. 5.12. Only in a couple of cases (e.g., chord #7 across a dense plasma) the comparison yields $L_{path} \approx$

2-3×λ_{mt} which unfortunately does not qualify for either treatment. To retain consistency of the plate→PFZ transmission calculation, the transitional cases are treated using the ballistic transport model.

In the absence of diffusive collisions and a volumetric source the 1D neutral density equation can be written as:

$$\frac{dN}{ds} = -\frac{N}{\lambda_{ion}} \tag{5.13}$$

where:

s - is the path-length coordinate starting at the plate.

An immediate solution of Eq. 5.13 is:

$$N = e\left(-\int_0^s \frac{dx}{\lambda_{ion}}\right) \tag{5.14}$$

Because the density is normalized to unity at the plate location, Eq. 5.14 provides transmission probability of a neutral anywhere along its path (within the validity of the ballistic model).

Because λ_{ion} is not an analytic function of space coordinates, the integration in Eq. 5.14 has to be carried out numerically. Moreover, λ_{ion} has to be calculated along the modeling path, based on the background plasma conditions, which are calculated using one of the two models, described in Section 5.2. The models, however, specify plasma conditions only at the knots, corresponding to the flux surfaces intersecting the Langmuir probes. The characteristic transport lengths (λ_{ion}, λ_{mt}) are then calculated at these points and interpolated logarithmically everywhere in-between. Note that the logarithmic interpolation of the transport

lengths implies an exponential radial profile of plasma parameters, which is approximately confirmed experimentally [72].

The transmission probability is calculated separately for the Fast- and FC-neutral populations. The final transmission probability is obtained as a weighted sum of the transmissions of the two populations:

$$f^i_{trans} = f^i_{Fast} \cdot R_n + f^i_{FC} \cdot (1 - R_n) \tag{5.15}$$

where:

f^i_{Fast} - is the transmission probability (plate→PFZ-reservoir) of a fast neutral originating at probe "i";

f^i_{FC} - is the transmission probability (plate→PFZ-reservoir) of a Franck-Condon neutral originating at probe "i";

f^i_{trans} - is the total transmission probability (plate→PFZ-reservoir) of any neutral originating at probe "i";

Fig. 5-5 summarizes the neutral transmission probability results, calculated for neutrals originating at each of the outer Langmuir probe location, including contributions from the fast and FC populations. The top panel on Fig. 5-5 shows an example of a hot-attached divertor plasma, and the bottom one, an example of a cold-detached plasma. The background plasma parameters are described by the electron-conduction model.

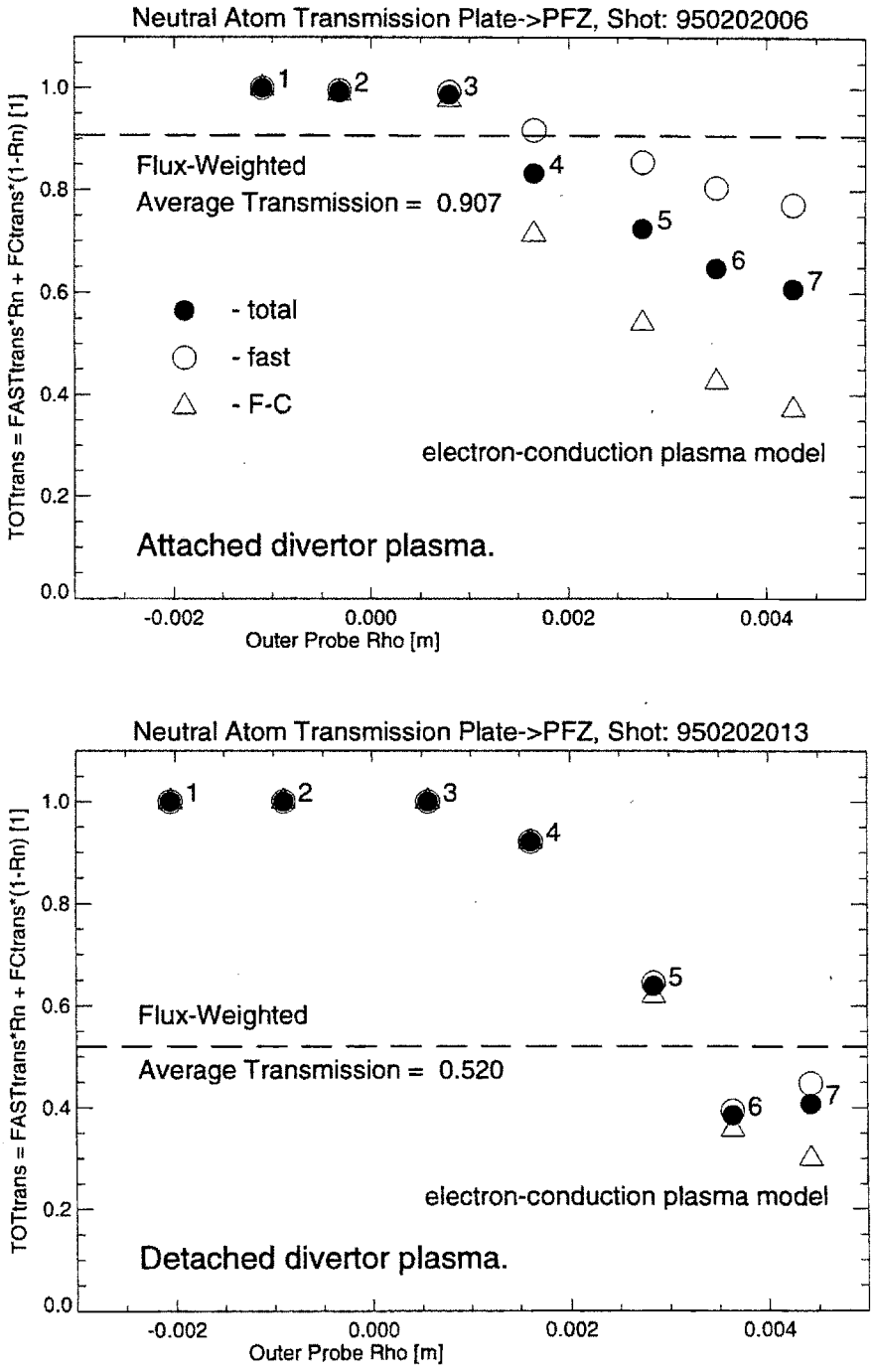

Fig. 5-5: Transmission probability of neutrals (emitted at a normal angle) from the divertor target into the PFZ-reservoir. For each of the outer probes the total, fast- and FC-atom transmission probability is plotted. Horizontal line indicates the weighted average transmission including the outer and inner vertical targets. Plasma is described by the electron-conduction model.

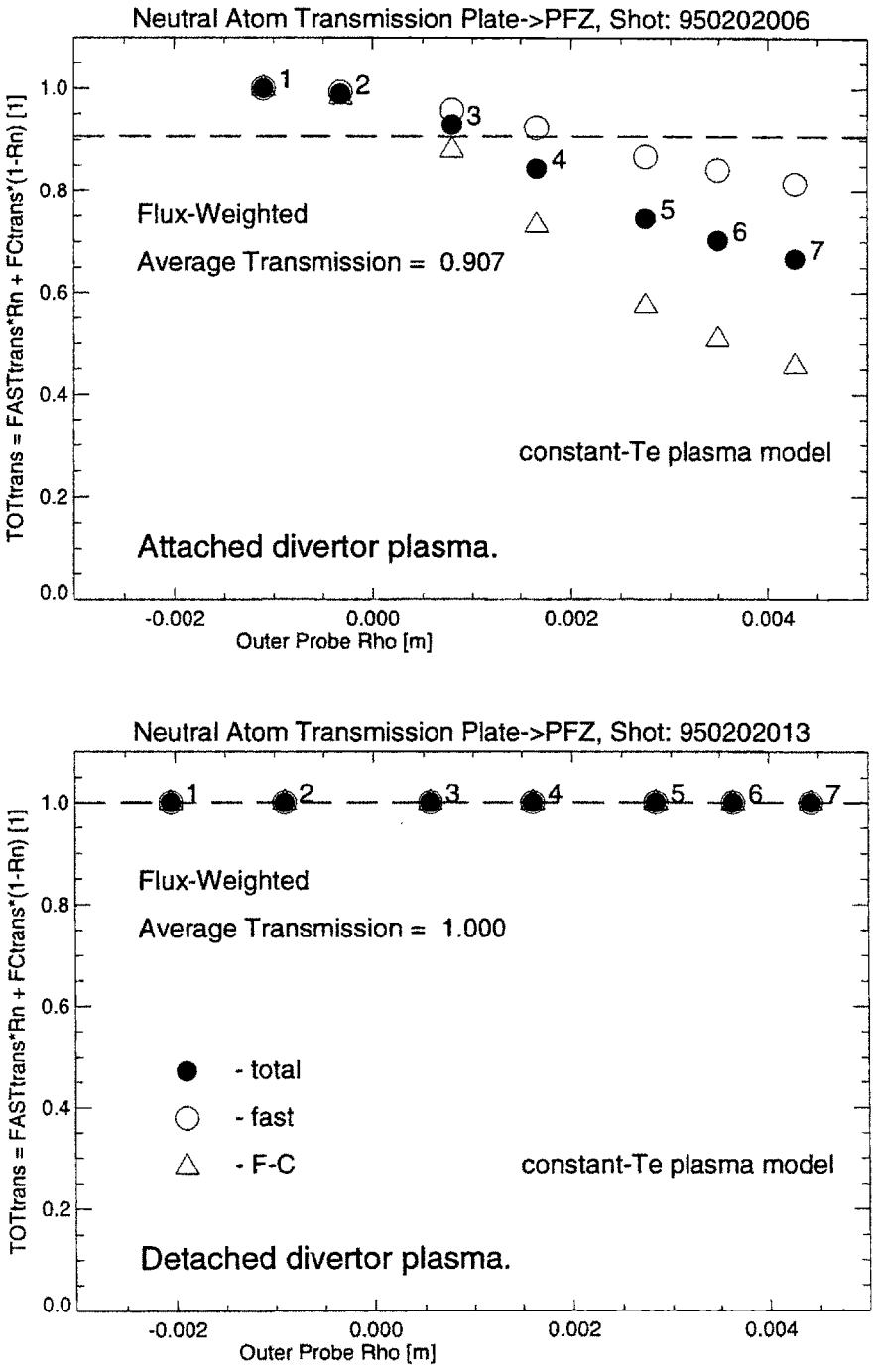

Fig. 5-6: Transmission probability of neutrals (emitted at a normal angle) from the divertor target into the PFZ-reservoir, calculated with the background plasma described by the constant-Te model. Same symbols are used as on the previous figure.

In order to compare the two plasma models, the calculations are repeated using the constant-Te model. Fig. 5-6 shows results of an identical calculation with the only difference being the background plasma model. When comparing Figs. 5-6 with 5-5 the most important observation is a significant difference in transmission across the detached plasma. In contrast, in the attached plasma the two models yield similar transmission results.

The final goal of this section is to estimate the neutral particle source fueling the PFZ neutral reservoir. The Langmuir probe measurements provide a poloidal ion flux source profile across the divertor target. When multiplied by the transmission probability, calculated above, a profile of transmitted flux is obtained. Fig. 5-7 shows the two profiles (original and transmitted) on the outer vertical target plate for the two example plasmas of interest (hot-attached vs. cold-detached). Only the results obtained with the electron-conduction plasma model are presented. The constant-Te plasma model produces an almost identical result for the attached plasma but it leads to close to unity transmission for the detached plasma.

The final PFZ-reservoir neutral particle source is given by:

$$\Gamma_{plate} = \int_{S^{out}_{divBN}} f^{i}_{trans}\left(J^{i}_{\perp sat}/\sigma\right)ds + \int_{S^{in}_{divBN}} f^{i}_{trans}\left(J^{i}_{\perp sat}/\sigma\right)ds \qquad (5.16)$$

where:

Γ_{plate} - is the total neutral particle flux fueling the PFZ-reservoir originating on one of the vertical target plates;

$J^{i}_{\perp sat}$ - is the ion saturation current density perpendicular to the plate at probe "i";

σ - is the electron charge;

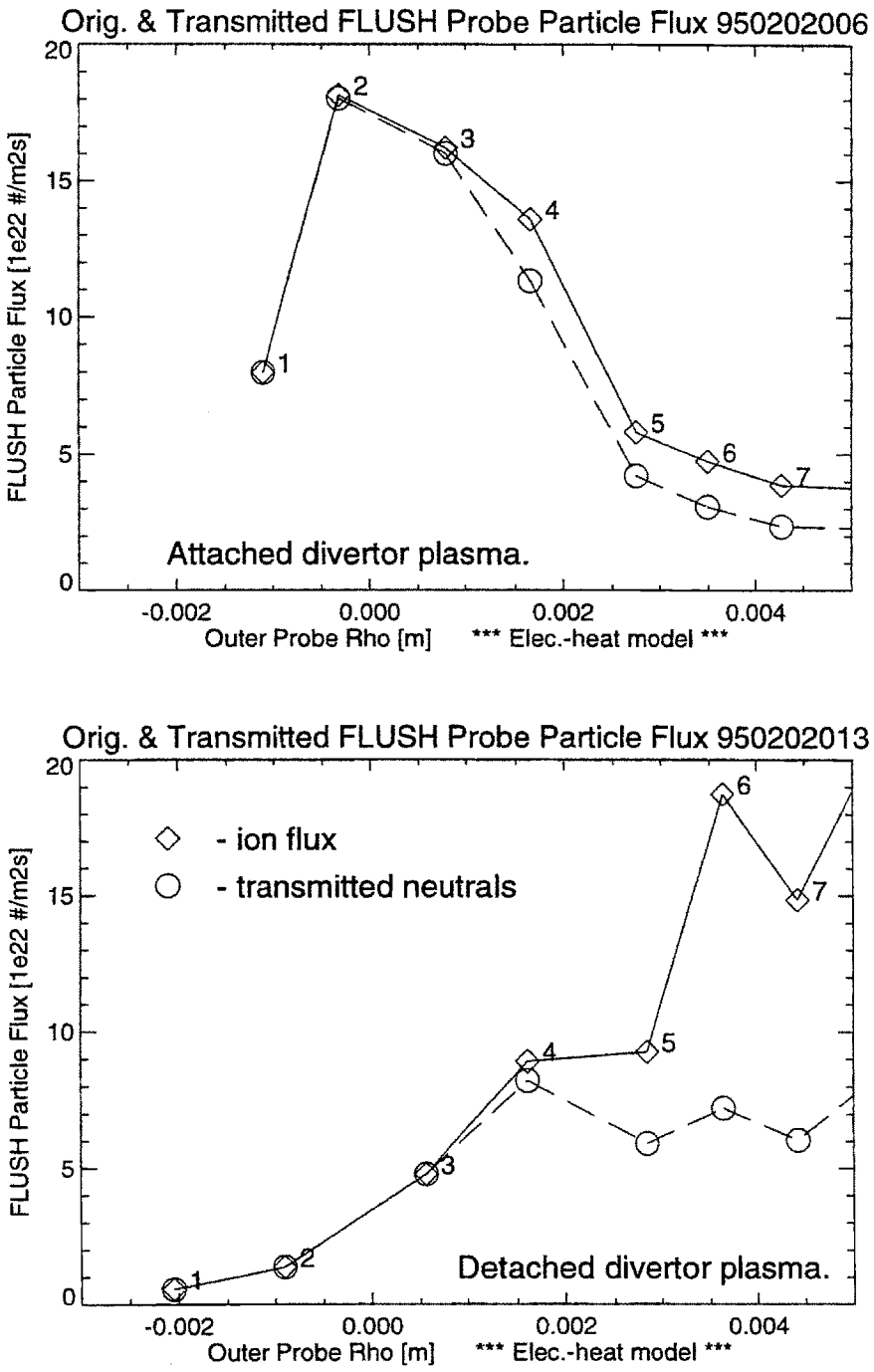

Fig. 5-7: Perpendicular ion flux striking the outer divertor target, as measured by the flush Langmuir probes, compared with the atom flux penetrating into the PFZ -reservoir. Atom transmission is calculated using the electron-conduction model for the background plasma description.

and the integration is carried over:

S^{in}_{divBN} - the inner vertical target plate (below the nose) surface and

S^{out}_{divBN} - the outer vertical target plate (below the nose) surface.

In the description above we have reported in detail only the calculations for the outer divertor target plate. An identical calculation is repeated for the inner divertor plate. During the discharges analyzed here the inner strike point was located just below the divertor nose. As a result the inner vertical target was connected (magnetically) to the divertor private-flux-zone. This causes the two plasma models to deliver almost identical results, thus only one set of numbers is reported in Table 5-4. The position of the inner vertical plate in the magnetic PFZ leads to a high transmission, $f^i_{trans} \approx 1$, but to a very low ion flux. Most of the inner divertor recycling occurs on the plate above the inner nose. Consequently the outer-divertor term in Eq. 5.16 dominates the inner one.

In order to facilitate the following discussion of the neutral transmission we define a new quantity, the average plate transmission coefficient:

$$f_{trans} = \frac{\int_{S^{out}_{divBN}} f^i_{trans}\left(J^i_{\perp sat}/\sigma\right)ds + \int_{S^{in}_{divBN}} f^i_{trans}\left(J^i_{\perp sat}/\sigma\right)ds}{\int_{S^{out}_{divBN}}\left(J^i_{\perp sat}/\sigma\right)ds + \int_{S^{in}_{divBN}}\left(J^i_{\perp sat}/\sigma\right)ds} \qquad (5.17)$$

This single number captures all of the above modeled neutral-plasma interactions and provides a very useful measure of the divertor plasma fan transparency to the plate neutrals. The average divertor transmission coefficient is plotted as a dashed line on Figs. 5-5 and 5-6. Fig. 5-8 compares the average plate-neutral transmission

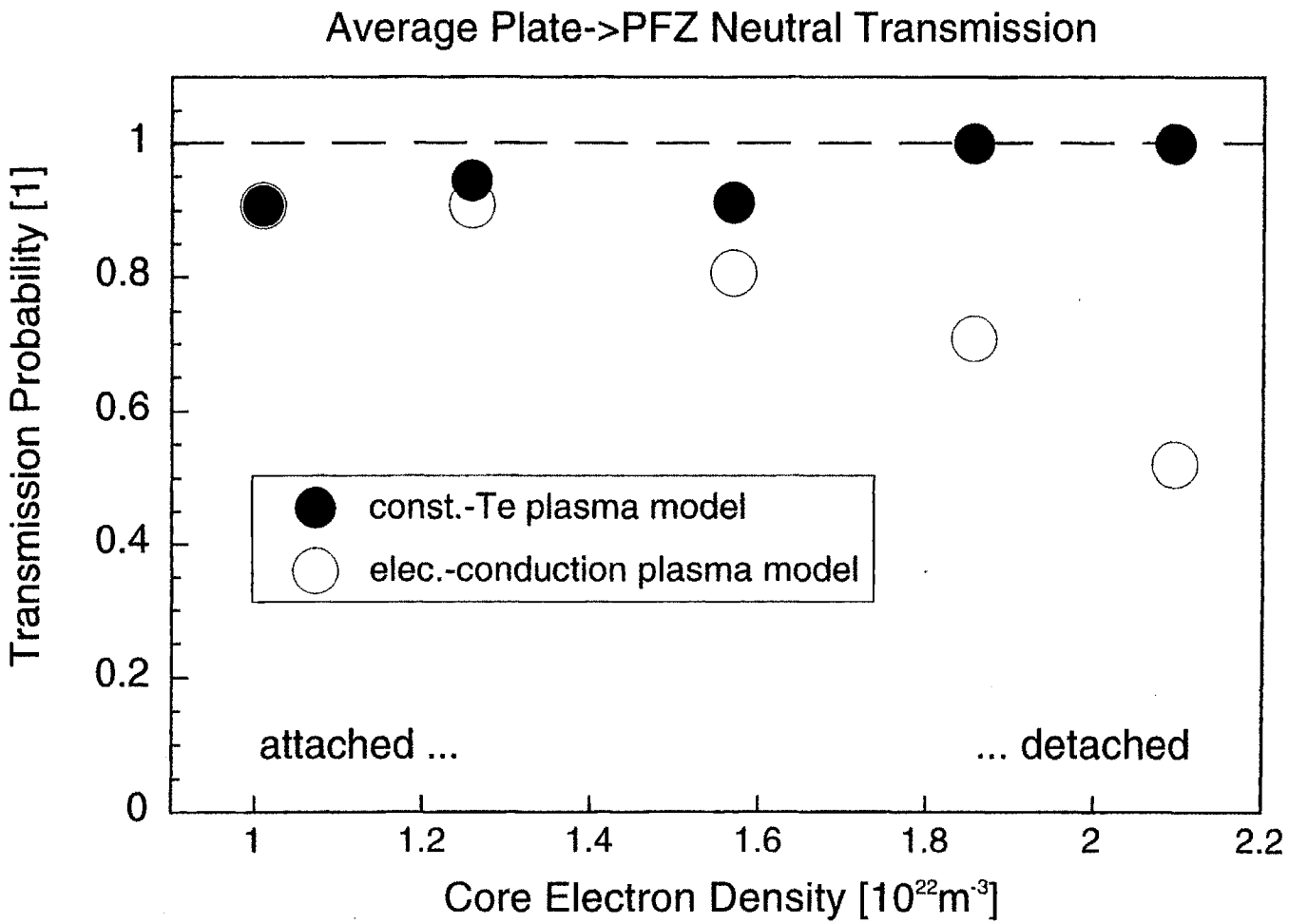

Fig. 5-8: Flux-weighted average (over the outer vertical target plate) of the transmission of neutrals from the target plate into the PFZ-reservoir. Results obtained with the two different plasma models are compared.

coefficient calculated with the two divertor plasma models plotted as function of core plasma density for the five discharges of interest; Table 5-5 contains the numerical details.

The most striking observation is that the two plasma models result in a vastly different dependence of the transmission on the core plasma density. The electron-conduction model results in the transmission considerably decreasing with the core density (from 0.9 to 0.5) whereas the constant-Te model leads to a smaller and opposite change in the calculated transmission (increasing from 0.9 to 1.0).

Fig. 5-8 shows no difference between the two plasma models for the hot-attached divertor (low $\bar{n}_e$). This is due to the peak of ion saturation current being located near or at the separatrix. Because most of the neutrals penetrate only across a thin layer of plasma the result is insensitive to the details of the plasma profile. In the detached cases (high $\bar{n}_e$), in contrast, the peak in ion saturation current occurs much higher along the plate, in the vicinity of the divertor nose. Thus most of the neutrals penetrate across the full width of the divertor plasma fan. As a result, their transmission probability depends critically on the plasma conditions encountered along the path. These, in turn, depend on the location of the detachment front (T ≈6 eV isotherm) . The electron-conduction model places the detachment front deep inside the divertor, in the vicinity of probe #3. As a result most of the neutrals have to penetrate through a hot, dense plasma with a full upstream pressure. This leads to the calculated low transmission probability ~0.5. The constant-Te model, in contrast, positions the detachment front above probe #7. Thus most of the neutral penetrate across a cold, detached plasma, which leads to the transmission probability ~1. The discrepancy between the two models is discussed in more detail in Section 5.6.

5.3.3 Neutral escape towards the target plates

The methodology described above for the ballistic transport of particles neutralizing on the target plates is applied to the neutrals escaping from the PFZ-reservoir in the direction of the plates. Also the same modeling chords are used for both calculations.

Again the ballistic transport condition is satisfied (Eq. 5.12). The transmission probability of a Franck-Condon atom between the plate and the PFZ-reservoir boundary is independent of direction of propagation. Thus the results obtained in the previous subsection can be used directly. Upon arriving at the plate neutral atoms undergo a similar reflection-emission process to that described earlier for ions. The previous assumption of a prompt molecular dissociation leads to a mirror-like reflection of F-C atoms. The final probability of "reflection of the plate", i.e., probability of a neutral launched towards the target reappearing back in the PFZ-reservoir is simply the square of the FC transmission probability (f^{i}_{FC}) calculated earlier in this section. This "plate-reflection" probability, as it will be referred to herein, depends on the underlying plasma model and varies with each spatial chord. Table 5-4 contains the numerical results.

Fig. 5-9 summarizes the calculations carried out here in terms of an average outer plate reflection probability (f^{out}_{refl}):

$$f^{out}_{refl} \cdot S^{out}_{pfz} = \int_{S^{out}_{pfz}} \left(f^{i}_{FC}\right)^2 ds \qquad (5.18)$$

where the integration is carried out along the outer PFZ-reservoir bounding surface, S^{out}_{pfz}, up to the divertor throat (just above chord #7).

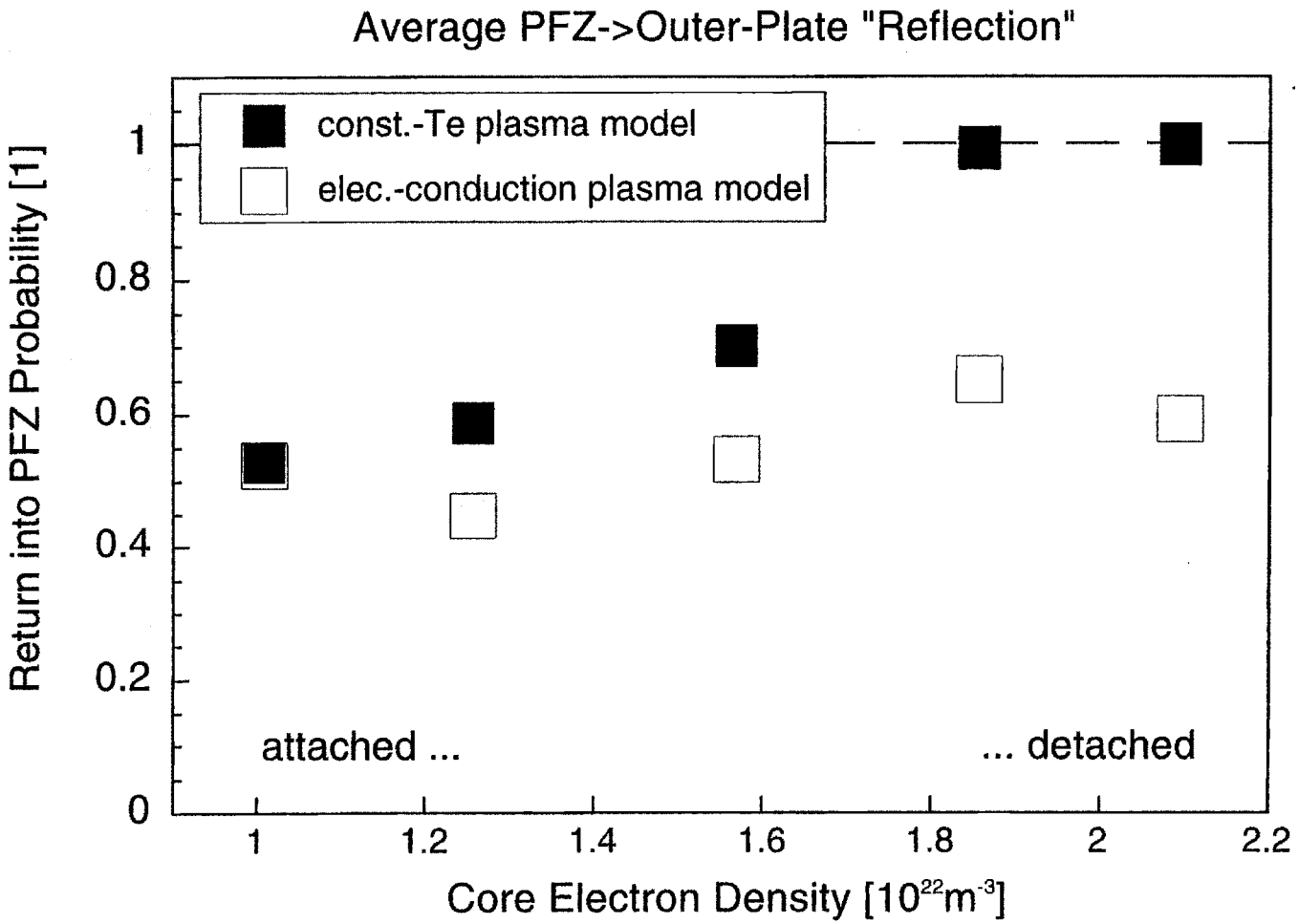

Fig. 5-9: Average outer plate "reflection" coefficient, defined as a probability of a neutral reappearing in the PFZ-reservoir upon reflecting off the outer target plate and double crossing the plasma-fan. Results obtained with the two plasma models are compared.

Fig. 5-9 illustrates a similar disagreement between the two plasma models to the one described for plate→PFZ transmission. While the electron-conduction model leads to a constant reflection across the density range, the constant-Te model leads to increasing plate reflection with core density due to decreasing temperature of the plasma fan in front of the target plate.

5.4 Importance of leakage flux

Because Alcator C-Mod divertor geometry is not completely closed the flux of neutral particles that escape through leaks in the divertor gas box is a source of significant neutral particle loss from the divertor plenum, especially at high divertor pressure (e.g., 30-60 mTorr).

There are two possible escape paths: (1) The first one is a toroidally continuous slot between the outer edge of the outer horizontal target plate and horizontal shelf of the vacuum vessel shown on Fig. 5-2. The height of this opening is ~1 cm but because of its toroidal continuity the total area is ~ 0.050 m^2. (2) The second escape path is through toroidally localized diagnostic openings in the divertor plate itself, the "open divertor modules", described already in Chapter 2. We define the diagnostic opening area through which particles escape without being returned back as a region extending from the second knee in the horizontal plate (R ≈0.70 m in Fig. 5-2) to the corner of the vacuum vessel (R ≈0.82 m in Fig. 5-2). There are five such diagnostic openings in Alcator C-Mod, each spanning 6° of the toroidal extent with the combined area ~0.045 m^2.

Because the neutral-neutral collision length is comparable to the leakage-slot height neutrals that escape through that slot are in a transitional regime at high pressures or in a molecular regime at low pressures. Therefore an expression for the molecular flow conductance provides a reasonable accuracy. Orifice-like conductance has to be corrected by an additional factor of one-half to account for the finite length of the slot [103]. The conductance across the diagnostic openings is better described by the molecular orifice-expression because of their much larger width-to-length ratio and typically much lower pressures measured there.

The total leakage flux of neutrals (Γ_{leak}) is a function of the conductance of the two escape paths and the pressure difference across the two paths:

$$\Gamma_{leak} = (p_{div} - p_{plate})\, C_{leak} + (p_{open} - p_{plate})\, C_{open} \qquad (5.19)$$

where:

C_{leak} - is the molecular conductance of the leakage slot below the outer edge of the horizontal target plate;

C_{open} - is the molecular conductance of the six diagnostic openings in the outer divertor structure;

p_{div} - is the neutral pressure measured by the divertor gauge;

p_{open} - is the neutral pressure measured by the open-divertor-module gauge;

p_{plate} - is the neutral pressure just above the outer horizontal divertor target plate, near its outer edge, for simplicity it will be referred here to as a "plate pressure".

The key difficulty of calculating the leakage flux lies in properly estimating the plate pressure (p_{plate}), because there is no direct measurement there.

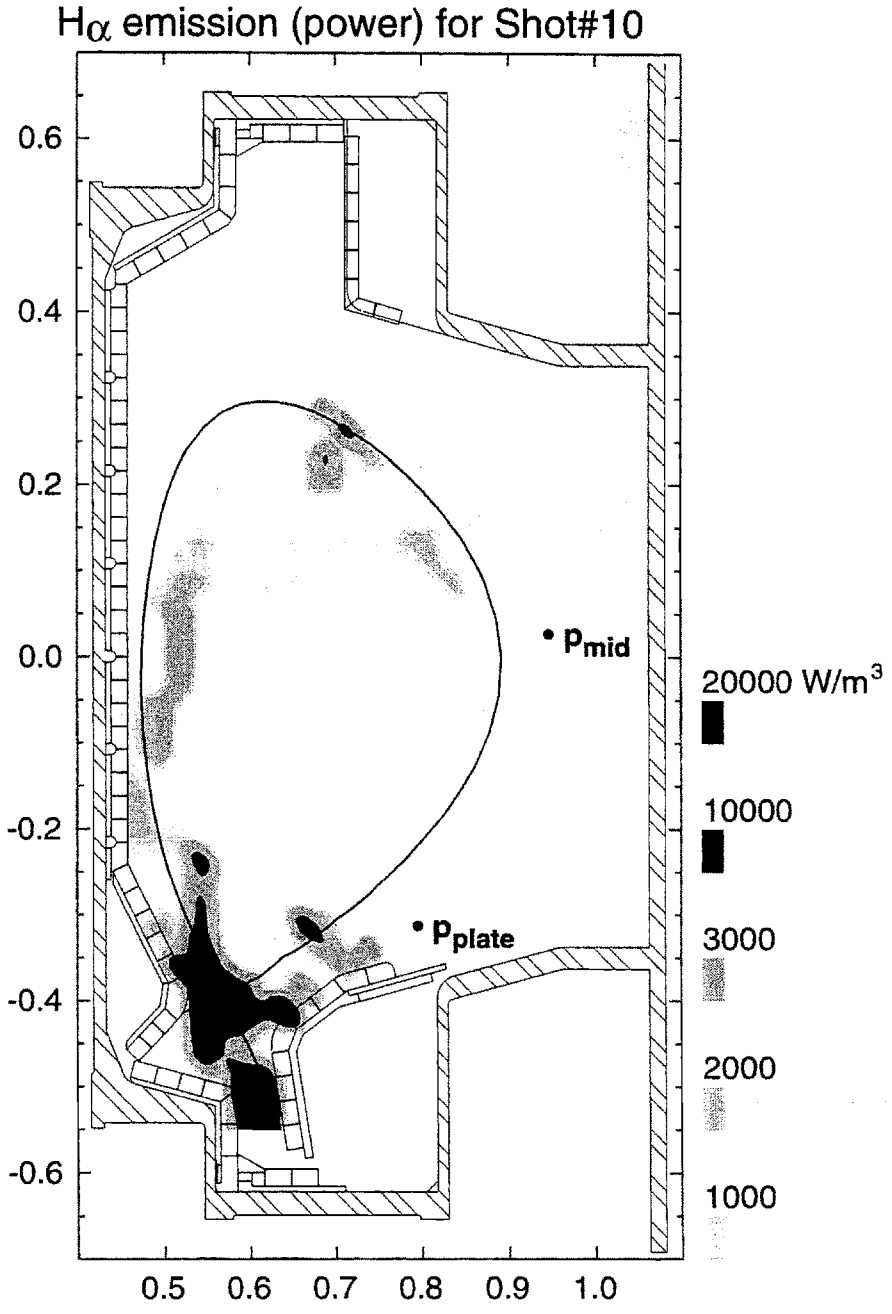

Fig. 5-10: A tomographic reconstruction of $H\alpha$ emission shows strong poloidal variations indicating neutral density gradients. The neutral pressure near the outer edge of the horizontal target plate (p_{plate}) may locally be higher than that measured at the midplane (p_{mid}).

Fig. 5-10 shows a representative poloidal profile of H_α emission. The emission, which is a measure of neutral particle density, indicates a neutral density gradient between the scrape-off-layer just above the target plate and the scrape-off-layer at the midplane, which may points to $p_{plate} > p_{mid}$. Unfortunately it was not possible to obtain an absolute neutral particle density from the H_α measurements because of extremely weak emission signal there.

Even though the measurement of the plate pressure (p_{plate}) is not available it is still possible to deduce its upper and lower limits. Because almost all of the recycling occurs in the divertor, the neutral flow is established from the divertor plenum towards the midplane volume driven by a neutral pressure gradient. Because of the direction of this flow the plate pressure cannot be lower than the midplane pressure, nor higher than the open module pressure. As a reasonable approximation we evaluate the plate pressure as an arithmetic average of its bounds.

Fig. 5-11 shows the leakage flux calculated using Eq. 5.19, together with the error bars depicting its lower and upper bound estimates resulting from the maximum and minimum estimates of the plate pressure respectively. Table 5-3 summarizes the numerical results. The net escape flux of neutrals across the plasma boundary (calculated in Section 5.6), included as a reference in Fig. 5-11, indicates increasing importance of the leakage flux as a loss mechanism of neutrals from the divertor. Thus the existing leakage openings in the divertor geometry may significantly limit its ability to confine neutrals. Because of this problem there are plans in Alcator C-Mod to close the existing leaks. This is discussed in detail in Chapter 7.

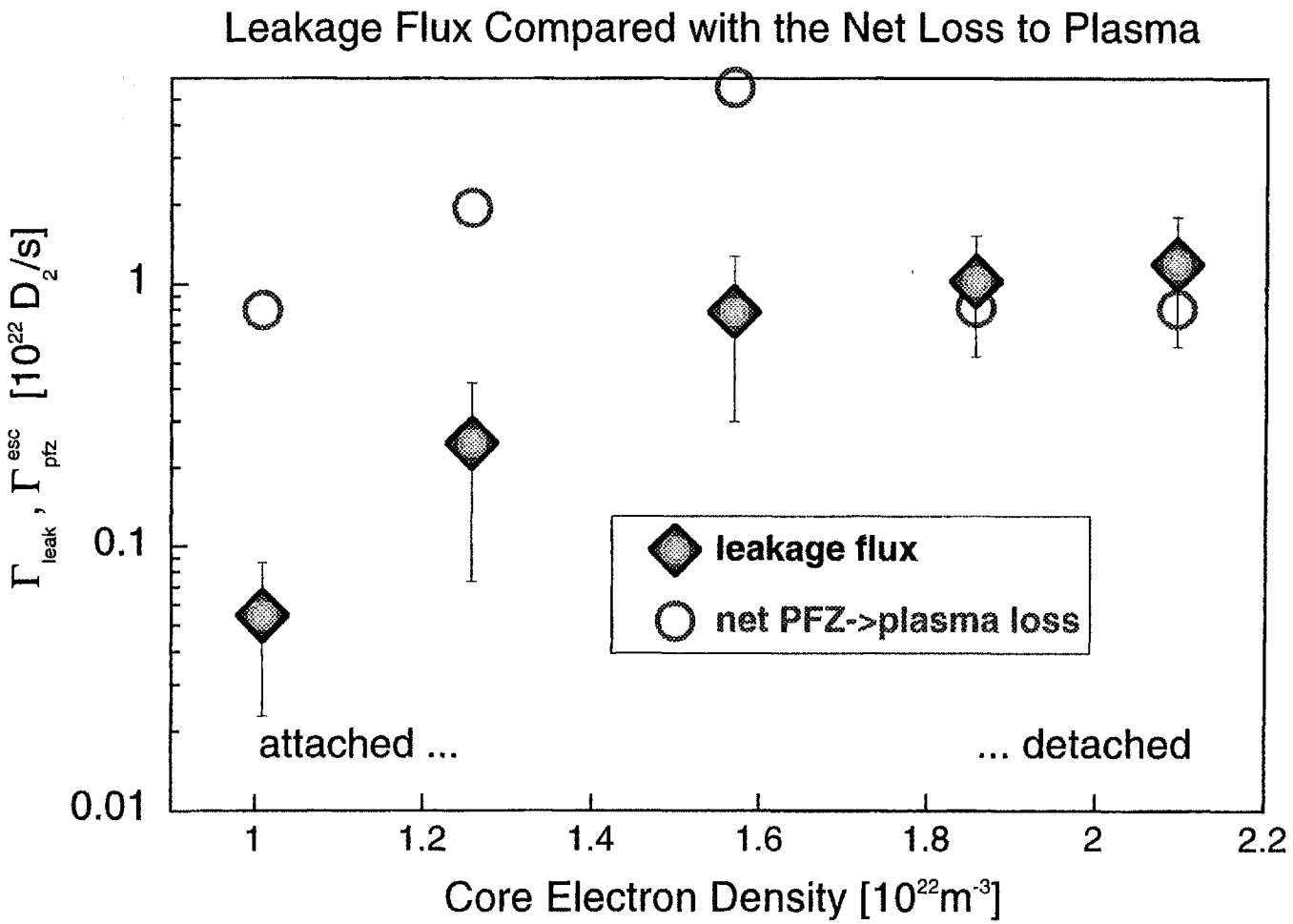

Fig. 5-11: Flux of neutrals escaping through the leaks in the divertor structure. The error bars indicate its upper and lower bounds resulting from different estimates of the plate pressure. As a reference the net escape flux towards the plasma channel is also plotted. Note a dramatically increasing significance of the leakage flux in the detached plasma state.

Plate pressure and resulting divertor lekage flux estimates .

Discharge Number:		6	7	10	11	13
core electron density	[1e20/m3]	1.01	1.26	1.57	1.86	2.09
divertor pressure	[mTorr]	1.8	8.4	25.9	32.7	38.2
Plate Pressure Estimates:						
p_Plate = p_Open	[mTorr]	0.65	2.06	8.24	14.56	15.98
p_Plate = average	[mTorr]	0.35	1.10	4.35	7.66	8.43
p_Plate = p_Mid	[mTorr]	0.05	0.15	0.46	0.75	0.87
Leakage Flux Estimates:						
minimum	[1e22 D2/s]	**0.03**	**0.17**	**0.49**	**0.50**	**0.61**
average	[1e22 D2/s]	**0.05**	**0.25**	**0.79**	**1.03**	**1.19**
maximum	[1e22 D2/s]	**0.08**	**0.32**	**1.09**	**1.56**	**1.78**
Reference:						
Net PFZ->plasma loss	*[1e22 D2/s]*	*0.80*	*1.94*	*5.55*	*0.82*	*0.81*

Table 5-3: Flux of neutral escaping through leaks in the divertor structure calculated using different assumptions about the neutral pressure above the outer horizontal divertor plate.

In order to resolve the uncertainty about the main chamber pressure gradient we recommend installing an additional pressure diagnostic near the outer edge of the horizontal divertor target plate. Alternatively the existing open-module pressure gauge can be adapted for this measurement by installing a "sniffing" tube to connect it to the volume of interest.

5.5 Neutral escape across the divertor throat

5.5.1 Diffusive transport of neutrals

The ballistic treatment used to calculate neutral transmission through a thin plasma channel in front of the target plate is not applicable to describe the neutral transport across a much thicker plasma fan plugging the divertor throat. The condition $\lambda_{mt} \ll L_{path}$ (Eq. 5.11) requires a diffusive treatment of neutral transport in this case.

Although diffusion theory is well established, the neutral diffusion equation is derived in Appendix D for completeness. Using the assumptions discussed in Section 5.2 the neutral diffusion equation can be written in a convenient form involving the characteristic interaction lengths:

$$\nabla \cdot \left(-\frac{\lambda_{mt}}{2} \nabla N \right) = -\frac{N}{\lambda_{ion}} \tag{5.20}$$

where:

N - is the neutral atom density.

Note that Eq. 5.20 does not include any volumetric source terms (only sink) because any additional sources (e.g., plate recycling) are treated separately. The neutral diffusion equation is first solved analytically (using an assumption of constant background parameters) in Section 5.5.2 and then numerically in Section 5.5.3 to obtain an estimate of the plasma albedo to neutrals.

5.5.2 Approximate analytic solution and plasma albedo

Even though the final solution needs to be obtained numerically it is helpful to review an approximate analytic solution to introduce the concept of plasma albedo and to gain insight into its dependence on plasma parameters.

Consider a slab-geometry along a spatial coordinate - x, as shown on Fig. 5-12 (top drawing), consisting of three uniform regions. The leftmost region (x<0) is filled with neutrals at constant temperature and density (N_0) moving along free-flight trajectories without collisions. This "ballistic" region (as referred to in Fig. 5-12) corresponds to the neutral PFZ-reservoir in Fig. 5-2. The coordinate x=0 corresponds to the plasma-fan boundary in Fig. 5-2 (ρ= -2 mm).

Upon crossing the boundary neutrals start to collide with the background plasma. If the plasma is sufficiently cold and dense then the momentum-transfer collisions dominate over ionizing collisions ($\lambda_{mt} \ll \lambda_{ion}$). Thus the loss term can be neglected in Eq. 5.20 leading to a linear density drop in this "diffusive" region (Fig. 5-12). The diffusive region extends between plasma boundary (x=0) and an "ionization front" (x = L) marked by a T ≈6 eV isotherm.

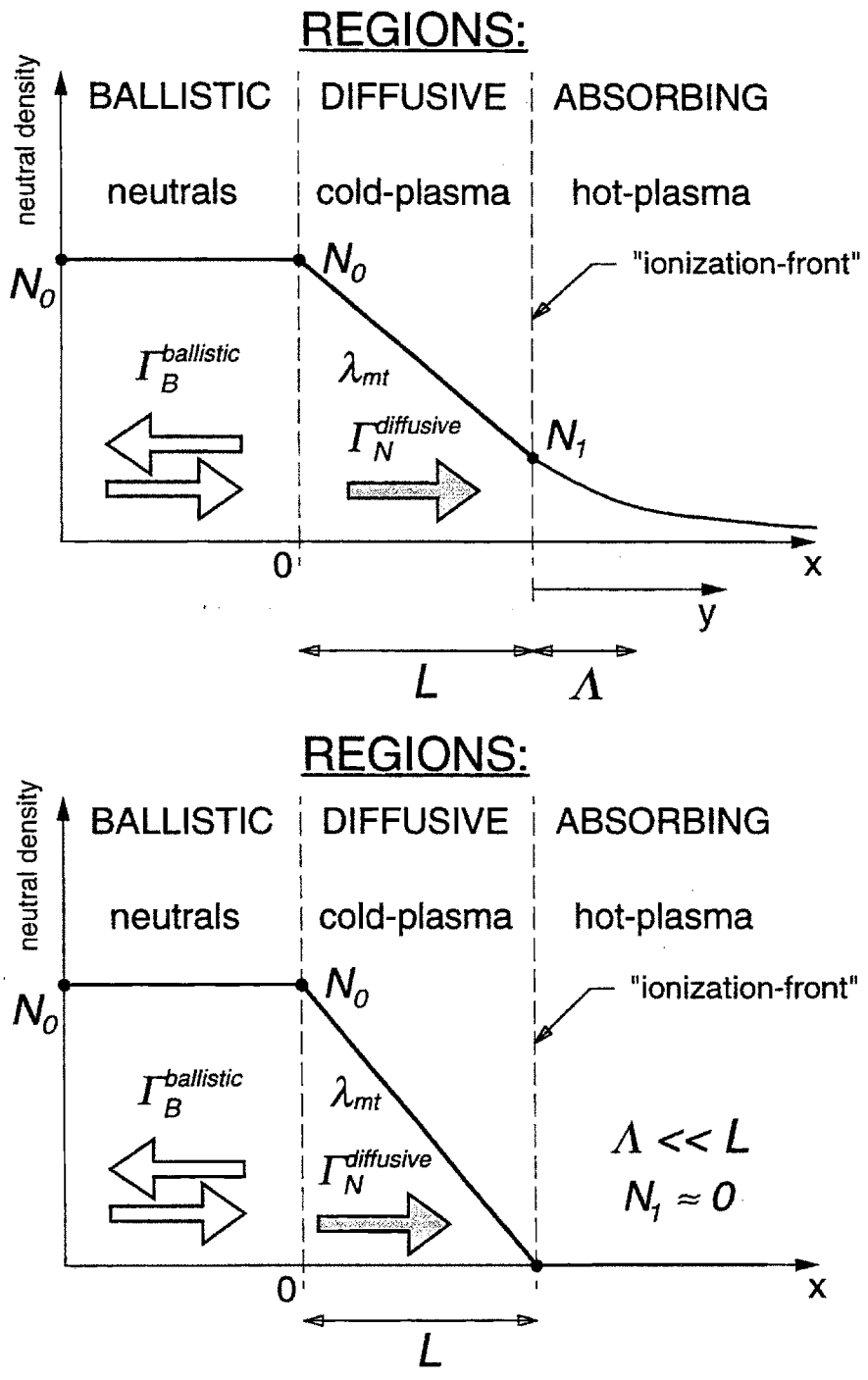

Fig. 5-12: Approximate (top) and a very approximate (bottom) analytic solutions of the neutral transport problem across plasma regions with different characteristics..

The "absorbing" region extends behind the "ionization front" and encompasses hot plasma where $\lambda_{mt} \approx \lambda_{ion}$, i.e., where ionizations become important. The T ≈6 eV isotherm is also often referred to as a "detachment front". In the slab geometry with constant plasma conditions the neutral diffusion equation (Eq. 5.20) simplifies to:

$$\frac{d^2}{dy^2} N - \frac{N}{\Lambda^2} = 0 \tag{5.21}$$

where for simplicity we have changed the coordinate system: y = x - L;
and we have defined a new characteristic transport length - Λ, that by analogy with a neutron transport theory will be referred to as the "absorption length":

$$\Lambda^2 = \lambda_{ion} \lambda_{mt} / 2 \tag{5.22}$$

The general solution to Eq. 5.21 is a sum of rising and decaying exponential. Upon applying the boundary conditions of the form:

$$\begin{cases} N = N_1 & \text{for} \quad y = 0 \\ N < \infty & \text{for} \quad y = \infty \end{cases} \tag{5.23}$$

the solution becomes:

$$N = N_1 e^{-y/\Lambda} \tag{5.24}$$

where:

N_1 - is the neutral density at the "ionization front" (unknown at present).

The matching condition (density and flux) at the ionization front allows us to write the full solution for both regions:

$$\begin{cases} N = N_0\left(1-\dfrac{x}{\Lambda+L}\right) & \text{for} \quad 0<x<L \\ N = N_0\dfrac{\Lambda}{\Lambda+L}e^{-y/\Lambda} & \text{for} \quad y=x-L>0 \end{cases} \tag{5.25}$$

Fig. 5-12 (top panel) shows this neutral density dependence.

In the limit of a very large diffusive zone compared with the characteristic absorption length:

$$\Lambda / L \ll 1 \tag{5.26}$$

the density at the ionization front $N_I \to 0$ and Eq. 5.25 simplifies to:

$$\begin{cases} N = N_0\left(1-\dfrac{x}{L}\right) & \text{for} \quad 0<x<L \\ N = 0 & \text{for} \quad x>L \end{cases} \tag{5.27}$$

The bottom panel of Fig. 5-12 illustrates this "very approximate" solution.

The flux of neutrals lost from the ballistic region is approximately given by the diffusive flux across the diffusive zone. For convenience we normalize the diffusive flux to the ballistic flux, which is known in the experiment:

$$\frac{\Gamma_N}{\Gamma_B} = \frac{-D_N \nabla N}{\frac{1}{4}\cdot v_0 N} \tag{5.28}$$

Recalling the definition of the diffusion coefficient (Eq. D.8) and using the solution from Eq. 5.25 we obtain the expression describing the reduction of the neutral loss from the pure free-flight escape by the diffusion process:

$$\frac{\Gamma_N}{\Gamma_B} = 2\frac{\lambda_{mt}}{L+\Lambda} \tag{5.29}$$

In the limit of a thick diffusive path compared with the absorption length (Eq. 5.26) the above equation simplifies to (to within the factor of 2):

$$\Gamma_N/\Gamma_B \cong \lambda_{mt}/L \tag{5.30}$$

This simple, yet important expression has been initially proposed by Krasheninnikov [115] to explain the reduction of neutral particle loss from a divertor plenum in the detached plasma state.

We define an albedo (A) as the inverse of the ratio of the flux incident on a surface (j_+) to the return flux (j_-):

$$A = j_-/j_+ \tag{5.31}$$

A standard neutron transport textbook (see for example Mehreblian and Holmes [116]) provides an albedo expression in terms of the diffusive and ballistic fluxes:

$$A = \frac{1-\frac{1}{2}\Gamma_N/\Gamma_B}{1+\frac{1}{2}\Gamma_N/\Gamma_B} \tag{5.32}$$

This expression has been successfully used for neutral transport modeling in tokamaks by Stacey and Mandrekas [117] and is subsequently adopted here to describe the scattering of neutrals off the divertor plasma.

5.5.3 Numerical solution and neutral escape probability

The approximate analytic solution of the neutral diffusion equation presented in the previous subsection (Eq. 5.24) is not sufficient to interpret the experimental data. Because of spatially varying plasma conditions Eq. 5.20 has to be solved numerically. Eq. 5.20 is an example of a Sturm-Liouville problem. A standard

boundary-problem matrix-inversion technique proved unsuccessful due to several orders of magnitude difference at the two ends of the solution and a resulting significant loss of numerical accuracy. Instead we use a "forward-marching" technique, where the solution, approximated everywhere locally by Eq. 5.24, is propagated along the modeling chord of interest. This solving-technique is possible here because of absence of volumetric sources (recall that the neutrals born on the target are treated separately), which causes the rising exponential term to vanish in the general solution to Eq. 5.20.

Figs. 5-13 and 5-14 (bottom plots) illustrate the neutral density profile along the modeling chord #9 (normalized to the PFZ-reservoir density) obtained using the marching technique for a representative attached- and detached-divertor discharges respectively. The top plots on both figures show, as a reference, the characteristic transport lengths.

The albedo is calculated from the neutral density gradient using Eqs. 5.32 and 5.28. In a real experiment there is no sharp boundary between the ballistic and diffusive regions: the change in plasma parameters occurs gradually. Following our earlier discussion in Section 5.3, the transition from ballistic to diffusive transport occurs at $x > \lambda_{mt}$. Therefore the plasma albedo is evaluated at a distance equal to λ_{mt}, which varies with plasma conditions, as indicated by a vertical line on Figs. 5-13 and 5-14.

When comparing the two representative discharges it is clearly seen that the region of $\lambda mt \ll \lambda ion$ (top plots on Figs. 5-13 and 5-14) extends much deeper into the plasma in the detached discharge. Upon recalling the simple analytic scaling (Eq. 5.30) it comes as no surprise that the albedo is much higher for the detached shot

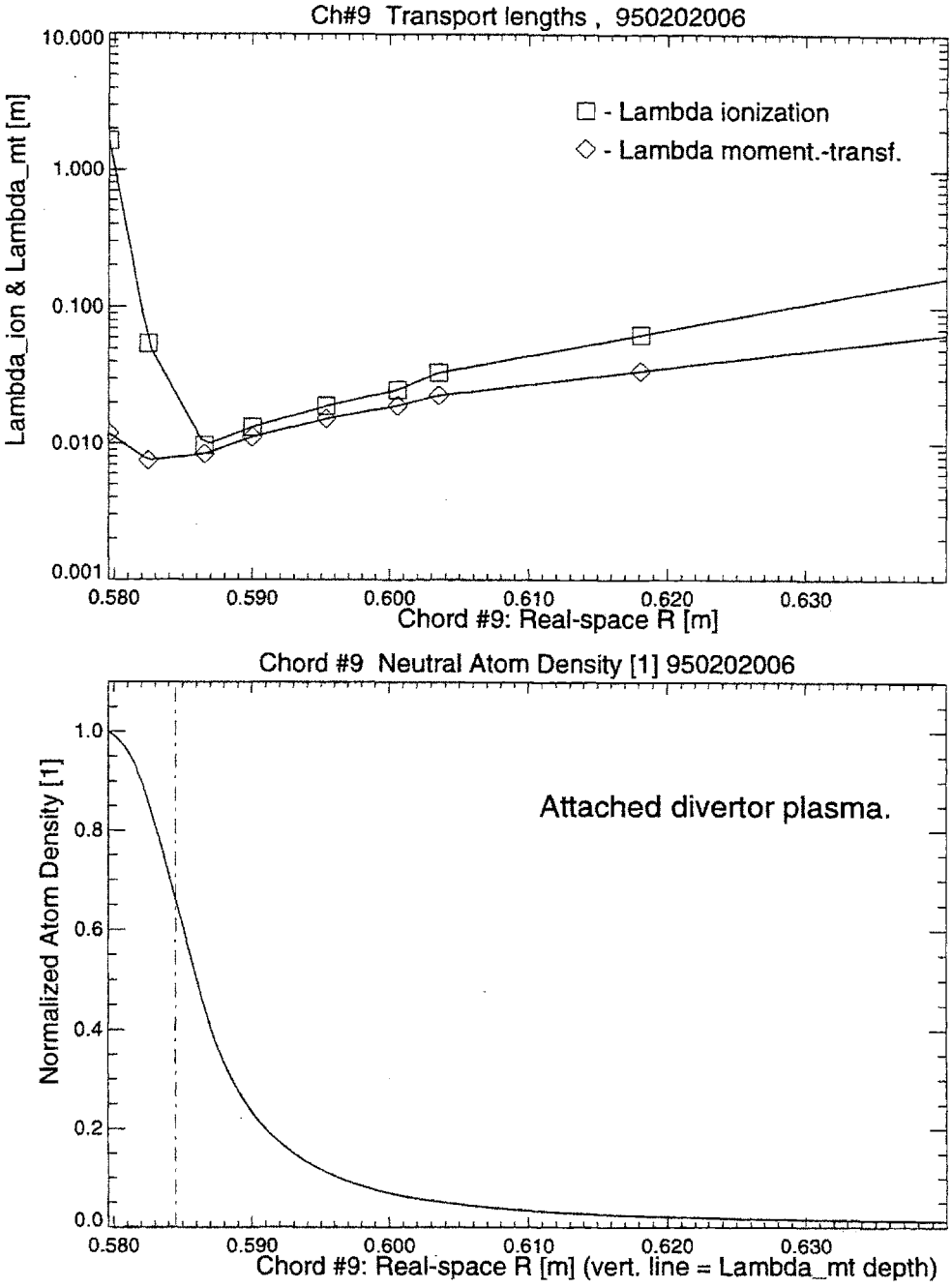

Fig. 5-13: Diffusive neutral transport calculation for a representative attached divertor discharge. The top plot shows ionization and momentum-transfer mean-free-paths, the bottom, a normalized neutral atom density. The data are plotted as a function of the real space R-coordinate of the modeling chord #9. Vertical line denotes the path length equal to the one momentum-transfer mean-free-path, where the albedo is calculated.

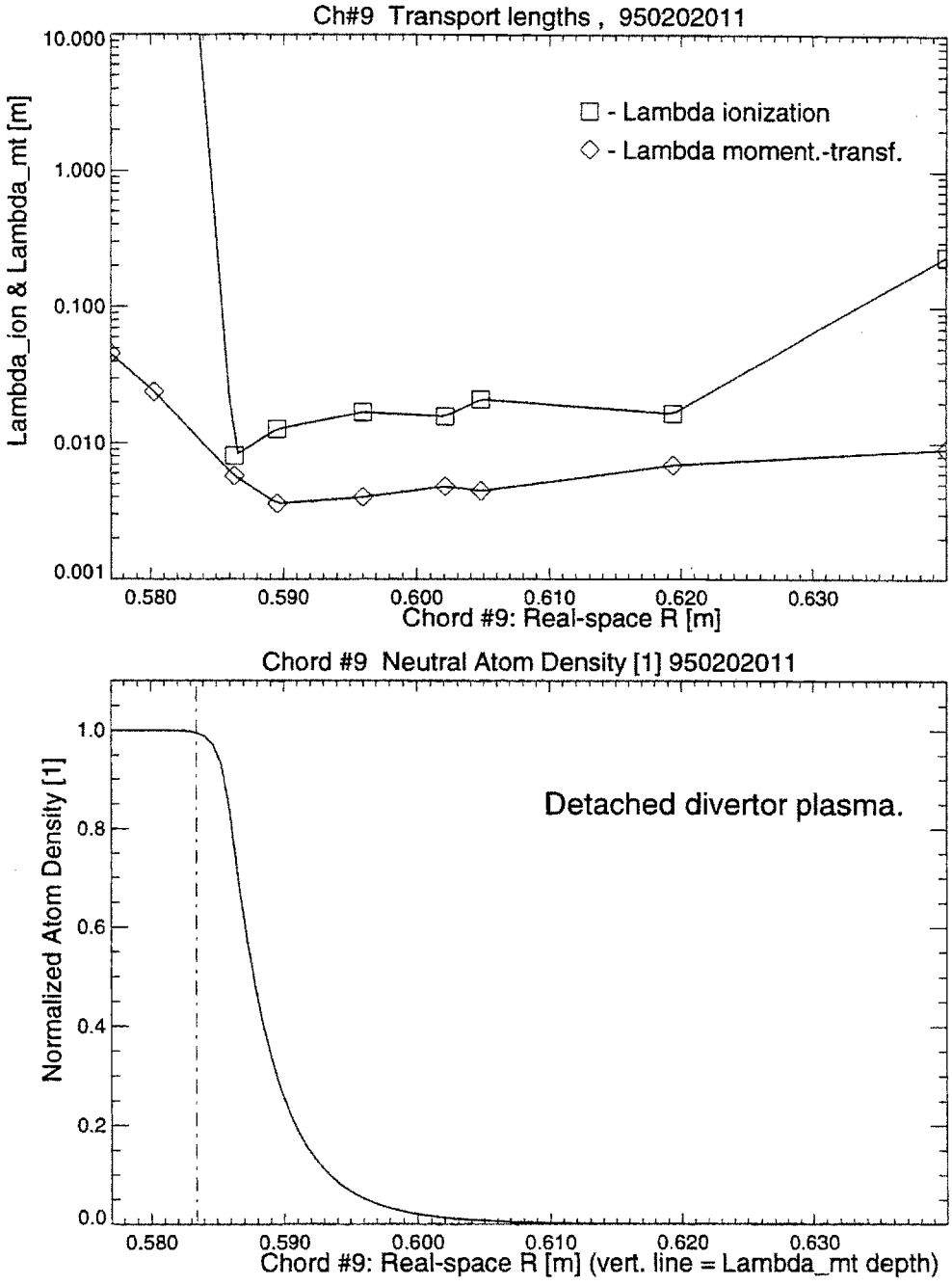

Fig. 5-14: Diffusive neutral transport calculation for a representative detached divertor discharge, presented in the fashion of the previous figure. Neutral atom density initially decreases less strongly leading to a larger albedo in comparison with a hot-attached divertor discharge.

where the "diffusive" region is much thicker. This overall trend is visible in Table 5-4 where the results for all 5 discharges of interest and two diffusive-transport chords (#9 and #10) are summarized.

A similar procedure should be applied for a diffusive-transport chord extending towards the inner common-flux zone (chord #11). Unfortunately it was not possible to obtain a spatial plasma profile there due to lack of upstream measurements. The only remaining alternative was to assume an in-out symmetry of plasma characteristics in the vicinity of the X-point. Unfortunately the experimental evidence for the common-flux-zone plasma is to the contrary. The private-flux-zone plasma, however, does not exhibit a significant in-out asymmetry. It is feasible that a neutral profile is symmetric (in-out with respect to the X-point) at low a penetration depth but differs significantly at a larger penetration depth. Recall that the plasma albedo to neutrals is calculated only at one λ_{mt} -depth, which rarely extends past the separatrix. Therefore a weighted average of albedo values calculated for chords #9 and #10 is substituted for the unknown albedo of chord #11.

5.5.4 Molecular processes

The analysis summarized above neglects the transport of molecules. Haas [88] has proposed a similar mechanism to the one described here, for reflection of hydrogen molecules at the cold edge plasma through ion-molecule elastic scattering. Haas further argues that the high plasma albedo to the neutral molecules is responsible for the observed (in DIIID and JET tokamaks) ionization source being much smaller than that predicted based on the neutral flux from a neutral pressure measurement.

Clearly in real experiments a combination of atomic and molecular processes occur. Including a more realistic picture of molecular dissociation here would lead to atoms starting their path at a position deeper in the plasma channel, reducing the thickness of the diffusive layer, thus reducing the albedo. However the additional elastic scattering of molecules would result in the total plasma albedo to neutrals being a combination of the molecular and atomic processes.

The hydrogen ion-molecule elastic scattering rate (calculated by Haas) is about an order of magnitude lower then the ion-atom momentum-transfer rate (dominated by charge-exchange collisions; see Appendix B) across the energy range of interest (0.1 -30 eV). Hence a room-temperature molecule has a momentum-transfer mean-free-path similar to that of a Franck-Condon atom. The interaction with ions, however, leads to heating of molecules and lengthening of their mean-free-path. It is therefore unlikely for the molecular scattering, when included in the calculations, to significantly change the albedo results.

5.6 Flux balance and plasma model discussion

Upon recalling the assumption about the uniformity of neutral conditions along the plasma boundary made earlier (in Section 5.2), the total ballistic flux of neutrals crossing the plasma-fan boundary (Γ_{pfz}^{bal}) can be written as:

$$\Gamma_{pfz}^{bal} = 1/4 \cdot n_{pfz}\, v_{pfz}\, S_{pfz} \tag{5.33}$$

where:

S_{pfz} - is the surface area of the plasma-fan/PFZ-reservoir boundary, i.e., the area of flux surface ρ = -2 mm.

The net flux of neutrals escaping from the PFZ-reservoir (Γ_{pfz}^{esc}) is reduced from this quantity by flux of neutrals returned to the control volume upon interactions with the plasma or the target plate:

$$\Gamma_{pfz}^{esc} = 1/4 \cdot n_{pfz}\, v_{pfz}\, S_{pfz} \cdot (1-A) \tag{5.34}$$

The discussion below focuses on the calculation of the total PFZ-reservoir albedo (A).

5.6.1 Summary of albedo calculations

From the ballistic (Section 5.3) and diffusive (Section 5.5) calculations we are able to calculate the plasma-fan albedo to neutrals escaping from the PFZ-reservoir (A):

$$A = \frac{\int_{S_{pfz}^{plate}} \left(f_{FC}^{i}\right)^2 ds + \int_{S_{pfz}^{throat}} A^i\, ds}{S_{pfz}^{plate} + S_{pfz}^{throat}} \tag{5.35}$$

where:

A^i - is the plasma albedo calculated for an individual modeling chord;

and the integration extends over:

S_{pfz}^{plate} - the surface area of the plasma-fan/PFZ-reservoir boundary in front of the target plates and

S_{pfz}^{throat} - the surface area of the plasma-fan/PFZ-reservoir boundary across the divertor throat.

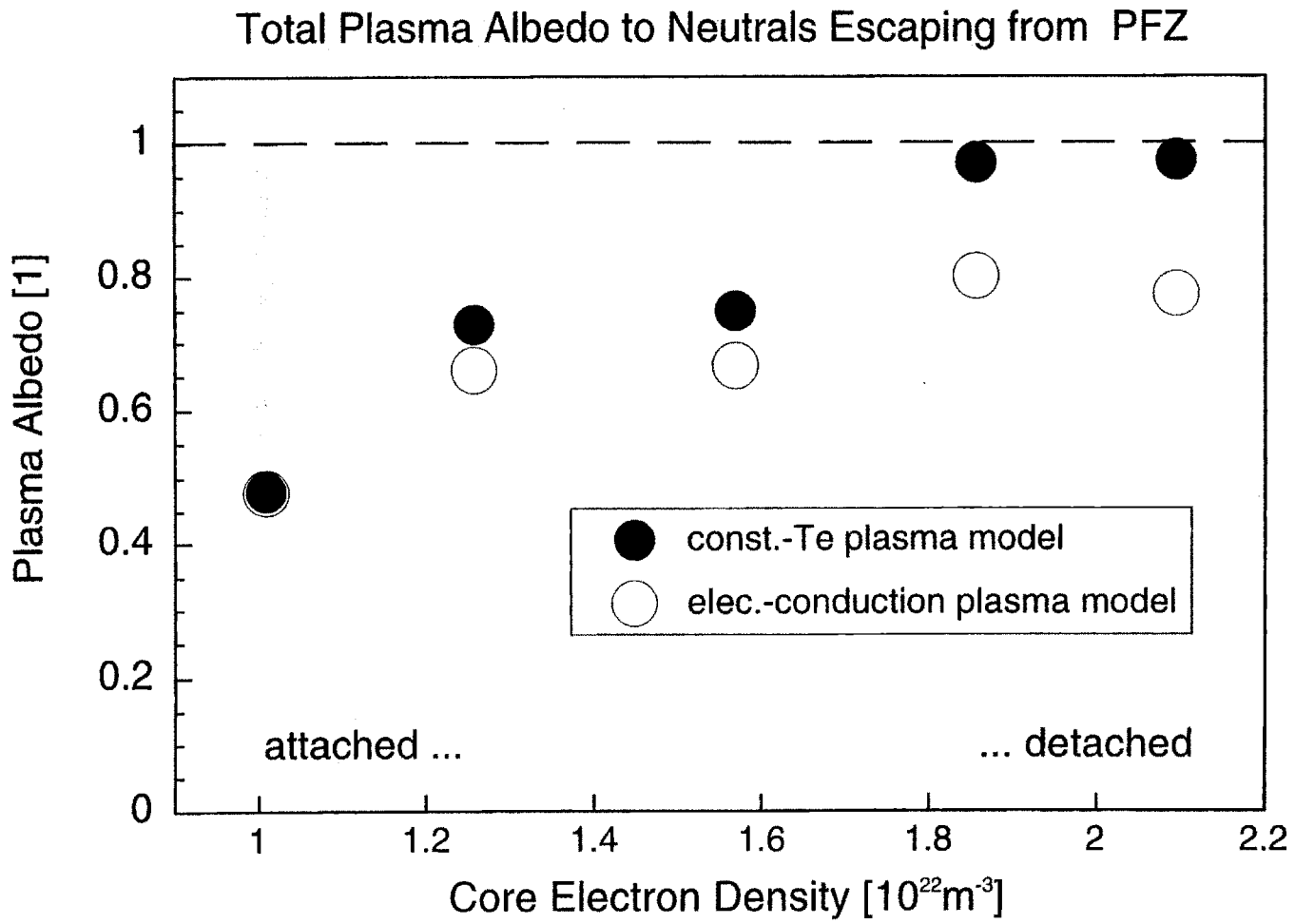

Fig. 5-15: Average plasma albedo (including plate reflection) to neutrals escaping from the PFZ-reservoir. Results obtained with the two plasma models are compared. The albedo reaches a value close to unity in the constant-Te detached-plasma cases.

Plasma ALBEDO to neutrals escaping from the PFZ-reservoir; Calculations summary:

Discharge Number:	6		7		10		11		13	
Ne_bar [1e20/m3]	1.01		1.26		1.57		1.86		2.09	
CHORD#	hot - attached divertor plasma ...				...		... cold - detached divertor plasma			
OUTER PLATE REFLECTION (ballistic neutral transport):										
plasma model used ->	Const.-Te	Elec.-Cond.	Const.-Te	Elec.-Cond.	Const.-Te	Elec.-Cond.	Const.-Te	Elec.-Cond.	Const.-Te	Elec.-Cond.
2	0.966	0.978	0.997	0.997	0.999	1.000	0.999	1.000	1.000	1.000
3	0.774	0.952	0.943	0.831	0.993	0.942	0.997	1.000	1.000	1.000
4	0.535	0.502	0.660	0.312	0.745	0.333	0.995	0.861	1.000	0.877
5	0.327	0.290	0.365	0.194	0.500	0.416	0.993	0.494	1.000	0.401
6	0.256	0.180	0.262	0.112	0.469	0.258	0.991	0.343	1.000	0.133
7	0.206	0.137	0.212	0.086	0.440	0.143	0.987	0.175	0.999	0.095
Weighted AVG. outer plate:	**0.53**	**0.52**	**0.59**	**0.45**	**0.70**	**0.53**	**0.99**	**0.65**	**1.00**	**0.59**
INNER PLATE REFLECTION (ballistic neutral transport):										
plasma model used ->	Elec.-Cond.		Elec.-Cond.		Elec.-Cond.		Elec.-Cond.		Elec.-Cond.	
12	0.870		0.970		0.996		0.998		1.000	
DIVERTOR THROAT PLASMA ALBEDO (diffusive neutral transport):										
plasma model used ->	Elec.-Cond.		Elec.-Cond.		Elec.-Cond.		Elec.-Cond.		Elec.-Cond.	
9	0.266		0.810		0.629		0.890		0.906	
10	0.412		0.870		0.860		0.979		0.971	
11	0.339		0.840		0.745		0.935		0.939	
Total PFZ-reservoir ALBEDO:										
plasma model used ->	Const.-Te	Elec.-Cond.	Const.-Te	Elec.-Cond.	Const.-Te	Elec.-Cond.	Const.-Te	Elec.-Cond.	Const.-Te	Elec.-Cond.
	0.481	***0.478***	***0.729***	***0.660***	***0.750***	***0.667***	***0.971***	***0.803***	***0.975***	***0.776***

Table 5-4: Summary of the albedo to escaping neutrals calculations. The top panel lists "reflection" off the outer target plate calculated with the two plasma models; the second panel, "reflection" off the inner target plate (both plasma models produce the same results); the third panel, albedo of the throat plasma (electron-conduction model only). The last panel summarizes the albedo results in terms of the weighted average over the PFZ-reservoir boundary.

This convenient single-number quantity - A captures the essence of neutral trapping ability of the divertor, including both reflection off the plates and scattering off the plasma.

Fig. 5-15 shows the PFZ-boundary albedo as a function of the core plasma density, while Table 5-4 provides the calculation details. Both the figure and the table compare results of calculations carried out with the two different plasma models (electron-conduction vs. constant-Te). For chords extending across the divertor throat (#9 - #11) only the electron-conduction model is used.

When using the constant-Te model about 50% of neutrals attempting to escape are returned back to the PFZ-reservoir in the attached case. This fraction increases to 98% in the detached case. This mechanism may explain the high neutral pressure sustained in the detached divertor state despite the drop in ion flux striking vertical target plates. The drop in the source term is balanced by improved trapping of neutrals in the divertor volume.

In the case of the electron-conduction model a weaker trend of albedo with the core density is visible in Fig. 5-15. The albedo increases from ~50% to ~80% from attached to detached state respectively. The trend is mostly caused by the increasing albedo to neutrals escaping across the divertor throat. This is strongly balanced by a constant reflectivity for neutrals escaping in the direction of the outer target plate.

5.6.2 Particle flux balance

Table 5-5 summarizes all the quantities contributing to the divertor neutral particle flux balance (Eq. 5-1) as a function of core plasma density. The top panel of the table lists "raw" measured or estimated fluxes:

- vertical target ion flux, as measured by the flush Langmuir probes;
- leakage flux in atomic equivalent, as calculated in Section 5.4;
- kinetic flux of atoms crossing the plasma-fan boundary;
- ratio of source to sink assuming all ballistic atoms from the PFZ are lost.

The factor of twenty disagreement between the raw source and sink fluxes has been already discussed in Chapter 4. The ratio is included here as a reference only.

The remaining two panels in Table 5-5 summarize the calculated results and flux balance obtained using the electron-conduction and constant-Te plasma models. Each of the two panels contain:

- average transmission probability plate→PFZ from Section 5.3;
- source-term atom flux: transmitted recycled ion flux (where the flush probe measurement is divided by a factor of three to give a perpendicular ion flux estimate - this is discussed in detail in the following section);
- plasma albedo to escaping neutrals reported earlier in this section;
- sink-term atom flux: a sum of the neutral PFZ-escape and the leakage fluxes;
- modeled source-to-sink flux ratio.

To simplify the comparison, Fig. 5-16 illustrates the flux balance source-to-sink term ratio for all three cases.

Divertor neutral particle flux balance with different plasma models.

parameter	units	hot/attached divertor ...				... cold/detached divertor
Discharge Number:		**6**	**7**	**10**	**11**	**13**
core electron density	[1e20/m3]	1.01	1.26	1.57	1.86	2.09
Measured/estimated fluxes						
Source: Flush probe BN div. ion flux	[1e22 D+/s]	5.95	15.21	19.90	8.30	5.41
Sink: Leakage (x2)	[1e22 2*D2/s]	0.11	0.50	1.57	2.06	2.39
Sink: PFZ-kinetic	[1e22 D0/s]	3.08	14.33	44.35	55.86	65.35
NO refl. & trans. Source/Sink:	x 20 !	*1.87*	*1.03*	*0.43*	*0.14*	*0.08*
Electron-conduction plasma model:						
plate-> PFZ transmission	[1]	0.907	0.908	0.807	0.709	0.520
Source: Ions->atoms transmitted /3	[1e22 D0/s]	1.80	4.61	5.35	1.96	0.94
PFZ-escape albedo	[1]	*0.478*	*0.660*	*0.667*	*0.803*	*0.776*
Sink: PFZ-neutrals lost + leak	[1e22 D0/s]	1.7	5.4	16.3	13.1	17.0
Modeled Source/Sink:	x 20 !	***1.05***	***0.86***	***0.33***	***0.15***	***0.05***
Constant-Te plasma model:						
plate-> PFZ transmission	[1]	0.907	0.945	0.912	1.000	1.000
Source: Ions->atoms transmitted /3	[1e22 D0/s]	1.80	4.79	6.05	2.77	1.80
PFZ-escape albedo	[1]	*0.481*	*0.729*	*0.750*	*0.971*	*0.975*
Sink: PFZ-neutrals lost + leak	[1e22 D0/s]	1.7	4.4	12.7	3.7	4.0
Modeled Source/Sink:	x 2 !	***1.05***	***1.09***	***0.48***	***0.75***	***0.45***

Table 5-5: Divertor neutral particle flux balance. The top panel reviews measured and estimated fluxes. The middle and the bottom panels summarizes flux balance calculations using the electron-conduction and the constant-Te plasma models respectively. Each of the two bottom panels lists: plate-PFZ transmission probability, transmitted renormalized atom flux (source flux), PFZ-boundary albedo (from the previous table), the total sink flux and the ratio of the source to sink fluxes. The ratio varies by about factor of 20 (across the core density range) for "raw" fluxes and the electron-conduction plasma model but only by a factor of ~2 for the constant-Te plasma model.

The most striking observation is the factor of 20 difference in the flux ratio between the attached and detached cases when the electron-conduction model is used to describe the background plasma. This ratio and its dependence is very similar to the "raw" flux ratio where no neutral transport calculations (reflection nor transmission) had been performed.

The result is dramatically different when the constant-Te model describes the plasma below the divertor throat. The particle flux balance is maintained to at least within 50% across the entire range of core plasma densities. This is an extremely satisfactory result considering the number of simplifying assumptions made throughout the calculations. It seems therefore that despite its simplicity the model contains the key processes contributing to the particle balance. The final result is independent (to within a factor of two) of the leakage flux estimate. The balance requires a constant renormalization of the ion flux measurement, which is discussed in Section 5.7.

The above comparison confirms our earlier presumption (in Section 5.3) about inapplicability of the electron-conduction model to the description of the plasma in front of the target plates upon divertor detachment. The model places the detachment front too deeply in the divertor. If the detachment front was indeed located in the vicinity of probe #3 then ~50% of neutrals heading towards the outer plate should be ionized and thus appear as an ion flux on the plate. But the experimental evidence clearly contradicts it: as shown in Table 5-5, the number of atoms that would be ionized exceeds the number of ions arriving at the target twenty-fold. This conclusion is independent of a potential error in the leakage flux estimate because in the electron-conduction model the loss term is strongly

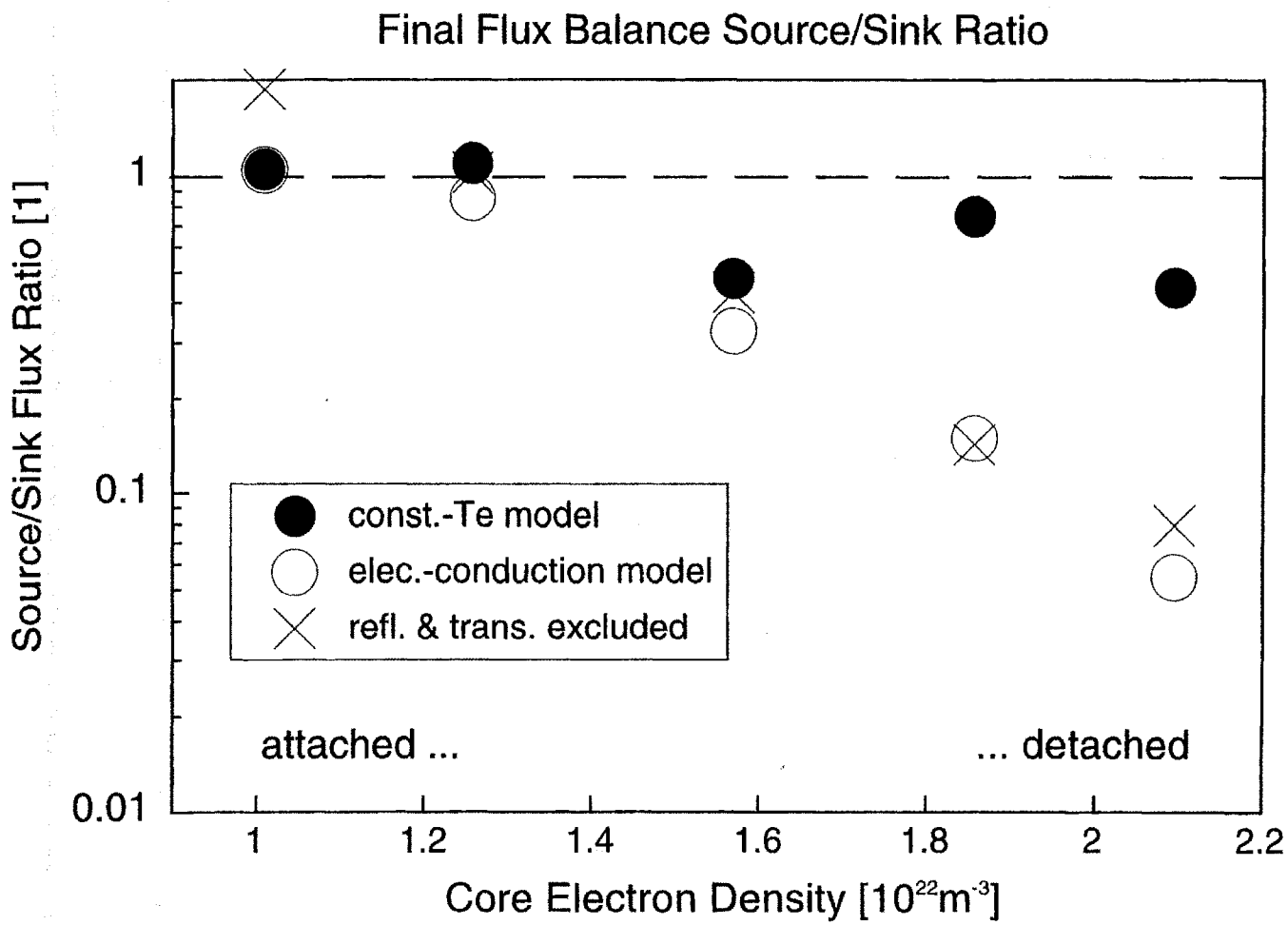

Fig. 5-16: Comparison of the source-to-sink ratio in the divertor neutral particle flux balance when different models are used for plasma description. Flux ratio excluding reflection and transmission is also shown for reference. The constant-Te model leads to an agreement within a factor of two across the density range examined here.

dominated by the net neutral escape flux. The conclusion is also independent of a potential error in the perpendicular ion flux estimate. Even if the flush-probe measurement was directly substituted into the flux balance there would still be a factor of six disagreement between the sink and source terms in detached cases, and a factor of six disagreement between the source and sink terms in attached ones. Substitution of the domed-probe measurement considerably worsens the balance across the entire density range.

It seems therefore that within the validity of the approach proposed here the constant-Te model provides a better description of the plasma below the divertor throat in comparison with the electron-conduction model. Thus in the remaining discussion the electron-conduction model is used only to describe the plasma in the divertor throat, whereas the plasma in front of the vertical target plates is described by the constant-Te model.

A planned Thomson-scattering system for the Alcator C-Mod divertor [32] will enable measurement of plasma parameters near the X-point and may provide the information useful in determining the position of the detachment front, and thus helpful in resolving this important uncertainty impacting the neutral transport analysis.

5.7 Domed- or flush-probe ion flux?

An accurate measure of the total ion flux striking the Alcator C-Mod divertor target plates has yet to be determined. The value of ion saturation current density, normal to the surface ($J^{i}_{\perp sat}$) used in Eq. 5.16 is derived from the flush Langmuir probe measurements. The flush probes were in ion saturation, i.e., negatively

biased with respect to the surrounding surface. However, it has been observed (on Alcator C-Mod and a number of other tokamaks) that such probes do not exhibit a constant (vs. voltage) ion saturation current value [29]. The collected ion current increases with increasingly negative probe bias. This may be partially due to sheath expansion [30]. Since the divertor surface is near the floating potential of the divertor probe characteristics, the above measurement yields an over-estimate of the ion flux to the divertor.

The domed Langmuir probes deliver an estimate of the ion flux parallel to the field lines. Because of their well-defined area, the ion saturation current is independent of voltage with sufficiently negative probe bias. To obtain ion saturation current density normal to the surface ($J^i_{\perp sat}$ in Eq. 5.16), the parallel current is multiplied by the sine of the magnetic field line incidence angle. A typical value of this angle for the outer divertor vertical target is 0.5-1°. It has been observed elsewhere [109, 110] that for grazing angles of incidence (below 3°) the sine law does not apply and cross-field particle transport may become important. Thus we would expect the above procedure to yield an under-estimate of the ion flux.

Table 5-7 lists the perpendicular ion fluxes measured by the two Langmuir probe systems. The total ion flux estimated from the domed probes is a factor of 7-10 times lower than that from the flush probes. Whereas this large discrepancy is the subject of ongoing investigations, the neutral particle flux balance calculations can provide a guidance for future more detailed analysis.

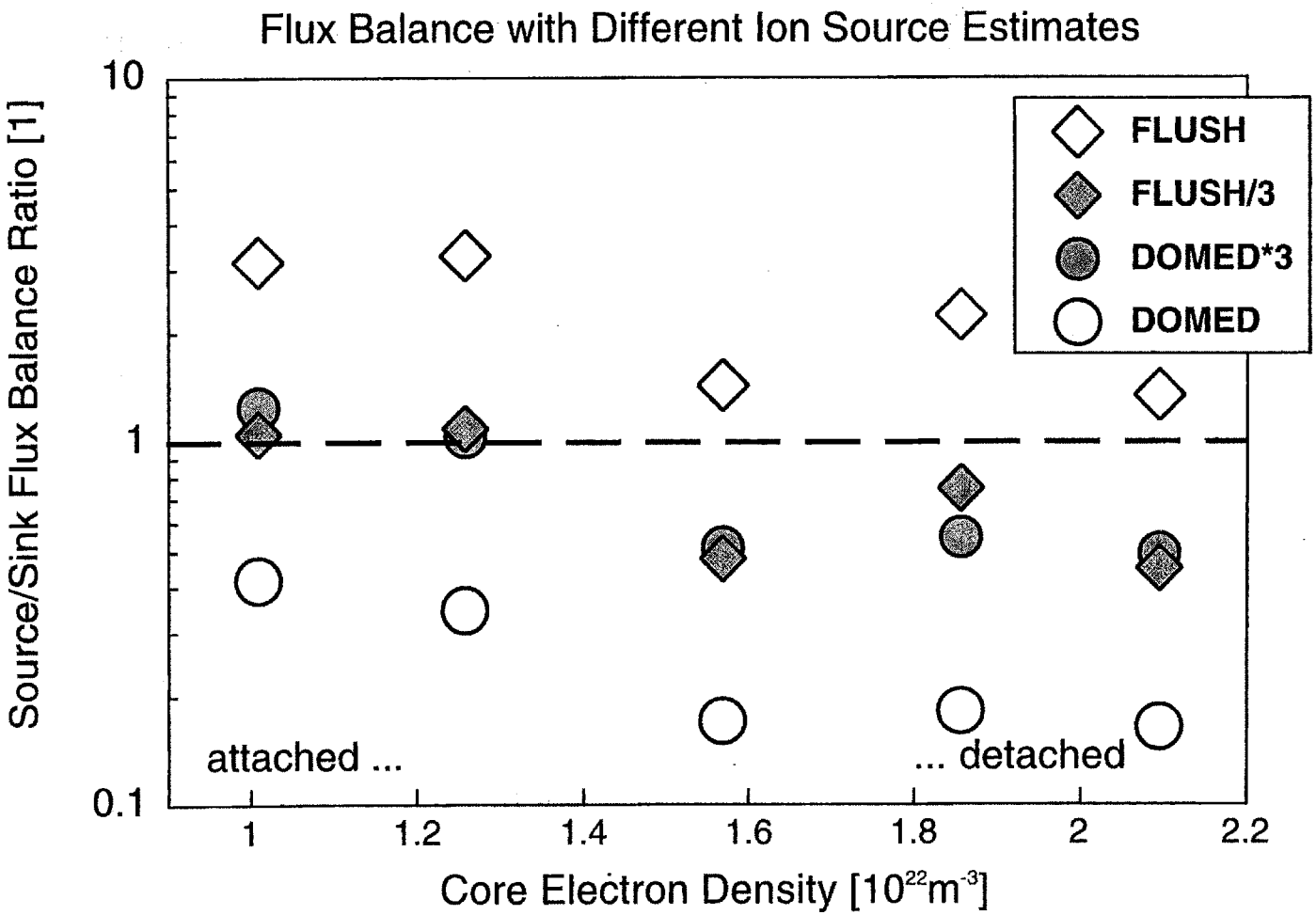

Fig. 5-17: Sensitivity of the divertor particle flux balance to the vertical target plate ion flux estimate. Both the flush and the domed-probe ion flux measurements can satisfy the balance to within a factor of two when multiplied by an appropriate constant.

Impact of Ion Flux assumption on the divertor neutral paricle flux balance.

parameter	units	hot/attached divertor ...				... cold/detached divertor
Discharge Number:		**6**	**7**	**10**	**11**	**13**
core electron density	[1e20/m3]	1.01	1.26	1.57	1.86	2.09
Particle loss:						
Leakage (atom equivalent)	[1e22 2*D2/s]	0.11	0.50	1.57	2.06	2.39
PFZ-kinetic	[1e22 D0/s]	3.08	14.33	44.35	55.86	65.35
PFZ-escape albedo		0.481	0.729	0.750	0.971	0.975
PFZ lost + leak		*1.7*	*4.4*	*12.7*	*3.7*	*4.0*
Biased Flush L-Probe:						
Flush Probe *transmitt	[1e22 D0/s]	5.40	14.38	18.15	8.30	5.41
Source/Sink	[1]	*3.16*	*3.28*	*1.43*	*2.25*	*1.35*
Biased Flush L-Probe/3:						
Flush Probe/3 *transmitt	[1e22 D0/s]	1.80	4.79	6.05	2.77	1.80
Source/Sink	[1]	***1.05***	***1.09***	***0.48***	***0.75***	***0.45***
Domed L-Probe*3:						
Domed Probe*sin(th)*3 *transmitt	[1e22 D0/s]	2.14	4.54	6.50	2.02	1.98
Source/Sink	[1]	***1.25***	***1.04***	***0.51***	***0.55***	***0.49***
Domed L-Probe:						
Domed Probe*sin(th) *transmitt	[1e22 D0/s]	0.71	1.51	2.17	0.67	0.66
Source/Sink	[1]	*0.42*	*0.35*	*0.17*	*0.18*	*0.16*

Table 5-6: Impact of ion flux estimate on the divertor neutral particle flux balance. The top panel reviews particle-loss fluxes. The following panels lists different source flux estimates and source-to-sink ratios using: flush Langmuir probe measurement, flush probe divided by 3, domed Langmuir probe measurement and domed probe multiplied by 3. Both measurements can satisfy the flux balance (Eq. 5.1) upon an appropriate renormalization.

Fig. 5-17 illustrates the sensitivity analysis of the divertor neutral particle flux balance where four different estimates of perpendicular divertor ion flux are used. For completeness Table 5-6 provides numerical details of the calculations. Neither of the two direct measurements satisfy the flux balance equation (Eq. 5.1). However, the neutral particle flux balance is satisfied to within a factor of two (which is within the accuracy of this analysis) when either the flush probe measurement is divided by three or domed-probe measurement is multiplied by three. Note that the required multiplier and divider is constant across the core density range examined and it does not fall below two when other leakage flux estimates are substituted in the calculation.

Kurz, in cooperation with the author, [118] has made an additional attempt to resolved the perpendicular ion flux uncertainty. The H_α tomographic reconstruction yields an emission pattern everywhere in the Alcator C-Mod vessel (shown, for example, on Fig. 5-10). This, combined with the knowledge of plasma temperature and density everywhere, allows the local ionization source to be calculated [37]. A volumetric integration delivers a total ionization source (number of ionization per second) within the entire tokamak plasma. In steady state this quantity should be equal to total number of neutralizations in the tokamak, i.e., the perpendicular ion flux integrated over the entire divertor surface including both horizontal and vertical plates. At least an order of magnitude smaller contribution from recycling on the inner wall and antenna limiters is neglected.

Table 5-7 compares the total ionization source in the tokamak with the perpendicular ion flux measurement (over the entire divertor surface) delivered by the two Langmuir probe systems. The ion flux required to sustain the divertor

Measured ion fluxes compared with ionization source and particle balance.

parameter	units	hot/attached divertor ...				... cold/detached divertor
Discharge Number:		**6**	**7**	**10**	**11**	**13**
core electron density	[1e20/m3]	1.01	1.26	1.57	1.86	2.09
DOMED probe TOT div. ion flux	*[1e22 D+/s]*	*1.5*	*2.8*	*5.1*	*3.1*	*2.8*
Total ionization source (from H_alpha tomography)	[1e22 #/s]	2.3	–	6.3	9.4	–
Ions required to sustain balance (from divertor particle flux balance)	[1e22 D+/s]	3.8	8.2	28.9	13.9	16.2
FLUSH probe TOT div. ion flux	*[1e22 D+/s]*	*12.4*	*26.6*	*40.3*	*26.5*	*20.8*

Table 5-7: Total ion flux striking the divertor. The table compares the flush- and domed-Langmuir probe measurement with the total ionization source (calculatied from the H_α tomography) and the ion flux required to sustained divertor particle flux balance.

natural particle balance is also included as a reference (assuming the constant-Te model). Recall, however, that the neutral flux balance includes the ion flux to the vertical plates only. The fraction of the flux to the vertical-plate (below the divertor "nose" - BN) to the total divertor ion flux can be calculated from the probe measurements. This fraction changes as a function of the core plasma density and associated divertor plasma regimes but is the same for both probe systems. The fraction is subsequently used to translate the neutral-balance vertical-plate ion flux to its total divertor equivalent.

While examining Table 5-7 one has to keep in mind that error bars on ionization source calculations extend by an order of magnitude in either direction. It is intriguing, however, to note that the ionization source result falls in-between the two probe measurement. Similarly the neutral particle flux balance delivers only a rough estimate (no better than a factor of three) of the total ion flux but it also falls in-between the two probe measurement.

While the neutral particle flux balance model is not accurate enough to allow us to draw definite conclusions about the proper estimate of the ion flux, its results are consistent with a value close to a geometric average of the two probe measurements. A more detailed study aimed at resolving the ion flux estimate uncertainty is necessary. In practice a proper measurement of the perpendicular ion flux striking an unbiased divertor surface is required. Recessed Langmuir probes have a potential to deliver such a measurement. At a very shallow angle of incidence a recessed Langmuir probe may be insensitive to the electron current while collecting the ion current. This is due to a significant difference in the Larmor radius for the two species. We recommend installation of this diagnostic in Alcator C-Mod divertor.

5.8 Model summary

The neutral particle flux balance model proposed in this chapter allowed us to obtain a factor of two agreement in the divertor particle flux balance across a range of plasma parameters spanning the sheath-limited, high-recycling, and detached divertor regimes. The findings of the analysis can be summarized as follows:

1) The "mystery" of high divertor pressure in the detached state is explained by an increase in divertor plasma albedo to escaping neutrals. Thus the decreasing source term (ion flux) is balanced by improved confinement of neutrals in the divertor volume.

2) Neutral escape through the leaks in the divertor structure becomes a significant loss channel at high divertor pressures.

In order to obtain a better accuracy the analysis presented in this chapter should be extended in future to include a more complete set of atomic processes and a more realistic geometry.

Chapter 6

Geometry Effects

Alcator C-Mod, through its plasma shaping capability and flexible divertor configuration, presents a unique opportunity to investigate the impact of various divertor geometries on plasma characteristics and neutral dynamics.

This chapter summarizes the dependence of neutral pressure on plasma and divertor geometry. Experimental observations of the effect of the ion B×∇B-drift direction, strike-point position, and flat-plate divertor geometry on neutral pressures are reported. As the flux balance model proposed in Chapter 5, is not well suited to analyzing geometry dependence, only a qualitative interpretation of the observed phenomena is provided in this chapter.

6.1 Ion B×∇B-drift direction

Results from other tokamaks [119] indicate a strong dependence of divertor plasma parameters (especially an in/out asymmetry) on the ion B×∇B-drift direction. If the toroidal field vector is directed clockwise, when seen from the top, the ions drift downwards [120]. In Alcator C-Mod this is the "normal" operating mode. For a series of experiments the direction of toroidal field has been reversed to investigate the effect of the ion B×∇B-drift direction. This change, however,

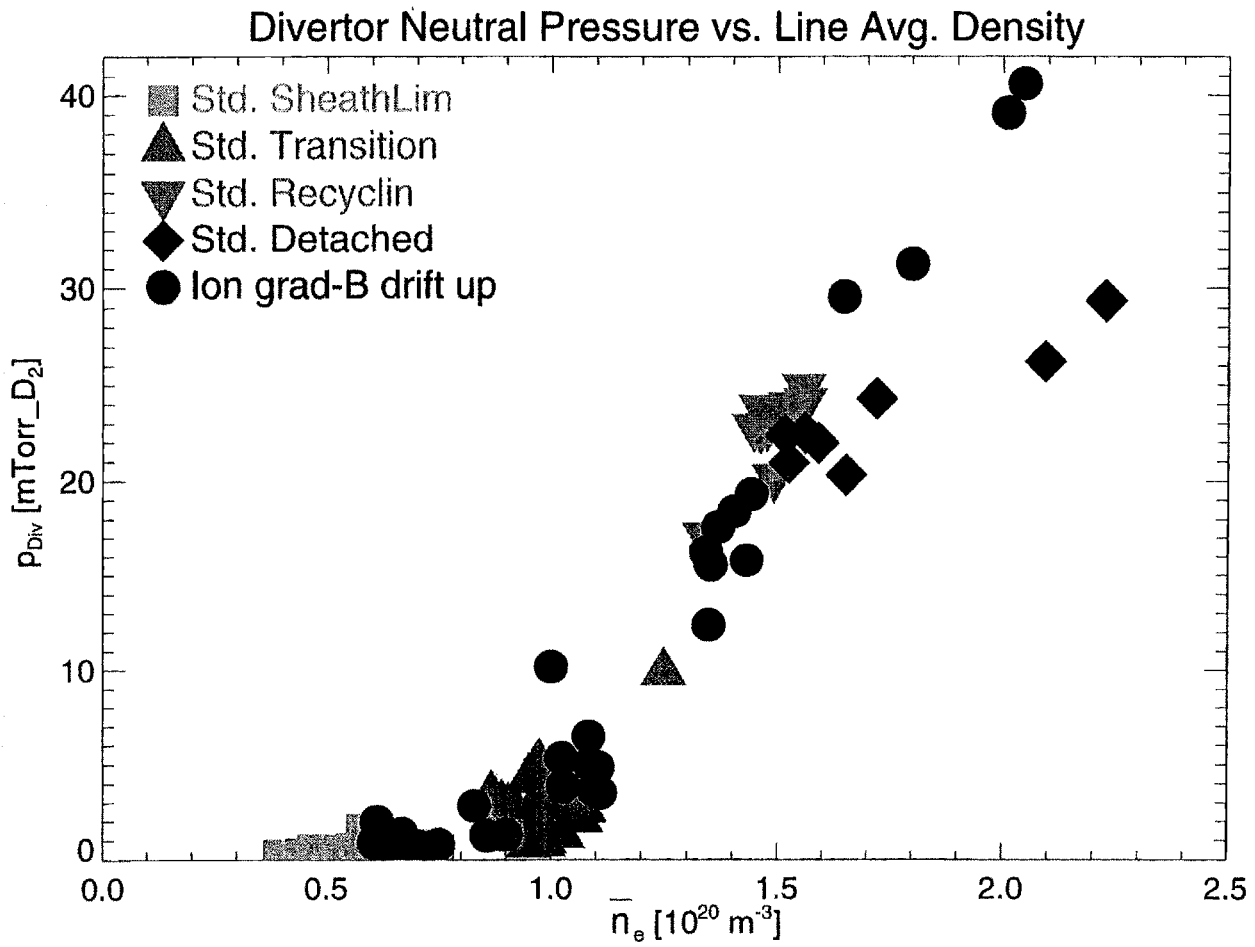

Fig. 6-1: Comparison of the divertor neutral pressure for the two ion B×∇B drift directions. The standard (towards the bottom divertor) drift direction data-set is the one discussed in Chapter 4 with the edge-plasma regimes marked with different symbols.

required also a reversal of plasma current direction to preserve the helicity dictated by the divertor hardware design [21].

Figs. 6-1 and 6-2 compare the neutral pressure results obtained with the two different ion drift directions. The set of discharges described in Chapter 4 serves as a "standard" direction reference. Fig. 6-1 plots the divertor neutral pressure and Fig. 6-2, the divertor-to-midplane compression ratio versus the line average core density. The edge plasma regimes defined in Chapter 4 are identified with different symbols for the reference (ion drift down) data set.

An immediate observation is that the difference between the two data sets is small. Except for the detached divertor regime the pressures are almost identical (including the midplane pressure - not shown). A slightly higher divertor pressure in the detached regime may be potentially due to a different detachment sequence. With the ion drift down, the plasma first detaches from the inner target, while with the ion drift up, it first detaches from the outer target [121]. The compression ratio (Fig. 6-2) is almost identical, within experimental error, for the two ion drift directions across the entire core plasma density range and all edge plasma regimes.

Hutchinson reports [122] a large in/out asymmetry, at moderate core densities $\bar{n}_e < 1 \cdot 10^{20}$ m^{-3}, of the divertor plasma parameters, which reverses with the ion drift direction. With the ion drift down the plasma density (and ion flux) is higher at the outer divertor target, while with the drift up the density (and flux) is higher at the inner target. Because the divertor-particle-reservoir is fueled by recycling from both targets the neutral pressure there is insensitive to any in/out divertor asymmetry. As a result the pressure follows the same scaling in both cases.

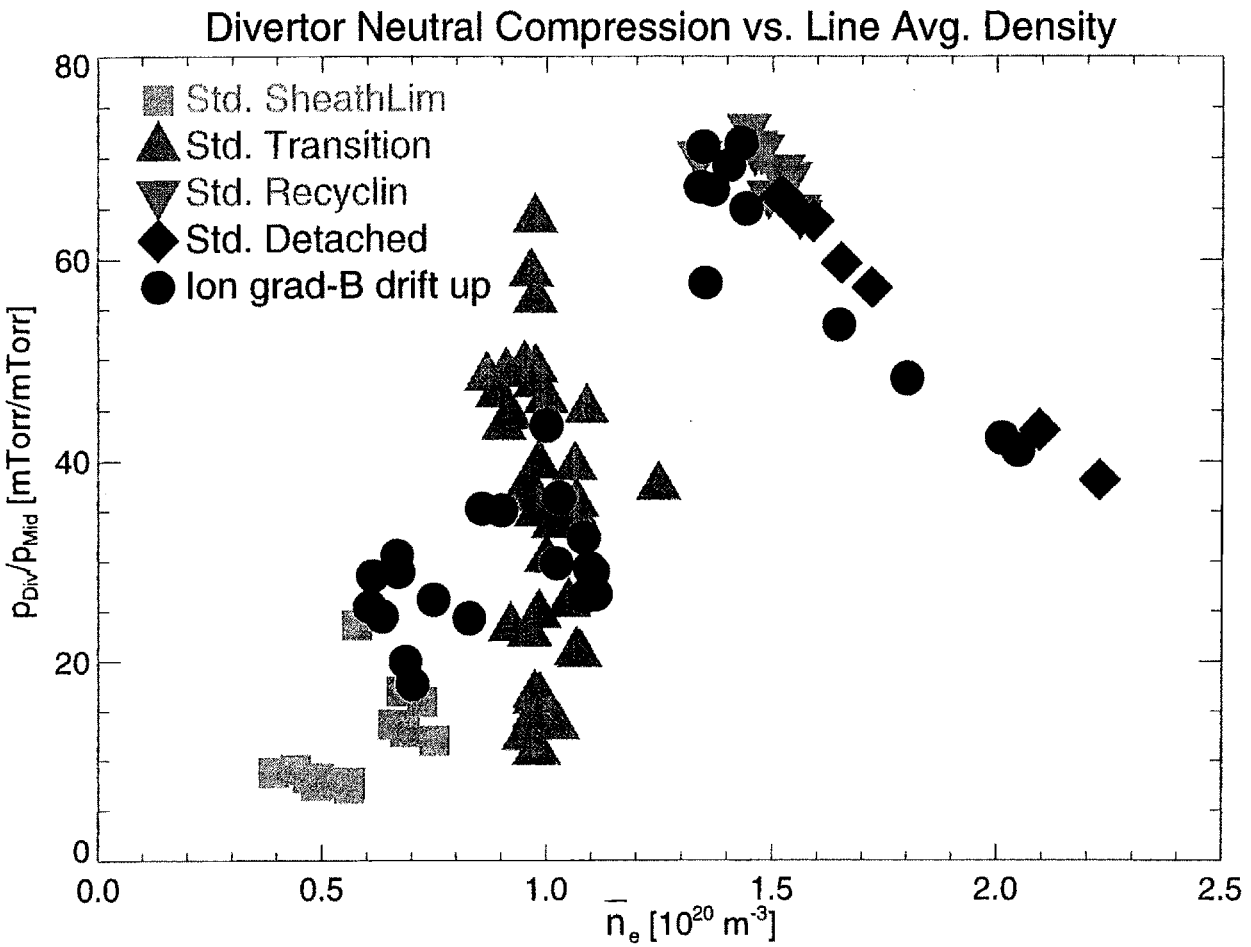

Fig. 6-2: Comparison of the divertor-to-midplane neutral compression ratio for the two ion B×∇B drift directions. The same data as on the previous figure are plotted here. There are no significant differences between the two drift-direction data sets.

At high core densities ($\bar{n}_e \approx 2 \cdot 10^{20}$ m^{-3}) the ion B×∇B-drift direction does not affect the divertor plasma parameters (except for the detachment sequence mentioned earlier), nor the neutral density there, as expressed by the neutral compression ratio (Fig. 6-2).

6.2 Strike-point location

One of the important variables impacting neutral particle dynamics is the divertor plasma geometry, specifically the position of the strike-point, which determines the location of the dominant neutral particle source in the divertor. Reports from other tokamaks indicate a strong dependence of the divertor neutral pressure on the strike-point position [123, 124]. This dependence was investigated in Alcator C-Mod by comparing a series of discharges differing only in the strike-point location.

Fig. 6-3 shows the geometry of three representative discharges used in the following analysis. The magnetic geometry is reconstructed using the MFIL magnetic reconstruction code [125]. The right-hand panel of Fig. 6-3 illustrates the slot divertor configuration where the outer divertor plasma channel is directed towards the very bottom plate of the divertor. The middle panel shows the standard divertor geometry already described in previous chapters where the strike-point is located on the vertical portion of the target plate. The last panel shows the flat plate divertor geometry where the strike-point is located above the divertor throat (above the nose) and most of the recycling occurs on the near horizontal portion of the target plate. The divertor geometry is classified here based on the outer strike point position.

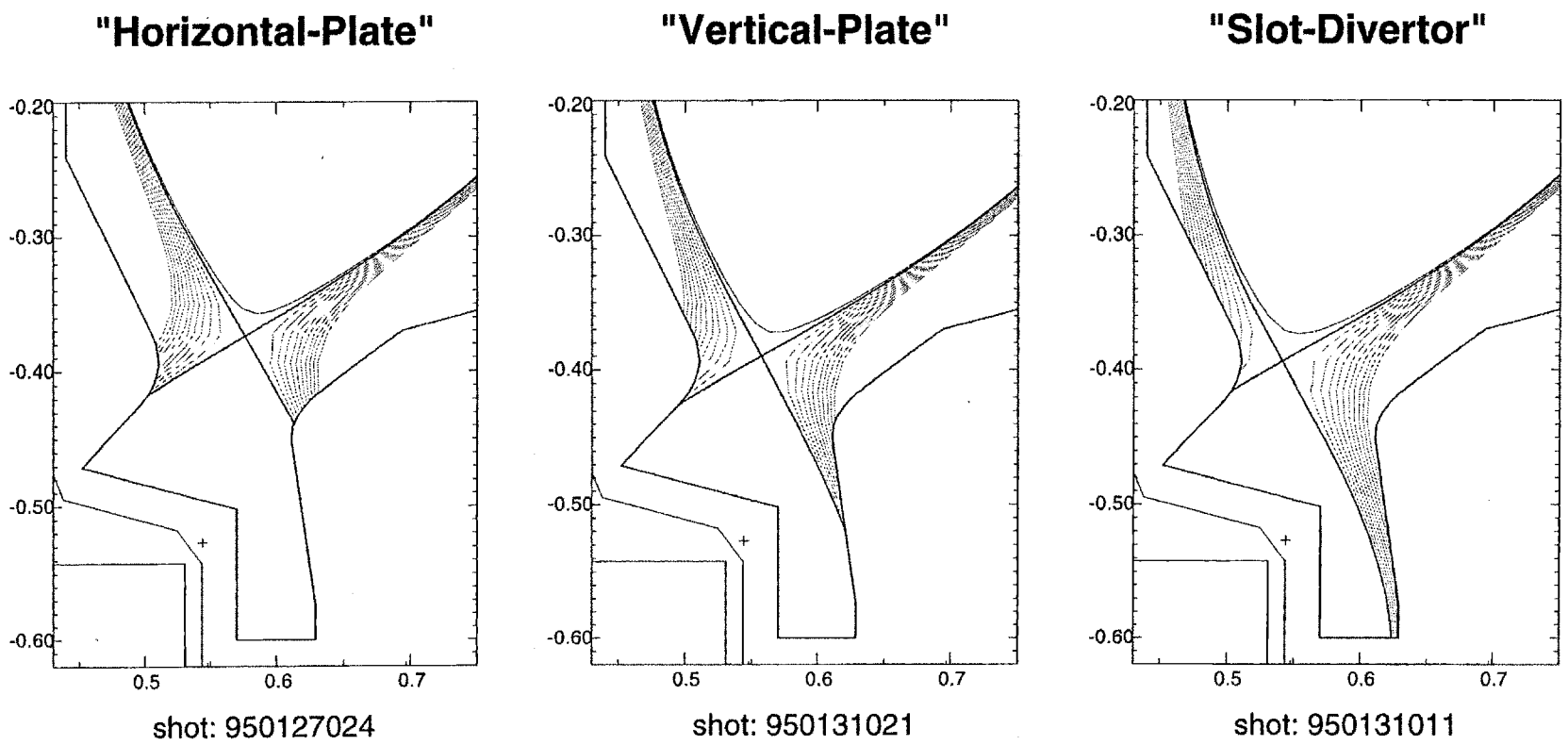

Fig. 6-3: Strike-point positions and corresponding divertor configurations analyzed in this section. The magnetic geometry is reconstructed with the MFIL code. The details of the divertor structure, specifically of the gas-box entrance, are omitted for picture clarity.

As shown in Chapters 4 and 5 the neutral pressure and compression depend strongly on the edge plasma characteristics, in fact much more strongly than on the divertor geometry. Currently only a limited data sample is available where all relevant plasma parameters are held constant except for divertor geometry. The steady state requirement further limits data sample size. Nevertheless the sample illustrates interesting trends, which are also confirmed by non steady-state data.

Fig. 6-4 and Fig. 6-5 present the dependence of the divertor neutral pressure, and of the divertor-to-midplane compression ratio, on the outer strike-point position. The data were recorded during steady-state, I_p =800 kA discharges with $\bar{n}_e \approx 1.8 \cdot 10^{20}$ m^{-3}. The coordinate used on the abscissa is not the strike-point position itself but the distance, ρ, between the outer strike point and the entrance to the gas-box (where the divertor pressure is measured) mapped to the tokamak midplane.

Variation in the strike-point position does not lead to any drastic changes in neutral pressure. The difference between the maximum and the minimum divertor pressures on Fig. 6-4 does not exceed a factor of two. Both the divertor pressure and compression ratio are maximized when the outer strike-point is positioned just above the gas-box entrance, at the bottom of the vertical target plate.

As soon as the strike-point moves off of the vertical plate to the divertor floor to form a slot divertor configuration, the pressure and compression decrease. The pressures measured by the gauge for the positive and negatives ρ values correspond to two different neutral particle reservoirs in the divertor. When ρ is negative the gauge measures the pressure in the private flux zone, whereas when ρ is positive the gauge measures pressure in the common flux zone. Because there

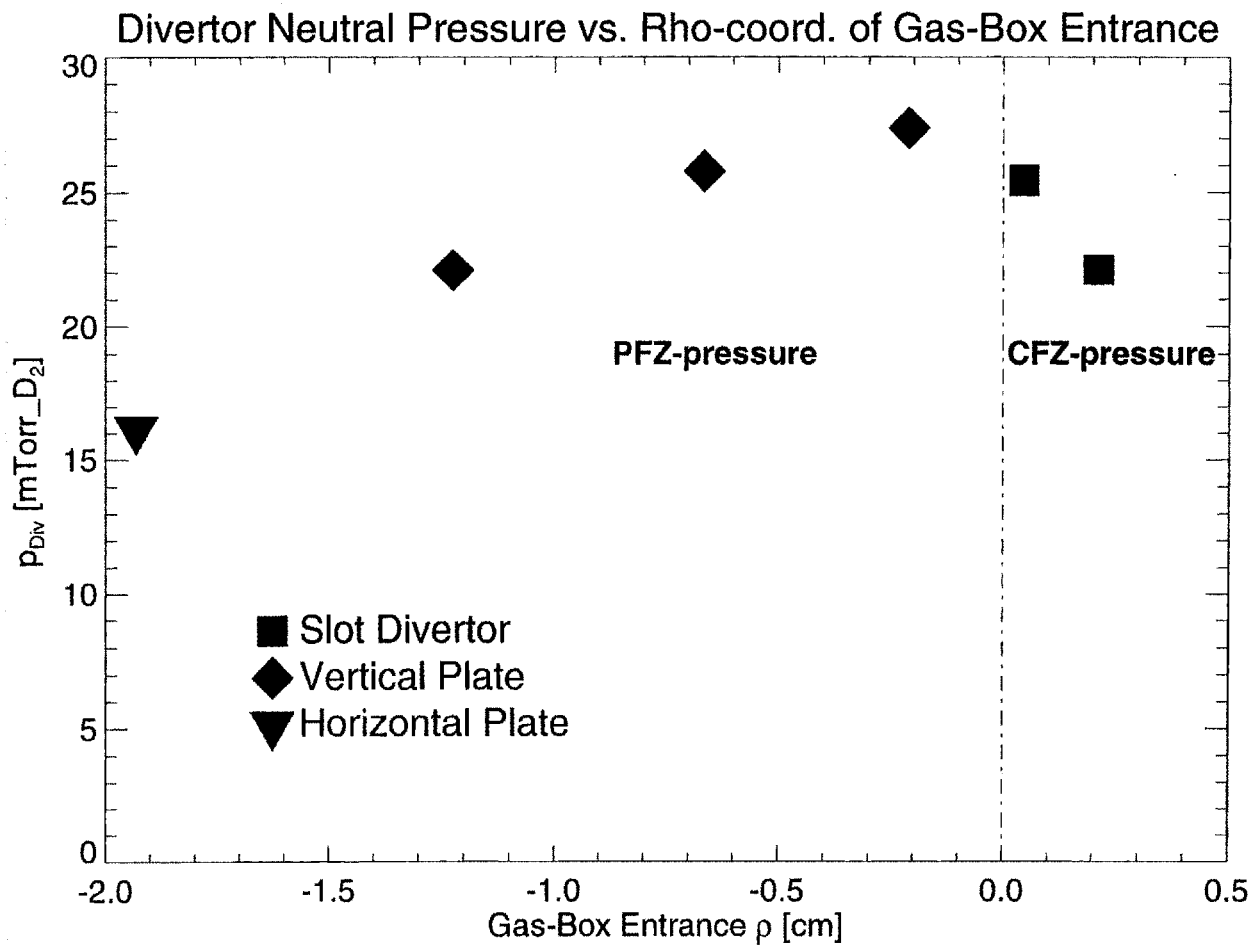

Fig. 6-4: Dependence of the divertor neutral pressure on the strike point position. Data are plotted versus ρ-space distance between the gas-box entrance and the separatrix. Positive and negative ρ values correspond to different neutral particle reservoirs (CFZ and PFZ respectively).

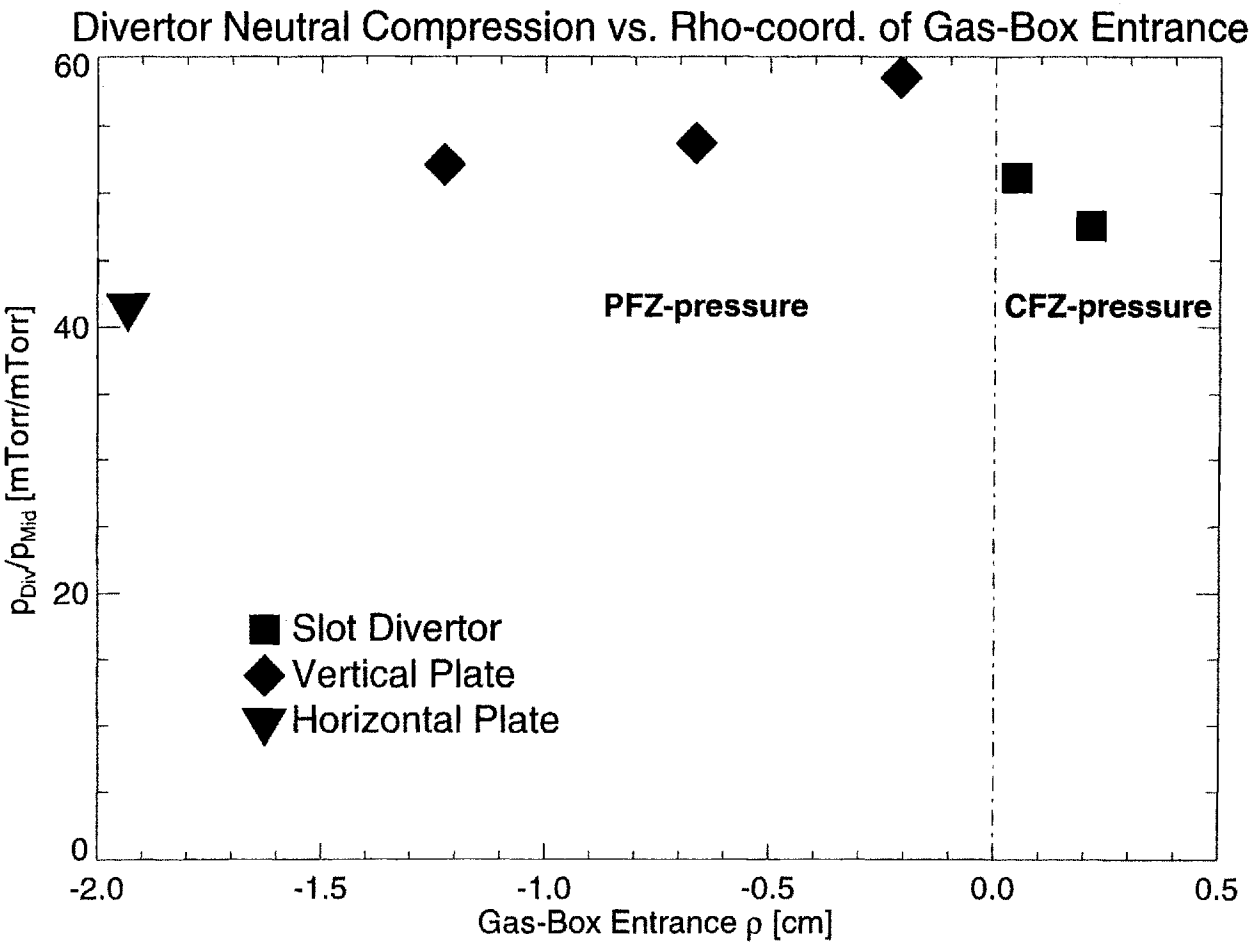

Fig. 6-5: Divertor-to-midplane compression ratio plotted as a function of the ρ-coordinate distance between the gas-box entrance and the strike-point. The same data-set as on the previous figure is shown.

is only one gauge measurement position no information about neutral pressure in the private flux zone of the slot divertor configuration is available. Results from other tokamaks, indicate that the neutral pressure in the common flux zone is lower than the neutral pressure in the private flux zone [78, 126], consistent with the Alcator C-Mod results.

When the strike-point moves up along the vertical plate (increasingly negative value of ρ) the pressure and compression decrease gradually dropping to about 50-60% of their maximum values. The minimum pressure and compression ratio corresponds to the strike-point located above the divertor nose. This flat-plate divertor geometry is analyzed in more detail in the following section.

6.3 Flat-plate divertor

The major difference between a vertical and a horizontal-target divertor is the sign of the poloidal angle with which the separatrix intersects the target plate and resulting particle trajectories leaving the target. Petravic [127] has shown that the two divertor geometry designs lead to very different plasma characteristics near the strike-point. While the impact of the geometry on the divertor plasma has been studied in some detail [128, 101] there are no extensive accounts (to the author's knowledge) of its impact on neutral dynamics.

Fig. 6-6 and Fig. 6-7 show the divertor and the midplane neutral pressure dependence on the line average core density. The attached and detached divertor states are identified with different symbols for the standard geometry reference data set (from Chapter 4). Most of the flat-plate discharges are in the recycling-attached divertor regime. Analysis of Langmuir probe data reveals that

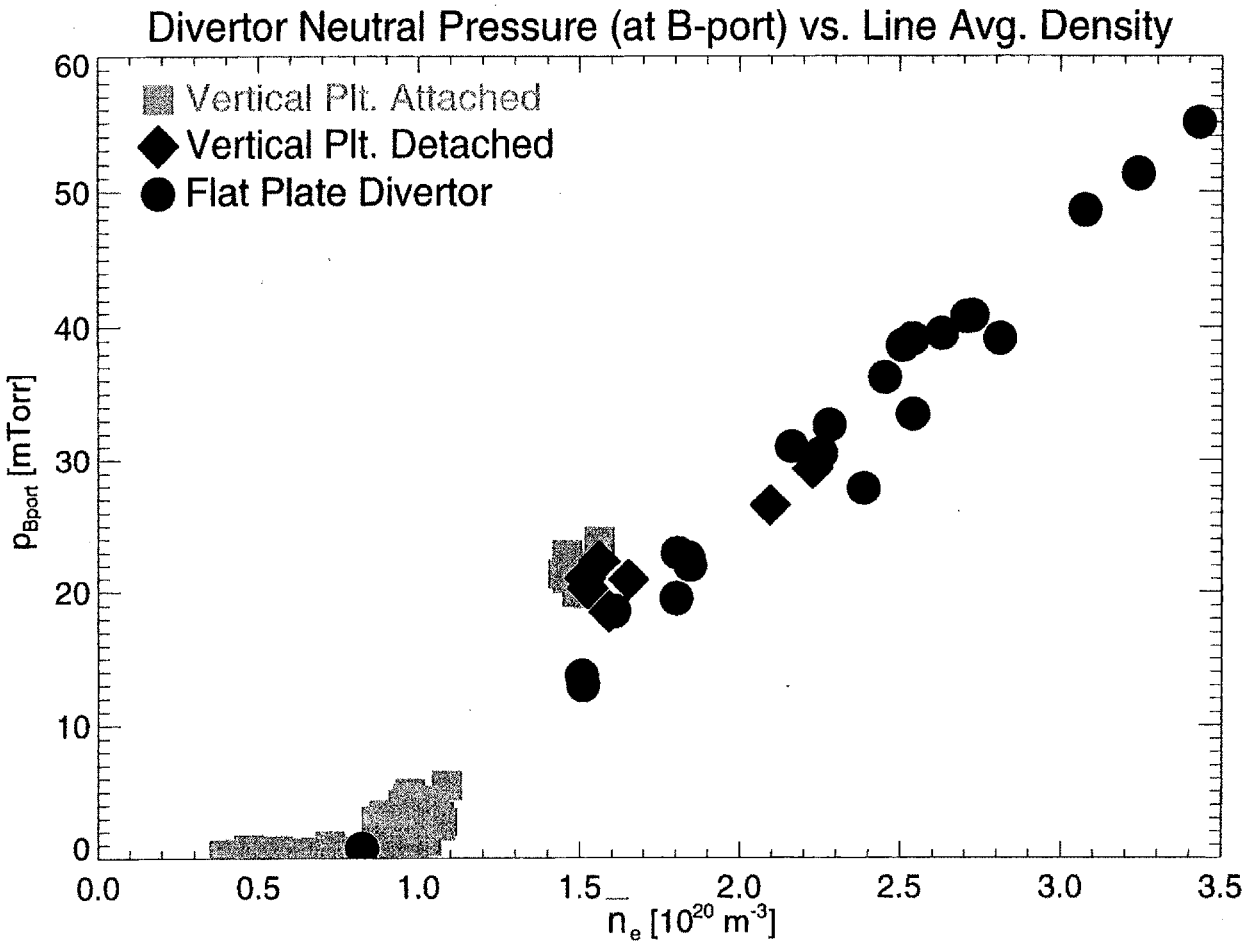

Fig. 6-6: Comparison of the divertor neutral pressure (measured by the B-port capacitance gauge) for the two divertor geometries: flat plate and vertical plate. The vertical plate data-set from Chapter 4 is used as a reference with symbols distinguishing attached (all regimes) and detached divertor discharges.

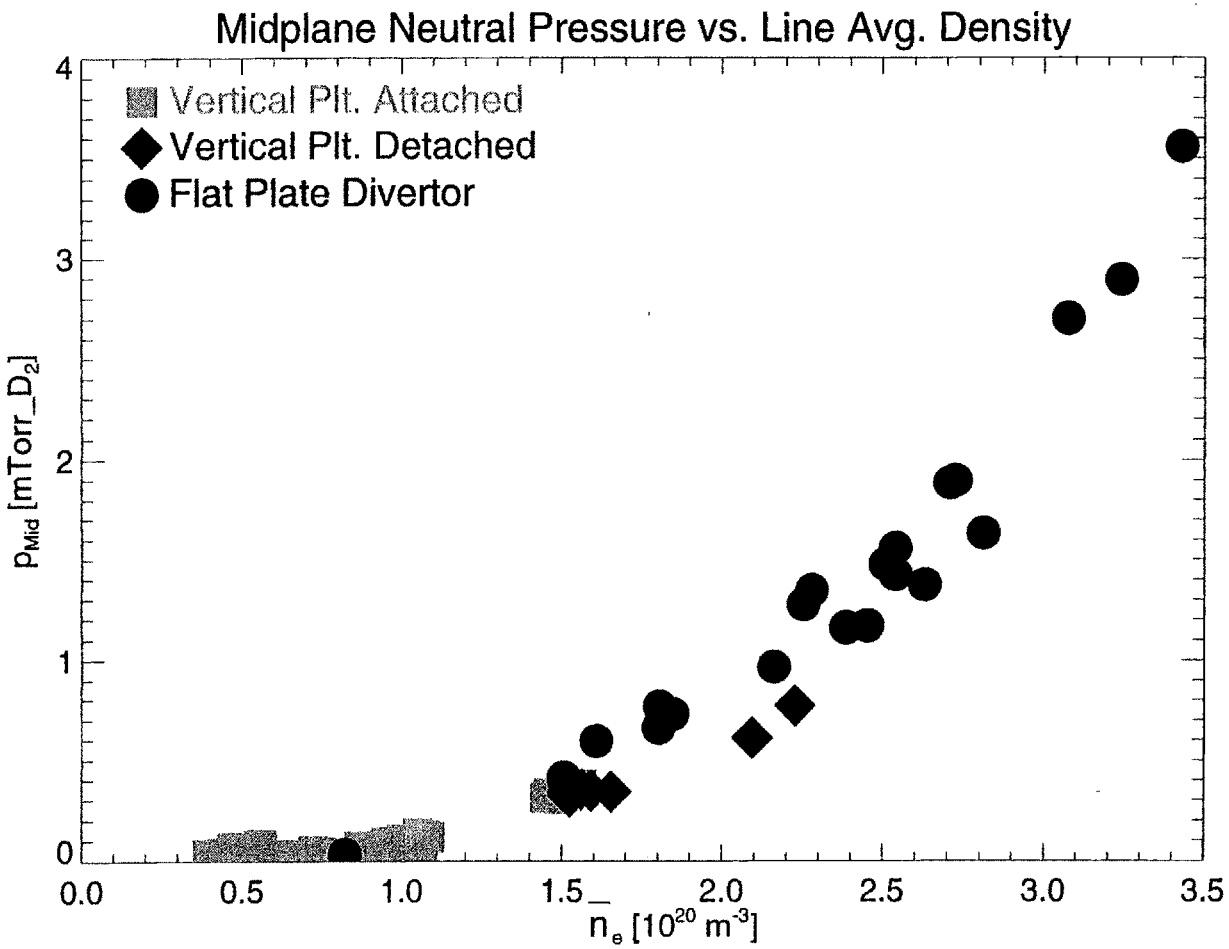

Fig. 6-7: Comparison of the midplane neutral pressure for the vertical- and flat-plate divertor geometries. Data are plotted as a function of the line averaged density.

detachment is much more difficult to obtain than for the vertical plate and starts only at higher core density ($\bar{n}_e \approx 3 \cdot 10^{20}$ m^{-3}) [101]. There are no significant differences in neutral pressure measured for the two different divertor geometries. For the same line averaged density (e.g., $\bar{n}_e \approx 1.5 \cdot 10^{20}$ m^{-3}) the divertor pressure is slightly lower (by ~30%) and the midplane pressure is slightly higher (by ~30%) in the flat-plate divertor cases compared with the vertical-plate ones.

Fig. 6-8 compares the divertor-to-midplane neutral compression ratio for the two geometries of interest. The flat-plate compression ratio is about one half of the maximum compression achieved in the standard geometry recycling plasmas. The flat-plate compression ratio decreases as a function of the line averaged density, similar to the standard geometry detached cases. The compression ratios for these two cases reach similar values at high plasma densities.

The above dependencies can be qualitatively understood upon examining ion fluxes fueling the divertor and the midplane particle reservoirs. Fig. 6-9 shows the ratio of the ion flux striking the vertical target plates to the total divertor ion flux. This ratio slowly decreases as a function of the core density for the flat-plate geometry case, leading to decreasing neutral compression ratio. Also note that the fraction of the ion flux striking the vertical target plates (most of which comes from the inner divertor) in the flat-plate case is similar to that of the standard-geometry detached case.

An analogy can be drawn between the attached horizontal plate discharges and the detached vertical plate discharges. Both types of discharges lead to a considerable increase of the midplane pressure resulting in a decrease in the compression ratio. Fig. 6-9 shows that both types of discharges lead to ion flux striking the horizontal

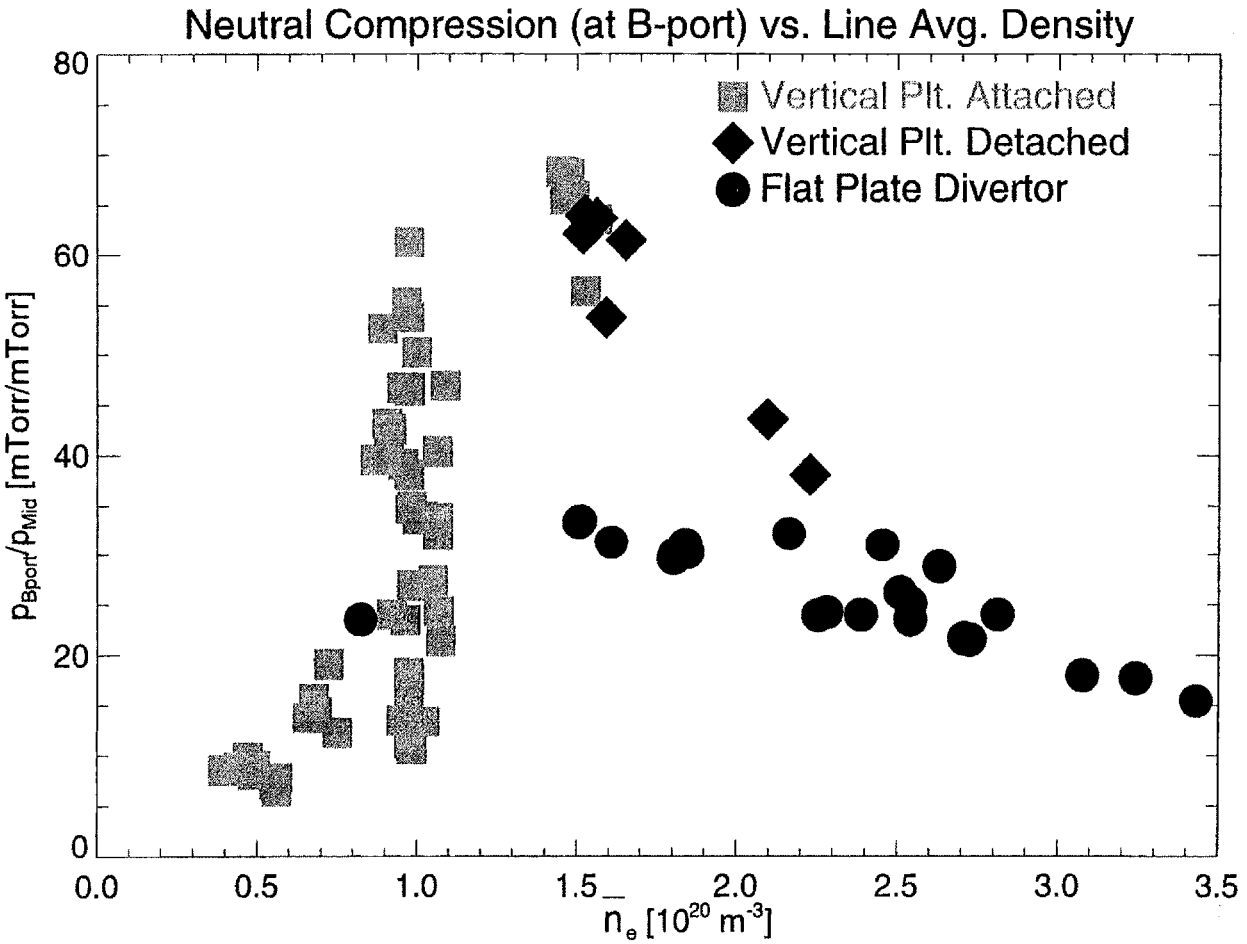

Fig. 6-8: Divertor-to-midplane compression ratio for the vertical and flat-plate divertor geometries.

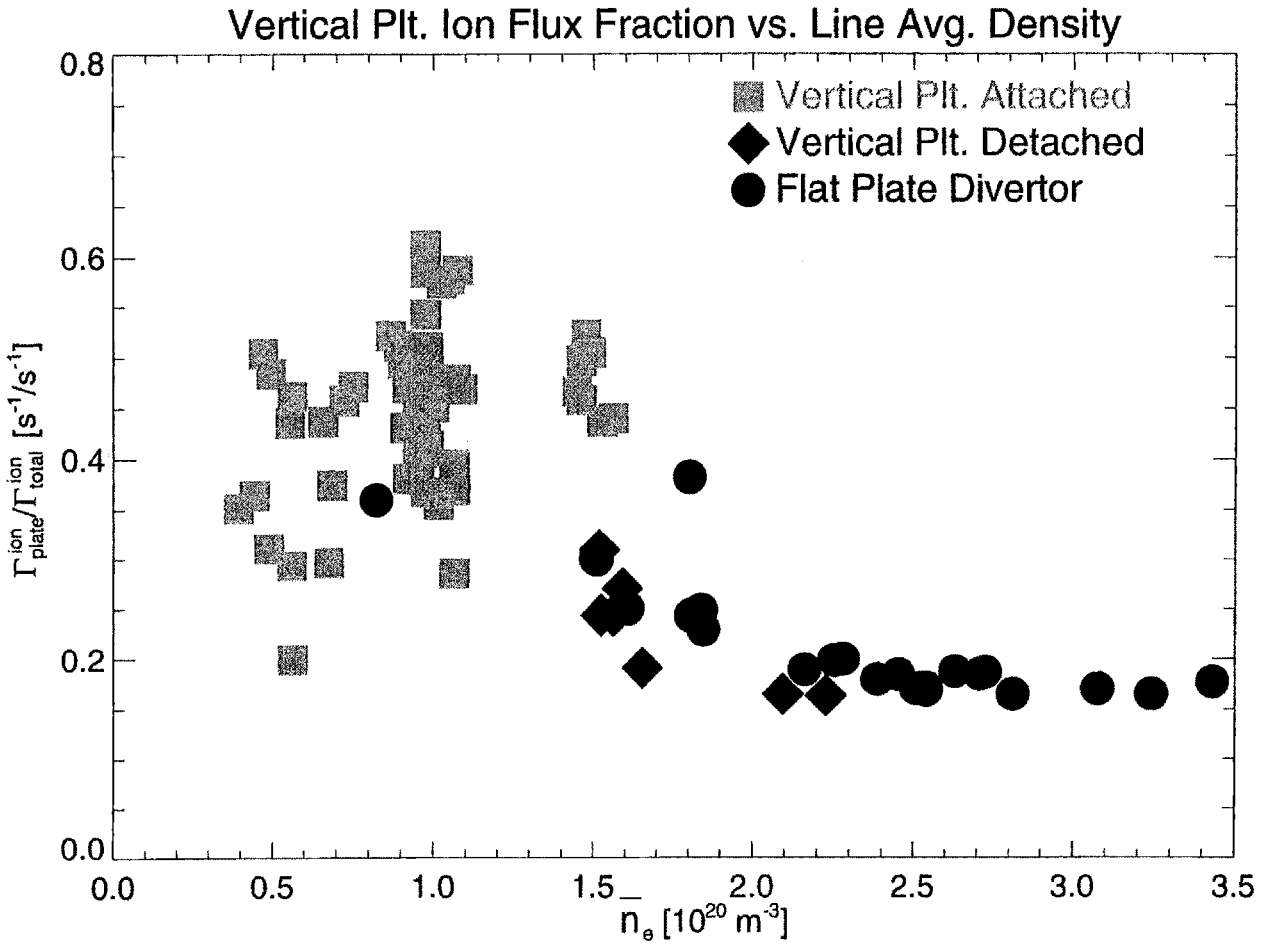

Fig. 6-9: Vertical-plate ion flux fraction (with respect to the total divertor ion flux) for the vertical- and flat-plate divertor geometries.

portion of the divertor target plate to significantly dominate over that striking the vertical plate. The increase in the particle source there leads to the increase in the midplane pressure.

The remaining question is the high neutral pressure sustained in the divertor in the flat plate geometry discharges despite the observation (on Fig. 6-9) that the dominant recycling source is located on the horizontal plate. While a quantitative answer would require detailed modeling, similar to that carried-out in Chapter 5, a qualitative answer can be obtained based on additional observations:

1) Fig. 6-10 shows the value of the ion flux (measured by the flush Langmuir probes) striking both vertical target plates, i.e., fueling the divertor reservoir. The flat plate case flux is relatively small but still larger than that fueling the standard-geometry detached discharges.

2) Fig. 6-11 shows the ratio of the open-divertor-module neutral pressure to the closed-divertor-module one. In the flat-plate geometry cases the two pressures are approximately equal across the entire density range, which indicates stagnation of the leakage flux through the diagnostic openings.

3) The neutrals attempting to escape from the divertor-reservoir are reflected from the PFZ-plasma through a mechanism similar to the one proposed in Chapter 5. For the typical flat-plate PFZ-plasma parameters (e.g., for the core density $\bar{n}_e \approx 2.5 \cdot 10^{20}$ m^{-3}: T $\approx$1.5 eV, n $\approx 1 \cdot 10^{20}$ m^{-3} at ρ =-2 mm) the momentum transfer collisions dominate over the ionizing collisions and the mean-free-path is short compared with a geometry scale length.

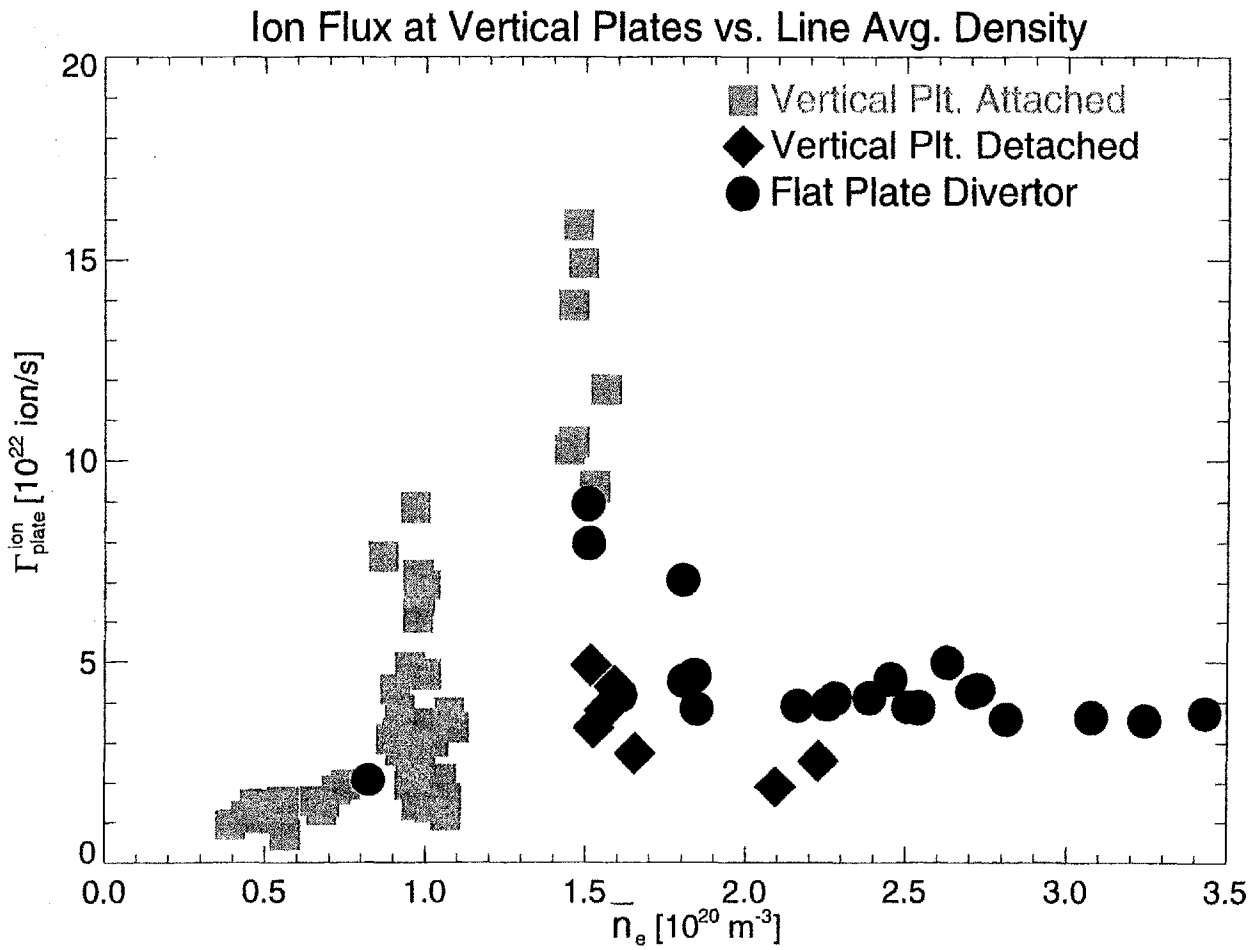

Fig. 6-10: Ion flux striking the vertical plates (measured by the flush Langmuir probes) for the two divertor geometries.

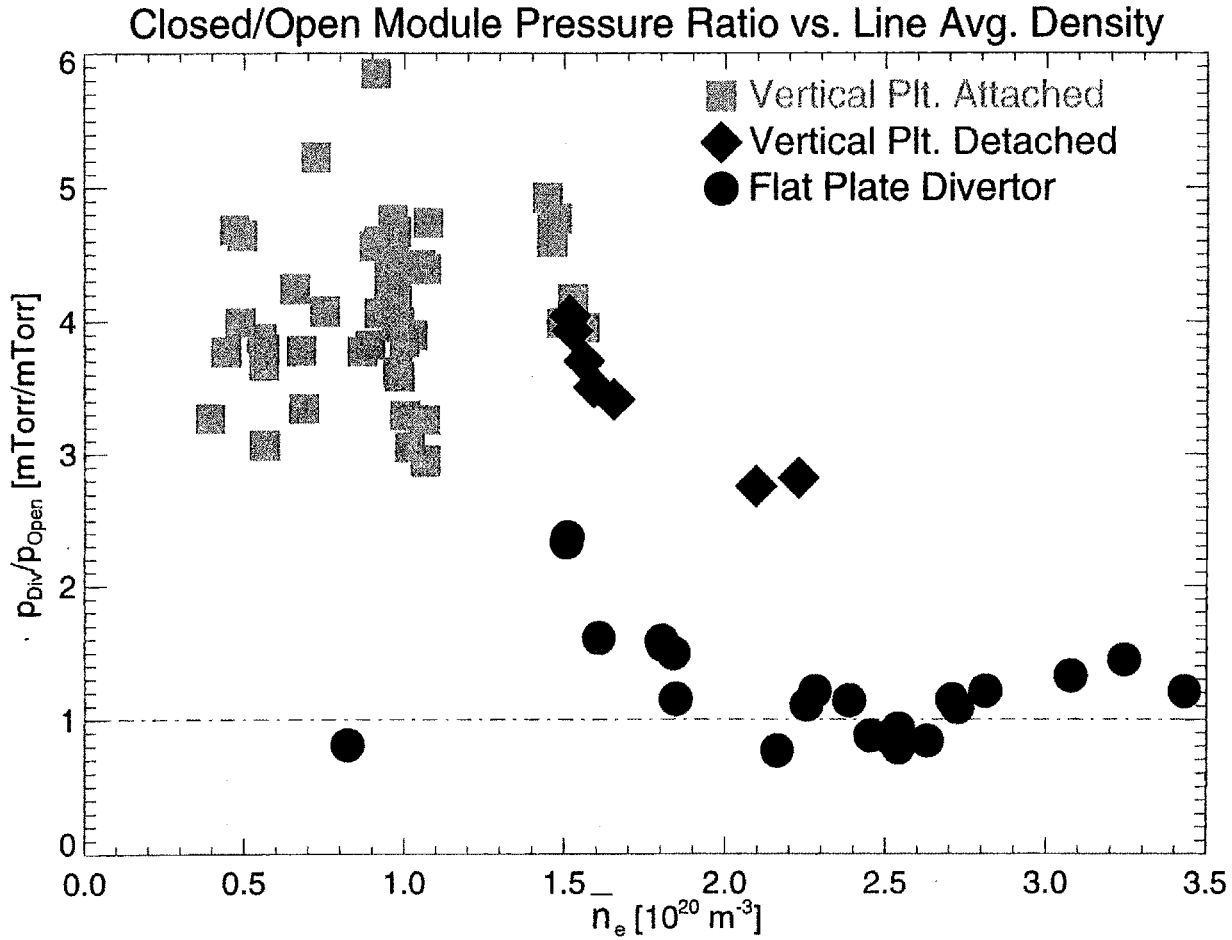

Fig. 6-11: Ratio of the divertor closed-module to the open-module neutral pressures for the two divertor geometries. Lack of a pressure gradient between the closed and opened divertor modules indicates a partial stagnations of the leakage flux.

Thus, the flat-plate geometry plasma may have an ability to sustain high divertor neutral pressure through a mechanism similar to the one modeled in Chapter 5 for the standard geometry detached discharges. While the fueling of the divertor particle reservoir is provided by a small but finite ion flux the particle loss is significantly reduced by reflections off the plasma plugging the throat. Two additional mechanisms reducing the divertor neutral particle loss in the flat-plate geometry are reduction of the private-flux-zone separatrix surface area and partial stagnation of the leakage flux.

6.5 Chapter summary

The experiments reported here, despite their limited scope, provided a useful insight into neutral pressure dependence on plasma and divertor geometry.

The ion B×∇B-drift direction has almost negligible effect on the neutral pressure and compression ratio. The outer strike-point position affects neutral population less strongly than the edge plasma characteristics. The divertor pressure and divertor-to-midplane compression ratio are maximized with the strike point position at the bottom of the vertical target plate.

Two divertor geometry configurations are of particular interest:

1) The slot divertor configuration may potentially lead to better neutral confinement in the divertor. The pressure measured with current diagnostics unfortunately cannot be directly compared with other configurations because the measuring plenum connects to a different plasma zone.

2) The divertor pressure in the flat-plate configuration is similar to the maximum measured in the vertical-plate configuration, whereas the compression ratio is about factor of two smaller. High divertor neutral pressure sustained by the flat-plate plasmas can be qualitatively explained by reflection of neutrals off the cold PFZ-plasma

While the interpretation provided here is only a qualitative one, we recommend that in future a full two-dimensional model is used to help us better understand impact of plasma and divertor configuration on the neutral dynamics.

Chapter 7

Effects of Divertor Modifications on Neutral Dynamics

The experimental observations combined with the neutral particle dynamics analysis carried out throughout this thesis lead us to believe that the ability of Alcator C-Mod to confine neutrals in the divertor can be significantly improved.

The current divertor hardware modification plans, formulated as a result of operational experience, include:

1) Closing the slot between the outer edge of the horizontal target plate and the vessel wall to eliminate the escape path for neutrals, thus reducing leakage-flux loss of particles from the divertor volume. This relatively inexpensive modification is planned for the Summer 1995.

2) Widening the divertor throat to increase the plasma flow towards the vertical target plates, below the nose, and reducing the flow above the nose. This modification requires a costly and complicated redesign of the entire divertor structure and is not presently scheduled. Preliminary plans call for reducing the inner divertor nose overhang and repositioning the plasma X-point so to reduce recycling on the upper sections of both inner and outer horizontal target plates.

These modifications have the potential to significantly improve the neutral confinement in the divertor. Whereas a detailed analysis of the effect of the modifications on overall plasma characteristics has yet to be carried out, the analysis presented below constitutes a first attempt to quantify the expected changes in the neutral particle dynamics which is of interest to this thesis.

The divertor flux balance model proposed in Chapter 5, which is used here, is an interpretative one and is not well suited for predictive analysis. The plasma background is fixed and is assumed unaffected by the divertor modifications. This is clearly far from truth, especially in the case of the divertor throat widening, which, besides neutral particles, affects divertor plasma characteristics, radiation patterns, and impurity dynamics. As a result the quantitative statements made in this chapter should only serve as a guidance for future more detailed modeling or as an aid in interpreting future experimental observations.

7.1 Midplane volume neutral flux balance

The midplane neutral particle flux balance is calculated by analogy with the divertor flux balance, discussed in detail in Chapter 5.

The midplane effective volume (see Fig. 2-10) is defined here as the vacuum portion of the main tokamak chamber bounded by the outer separatrix surface area between the stagnation-point and the X-point, outer horizontal divertor target plate, and top and outside vessel walls.

In steady-state the neutral flux balance equation for the midplane-volume can be written by analogy with the divertor balance (Eq. 5.1):

$$0 = \Gamma_{leak} + f_{transAN} \cdot \Gamma_{plateAN} - \Gamma_{sol}^{esc} \qquad (7.1)$$

where:

Γ_{leak} - is the flux of neutrals arriving into the midplane volume through leaks in the divertor structure, this flux has been defined and calculated in Section 5.4 as a sink term in the divertor flux balance;

$\Gamma_{plateAN}$ - is the total ion flux striking the outer horizontal target plate "above the nose" (AN);

$f_{transAN}$ - is the average transmission coefficient outer-horizontal-plate→ midplane-volume;

Γ_{sol}^{esc} - is the net flux of neutrals escaping from the midplane volume into the outer SOL plasma.

Note that Eq. 7.1 does not contain any term describing transmission of neutrals across the plasma-fan plugging the divertor throat (e.g., along chord #9 on Fig. 5-1). The diffusive neutral transport calculations, carried out in Section 5.5, produce, as a byproduct, an estimate of transmission probability of a neutral from the PFZ-reservoir to the midplane-volume. This probability is less than 0.005 for attached divertor plasma cases (when the neutral flux is low) and much less than 0.001 for detached cases (when the neutral flux is high). The downward transmission trend is due to increasing SOL plasma thickness with core density. As a result, the transmitted flux is negligible compared to the leakage (Γ_{leak}) and recycling ($\Gamma_{plateAN}$) fluxes fueling the midplane-volume. This conclusion has also been confirmed by test DEGAS simulations (i.e., following the fate of a "test" particle launched from the divertor) [129]. The observation above renders an earlier author's hypothesis [83] of increasing plasma fan transparency to neutrals being responsible for the midplane pressure rise invalid.

Midplane reservoir neutral particle flux balance

Core electron density [1e20/m3]		**1.0**	**1.3**	**1.6**	**1.9**	**2.1**
Corresponding discharge:		6	7	10	11	13
Midplane Pressure	*[mTorr]*	*0.05*	*0.15*	*0.46*	*0.75*	*0.87*
Midplane source fluxes:						
Leakage flux	[1e22 2*D2/s]	0.11	0.50	1.57	2.06	2.39
Flush-probe ion flux	[1e22 D+/s]	1.08	1.91	4.66	7.18	8.11
Domed-probe ion flux	[1e22 D+/s]	0.25	0.47	1.19	1.68	1.64
sqrt(Flush*Domed)	[1e22 D+/s]	0.52	0.95	2.35	3.47	3.65
GplateAN*0.2	0.20	0.10	0.19	0.47	0.69	0.73
ion fraction	ion/(ion+leak)	0.49	0.28	0.23	0.25	0.23
Source=Leak+Ion*0.2	[1e22 D0/s]	0.21	0.68	2.04	2.75	3.12
Midplane loss flux:						
Sink= Gsol_esc	[1e22 D0/s]	0.22	0.66	2.08	3.40	3.94
Midplane flux balance:						
Source/Sink	[1]	**0.99**	**1.03**	**0.98**	**0.81**	**0.79**

Table 7-1: Midplane reservoir neutral particle flux balance. The table lists the fluxes constituting Eq. 7.1 as well as the final source/sink ratio by analogy to the divertor flux balance in Chapter 5.

Table 7-1 lists the fluxes included in Eq. 7.1. The fluxes are calculated for the five representative discharges selected in Chapter 5, which provide a good coverage of the edge plasma regimes.

The difficulty of obtaining a proper estimate of the perpendicular ion flux has been discussed in Section 5.7. A similar, but somewhat smaller, problem occurs for the horizontal shelf ion flux measurements: the biased flush-probe measurement yields a value a factor of four higher than the domed-probe measurement across the entire density range. Following the conclusion reached in Section 5.7, a geometric average of the two measurement is used as the outer horizontal plate ion flux estimate ($\Gamma_{plateAN}$) for the remainder of this chapter. Table 7-1 summarizes all three horizontal shelf ion flux measures. An additional small recycling source of neutrals from antenna limiters is neglected.

The average transmission coefficient of neutrals from the outer-horizontal-plate to the midplane-volume ($f_{transAN}$) is primarily a function of geometry and to a smaller extent, of SOL-plasma parameters. Neutrals leaving the surface have an average (over the horizontal plate) ~18°-wide view of the midplane volume. Because of the cosine-law angular distribution of their velocities, the transmission probability plate→midplane is ~2.5%. Upon entering the SOL-plasma the neutrals undergo a similar diffusion/absorption process to the one in the divertor volume (described in Section 5.5). The SOL-plasma albedo to neutrals calculated using the model from Section 5.5 is approximately 0.5 (with a neglected ±0.15 variation) across the core density range of interest. The neutrals that are reflected off the SOL-plasma (at one λ_{mt} depth) have a ~40°-wide view of the midplane volume. Hence the transmission increases to about 12.5%. The remaining reflected neutrals

(~0.4) strike the horizontal target plate and start the "trip" towards the plasma all over again. The final transmission probability increases to $f_{transAN} \approx 20\%$, when the effect of multiple trips is taken into account as a sum of a geometric series.

The net flux of neutrals escaping from the midplane volume towards the outer SOL plasma (Γ_{sol}^{esc}) is determined by the kinetic flux of neutrals, the SOL-plasma albedo, and the plasma surface "visible" to neutrals. Using the molecular flow condition, which is well justified for the midplane-volume neutral particles because of a much lower pressure, despite a slightly a larger distance between bounding surfaces when compared to the divertor plenum (see Section 5.2), the net escape flux can be written as:

$$\Gamma_{sol}^{esc} = \frac{1}{4} v_0 \cdot 2 \int_{S_{core}^{out}} n_{mid}(s)\left(1 - A_{sol}(s)\right) ds \qquad (7.2)$$

where:

v_0 - is the kinetic speed of a room-temperature deuterium molecule;

$n_{mid}(s)$ - is the neutral molecular density as a function of a poloidal space coordinate-s in the midplane volume, had such a measurement been possible;

$A_{sol}(s)$ - is the outer SOL-plasma albedo to neutrals as a function of space;

and the integration extends over:

S_{core}^{out} - the outer separatrix surface area between the stagnation-point and the X-point.

Because of lack of a spatial resolution of the measurements we approximate the integral in Eq. 7.2 by a product of the respective quantities:

$$\Gamma_{sol}^{esc} = 2(1 - A_{sol}) \cdot \frac{1}{4} v_0 \, n_{mid} \cdot S_{core}^{out} \qquad (7.3)$$

where:

n_{mid} - is the midplane neutral molecular density deduced from the midplane pressure measurement and

A_{sol} - the SOL-plasma albedo to neutrals is evaluated at the tokamak midplane using the fast-scanning probe data directly. The albedo evaluated with the model from Section 5.5 varies by less than 30% across the plasma density range. For simplicity it is approximated by a constant value ($A_{sol} \approx 0.5$).

Table 7-1 lists the midplane→SOL neutral escape flux (Γ_{sol}^{esc}) as well as the ratio of the source to the sink terms in the midplane-volume particle balance equation (Eq. 7.1). The 20% difference between the low and high density flux balance is mostly due to our having neglected variations in the SOL-plasma albedo. In the subsequent calculations the above small error is corrected by substituting the total source flux for the loss flux.

7.2 Effect of leak-slot closing on midplane pressure

In order to quantify potential changes due to closing the divertor leak we define a new quantity:

R_{plug} - a leakage flux reduction resulting from plugging the divertor slot:

$$R_{plug} = \frac{\Gamma_{leak}^{after}}{\Gamma_{leak}^{today}} \tag{7.4}$$

Eq. 7.1 describing the midplane-volume particle flux balance can be easily modified to include the effect of reducing the leakage flux:

$$0 = R_{plug} \cdot \Gamma_{leak} + f_{transAN} \cdot \Gamma_{plateAN} - \Gamma_{sol}^{esc} \tag{7.5}$$

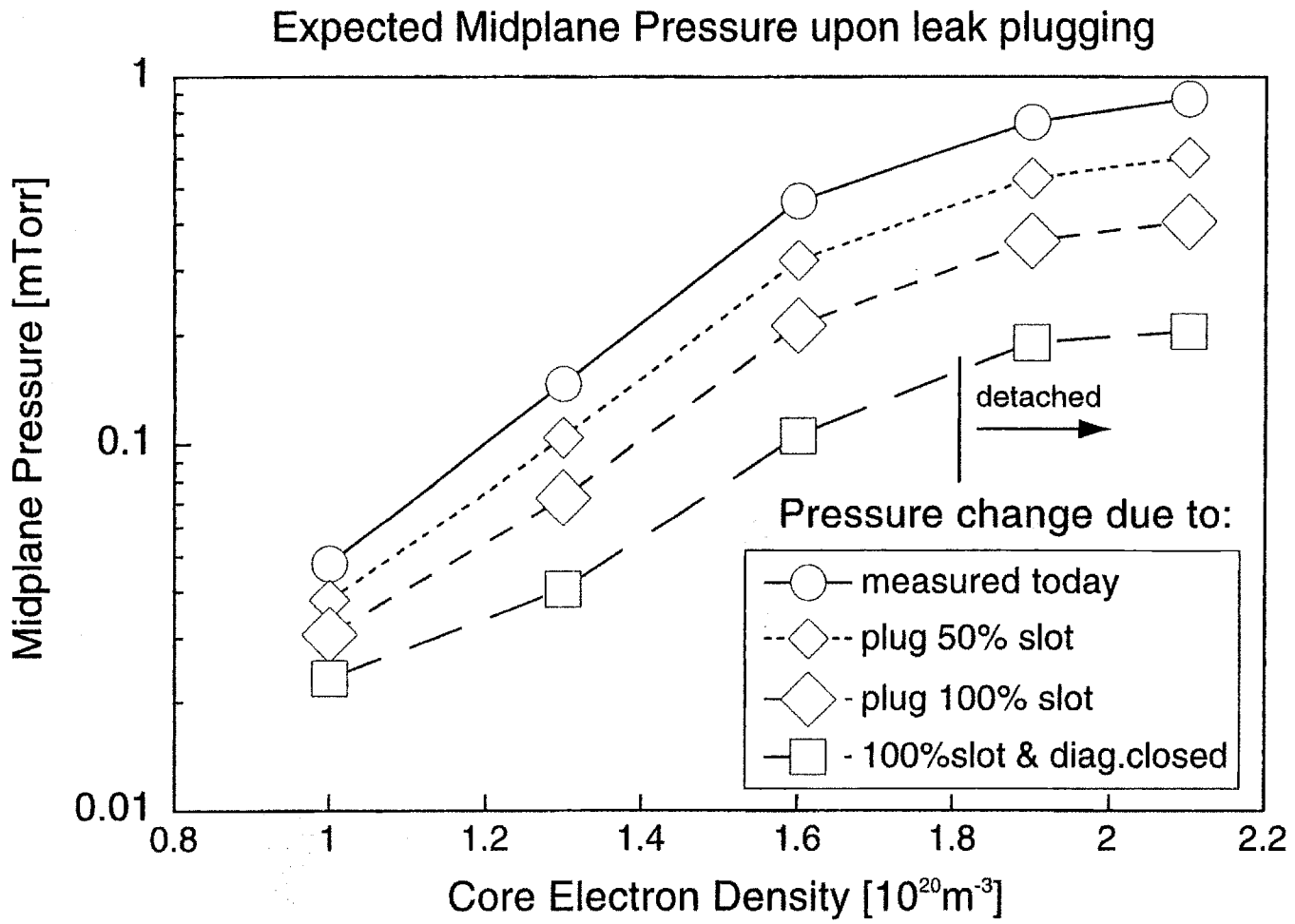

Fig. 7-1: Effects of different levels of leakage-escape-path closings on the midplane pressure. Diamonds correspond to 50% and 100% efficiency in closing the slot below the outer edge of the target plate. Squares depict a complete closing of the leakage path including the slot and the diagnostic-openings.

Eq. 7.5 allows us to calculate midplane pressure resulting from varying levels of reduction of the leakage flux. Fig. 7-1 shows the expected pressure in absolute units, whereas Table 7-2 summarizes the numerical results in terms of a relative pressure change with respect to the one measured today. The data from the five discharges modeled in Chapter 5 serve as a reference throughout this chapter.

R_{plug} =0.6 is equivalent to about 50% efficiency in the slot plugging. As a result the midplane pressure drops only to about 70% of today's value across the plasma density range of interest.

Even a 100% efficiency in plugging the slot results in R_{plug} =0.3 only because the neutral escape through the diagnostic openings in the divertor structure accounts for about 1/3 of the leakage (Section 5.4). This leads to the midplane pressure dropping to about 50%.

One also has an option to shut-down the diagnostics that require a vertical view of the plasma through the divertor slot in order to close this leakage path. Even though not desirable operationally we consider this drastic measure. R_{plug} =0.0 leads to a moderate improvement from the R_{plug} =0.3 case. The resulting midplane pressure drops by an additional 25% (of today's value). It seems therefore that closing the divertor diagnostic openings does not produce any major improvement and thus it is not recommended.

7.3 Effect of throat widening on midplane pressure

The goal of the divertor geometry modification plans is to reduce the ion flux recycling above the nose and to increase the ion flux recycling on the vertical

section of the divertor plates (below the nose). Even without a knowledge of exact future geometry we can attempt to quantify proposed changes by introducing a new quantity (analogous to the one defined by Eq. 7.4):

R_{nose} - a reduction in ion flux striking above the divertor nose:

$$R_{nose} = \frac{\Gamma_{plateAN}^{after}}{\Gamma_{plateAN}^{today}} \tag{7.6}$$

For simplicity the change in recycling on the inner divertor target is neglected throughout the analysis here. It is difficult to predict the expected improvement (decrease) in the ion flux recycling as a result of the hardware modifications. For the purpose of the sensitivity study presented below we assume R_{nose} =0.75, 0.5, and 0.25. Results for R_{nose} =1 (status quo) and R_{nose} =0 (removing the horizontal flux completely) are also included for reference.

Eq. 7.5 is further modified to include the effect of reducing the outer-horizontal-plate recycling flux:

$$0 = R_{plug} \cdot \Gamma_{leak} + R_{nose} \cdot f_{transAN} \cdot \Gamma_{plateAN} - \Gamma_{sol}^{esc} \tag{7.7}$$

Eq. 7.7 allows us to calculate midplane pressure resulting from any or both of the planned divertor hardware modifications. Table 7-2 contains a comprehensive lists of numerical results for all considered cases of interest (for both R_{nose} and R_{plug}) in terms of a relative midplane pressure change with respect to the one measured today.

Expected midplane pressure upon slot closing and throat widening

Core density [1e20/m3]		1.0	1.3	1.6	1.9	2.1
Corresponding discharge:		6	7	10	11	13
Measured pressures:						
midplane pressure	*[mTorr]*	*0.05*	*0.15*	*0.46*	*0.75*	*0.87*
divertor pressure	[mTorr]	1.8	8.4	25.9	32.7	38.2
divertor compression	[1]	38	57	56	43	44
Midplane balance fluxes:						
IonFlux_AN (avg)	[1e22 D+/s]	0.52	0.95	2.35	3.47	3.65
Ion Transmitted	**0.2**	0.10	0.19	0.47	0.69	0.73
Ion fraction	*Ion/Source*	*0.49*	*0.28*	*0.23*	*0.25*	*0.23*
Leakage (avg.)	[1e22 2*D2/s]	0.11	0.50	1.57	2.06	2.39
Leak fraction	*Leak/Source*	*0.51*	*0.72*	*0.77*	*0.75*	*0.77*
Gmid_esc*2/2	[1e22 D0/s]	0.22	0.66	2.08	3.40	3.94
Ratio of Expected New/Old midplane pressure:						
R_plug	**R_nose**					
1.0	1	1.00	1.00	1.00	1.00	1.00
1.0	0.75	0.88	0.93	0.94	0.94	0.94
1.0	*0.5*	*0.76*	*0.86*	*0.88*	*0.87*	*0.88*
1.0	0.25	0.63	0.79	0.83	0.81	0.82
1.0	0	0.51	0.72	0.77	0.75	0.77
R_plug	**R_nose**					
0.6	1	0.79	0.71	0.69	0.70	0.69
0.6	0.75	0.67	0.64	0.63	0.64	0.64
0.6	0.5	0.55	0.57	0.58	0.57	0.58
0.6	0.25	0.43	0.50	0.52	0.51	0.52
0.6	0	0.31	0.43	0.46	0.45	0.46
R_plug	**R_nose**					
0.3	*1*	*0.64*	*0.49*	*0.46*	*0.48*	*0.46*
0.3	0.75	0.52	0.42	0.40	0.41	0.41
0.3	*0.5*	*0.40*	*0.36*	*0.35*	*0.35*	*0.35*
0.3	0.25	0.28	0.29	0.29	0.29	0.29
0.3	0	0.15	0.22	0.23	0.22	0.23
R_plug	**R_nose**					
0.0	1	0.49	0.28	0.23	0.25	0.23
0.0	0.75	0.37	0.21	0.17	0.19	0.18
0.0	0.5	0.24	0.14	0.12	0.13	0.12
0.0	0.25	0.12	0.07	0.06	0.06	0.06
0.0	0	0.00	0.00	0.00	0.00	0.00

Table 7-2: Effects of planned divertor modifications on the midplane pressure. The top panel reviews the measured neutral pressures while the middle panel, the components of the particle flux balance. The bottom panel summarizes the expected relative changes in the midplane pressure as a function of different modification levels (defined in the text).

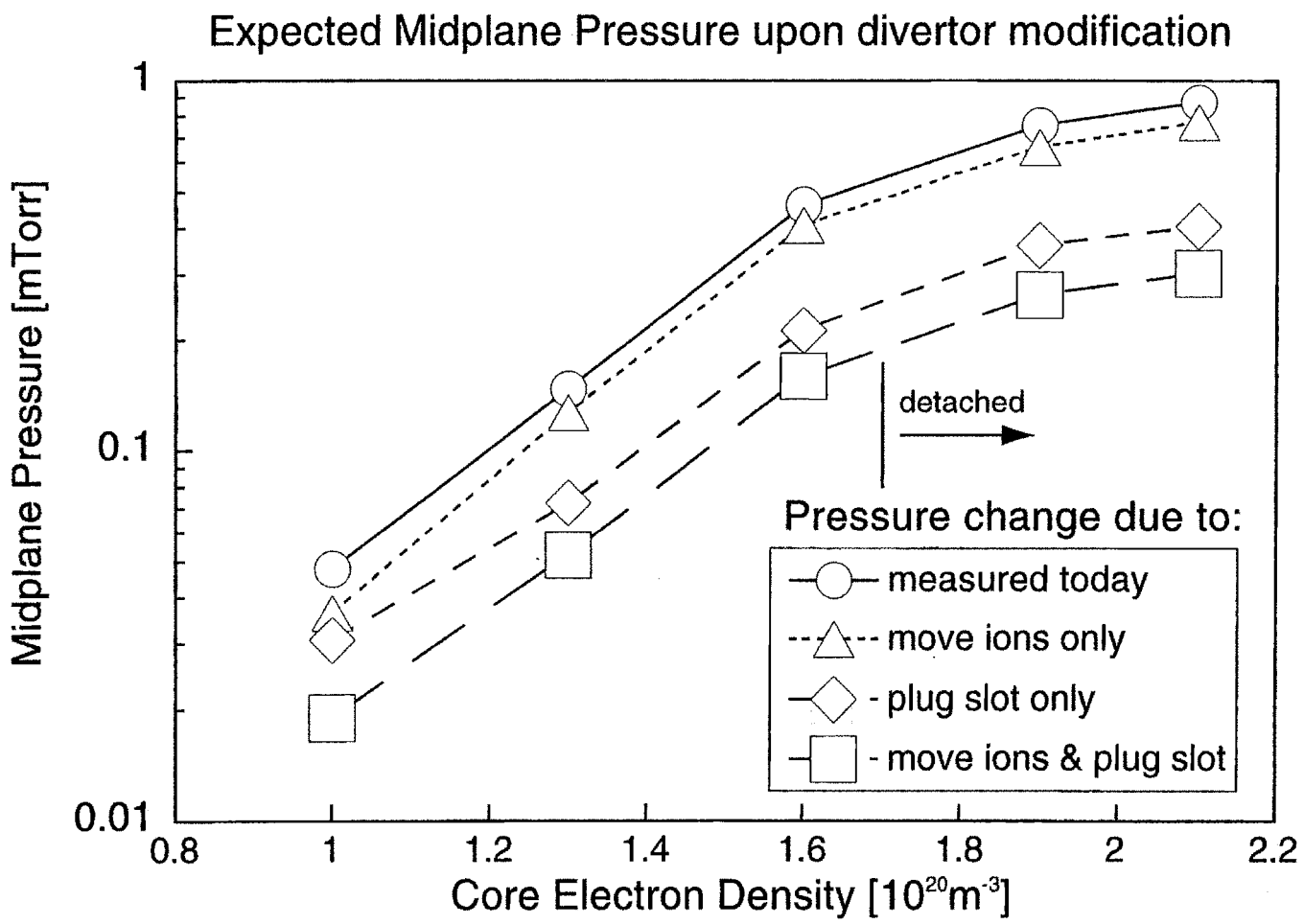

Fig. 7-2: Effects of planned divertor modifications on the midplane pressure. The expected pressure (in mTorr) is plotted for selected cases from Table 7-2. "Move ions only" corresponds to R_{nose}=0.5 & R_{plug}=1, i.e., the outer horizontal plate recycling is reduced by 50%. "Plug slot only" case corresponds to R_{plug}=0.3 & R_{nose}=1, i.e., the leakage-slot (but not the diagnostic openings) is entirely closed. The last case combines the effect of both modifications.

To render the results easier to comprehend only selected cases are presented in a graphical form on Fig. 7-2 as an absolute midplane pressure after the modifications. For reference the midplane pressure measured in today's experiments is also plotted (circles).

The value of R_{nose} =0.5 (and R_{plug} =1, no change), which is denoted as a "move ions only" case on Fig. 7-2 (triangles), appears to be a reasonably achievable goal of 50% ion flux reduction. It leads to a rather moderate midplane pressure decrease to about 85% of today's value. The "plug slot only" case on Fig. 7-2 (diamonds), results from a 100% efficiency in closing the leakage slot (but not the diagnostic openings) discussed already in details in the previous section. That the leakage slot closing is much more efficient in reducing the midplane pressure (by ~50%) than the plate redesign (by ~15%), except for the lowest density case. The last case "move ions & plug slot" on Fig 7-2 (squares) is the combination of the two divertor modification, resulting in midplane pressure reduction to about 35% of its today's value.

7.4 Change in divertor pressure

The neutral particle flux balance in the divertor has been analyzed in Chapter 5. The flux balance equation (Eq. 5.1) is easily modified to include the effects of the hardware modifications defined in the previous sections:

$$0 = f_{trans} \cdot (\Gamma_{plate} + (1\text{-}R_{nose}) \cdot \Gamma_{plateAN}) - (1\text{-}A) \cdot \Gamma_{pfz}^{kin} - R_{plug} \cdot \Gamma_{leak} \qquad (7.8)$$

It is assumed in the above balance equation that any ion flux removed from the outer horizontal target plate (above the nose) reappears on the vertical plate (below

the nose). Also recall that the inner target flux is held constant. As a result the total ion flux towards the divertor is unchanged.

To simplify the analysis, the vertical plate ion flux (Γ_{plate}) necessary to maintain particle balance is substituted for an estimate based on measurements. The required ion flux is within a factor of two in agreement with a geometric average of the flush and domed Langmuir probe measurements (recall Section 5.7). All the remaining quantities in Eq. 7.8 have been defined and calculated earlier in Chapters 5 and 7.

The divertor pressure appears in two terms in Eq. 7.8, in the escape flux (Γ_{pfz}^{kin}) and in the leakage flux (Γ_{leak}). An average-value estimate of the leakage flux involves midplane, open-port and divertor pressures (recall Section 5.4). All three change as a result of a divertor modification. To simplify the analysis we neglect midplane pressure in the leakage flux estimate (~10% error) and assume that the open port pressure is proportional to the divertor one. Note that no assumption is required about the proportionality constant (which is typically: p_{open} ~1/4 p_{div}) as long as it does not vary across the core density range of interest.

Substituting the appropriate quantities into Eq. 7.8 allows us to calculate the divertor neutral pressure after divertor modifications. Table 7-3 summarizes the numerical results while Fig. 7-3 presents the results for representative modification cases in the form identical to that of the previous section.

There is little or no effect on the divertor pressure in the attached divertor plasma cases while the effect of both modifications may be significant in the detached cases. The observed differences in each of the two hardware modification plans can be explained by:

Expected divertor pressure upon slot closing and throat widening

Core density [1e20/m3]	1.0	1.3	1.6	1.9	2.1
Corresponding discharge:	6	7	10	11	13
Measured pressures:					
midplane pressure [mTorr]	0.05	0.15	0.46	0.75	0.87
divertor pressure [mTorr]	*1.8*	*8.4*	*25.9*	*32.7*	*38.2*
divertor compression [1]	38	57	56	43	44
Measured/estimated fluxes					
IonFlux_AN (avg.) [1e22 D+/s]	0.52	0.95	2.35	3.47	3.65
IonFlux_BN (req.) [1e22 D+/s]	1.88	4.64	13.89	3.69	4.01
Leakage (avg.) [1e22 2*D2/s]	0.11	0.50	1.57	2.06	2.39
PFZ escape (kin.) [1e22 D0/s]	3.08	14.33	44.35	55.86	65.35
plateBN -> PFZ transmission	0.907	0.945	0.912	1.000	1.000
PFZ-escape albedo	0.481	0.729	0.750	0.971	0.975
Ratio of Expected new/old divertor pressure:					
R_plug **R_nose**					
1.0 1	1.00	1.00	1.00	1.00	1.00
1.0 0.75	1.07	1.05	1.04	1.24	1.23
1.0 0.5	*1.14*	*1.10*	*1.08*	*1.47*	*1.45*
1.0 0.25	1.21	1.15	1.13	1.71	1.68
1.0 0	1.28	1.20	1.17	1.94	1.91
R_plug **R_nose**					
0.6 1	1.03	1.05	1.05	1.29	1.31
0.6 0.75	1.10	1.10	1.10	1.59	1.61
0.6 0.5	1.17	1.15	1.14	1.89	1.91
0.6 0.25	1.24	1.21	1.19	2.20	2.21
0.6 0	1.31	1.26	1.23	2.50	2.51
R_plug **R_nose**					
0.3 1	*1.05*	*1.09*	*1.10*	*1.64*	*1.71*
0.3 0.75	1.12	1.14	1.14	2.03	2.10
0.3 0.5	*1.19*	*1.20*	*1.19*	*2.41*	*2.49*
0.3 0.25	1.26	1.25	1.23	2.80	2.88
0.3 0	1.34	1.31	1.28	3.18	3.27
R_plug **R_nose**					
0.0 1	1.07	1.13	1.14	2.26	2.47
0.0 0.75	1.14	1.18	1.19	2.79	3.03
0.0 0.5	1.22	1.24	1.24	3.32	3.59
0.0 0.25	1.29	1.30	1.29	3.86	4.15
0.0 0	1.36	1.36	1.34	4.39	4.71

Table 7-3: Effects of planned divertor modification on the divertor pressure. The table is compiled in the same form as Table 7-2. It reviews the relevant pressures and fluxes and summarizes the expected relative changes in the divertor pressure.

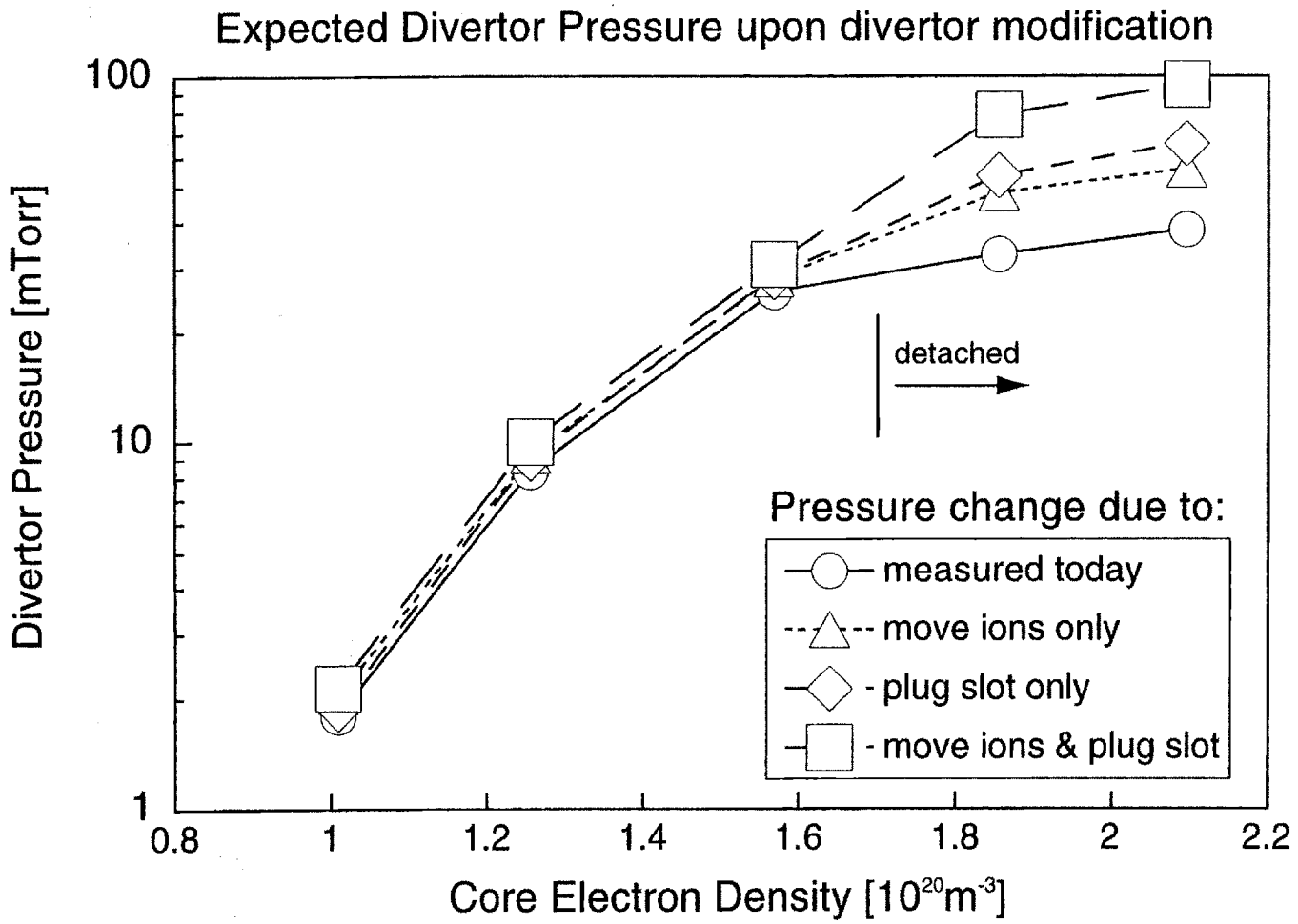

Fig. 7-3: Effects of planned divertor modifications on the divertor pressure. Same symbols are used as in Fig. 7-2. Note that the change in pressure is significant only in the detached divertor state.

1) Redesigning of the divertor target geometry ("move ions only" case, marked with triangles on Fig. 7-3) causes 50% of the horizontal plate ion flux to be redirected to the vertical plate. In attached plasmas, however, most of the ion flux already flows towards the vertical plates. Thus the divertor pressure increases only by about 10% as a result of the additional source term. In the detached plasmas only about ~30% of the outer divertor ion flux flows towards the vertical plate thus the flux redirected from the horizontal plate leads to a significant increase of the source term in Eq. 7.8. As a result divertor pressure increases by ~50% in the detached cases. This result may be inaccurate, however, because it neglects the ion momentum removal in the detached state.

2) Closing of the leakage slot ("plug slot only" case, marked with diamonds on Fig. 7-3) causes a constant 70% drop in the leakage flux across the entire core density range. Recall, however, from Fig. 5-11 the varying significance of this loss mechanism with changing plasma conditions. In attached plasmas loss of neutrals through the leakage slot is small compared with the loss towards the plasma fan plugging the divertor throat. As a result the divertor pressure increase is almost negligible - only ~10%. In the detached cases an increasingly colder plasma reflects most of the neutrals towards the divertor volume (Section 5.6) such that the leakage flux becomes comparable of greater from the net loss towards the plasma. Reducing the leakage results in an increase in the divertor pressure by ~65%.

As expected, the combination of the two modifications ("move ions & plug slot" case, marked with squares on Fig. 7-3) leads to a divertor pressure increase in the detached cases, by a factor of ~2.5, while having an almost negligible effect (~20% increase) in the attached cases. Leak slot closing has a slightly stronger effect than redirecting ion flux.

7.5 Modification summary in terms of the divertor compression

Table 7-4 and Fig. 7-4 summarize the results of this chapter in terms of divertor compression, defined as the ratio of divertor to midplane pressure. Table 7-4 contains a comprehensive list of numerical results in terms of a relative improvement, while Fig. 7-4 presents selected cases in absolute units (here compression ratio).

Whereas there is no new information contained in Table 7-4 and Fig. 7-4 (compression is a quotient of the two calculated pressures) the compression ratio constitutes a very important figure of merit measuring the quality of neutral confinement in the divertor. Fig 7-4 leads us to three important conclusions:

1) Closing of the leakage slot ("plug slot only" - diamonds) leads to a significantly greater improvement compared with redesigning of the divertor target geometry ("move ions only" - triangles).

Expected divertor compression upon slot closing and throat widening

Core density [1e20/m3]	1.0	1.3	1.6	1.9	2.1
Corresponding discharge:	6	7	10	11	13
Measured pressures:					
midplane pressure [mTorr]	0.05	0.15	0.46	0.75	0.87
divertor pressure [mTorr]	1.8	8.4	25.9	32.7	38.2
divertor compression [1]	*38*	*57*	*56*	*43*	*44*
Measured/estimated fluxes					
IonFlux_AN (avg.) [1e22 D+/s]	0.52	0.95	2.35	3.47	3.65
IonFlux_BN (req.) [1e22 D+/s]	1.88	4.64	13.89	3.69	4.01
Leakage (avg.) [1e22 2*D2/s]	0.11	0.50	1.57	2.06	2.39
PFZ escape (kin.) [1e22 D0/s]	3.08	14.33	44.35	55.86	65.35
plateBN -> PFZ transmission	0.907	0.945	0.912	1.000	1.000
PFZ-escape albedo	0.481	0.729	0.750	0.971	0.975
Ratio of Expected new/old divertor compression:					
R_plug **R_nose**					
1.0 1	1.00	1.00	1.00	1.00	1.00
1.0 0.75	1.22	1.13	1.11	1.32	1.30
1.0 0.5	*1.50*	*1.28*	*1.23*	*1.68*	*1.65*
1.0 0.25	1.90	1.46	1.36	2.10	2.04
1.0 0	2.49	1.66	1.52	2.60	2.49
R_plug **R_nose**					
0.6 1	1.29	1.47	1.52	1.84	1.89
0.6 0.75	1.63	1.72	1.73	2.49	2.54
0.6 0.5	2.12	2.02	1.98	3.29	3.31
0.6 0.25	2.88	2.40	2.28	4.29	4.26
0.6 0	4.25	2.91	2.67	5.57	5.45
R_plug **R_nose**					
0.3 1	*1.63*	*2.20*	*2.37*	*3.44*	*3.69*
0.3 0.75	2.16	2.69	2.83	4.90	5.19
0.3 0.5	*3.00*	*3.37*	*3.43*	*6.88*	*7.19*
0.3 0.25	4.58	4.38	4.28	9.74	10.00
0.3 0	8.68	6.03	5.55	14.20	14.24
R_plug **R_nose**					
0.0 1	2.20	4.07	4.96	8.96	10.55
0.0 0.75	3.13	5.71	6.89	14.76	17.26
0.0 0.5	5.00	8.98	10.75	26.35	30.69
0.0 0.25	10.60	18.79	22.34	61.14	70.98
0.0 0	∞	∞	∞	∞	∞

Table 7-4: Effects of planned divertor modifications on the divertor-to-midplane neutral compression ratio. The table is compiled in the form of the two previous tables. The expected relative improvement in the compression ratio is listed for various levels of hardware modifications.

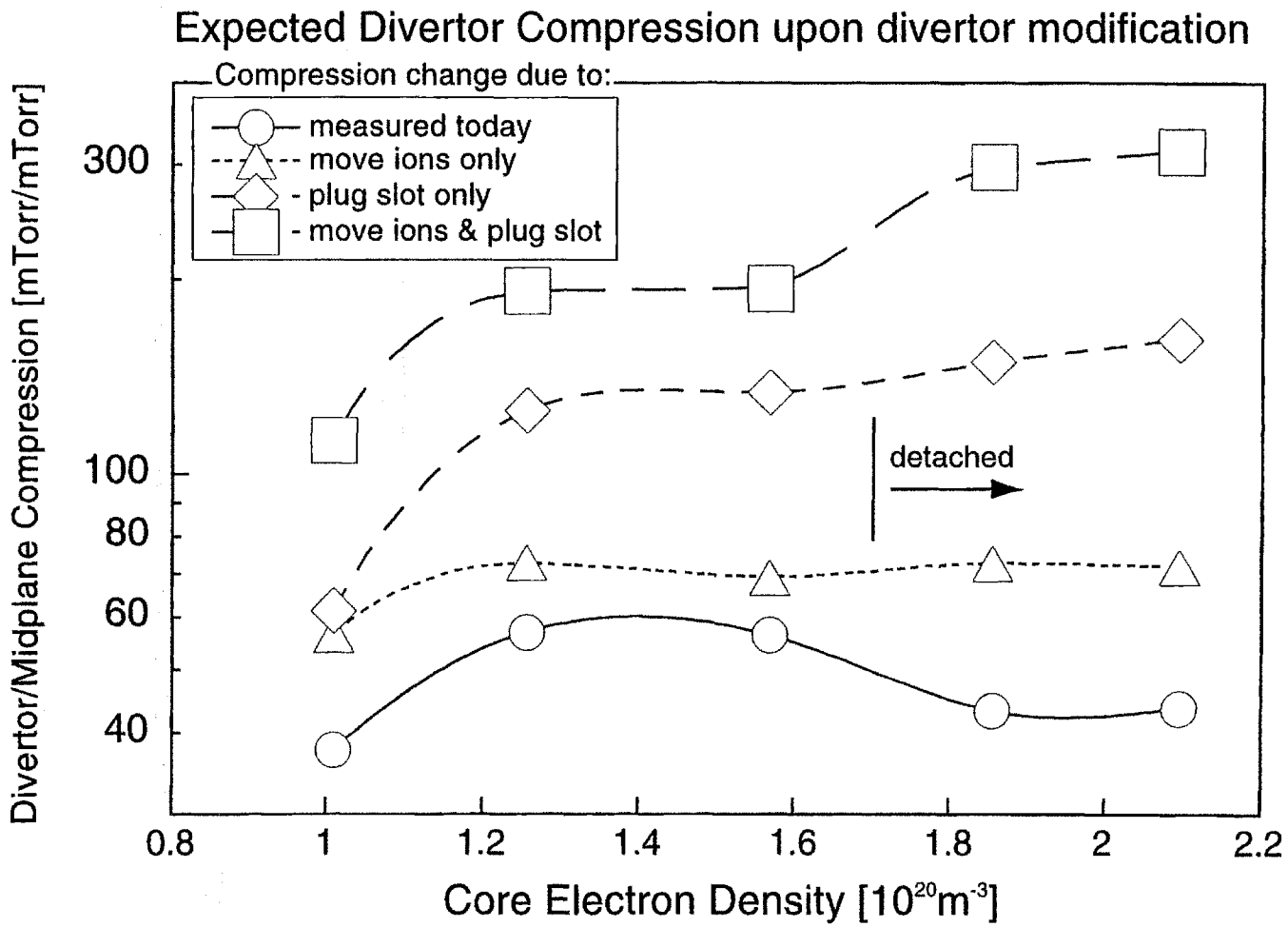

Fig. 7-4: Effects of planned divertor modifications on the divertor-to-midplane compression ratio. Same symbols are used as in the two previous figures. Note that the leak-slot closing has a stronger effect than the target-plate modifications. As a result of the modifications the compression ratio should no longer decrease in detached plasmas.

2) Any of the two modifications leads to a qualitative change in the compression dependence on the core density. The compression ratio should no longer decrease in detached plasmas, as is observed in current experiments ("measured toady" - circles).

3) The combined effect of both changes ("move ions & plug slot" - squares) leads in theory to compression ratio increasing by a factor of 3-7 from the one observed today.

As mentioned earlier, however, the quantitative results of the above analysis have to be treated with extreme caution. The potential error may be especially large when predicting the effects of divertor geometry modifications. Any such modification will lead to a global change of divertor plasma, e.g., it will effect plasma characteristics, the radiation pattern, impurity confinement, and the neutral population. All of these changes will affect the neutral dynamics, which in turn will affect the divertor plasma. Thus a true, self-consistent, predictive code is required to model the effect of divertor geometry modification correctly. This is well beyond the scope of this thesis. Closing the leakage slot primarily affects neutral dynamics, thus the potential error is smaller in this case. However an increased divertor neutral density will lead to an increased ionization source and ion flux striking the target. This change in the neutral source term has not been taken into account in Eq. 7.8.

In the above analysis we have also assumed that the proposed divertor hardware modifications will not affect thresholds of the edge plasma regimes (determined by the parallel heat transport). An increase in the divertor pressure, due to better confinement of neutrals, may lead to increased divertor plasma density and, in

consequence, to shifting the transitions to high recycling and detached divertor regimes to lower core plasma densities. Shimada [130] draws our attention to the fact that the core density required for divertor detachment in ITER may be at or above the Greenwald limit. Thus any mechanism leading to lowering of the critical detachment density is of a paramount importance to ITER design.

Chapter 8

Thesis Summary and Conclusions

This thesis has presented an experimental study of neutral particle dynamics in Alcator C-Mod – a high power density and high plasma density tokamak with an advanced poloidal divertor. The work focused on the investigation of neutral transport in the tokamak vessel, neutral particle confinement in the divertor, and interaction of neutrals with the edge plasma. The primary diagnostic used in the experiment was a set of neutral pressure gauges, installed in the tokamak by the author, which included standard industrial gauges and special-purpose gauges built for high-noise, high magnetic field operation inside the Alcator C-Mod divertor.

The major experimental observations can be summarized as follows:

1) The divertor and midplane neutral pressures depend most strongly on the edge plasma regimes defined by the scrape-off-layer parallel heat transport. Both pressures are low ($p_{mid} \approx 0.05$ mTorr, $p_{div} \approx 0.5$ mTorr) in the sheath-conduction limited regime, rise rapidly through the high-recycling regime and more slowly through the detachment regime, reaching $p_{mid} \approx$1-4 mTorr, $p_{div} \approx$ 30-60 mTorr. The dependence on the core plasma density or input power is indirect.
2) The divertor-to-midplane neutral compression ratio provides a convenient measure of the ability of the divertor to confine neutrals. The compression

is low (~10) in the sheath-limited regime, reaches the maximum (~70) in the high-recycling regime and decreases through the detached state.

3) Variations in the divertor geometry have a much weaker effect (compared with the edge plasma characteristics) on the divertor pressure and compression ratio, affecting less than a factor of two change.

4) The divertor pressure and compression ratio are maximized when the strike point is located at the bottom of the vertical target plate.

5) The divertor pressure in the flat-plate configuration is similar to that measured in the vertical-plate configuration, whereas the compression ratio is about a factor of two smaller.

6) The ion $B \times \nabla B$-drift direction has a negligible effect on the neutral pressure and compression ratio.

We have proposed a simple physics-based model aimed at a quantitative interpretation of the divertor neutral pressure measurements across a range of edge plasma parameters. Despite its limitations, the divertor neutral particle flux balance model resulted in a factor of two agreement in connecting independent experimental observations (i.e., pressures, edge plasma characteristics, and ion fluxes). The fundamental findings of the neutral flux balance analysis can be summarized as follows:

1) The divertor neutral pressure is primarily determined by the ion recycling source, the PFZ-plasma characteristic, and the divertor geometry.

2) The high neutral pressure sustained in the detached divertor state, despite a considerable drop in the recycling source, can be explained by the scattering of neutrals off the cold PFZ-plasma plugging the divertor throat

and reflection off the target plates, provided the detachment front is well separated from the plates.

3) Neutral escape through the leaks in the divertor structure becomes a significant loss channel at high divertor pressures.

In addition Appendix A shows that neither the fueling (except for transient events), nor the wall pumping affects the neutral particle dynamics.

Despite its moderate success, the neutral flux balance model proposed in the thesis greatly oversimplifies the complex neutral-plasma interactions in a tokamak divertor. We recommend that in the future a self-consistent two-dimensional model containing all relevant atomic physics phenomena is used to help us understand better the processes responsible for the observed experimental dependencies.

A relatively small number of additional diagnostics installed in Alcator C-Mod would help resolve key uncertainties encountered during the neutral transport analysis. Some of these diagnostic are already included in the Alcator C-Mod upgrade plans. The list below summarizes the desired experimental parameters, recommended diagnostics, and current implementation plans:

1) Localization of the detachment front and the SOL midstream characterization – divertor Thomson scattering system – to be installed for the Fall 1995 campaign.

2) Perpendicular ion flux towards the divertor target – recessed Langmuir probes – potentially planned for the Fall 1995.

3) Neutral pressure above the horizontal target – a new pressure gauge there, or alternatively, a sniffing tube around the open port gauge – no immediate plans.

Additional information provided by these diagnostics would improve our understanding of both the edge plasma physics and the neutral particle dynamics. Knowing the position of the detachment-front, particle flux towards the target, and the leakage flux, it would be possible to predict neutral pressure in the divertor and compare it with the measured value, thus cross-checking the measurement and the model proposed in the thesis. We recommend the installation of all of the above diagnostics.

The analysis carried out throughout the thesis led us to believe that the ability of Alcator C-Mod to confine neutrals in the divertor can be significantly improved. The two currently proposed modifications of the Alcator C-Mod divertor – closing the leakage-slot and redesigning the target plate geometry – will have a profound effect on neutral particle dynamics in the tokamak chamber. The neutral particle flux balance model allowed us to predict expected changes in the divertor and midplane pressures. These predictions are, however, speculative, because the changes in plasma characteristics have been neglected. The statements made below can only serve as a guidance for a more detailed future analysis. Within the limitations of the present model we found that:

1) Both modifications lead to a considerable increase in the compression ratio, especially in the detached-divertor regime, possibly by a factor of three to seven.
2) Closing the leakage slot causes a much greater improvement than redesigning of the divertor target geometry.

3) While the improvement (drop) in the midplane pressure occurs across the entire plasma density range, the improvement (increase) in the divertor pressure is significant in the detached state only.

4) The increase (decrease) in the divertor (midplane) pressure does not exceed a factor of three and is more typically only a factor of two.

When comparing the two proposed modifications, from the point of view of divertor neutral confinement, it seems that the divertor geometry redesign is less strongly justified compared with the leak-slot closing. The compression ratio improvement resulting from the geometry change is no better (most likely, a factor of two weaker) than that resulting from the leak-plugging, whereas the cost and man-power involved is probably at least a factor of ten higher. Gains in plasma characteristics (e.g., removal of the inner-divertor-nose radiating zone), however, may very well justify this modification in the near future. The improvement in neutral particle divertor confinement will come as an added bonus.

As mentioned before, one of the high heat flux solutions envisioned for ITER is the dynamic gas target divertor. This scheme requires a high neutral pressure to be sustained in the divertor chamber with a minimal effect on the pressure in the main tokamak chamber. We therefore recapitulate the major findings of this thesis in terms of measures that lead to the optimal neutral particle confinement in the divertor chamber:

1) The high-recycling divertor regime corresponds to the maximum compression ratio in the present Alcator C-Mod divertor configuration.

2) A tight divertor structure, i.e., no leakage-openings, is required to prevent loss of neutrals from the divertor volume.

3) Vertical-plate divertor configuration leads to a compression ratio about a factor of two higher than the horizontal-plate configuration.

4) The recycling source should be minimized above the divertor throat to reduce the main chamber neutral pressure and maximized below the throat to increase the divertor pressure.

5) A narrow divertor throat (tight baffling) is unnecessary because the PFZ-plasma itself prevents the neutrals from escaping across the throat through scattering and ionization processes, provided the mean-free-paths are much shorter than a typical escape distance.

A scientific study, no matter how extensive, is never complete. This thesis is no exception. For example, the full Alcator C-Mod potential for producing reactor-grade plasmas and their impact on neutral particle dynamics is yet to be explored. Also, the observations and analysis of the effect of the divertor structure modifications on the neutral dynamics will provide extremely useful data to examine further the correlation between the divertor geometry and its ability to confine neutrals.

It is the author's hope that the study presented in this thesis will contribute to our understanding of the neutral particle dynamics in the vicinity of a thermonuclear plasma and will inspire a continuing improvement in this exciting research area.

Appendix A

Wall Pumping

One of the still unsolved problems of a commercial tokamak reactor is retention of hydrogen isotopes by its first wall material. The large number of experiments performed to date in graphite- [131, 132, 133] and beryllium-wall [134, 135] tokamaks indicate that the first-wall hydrogen reservoir may exceed particle plasma content by orders of magnitude. In the case of tritium that constitutes a large radioactive material inventory. Alcator C-Mod, the only current high performance tokamak with high-Z metal (molybdenum) wall, allows investigation of the retention and release of hydrogen isotopes in a metal wall under reactor-relevant conditions.

The author, in cooperation with G. McCracken, performed a preliminary investigation of the wall-pumping issue in Alcator C-Mod. Since the problem is not central to the thesis this appendix provides only a summary and updated calculations. The details of the analysis have been reported earlier [111, 136]. A useful order-of-magnitude comparison of particle fluxes provided here (in Table A-1) supports some of the assumptions made elsewhere in the thesis.

A.1 Fueling and pumping rates

The wall pumping and retention measurements are based on a total particle balance inside the Alcator C-Mod vacuum vessel. Fast time-scale measurements of gas puffing rate, electron plasma count, and neutral particle count allow us to infer wall pumping rate during a discharge as the closing term of the total particle balance equation:

$$P_{wall} = I_{piezo} + I_{caplr} - \frac{\mathrm{d}\, N_e/2}{\mathrm{d}t} - \frac{\mathrm{d}N_N}{\mathrm{d}t} \qquad \text{(A.1)}$$

where the symbols used are as follows:

I_{piezo} - is the particle input rate through the piezo-valve;

I_{caplr} - is the particle input rate through the capillary valve;

N_e - is the total electron count in the plasma;

N_N - is the total neutral count in the vessel;

P_{wall} - is the wall pumping (loading) rate;

and all the terms (except N_e) are expressed in molecules/s.

Whereas the capillary input rate is measured during discharges through the depletion of the plenum pressure, the piezo-valve input rate is inferred from additional calibration experiments (recall Chapter 2). Because of a smaller accuracy of the latter, data presented in Fig. A-1 were collected during a capillary-only phase of a discharge. Time integrated data shown on Fig. A-2 contains input from both valves.

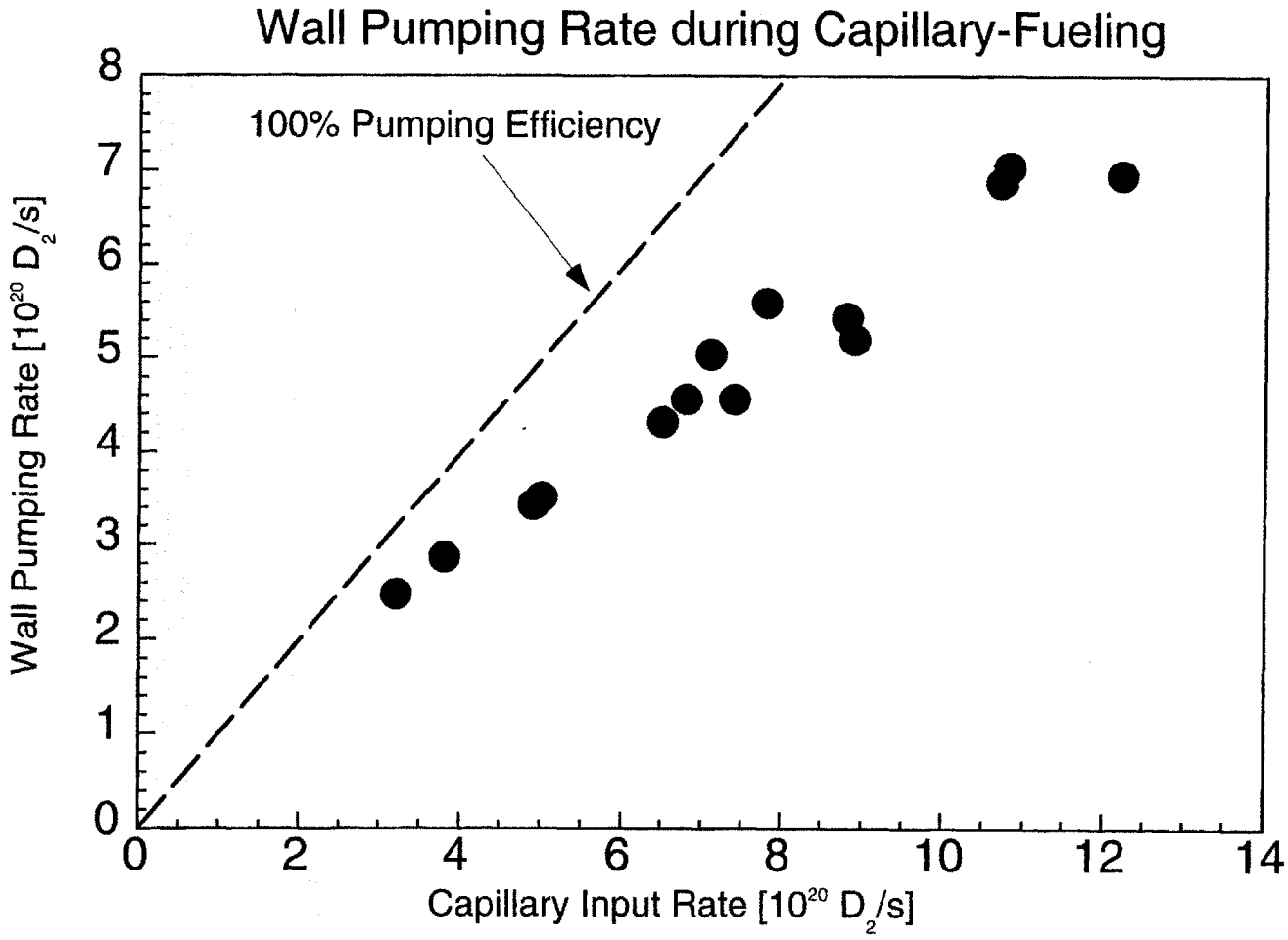

Fig. A-1: Wall pumping rate, calculated with Eq. A.1 during a capillary-injection phase of a discharge, plotted versus the capillary input rate. The entire tokamak vessel is treated as a lump component.

The interferometer-measurements combined with the reconstruction algorithm of Luke [24] (recall Section 2.2) provide the total electron plasma count (N_e). Note an implicit assumption of Z_{eff}=1 in Eq. A.1. This assumption is satisfied in high density Alcator C-Mod plasmas ($\bar{n}_e \geq 1.5 \cdot 10^{20}$ m^{-3}) but only approximately in low density plasmas [137].

The neutral pressure measurements provide the total neutral particle count (N_N). During collection of the data presented in this appendix only the midplane gauge was operational. In order to account for the particle inventory in the divertor-volume (which also includes bottom vertical diagnostic ports) the particle count in the midplane-volume was multiplied by a volume ratio (~1/20) and the average compression ratio (~40). This approximation may result even in a ~100% error in the divertor neutral particle content, but because this quantity is one of less significant terms in Eq. A.1 the final error does not exceed 20%.

Fig. A-1 shows the wall pumping rate calculated with Eq. A.1 as a function of the capillary-valve input rate. All data come from single bottom null 800 kA ohmic discharges. All time slices correspond approximately to the middle of the capillary-only discharge phase. Fig. A-1 shows that the wall pumping rate varies from ~80% of the fueling flux at low input rates (~$3 \cdot 10^{20}$ D_2/s) to ~50% at high input rates (~10^{21} D_2/s).

Table A-1 compares order-of-magnitude estimates of particle fluxes in Alcator C-Mod. It lists the fueling and wall pumping rates illustrated in Fig. A-1. In addition, Table A-1 contains an estimate of turbo-pump exhaust rate. The author has constructed an empirical expression for the turbo-pump exhaust rate (as a function

Particle Fluxes in Alcator C-Mod			
at core plasma density [10^{20} m^{-3}]	~0.5	-	~2.0
turbo-pump exhaust rate	10^{18}	-	10^{19}
valve fueling rate	10^{20}	-	10^{21}
wall pumping rate	10^{20}	-	10^{21}
midplane-reservoir neutral flux	10^{21}	-	10^{22}
divertor-reservoir neutral flux	10^{22}	-	10^{23}
divertor ion flux	10^{22}	-	10^{23}
all fluxes in units: [particles/sec]			

Table A-1: Order-of-magnitude comparison of particle fluxes in Alcator C-Mod discharges. Turbo-pump exhaust rate is negligible in comparison with the valve fueling and wall pumping rates. All three, in turn, are negligible in comparison with the neutral-particle-balance and ion fluxes.

of pressure) by following long-time pressure history in a well conditioned chamber. The turbo-pump exhaust rate is negligible in comparison with the wall pumping and the fueling rates, which allowed us to neglect it in Eq. A.1.

In addition, Table A-1 compares the fueling and pumping rates with the neutral-particle-balance and ion fluxes calculated in Chapters 5 and 7. All of the balance fluxes are at least an order of magnitude larger than the fueling and pumping rates. Therefore these rates were neglected in the neutral flux balance equations in Chapters 5 and 7.

Analysis of the time history of the wall pumping rate (not shown) suggest that the entire chamber walls exposed to a flux of ~10^{21} D_0/s start to saturate after about 0.1 sec. Because of the relative magnitude of particle fluxes (in Table A-1) and surface areas exposed to the plasma, we estimate that the divertor target plates saturate within ≤10 ms after diversion of the plasma. Thus the unity recycling coefficient at the target was used in Chapters 5 and 7.

A.2 Wall retention and release

Eq. A.1, upon integrating, provides a measure of the total number of particles retained by the walls during a discharge. Fig. A-2 plots the number of retained particles (molecules) versus the total number of particles introduced into the vessel through the fueling valves. A dependence similar to the one in Fig. A-1 is observer here. The fraction of particles retained by the walls decreases from ~80% at low fueling and density discharges to ~60% at high fueling and density discharges.

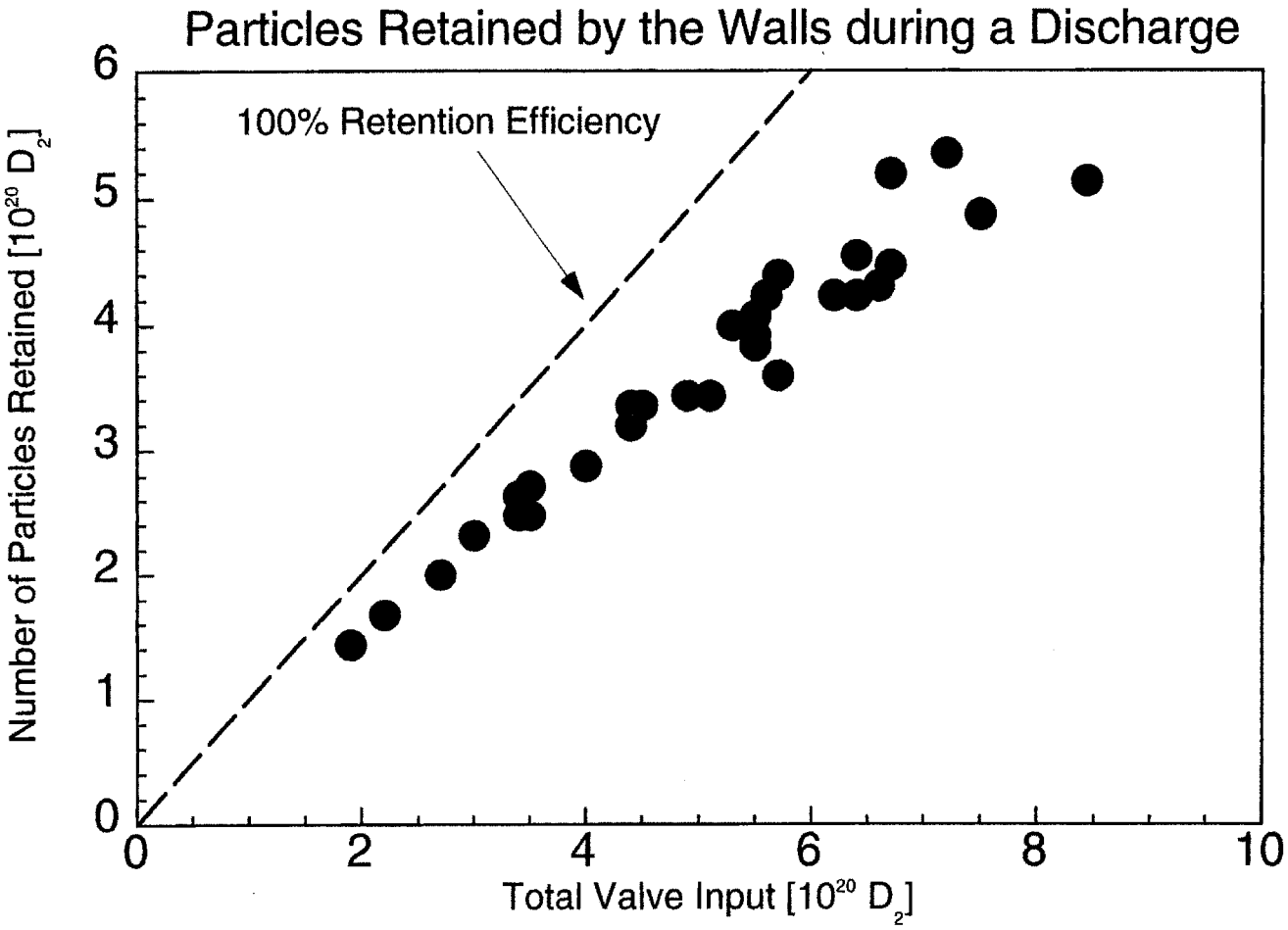

Fig. A-2: Total number of particles retained by the Alcator C-Mod walls plotted as a function of total number of particles introduced into the vessel.

A second important conclusion from Fig. A-2 is that the number of particles retain by the walls is only 5-10 times larger than the plasma particle count. This is in contrast to graphite tokamaks where the wall hydrogen inventory may exceed plasma count by orders of magnitude [131].

After a discharge the walls release retained hydrogen through diffusion and outgassing processes. Having characterized the turbo-molecular pumps we can quantify the release rate by following the vessel pressure over a long period of time after a discharge:

$$R_{wall} = \frac{N_N}{\tau_{turbo}} + \frac{dN_N}{dt} \qquad \text{(A.2)}$$

where:

R_{wall} - is the wall release rate in molecules/sec;

τ_{turbo} - is the effective pumping speed (including conductance) of deuterium by Alcator C-Mod turbo-molecular pumps, which is a function of pressure.

Measurements with a residual gas analyzer indicate that the gas in the vessel is dominated by hydrogen isotopes for at least 1000 sec. after a discharge. Thus impurity outgassing is neglected in Eq. A.2. A typical release rate is about $5 \cdot 10^{18}$ D_2/s immediately after a discharge, but decreases to below 10^{17} D_2/s in less then 100 sec.

Upon integration, Eq. A.2 provides a measure of the total number of particles released by the walls. Fig. A-3 plots this quantity versus the total number of particles retained by the walls (from Fig. A-2). The observed lack of strong variation in the number of released particles may be due to a relatively constant concentration of deuterium near the molybdenum surface combined with the

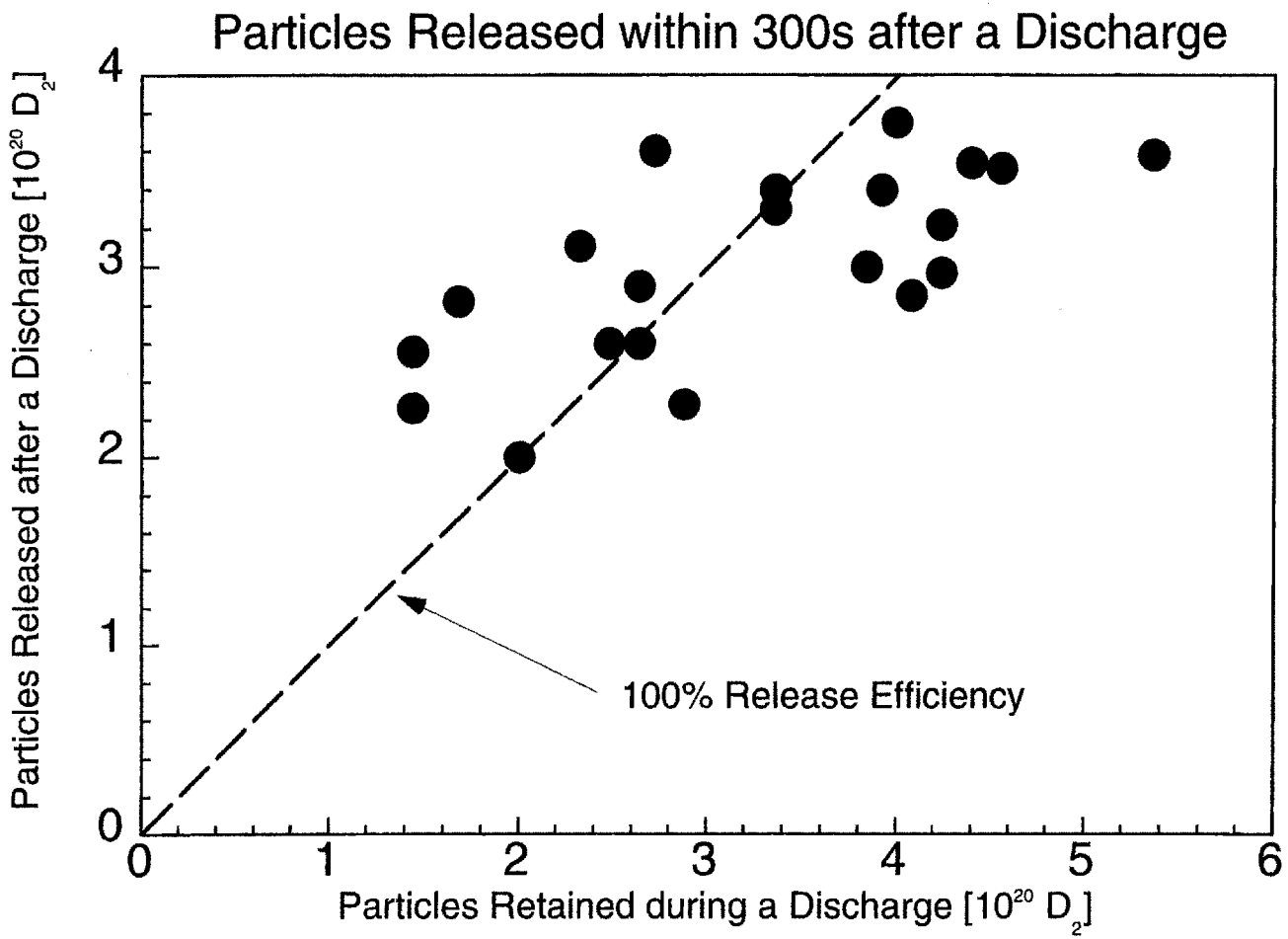

Fig. A-3: Total number of particles released by the walls within 300 sec. after a discharge plotted as a function of number of particles retained during the corresponding discharge (but not the total wall inventory).

constant integration time. The integration is carried out for 300s (when the outgassing rate drops to about 5% of its initial value), which is about one-half of the time between the discharges. The fraction of released particles varies from ~150% at low wall inventory to ~70% at high inventory. The surplus of released particles after low density discharges is presumed to be caused by continued outgassing after earlier high density ones.

A.3 Wall pumping summary

We found that the wall pumping rate depends strongly on the fueling rate (it is fairly independent of plasma current, or electron temperature). The wall reservoir starts to saturate at a rate of ~10^{21} D_0/s after about 0.1 sec. The total deuterium wall reservoir in Alcator C-Mod does not exceed 10× the plasma particle content, which is at least an order of magnitude smaller than the wall reservoir in graphite tokamaks. Even though the release rate is 100-1000× slower than the pumping rate, in molybdenum (unlike in graphite) at least 50% of the particles pumped during a 1 sec. discharge are released within 100 sec. after the shot.

From the perspective of hydrogen isotope retention in a tokamak first wall, molybdenum seems to be a better reactor material candidate than graphite [138], since there will be no large inventory of tritium stored in the wall. The topic is far from being explored and warrants much more extensive research. This, however, is outside the scope of this thesis.

Appendix B

Atomic Physics Data

This appendix reviews the data adopted from the literature to describe the atomic processes included in the calculations carried out throughout the thesis (primarily in Chapter 5). In most instances there are multiple sources of information not necessarily agreeing with each other. The author's choice was primarily dictated by the acceptance of a given expression by the edge plasma physics community and its ease of use in a computer code.

The particle and energy reflection coefficients were calculated using approximate analytic expression given by Thomas [113]. The coefficients are functions of projectile and target masses and reduced energy of the system. Fig B-1 presents results for a deuterium ion impacting onto a molybdenum target plotted versus ion energy. Both coefficients decrease with increasing impact energy.

The electron-impact ionization rate was calculated using a polynomial fit proposed by Janev [139]. Fig. B-2 shows the reaction rate as a function of the electron temperature. The isotope distinction between hydrogen and deuterium is unnecessary due to a much higher speed of the electron compared with an ion.

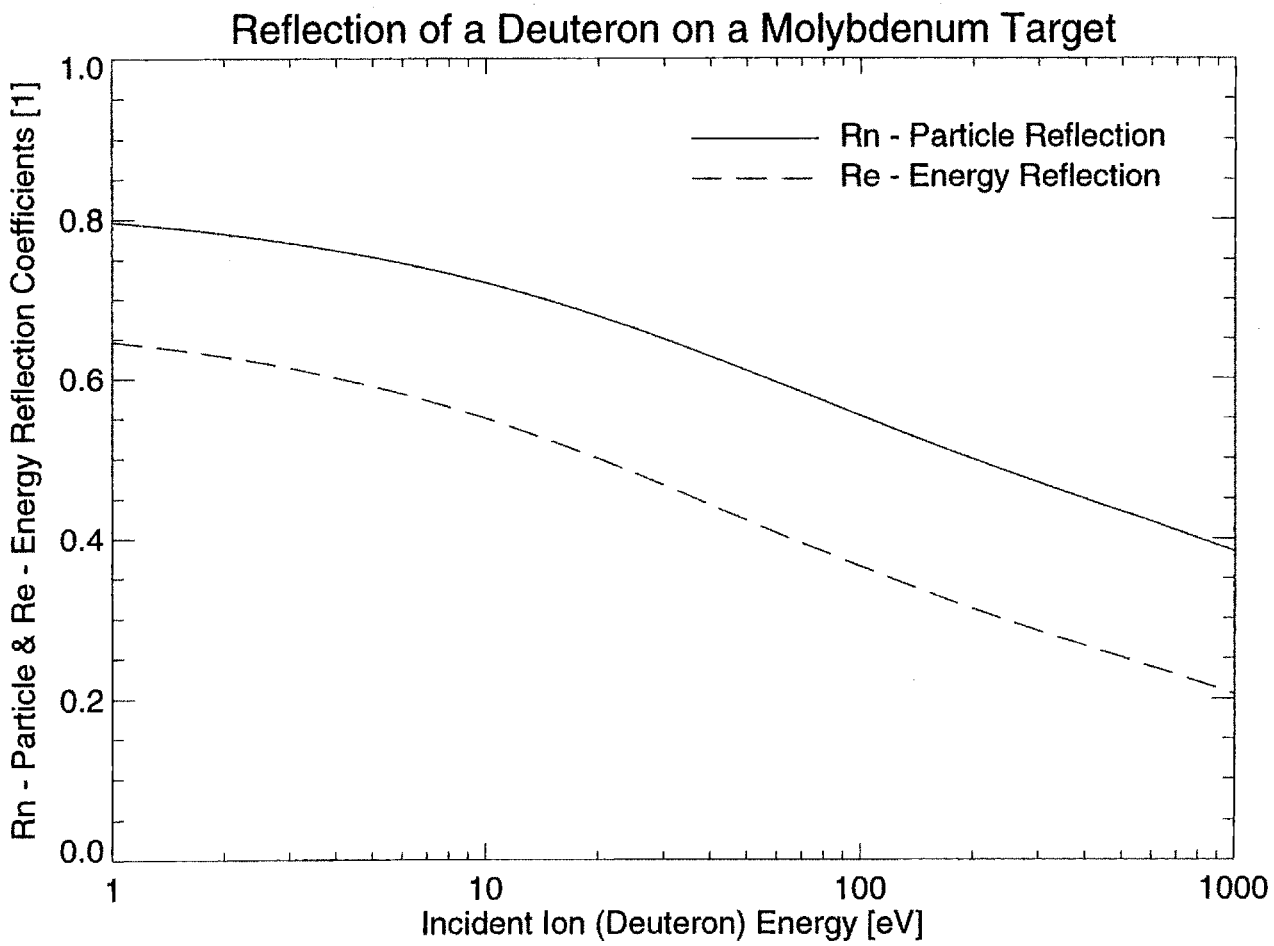

Fig. B-1: Particle (R_n) and energy (R_e) reflection coefficients plotted as a function of deuterium ion energy impacting onto a molybdenum target.

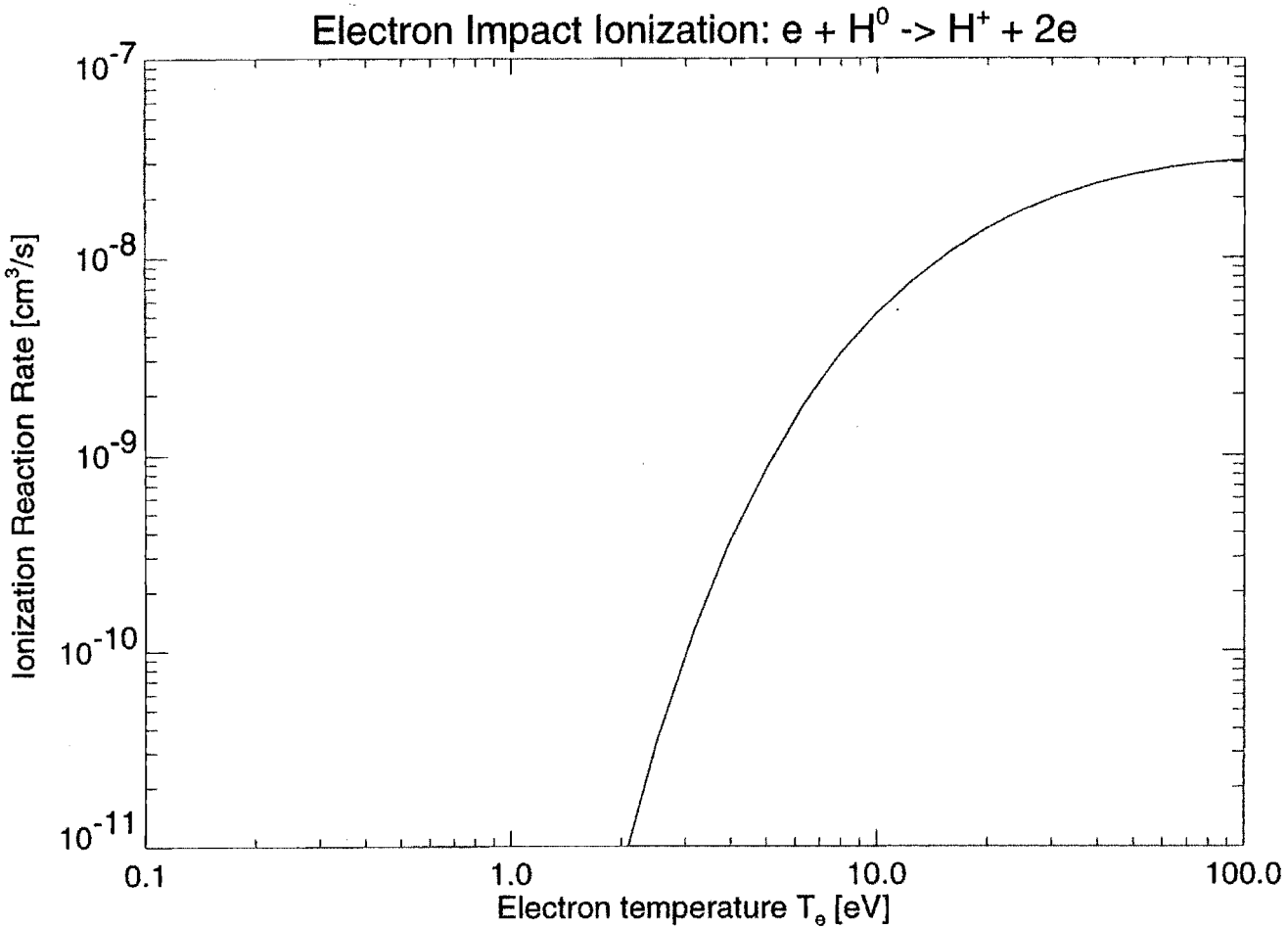

Fig. B-2: Reaction rate for electron-impact ionization of a hydrogen (or deuterium) atom.

Janev [139] also provides a polynomial fit for hydrogen ion-atom charge-exchange rate. Fig. B-3 shows the rate, which is a function of both the atom energy and the ion temperature. We use the widely adopted requirement of equal relative velocities [140] to translate the hydrogen reaction rate to the deuterium one:

$$K_{cx}^{D}(E_{atom}, T_{ion}) = K_{cx}^{H}(E_{atom}/2, T_{ion}/2) \qquad \text{(B.1)}$$

where:

K_{cx}^{D} - is the deuterium charge-exchange rate;

K_{cx}^{H} - is the hydrogen charge-exchange rate;

E_{atom} - is the atom energy;

T_{ion} - is the ion temperature.

The resulting deuterium charge-exchange reaction rate, included in Fig. B-3, is used throughout the thesis.

The total momentum-transfer rate is the sum of the charge-exchange and the elastic-collision momentum-transfer rates (Eq. 5.9). It seems, however, that the literature lacks a unanimous opinion of the relative importance of the two processes. Dalgarno [141] shows that over a wide range of energies the momentum-transfer cross-section is twice the charge-exchange cross-section in the center-of-mass (cm) frame, which implies that charge-exchange provides the dominant contribution to the momentum transfer process. Similarly, Wadehra [142], who has calculated deuterium momentum-transfer including both channels, states that charge-exchange dominates for energies E_{cm} >5 eV. Bachmann and Belitz [143] have recently calculated ion-atom elastic-collision momentum-transfer rates, using a classical approximation. These rates are typically ~1/5 of the

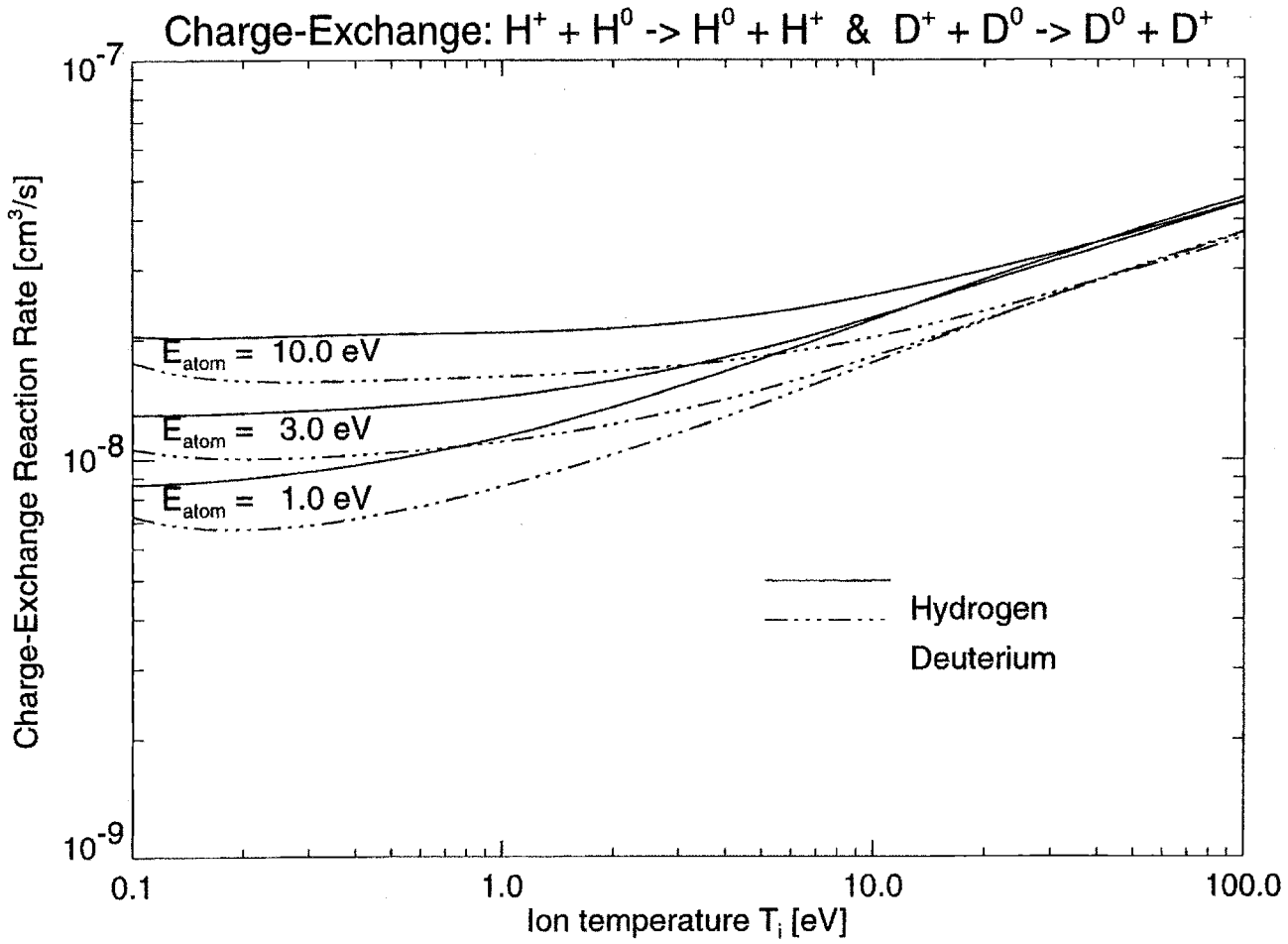

Fig. B-3: Reaction rate for hydrogen charge-exchange (solid line) calculated with the polynomial fit. The deuterium charge-exchange reaction rate (dash-dot line) is derived from the hydrogen data using Eq. B.1.

charge-exchange rates (compared with ref. [139]) for the energy range of interest here (few eV). However, elastic-collision and total momentum-transfer cross-sections calculated recently by Schultz et al. [104] using a semi-classical approximation are 2-5 times higher than those of Bachmann and Belitz.

In view of these uncertainties, for the thesis we adopt a sensitivity-analysis approach. All the calculations in the main part of the thesis are carried out assuming that charge-exchange significantly dominates the momentum-transfer rate, i.e., the elastic collisions are neglected:

$$K_{mt} = 1 \cdot K_{cx} \tag{B.2}$$

All affected calculations are then repeated using the assumption that elastic-collisions are as important as charge-exchange events, i.e.:

$$K_{mt} = 2 \cdot K_{cx} \tag{B.3}$$

Appendix E reports the results of flux balance calculations using Eq. B.3 and discusses differences resulting from the two different assumptions about the importance of the elastic collisions.

Schultz et al. [104] also provide cross-sections for atom-atom and molecule-molecule momentum-transfer collisions. These are used to calculate the mean-free-paths listed in Table 5-2.

Finally, in all of the expressions used here any dependence on particle density is neglected. This introduces a negligible error compared with the overall accuracy of the analysis.

Appendix C

Electron-Conduction Plasma Model

This appendix describes the "electron-conduction" model, which is used throughout the thesis (as one of the two alternatives) to model the plasma parameters in the divertor space.

The model interpolates plasma electron temperature along the common-flux-zone (CFZ) field lines between the Langmuir-probe measurements down- (divertor probes) and up-stream (reciprocating probe) through an electron heat-conduction equation. The 1D interpolation is repeated along each flux surface of interests independently. The standard Spitzer's expression [144] is used for the heat conductivity. In a specific implementation, proposed by Kesner [99], SOL-radiation occurs at a discrete point in space where T =10 eV. As a result, the electron temperature is described by a relatively simple differential equation (adopted here after Kurz [37]):

$$\frac{\mathrm{d}}{\mathrm{d}s}\left(\kappa_0 T^{5/2}\frac{\mathrm{d}T}{\mathrm{d}s}\right) = R_0\delta(s-s_r) - H_0\Theta(s-s_h) \qquad \text{(C.1)}$$

where:

s - is the coordinate measured along a field line in the direction away from the target;

T - is the plasma electron temperature;

s_r - is the s-space position of the T =10 eV isotherm;

s_h - is the X-point position in the s-space;

κ_0 - is the heat-conductivity constant;

R_0 - is the radiation constant;

H_0 - is the cross-field-diffusion heating constant;

The delta function (δ) in Eq. C.1 marks a discrete point in space (T =10 eV), where all of the SOL-radiation occurs. The Heavyside step-function (Θ) indicates the perpendicular heat diffusion from the core plasma into the SOL above the X-point (s_h). These simplified source terms allow one to solve Eq. C.1 analytically. Both Kesner and Kurz provide details of the solution.

Additionally Kurz [37] assumes a linear plasma pressure drop along a field line in the cold plasma region, where T <6 eV. This leads to the following expression for the plasma pressure (p):

$$p = p_1 + (p_1 - p_0)\left(\frac{s}{s_{cx}} - 1\right)\cdot\Theta(s_{cx} - s) \qquad \text{(C.2)}$$

where:

p_0 - is the plasma pressure measured upstream by the scanning Langmuir probe;

p_1 - is the plasma pressure measured downstream by the divertor Langmuir probes;

s_{cx} - is the s-space coordinate of the T =6 eV isotherm – in this simplified model this corresponds to the detachment front location.

When the plasma flow is neglected, Eqs. C.1 and C.2 combined with the plasma pressure equation determine electron plasma density (n):

$$p = 2\,n\,T \qquad \text{(C.3)}$$

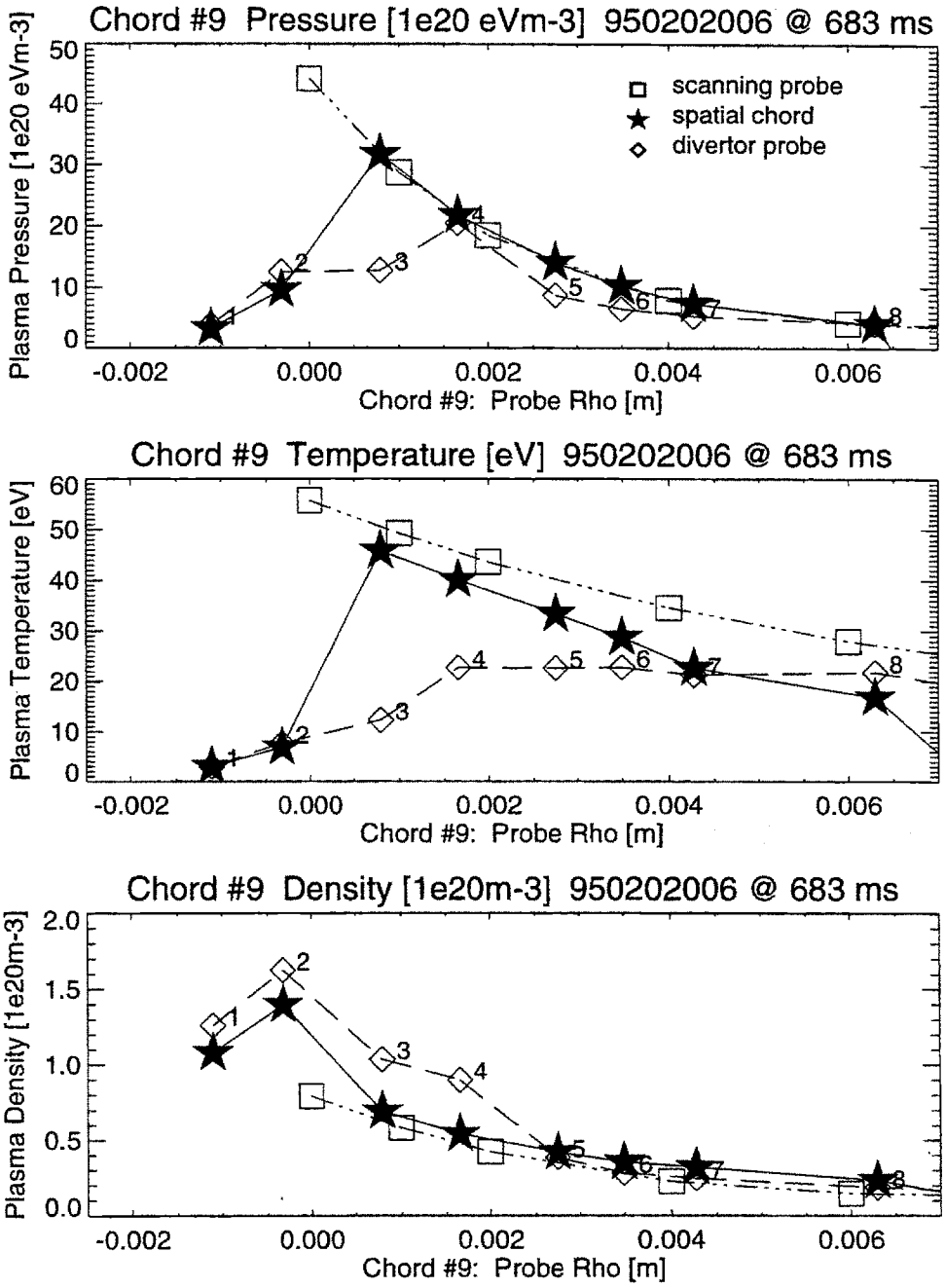

Fig. C-1: Plasma profile along a spatial chord #9 (see Fig. 5-1) obtained using the "electron-conduction" model connecting the scanning- and divertor-probe measurements. A representative attached divertor discharge is shown.

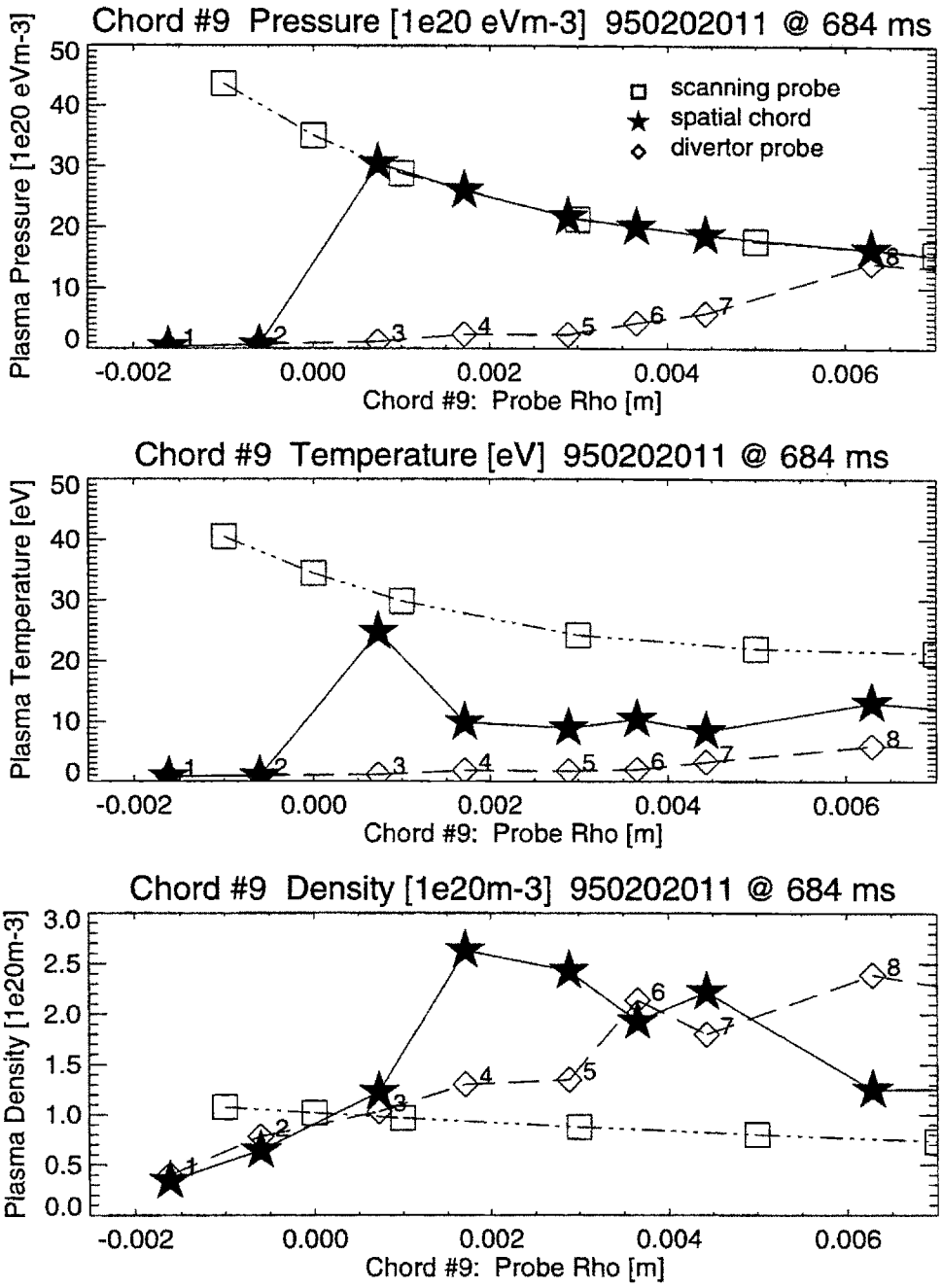

Fig. C-2: Plasma profiles equivalent to those on the previous figure for a representative detached divertor discharge.

The private-flux-zone (PFZ) plasma is more difficult to describe, because of the lack of corresponding up-stream measurements. 2D modeling with the UEDGE code [145] indicates that plasma parameters are nearly constant along the private-flux-zone field-lines. As a reasonable approximation PFZ density and temperature are linearly interpolated along the field lines connecting the inner and outer target probe measurements.

The above description of the divertor- and SOL-plasma has been implemented as a computer code by Kurz for Alcator C-Mod data analysis [37]. The code is adopted here to calculate background plasma parameters necessary for neutral transport modeling. Figs. C-1 and C-2 show resulting plasma profiles calculated along the spatial chord #9 (extending from the PFZ-boundary across the divertor throat; recall Fig. 5-2), compared with the probe measurements for representative attached and detached divertor discharges respectively. Note that because of uncertainty about EFIT flux-surface mapping the fast-scanning probe profiles are shifted by ρ = -2 mm (following Labombard's prescription [72]) to preserve consistency in parallel plasma pressure gradient.

Appendix D

Diffusive Neutral Transport

The fluid neutral transport equations are well known and can be found in numerous references. For example, Lehnert [146] provides a comprehensive analysis of equilibrium between the plasma and the neutral gas. Instead of adopting a prepared solution, however, we derive here the fluid neutral transport equation for completeness and to examine the assumptions involved. The transport equation is then used to calculate plasma albedo to neutrals in Section 5.5.

A fluid description of a medium requires a high level of collisionality of its components. Recall from Section 5.2 that the neutral-neutral collisions are infrequent ($\lambda_{nn} \gg L$). The fluid description is warranted here by a sufficient ion-neutral collision frequency ($\lambda_{in} \ll L$). This results in a close coupling between the ion and neutral populations. In a fluid description the neutral flux and density are described by well established continuity and momentum balance equations. In the absence of a volumetric source of neutrals (no recombination) the continuity equation contains only the loss term, resulting from electron-impact ionization:

$$\nabla \cdot \vec{\Gamma}_N = -NnK_{ion} \tag{D.1}$$

where:

N - is the neutral atom density;

n - is the plasma density (ions or electrons);

K_{ion} - is the ionization reaction rate;

and the diffusive flux of neutrals is simply given by the product of the density and a neutral drift velocity:

$$\vec{\Gamma}_N = \vec{v}_D N \tag{D.2}$$

The momentum balance equation is:

$$\frac{d}{dt}\left(MN\vec{v}_D\right) = -\nabla p - MNn\vec{v}_D K_{mt} - MNn\vec{v}_D K_{ion} \tag{D.3}$$

where:

p - is the neutral pressure;

M- is the mass of a deuteron;

K_{mt} - is the momentum transfer reaction rate (this includes both charge exchange and elastic collisions with ions);

Note that the middle RHS term in Eq. D.3 describes momentum exchange with ions through the collisions which conserve particles whereas the last RHS term describes momentum loss due to change in particle population. Because Eq. D.3 is intended to describe cross-field neutral transport (in spite of its general vector form), the perpendicular ion drift velocity is neglected in the momentum exchange term.

Upon expanding the total time derivative and substituting the continuity equation for the ionization term in the momentum balance equation it simplifies to:

$$\frac{\partial}{\partial t}\left(MN\vec{v}_D\right) = -\nabla\left(MNv_D^2 + NT_N\right) - MNn\vec{v}_D K_{mt} \tag{D.4}$$

where:

T_N - the neutral temperature multiplied the density was substituted for the neutral pressure.

Because we consider neutral transport in the direction perpendicular to the magnetic field the drift flow to be subsonic, i.e., neutral fluid drift velocity is much smaller than the atom thermal velocity. This allows us to neglect the convective energy gradient when compared with the thermal energy gradient in Eq. D.4. Thus in steady state Eq. D.4 simplifies to:

$$0 = -\nabla\left(NT_N\right) - MNn\vec{v}_D K_{mt} \tag{D.5}$$

Eq. D.5, combined with the definition in Eq. D.2, yields a useful expression for the neutral flux as a function of a neutral pressure gradient:

$$\vec{\Gamma}_N = -\frac{\nabla\left(NT_N\right)}{MnK_{mt}} \tag{D.6}$$

The above can be directly compared with the Fick's law, expressing the flux as a function of a neutral density gradient:

$$\vec{\Gamma}_N = -D_N \nabla N \tag{D.7}$$

In order to simplify the following treatment we assume a constant neutral temperature (assumed equal to the Franck-Condon dissociation energy in Chapter 5). Recall, however, that the neutral and ion fluids are well coupled through the elastic and charge-exchange collisions. As a result the assumption of constant neutral temperature is applicable only in the region of cold plasma (referred to as a "diffusive" region in Section 5.5), where T $\approx$3 eV; it becomes inaccurate in the hot plasma region ("absorbing" in Section 5.5) where T $\gg$3 eV. In consequence Eq. D.7 overestimates the neutral diffusive flux in comparison with Eq. D.6 because the neutral pressure gradient is less steep than the density gradient. The potential error is larger in attached hot plasma cases then in the

detached cases, where the neutrals are separated from the hotter plasma region by a thicker layer of cold plasma with the temperature close to ~3 eV (Franck-Condon energy). Because the accuracy of the flux balance calculations carried out in Chapter 5 is at best a factor of two the above assumption is acceptable in this treatment. It should be corrected, however, in a future more accurate analysis.

The assumption of constant neutral temperature allows us to derive the expression for the neutral diffusion coefficient and to derive the neutral diffusion equation. Using the definition of the momentum transfer mean-free-path (Eq. 5.8) the neutral diffusion coefficient becomes:

$$D_N = \frac{T_N}{MnK_{mt}} = \frac{v_0 \lambda_{mt}}{2} \tag{D.8}$$

Fick's law (Eq. D.7) combined with the above expression for the diffusion coefficient can be directly inserted into the continuity equation (Eq. D.1) to yield:

$$\nabla \cdot \left(-\frac{v_0 \lambda_{mt}}{2} \nabla N \right) = -NnK_{ion} \tag{D.9}$$

Upon substituting the ionization mean-free-path for the reaction rate (Eq. 5.10) and recalling the constant neutral temperature assumption we finally obtain the neutral diffusion equation in an elegant form involving only the characteristic interaction lengths and the neutral density itself:

$$\nabla \cdot \left(-\frac{\lambda_{mt}}{2} \nabla N \right) = -\frac{N}{\lambda_{ion}} \tag{D.10}$$

Eq. D.10 is used in Section 5.6 to describe diffusive transport of neutrals across plasma plugging the divertor throat.

Appendix E

Momentum-Transfer Rate Uncertainty

This appendix discusses the effect of uncertainty in the atom-ion momentum-transfer rate. We assume here that the elastic collisions have a contribution equal to that of the charge-exchange events to the momentum transfer rate (Eq. B.3). This is in contrast to Chapters 5 and 7, where elastic collisions have been neglected (Eq. B.2).

The momentum-transfer rate enters directly the plasma albedo calculated in Section 5.5 using the diffusive neutral transport model. Following the simplified analytic scaling (Eq. 5.30) a shorter momentum-transfer mean-free-path leads to an increased albedo. The actual change, however, is stronger from that resulting from Eq. 5.30 because of a non-linearity of the full solution of Eq. 5.20. The above calculated albedo is then integrated over the PFZ-boundary (using Eq. 5.35), together with the ballistic plate reflection (unaffected by the momentum-transfer rate change), to yield the total albedo to neutrals escaping from the PFZ-reservoir. This quantity, calculated for both background plasma models, is listed in Table E-1, where the remaining components of the divertor particle flux balance (Eq. 5.1) are also included.

Divertor neutral particle flux balance including atom-ion elastic collisions.

parameter	units	hot/attached divertor ...				... cold/detached divertor
Discharge Number:		**6**	**7**	**10**	**11**	**13**
core electron density	[1e20/m3]	1.01	1.26	1.57	1.86	2.09
<u>Measured/estimated fluxes</u>						
Source: Flush probe BN div. ion flux	[1e22 D+/s]	6.0	15.2	19.9	8.3	5.4
Sink: Leakage (x2)	[1e22 2*D2/s]	0.1	0.5	1.6	2.1	2.4
Sink: PFZ-kinetic	[1e22 D0/s]	3.1	14.3	44.4	55.9	65.3
NO refl. & trans. Source/Sink:	x 20 !	*1.87*	*1.03*	*0.43*	*0.14*	*0.08*
<u>Electron-conduction plasma model:</u>						
plate-> PFZ transmission	[1]	0.907	0.908	0.807	0.709	0.520
Source: Ions->atoms transmitted /3	[1e22 D0/s]	1.8	4.6	5.4	2.0	0.9
PFZ-escape albedo	[1]	*0.654*	*0.687*	*0.756*	*0.828*	*0.800*
Sink: PFZ-neutrals lost + leak	[1e22 D0/s]	1.2	5.0	12.4	11.7	15.5
Modeled Source/Sink:	x 20 !	***1.53***	***0.92***	***0.43***	***0.17***	***0.06***
<u>Constant-Te plasma model:</u>						
plate-> PFZ transmission	[1]	0.907	0.945	0.912	1.000	1.000
Source: Ions->atoms transmitted /3	[1e22 D0/s]	1.8	4.8	6.1	2.8	1.8
PFZ-escape albedo	[1]	*0.657*	*0.756*	*0.839*	*0.996*	*0.999*
Sink: PFZ-neutrals lost + leak	[1e22 D0/s]	1.2	4.0	8.7	2.3	2.4
Modeled Source/Sink:	x 2 !	***1.54***	***1.20***	***0.70***	***1.22***	***0.74***

Table E-1: Divertor neutral particle flux balance, calculated assuming that the atom-ion elastic collisions are as important as the charge-exchange events in the momentum transfer rate. The table lists the same quantities as Table 5-5, where the elastic collisions have been neglected.

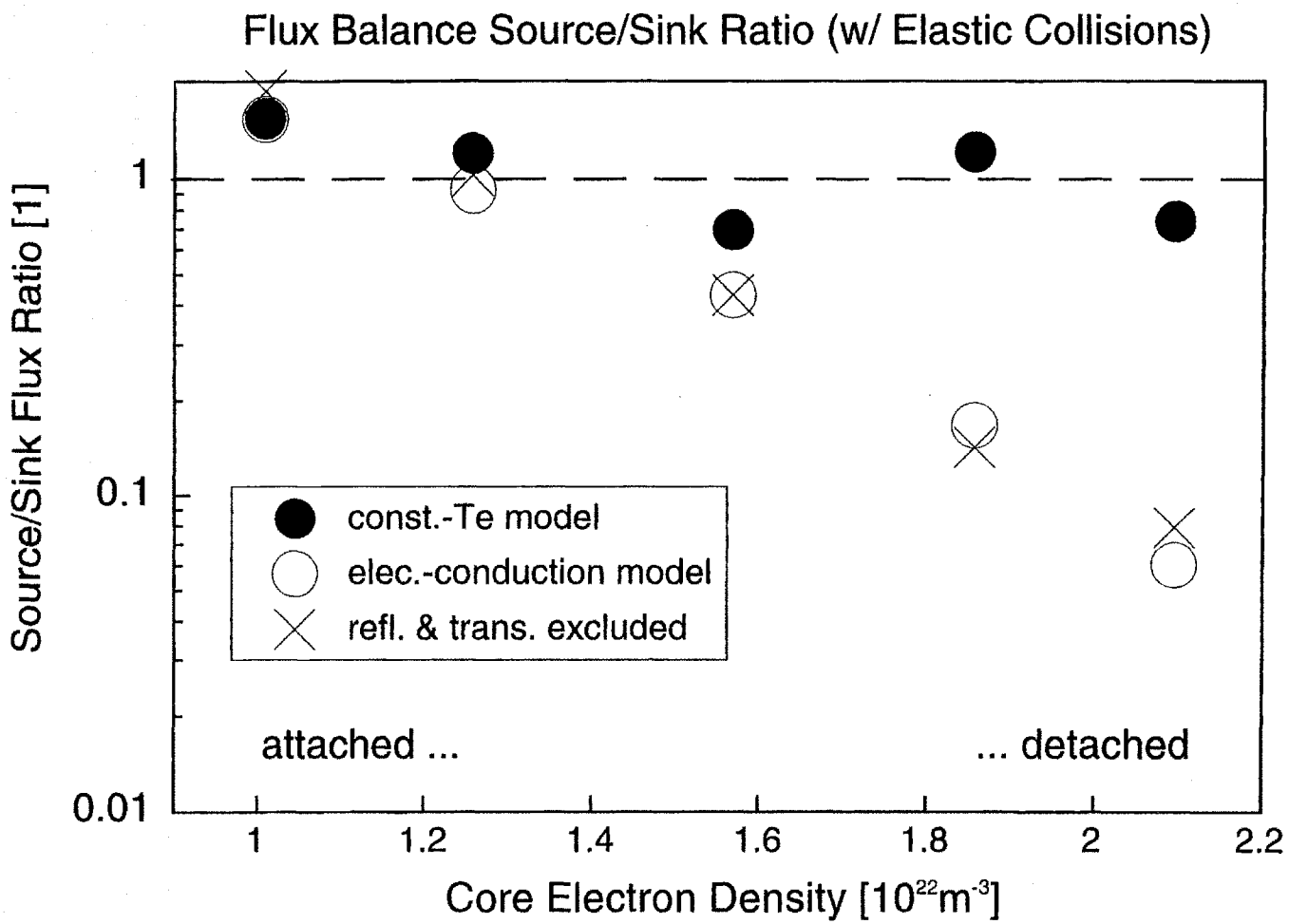

Fig. E-1: Comparison of the source-to-sink ratio in the divertor neutral particle flux balance, calculated assuming that the atom-ion elastic collisions are as important as the charge-exchange events in the momentum transfer rate. The figure is equivalent to Fig. 5-16, where the elastic collisions have been neglected. The conclusions of the thesis are independent of the present uncertainty in the atom-ion momentum-transfer rate.

Fig. E-1 shows the source-to-sink ratio, also included in Table E-1, modeled using the modified momentum-transfer rate. There is no significant difference between Fig. E-1 and the corresponding Fig. 5-16 in Chapter 5. The sink term is slightly weaker than in the corresponding Table 5-5 but the balance is still maintained to within a factor of two across the entire plasma density range of interest. All the conclusions of the analysis in Chapter 5 are still valid. Doubling the momentum-transfer rate actually emphasizes neutral-scattering as the main process responsible for the neutral confinement in the divertor by the cold SOL-plasma.

The change in the momentum-transfer rate impacts, however, the analysis carried out in Chapter 7. Because of a much higher albedo the net escape flux towards the plasma (Γ_{pfz}^{esc}) becomes, in the detached-divertor state, much smaller than the leakage flux. As a result, closing leaks in the divertor structure has a much stronger effect, suppressing the dominant loss mechanism of the neutrals. This leads to the expected divertor pressure and compression to reach 200 mTorr and 700 respectively, i.e., values double of those predicted without the elastic collisions. Thus if elastic collisions are large it makes it more important to implement the proposed structural changes of the Alcator C-Mod divertor hardware.

In summary, the general conclusions of the thesis are independent of the current uncertainty in the atom-ion momentum-transfer rate.

References

[1] P. C. Stangeby and G. M. McCracken, "Plasma Boundary Phenomena in Tokamaks", *Nuclear Fusion*, **30 (7)**, pp. 1225-1379, 1990.

[2] D. B. Heifetz, "Neutral Particle Transport", in *Physics of Plasma-Wall Interactions in Controlled Fusion* (D. E. Post, R. Berish eds.), Proc. NATO Advanced Study Institute Val-Morin, Quebec, 1984, NATO ASI Series, Vol. 131, Plenum Press, New York, pp. 695-771, 1986.

[3] J. Wesson, *"Tokamaks"*, Clarendon Press, Oxford, 1987.

[4] C. S. Pitcher and P. C. Stangeby, "Experimental Divertor Physics", to appear in *Plasma Phys. Controlled Fusion.*

[5] D. E. Post, R. F. Mattas, "Impurity Control Systems for Reactor Experiments", in *Physics of Plasma-Wall Interactions in Controlled Fusion* (D. E. Post, R. Berish eds.), Proc. NATO Advanced Study Institute Val-Morin, Quebec, 1984, NATO ASI Series, Vol. 131, Plenum Press, New York, pp. 695-771, 1986.

[6] *"ITER Design Report"*, 4th Technical Advisory Committee Meeting, San Diego Joint Work Site, 1994.

[7] G. Janeschitz, et al., *J. Nucl. Mater.*, **220-222**, pp. 73-88, 1995.

[8] G. Janeschitz, et al., *"The Physics Basis and Design of the ITER Divertor and of the Pumping, Fueling System"*, ITER-JCT Joint Worksite Garching, 1994.

[9] Kaye S. M., et al., *J. Nucl. Mater.*, **121**, pp. 115-125, 1984.

[10] Greenwald M., private communication, Nov. 1994

[11] M. Greenwald et al., *Phys. Plasmas*, **2(6)**, p. 2308, 1995.

[12] I. H. Hutchinson et al., *Phys. Plasmas*, **1(5)**, p. 1511, 1994.

[13] E. Apgar, B. Coppi, A. Gondhalekar, H. Helava, D. Komm., et al. in *Plasma Physics and Controlled Fusion Research* 1976, Berchtesgaden, (IAEA, Vienna), Vol. I, p. 247, 1977.

[14] M. Gaudreau, A. Gondhalekar, M. H. Hughes, D. Overskei, and D. S. Pappas, *Phys. Rev. Lett.*, **39**, p. 199, 1977.

[15] B. Lipschultz, et al., *J. Nucl. Materials*, **162-164**, pp. 793-798, 1989.

[16] Alcator Group, *"The Physics and Engineering of Alcator C-Mod"*, MIT Plasma Fusion Center Report PFC/RR-88-11, 1988.

[17] Alcator Group, internal communications, July 1995.

[18] W. Beck, "Alcator C-Mod Toroidal Field Magnet Assembly", in *Proc. of the 14th IEEE/NPSS Symposium on Fusion Engineering*, San Diego, October 1991.

[19] H. Becker, internal communication, June 1994.

[20] G. Tinios, *"Axisymmetric Control in Alcator C-Mod"*, Doctoral Dissertation, M.I.T. Department of Nuclear Engineering, 1995.

[21] B. LaBombard, B. Lipschultz, S. Kochan, "Design of Limiter/Divertor First-Wall Components for Alcator C-Mod", in *Proc. of the 14th IEEE/NPSS Symposium on Fusion Engineering*, San Diego, October 1991.

[22] T. Luke, J. H. Irby, *Bull. Am. Phys. Soc.*, **34**, 1989.

[23] T. Luke, J. H. Irby, *Bull. Am. Phys. Soc.*, **35**, 1990.

[24] T. C. T. Luke, *"Measurement of Particle Transport Coefficients on Alcator C-Mod"*, Doctoral Dissertation, M.I.T. Department of Physics, 1994.

[25] B. Labombard, *"Edge Database Dictionary"*, unpublished on-line document, MIT Alcator-group, June 1994.

[26] R. Watterson et al., *Bull. Am. Phys. Soc.*, **38 (10)**, p. 1955, 1993.

[27] B. Labombard, B. Lipschultz, D. Jablonski, *Bull. Am. Phys. Soc.*, **38 (10)**, p. 1955, 1993.

[28] D. Jablonski, B. Labombard, B. Lipschultz, J. Weaver, Y. Habib, *Bull. Am. Phys. Soc.*, **38 (10)**, p. 1955, 1993.

[29] B. Labombard, private communication, Nov. 1994.

[30] J. P. Gunn, C. Boucher, B. L. Stansfield, S. Savoie, *Rev. Sci. Instrum.*, **66 (1)**, p. 154, Jan. 1995.

[31] B. Labombard, private communication, May 1995.

[32] D. Johnson et al., *Bull. Am. Phys. Soc.*, **39 (7)**, p. 1670, 1994.

[33] E. E. Thomas Jr., *"The Development of an Omegatron Plasma Ion Mass Spectrometer for Alcator C-Mod"*, Masters Thesis, M.I.T. Department of Physics, 1993.

[34] J. L. Terry, J. A. Snipes, C. Kurz, *Rev. Sci. Instrum.*, **66 (1)**, p. 555, January 1995.

[35] J. L. Terry et al., *Bull. Am. Phys. Soc.*, **38 (10)**, p. 1955, 1993.

[36] C. Kurz, J. A. Snipes, J. L. Terry, B. Labombard, B. Lipschultz, G. M. McCracken, *Rev. Sci. Instrum.*, **66 (1)**, p. 619, January 1995.

[37] C. Kurz, *"Tomography of Light Emission from the Plasma Edge of Alcator C-Mod"*, Doctoral Dissertation, M.I.T. Department of Nuclear Engineering, 1995.

[38] R. Childs, J. Goetz, M. Graf, A. Hubbard, J. Rice, and T. Toland, "Design, Control and Operation of the Vacuum and Gas System for Alcator C-Mod", in *Proc. of the 15th IEEE/NPSS Symposium on Fusion Engineering, Haynnis, October 1993.*

[39] J. L. Terry, private communication, May 1995.

[40] V. Zanza, D. Frigione, *Bull. Am. Phys. Soc.*, **39 (7)**, p. 1567, 1994.

[41] J. A. Urbahn, *"The Design and Performance of a Twenty Barrel Hydrogen Pellet Injector for Alcator C-Mod"*, Doctoral Dissertation, M.I.T. Department of Nuclear Engineering, 1994.

[42] D. Jablonski, B. Labombard, B. Lipschultz, G. M. McCracken, *Bull. Am. Phys. Soc.*, **39 (7)**, p. 1670, 1994.

[43] D. Jablonski, private communication, Dec. 1994.

[44] MKS-626 Baratron Type Absolute Pressure Transducer is a product of *MKS Instruments, Inc.*, Andover, MA, 1993.

[45] MKS-131 Baratron Type Absolute Pressure Transducer is a product of *MKS Instruments, Inc.*, Andover, MA, 1976.

[46] C. Tilford, oral presentation at the American Vacuum Society New England Chapter Dinner Meeting, Cambridge, Feb. 15, 1995.

[47] G. D. Martin, Jr., in *1961 Transactions of the 8th Vacuum Symposium and 2nd International Congress of the American Vacuum Society*, Pergamon, New York, p. 476, 1962.

[48] A. R. Filippelli, *J. Vac. Sci. Technol. A*, **5 (2)**,. p 249, 1987.

[49] P. C. Arnold and S. C. Borichevsky, *J. Vac. Sci. Technol. A*, **12(2)**, p. 550, 1994.

[50] D. G. Bills, *J. Vac. Sci. Technol. A*, **12(2)**, p. 574, 1994.

[51] P. C. Arnold, D. G. Bills, M. D. Borenstein, and S. C. Borichevsky, *J. Vac. Sci. Technol. A*, **12(2)**, p. 580, 1994.

[52] VARIAN-843 Ratiomatic Ionization Gauge Control is a product of *Varian, Inc.*, Lexington, MA, 1978.

[53] A. Niemczewski, internal communication to the Alcator-group, March 1995.

[54] H. F. Dylla, *J. Vac. Sci. Technol.*, **20(2)**, p. 119, 1982.

[55] B. L. Stansfield, B. Bergevin, J. M. Larsen, *J. Vac. Sci. Technol. A*, **4 (5)**, p. 2284, 1986.

[56] N. Ogiwara, and M. Maeno, *J. Vac. Sci. Technol. A*, **6(5)**, p. 2870, 1988.

[57] G. Lewin and G. Martin, PPL Report MATT-203, 1963.

[58] G. Haas et al, *J. Nucl. Mater.*, **121**, p. 151, 1984.

[59] G. Haas, US Patent No. 4792763.

[60] S. S. Medley, *Rev. Sci. Instrum.*, **66 (1)**, p. 297, January 1995.

[61] ATE-6-50M Automatic Test Equipment Power Supply is a product of *Kepco, Inc.*, Flushing, NY, 1976.

[62] A. Niemczewski, *"The Ratiomatic and Divertor Gauge Instructions"*, unpublished on-line document, MIT Alcator-group, Dec. 1994.

[63] J. Bosco, S. Fairfax, *"The Alcator C-Mod Control System"*, in Proceedings of the 14th IEEE/NPSS Symposium on Fusion Engineering, San Diego, October 1991.

[64] C. C. Klepper, private communication, October 1993.

[65] G. Haas, private communication, Feb. 1994.

[66] S. Wolfe, *"Bgage_Vac"*, unpublished on-line document, MIT Alcator-group, Apr. 1994.

[67] T. A. Delchar, *"Vacuum Physics and Techniques"*, Chapman & Hall, London, 1993.

[68] G. J. Schulz and A. V. Phelps, *Rev. Sci. Instrum.*, **28**, p. 1051, 1957.

[69] G. Lewin and G. Martin, *Rev. Sci. Instrum.*, **33,** p. 447, 1962.

[70] C. C. Klepper, T. E. Evans, G. Haas, G. L. Jackson, R. Maingi, *J. Vac. Sci. Technol. A*, **11 (2)**, p. 446, 1993.

[71] A. Niemczewski, B. Lipschultz, B. Labombard, G. M. McCracken, *Rev. Sci. Instrum.*, **66 (1)**, p. 360, January 1995.

[72] B. LaBombard, J. Goetz, C. Kurz, D. Jablonski, B. Lipschultz, G. McCracken, A. Niemczewski, et al., *Phys. Plasmas*, **2(6),** p. 2242, 1995.

[73] T. W. Petrie et al., *J. Nucl. Mater.*, **196-198**, p. 848, 1992.

[74] G. Janeschitz et al., *Proc. 19th European Conference on Controlled Fusion and Plasma Physics*, Innsbruck, EPS, Petit-Lancy, Switzerland, Vol. **16C**, Part II, p. 727, 1993.

[75] G. F. Matthews, *J. Nucl. Mater.*, **220-222**, p. 104, 1995.

[76] P. C. Stangeby, *Nucl. Fusion*, **33**, p. 1695, 1993.

[77] T. W. Petrie et al., *J. Nucl. Mater.*, **196-198**, p. 848, 1992.

[78] Ph. Ghendrich et al., *J. Nucl. Mater.*, **220-222**, p. 305, 1995.

[79] B. LaBombard for the Alcator group, *"Divertor Detachment and 'Death-Rays' on Alcator C-Mod"*, Euratom/DOE Workshop on Plasma Edge and Divertor Physics, Garching, May 1995.

[80] B. LaBombard et al., "Evidence of Strong Plasma-Neutral Coupling in the Alcator C-Mod Divertor", to appear in *Bull. Am. Phys. Soc.*, **40**, 1995.

[81] D. A. Knoll, P. R. McHugh, S. I. Krasheninnikov, and D. J. Sigmar, presented at *1995 Sherwood International Fusion Theory Conf.*, paper no. 1C26, Incline Village, Nevada, April 1995.

[82] D. A. Knoll et al., "Characterization of C-Mod Like Detached Divertor Plasmas", to appear in *Bull. Am. Phys. Soc.*, **40**, 1995.

[83] A. Niemczewski, B. LaBombard, B. Lipschultz, G. McCracken, *"Neutral Gas Compression in the Alcator C-Mod Divertor, Experimental Observations"*, MIT Plasma Fusion Center Report PFC/RR-94-13, November 1994.

[84] S. J. Fielding, P. C. Johnson, and D. Guilhem, *J. Nucl. Mater.*, **128-129**, p. 390, 1984.

[85] G. L. Jackson et al., *Bull. Am. Phys. Soc.*, **32**, p.1899, 1987.

[86] S. L. Allen et al., *J. Nucl. Mater.*, **162-164**, p. 80, 1989.

[87] G. Haas et al., *Proc 18th European Conf. on Controlled Fusion and Plasma Physics*, Vol. III, p. 101, Berlin, 1991.

[88] G. Haas et al., *J. Nucl. Mater.*, **196-198**, p. 481, 1992.

[89] D. Reiter, "Neutral gas transport in fusion devices: Atomic and surface data aspects", in *Atomic and Plasma-Material Interaction Processes in Controlled Thermonuclear Fusion* (R. K. Janev and H. W. Drawin eds.), Elsevier Science Publishers, Amsterdam, 1993.

[90] D. B. Heifetz et al., *J. Comp. Phys.*, **46**, p. 309, 1982.

[91] D. B. Heifetz and D. E. Post, *Computer Phys. Comm.*, **29**, p. 287, 1983.

[92] D. P. Stotler et al., in *Proc. 15th. IAEA Intl. Conf. on Plasma Physics and Controlled Nuclear Fusion Research*, paper no. D-3-III-1-2(R), Seville, Spain, Sept. 1994.

[93] D. Stotler, internal communication, Sept. 1994.

[94] M. Fenstermacher, oral presentation during *36th Annual Meeting of the APS Division of Plasma Physics*, Minneapolis, November 1994.

[95] R. Vesey et al., "Neutral Particle Modeling of Alcator C-Mod Divertor Plasmas", to appear in *Bull. Am. Phys. Soc.*, **40**, 1995.

[96] J. Irby, private communication, Dec. 1994.

[97] M. Keilhacker, K. Lackner, K. Behringer et al., *Phys. Scr.*, **T2/2**, p. 443, 1982.

[98] F. Wagner and K. Lackner, in *Physics of Plasma-Wall Interactions in Controlled Fusion* (D. E. Post, R. Berish eds.), Proc. NATO Advanced Study Institute Val-Morin, Quebec, 1984, NATO ASI Series, Vol. 131, Plenum Press, New York, p. 931, 1986.

[99] J. Kesner, *Physics of Plasmas*. **2**, p. 1982, 1995.

[100] J. A. Goetz et al., *J. Nucl. Mater.*, **220-222**, p. 971, 1995.

[101] B. Lipschultz et al., "An Investigation of the Extent of Divertor Detachment in Alcator C-Mod", in *Proc 22nd European Conf. on Controlled Fusion and Plasma Physics*, Bournemouth, UK, 1995.

[102] C. H. Skinner et al., "Measurements of tritium recycling in TFTR; neutral hydrogenic velocities in TFTR and C-Mod", to appear in *Bull. Am. Phys. Soc.*, **40**, 1995.

[103] J. F. O'Hanlon, *"A User's Guide to Vacuum Technology"*, John Wiley & Sons, New York, 1989.

[104] D. R. Schultz, S. Yu. Ovchinnikov, and S. V. Passovets, *"Elastic and related cross sections for low energy collisions among hydrogen and helium ion, neutrals, and isotopes"*, to be published.

[105] R. K. Janev and H. W. Drawin eds., *"Atomic and Plasma-Material Interaction Processes in Controlled Thermonuclear Fusion"*, Elsevier Science Publishers, Amsterdam, 1993.

[106] D. E. Post, *J. Nucl. Mater.*, **220-222**, p. 143, 1995.

[107] H. C. Howe Jr., *J. Nucl. Mater.*, **111-112**, p. 424, 1982.

[108] D. Heifetz, D. Post, M. Petravic, J. Weisheit, and G. Bateman, Princeton Report PPPL-1843, 1981.

[109] G. F. Matthews et al., *Plasma Phys. Controlled Fusion*, **32 (14)**, p. 1301, 1990.

[110] C. S. Pitcher, *J. Nucl. Mater.*, **196-198**, p. 241, 1992.

[111] A. Niemczewski, G. McCracken, "Deuterium Retention by Molybdenum Walls of the Alcator C-Mod Tokamak", presented at *American Nuclear Society 1994 Student Conference, Eastern Region*, M.I.T., Cambridge, MA, March 1994.

[112] P. C. Stangeby, "The Plasma Sheath", in *Physics of Plasma-Wall Interactions in Controlled Fusion* (D. E. Post, R. Berish eds.), Proc. NATO Advanced Study Institute Val-Morin, Quebec, 1984, NATO ASI Series, Vol. 131, Plenum Press, New York, 1986.

[113] E. W. Thomas, R. K. Janev, and J. Smith, *Nucl. Instrum. Meth.*, **B69** ,pp. 427-436, 1992.

[114] H. S. W. Massey and E. H. S. Burhop, *"Electronic and Ionic Impact Phenomena"*, Oxford at the Clarendon Press, London, 1952.

[115] S. Krasheninnikov, private communication, Dec. 1994.

[116] R. V. Mehreblian, D. K. Holmes, *"Reactor Analysis"*, McGraw-Hill, New York, 1960.

[117] W. M. Stacey and J. Mandrekas, *Nuclear Fusion*, **34 (10)**, p. 1385, 1994.

[118] C. Kurz, private communication, June 1995.

[119] G. Janeschitz, M. Lesourd, J. Lingertat, G. Vlases, *Proc 20th European Conf. on Controlled Fusion and Plasma Physics*, Vol. II, p. 559, 1993.

[120] F. F. Chen, *"Introduction to Plasma Physics and Controlled Fusion, Vol. 1"*, Plenum Press, New York, London, 1984.

[121] B. Labombard, internal communication, May 1995.

[122] I. H. Hutchinson for the Alcator group, *"Overview of Alcator C-Mod Divertor Research"*, Euratom/DOE Workshop on Plasma Edge and Divertor Physics, Garching, May 1995.

[123] C. C. Klepper, *Nucl. Fusion*, **32 (5)**, p. 855, 1992.

[124] D. J. Campbell for the JET Team, in *Proc. 15th. IAEA Intl. Conf. on Plasma Physics and Controlled Nuclear Fusion Research*, paper no. IAEA-CN60/A-4-I-a, Seville, Spain, Sept. 1994.

[125] I. H. Hutchinson et al., "Plasma Shape Control: A General Approach and its Application to Alcator C-Mod", submitted to *Fusion Technology*.

[126] C. C. Klepper et al., *J. Nucl. Mater.*, **196-198**, p. 1090, 1992.

[127] M. Petravic, *J. Nucl. Mater.*, **145-147**, p. 841, 1987.

[128] C. G. Lowry et al., *"Comparison of Vertical and Horizontal Plate Operation with the JET Mark I Divertor"*, JET Report, 1994.

[129] D. P. Stotler, private communication, Dec. 1994.

[130] M. Shimada, G. M. McCracken, *J. Nucl. Mater.*, **220-222**, p. 89, 1995.

[131] D. B. Heifetz, M. I. Baskas, H. F. Dylla, and M. Ulrickson, *J. Nucl. Mater.*, **145-147**, p. 326, 1987.

[132] T. Loarer et al., *J. Nucl. Mater.*, **220-222**, p. 183, 1995.

[133] G. Haas et al., "Particle Exhaust and Wall Pumping in ASDEX Upgrade", in *Proc 22nd European Conf. on Controlled Fusion and Plasma Physics*, Bournemouth, UK, 1995.

[134] J. Ehrenberg et al., *J. Nucl. Mater.*, **196-198**, p. 992, 1992.

[135] P. Andrew, M. Pick, *J. Nucl. Mater.*, **220-222**, p. 601, 1995.

[136] A. Niemczewski, internal communication to the Alcator-group, April 1994.

[137] E. Marmar, private communication, July 1995.

[138] R. A. Causey, *J. Nucl. Mater.*, **162-164**, p. 151, 1989.

[139] R. K. Janev, W. D. Langer, K. Evans Jr., D. E. Post Jr., *"Elementary Processes in Hydrogen-Helium Plasmas"*, Springer Verlag, Berlin, 1987.

[140] F. J. de Heer, in M. R. C. McDowell, A. M. Ferendeci (Eds.), *"Atomic and Molecular Processes in Controlled Thermonuclear Fusion"*, New York, 351, 1980.

[141] A. Dalgarno, *Phil. Trans. Roy. Soc.* (London), **A-250**, p. 426, 1958.

[142] J. M. Wadehra, *Phys. Rev. A*, **20**, 1859, 1979.

[143] P. Bachmann and H. J. Belitz, *"Elastic Processes in Hydrogen-Helium Plasmas: Collision Data"*, Max Planck Institut für Plasmaphysik Report IPP 8/2, 1993.

[144] L. Spitzer, *"Physics of Fully Ionized Gases"*, Interscience Publishers, 1965.

[145] F. Wising, D. A. Knoll, and T. D. Rognlien, presented at *1995 Sherwood International Fusion Theory Conf.*, paper no. 2D24, Incline Village, Nevada, April 1995.

[146] B. Lehnert, *Physica Scripta*, **12**, p. 327, 1975.